INVESTIGATION OF ACTIVE SLIP SYSTEMS IN HIGH PURITY SINGLE CRYSTAL NIOBIUM

By

Derek Baars

A DISSERTATION

Submitted to
Michigan State University
in partial fulfillment of the requirements
for the degree of

Materials Science and Engineering – Doctor of Philosophy

2013

ProQuest LLC.
789 East Eisenhower Parkway
P.O. Box 1346
Ann Arbor, MI 48106 - 1346

ABSTRACT

INVESTIGATION OF ACTIVE SLIP SYSTEMS IN HIGH PURITY SINGLE CRYSTAL NIOBIUM

By

Derek Baars

The superconducting radio-frequency (SRF) community uses high purity niobium to manufacture SRF cavities for a variety of accelerator applications. Cavities are either made from large-grain sheets cut directly from the ingot and formed, or the ingot microstructure is broken down to form polycrystalline sheets or tubes. Reducing the number of costly electron beam welds to assemble the cavities is also desired. A greater understanding of the active slip systems and their relation to subsequent dislocation substructure would be of use in all these areas, to better understand how large grain niobium deforms and to develop more accurate computational models that will aid in the design and use of more cost-effective forming methods. Studies of slip in high-purity niobium suggest that temperature, material purity, and crystal orientation affect which slip systems are active during deformation, though have not examined the somewhat lesser purity niobium used for SRF cavities. As a step toward these goals, two sets of SRF-purity single crystal niobium samples were deformed to 40% strain in tension at room temperature. The first set was cut and welded back together. The second set consisted of deliberately orientated samples that resolved shear stress onto desired slip systems to evaluate different combinations of slip. Determining likely active slip systems was complex, though the evidence suggests that {112} slip may be dominant at yield at room temperature as suggested by theory, though {110} slip could not be ruled out.

To my incredibly patient wife, who believes in me.
To my parents, who told me to do my best and be whatever I wanted.

ACKNOWLEDGEMENTS

I sincerely thank my advisor Dr. Bieler, who always had time to answer questions. I also thank my graduate committee members Dr. Crimp, Dr. Grummon, and Dr. Grimm for all the time and energy spent to evaluate my progress.

Thanks to Chris Compton, my supervisor at the National Superconducting Cyclotron Laboratory.

Thanks to the organizations that supported me financially, MSU Department of Chemical Engineering and Materials Science, the National Superconducting Cyclotron Laboratory, and Fermi National Laboratory.

Last and certainly not least, thank you to all my fellow graduate students for your help, support, encouragement, instruction, and friendship.

TABLE OF CONTENTS

LIST OF TABLES

LIST OF FIGURES

KEY TO SYMBOLS AND ABBREVIATIONS

σ^*	Resolved shear stress (effective stress)
$\bar{u}$	Position on Peierls energy hill
b	Burgers vector
BCC	Body-centered cubic
BCP	Buffered chemical polish
BCS	Barden-Cooper-Schriefer
CPFEM	Crystal plasticity finite element modeling
CRSS, τ_{CRSS}	Critical resolved shear stress
D_k	The elastic interaction model taking kink diffusivity into account
E_{acc}	Average accelerating electric field
e-beam	Electron beam
EBSD	Electron backscatter diffraction
ECCI	Electron channeling contrast imaging
EDM	Electro-discharge machining
EI	Elastic interaction model
FCC	Face-centered cubic
FEGSEM	Field-emission gun scanning electron microscope
GND	Geometrically necessary dislocation
LAM	Local average misorientation
LT	Line tension approximation model

MRSS	Maximum resolved shear stress
Nb	Niobium
ODF	Orientation distribution function
OIM	Orientation imaging microscopy
OIM	Orientation imaging microscopy
PF	Pole figure
Q_0	Quality factor
q_s	Kink pair separation distance for unstable equilibrium for elastic interaction model
RF	Radio-frequency
RGSS	Resolved glide shear stress
R_S	Surface resistance
SEM	Scanning electron microscope
SRF	Superconducting radio-frequency
SSD	Statistically stored dislocation
T	Temperature
T_c	Superconducting transition temperature
TEM	Transmission electron microscopy
β	Fraction of the speed of light
Λ_A	Spatial resolution parallel to the tilt axis
Λ_P	Spatial resolution perpendicular to the tilt axis

$\varphi_1 \Phi \varphi_2$	Bunge Euler angle notation: phi one, phi, phi two

I. Introduction

A. A brief overview of Superconducting radio-frequency technology

Superconducting radiofrequency (SRF) technology is and will be used in state of the art heavy ion linear colliders, storage rings, recirculation linear accelerators, and free electron lasers [1]. The technology uses specially shaped cells and radiofrequency induction to generate powerful oscillating electromagnetic fields that resonate within the cells to accelerate a beam of charged particles [1]. The exact geometry of the cell depends on the resonating frequency, resonating mode, and fraction of the speed of light (β) to be achieved while operating [1]. Multiple cells are assembled in series into cavities. For example, Figure I-1 shows two very different cell geometries for different functions; Figure I-1a shows a cavity comprised of 7 elliptical cells designed to accelerate protons to ~80% the speed of light, while in Figure I-1b shows a cell that will be used to re-accelerate exotic ions to ~4% the speed of light. Cavities are then placed into cryomodules that are filled with liquid helium (4 K) to cool the cavity below the critical temperature, causing the cavity to enter the superconducting state [1]. A linear accelerator, for example, is ultimately composed of many cryomodules in series [1].

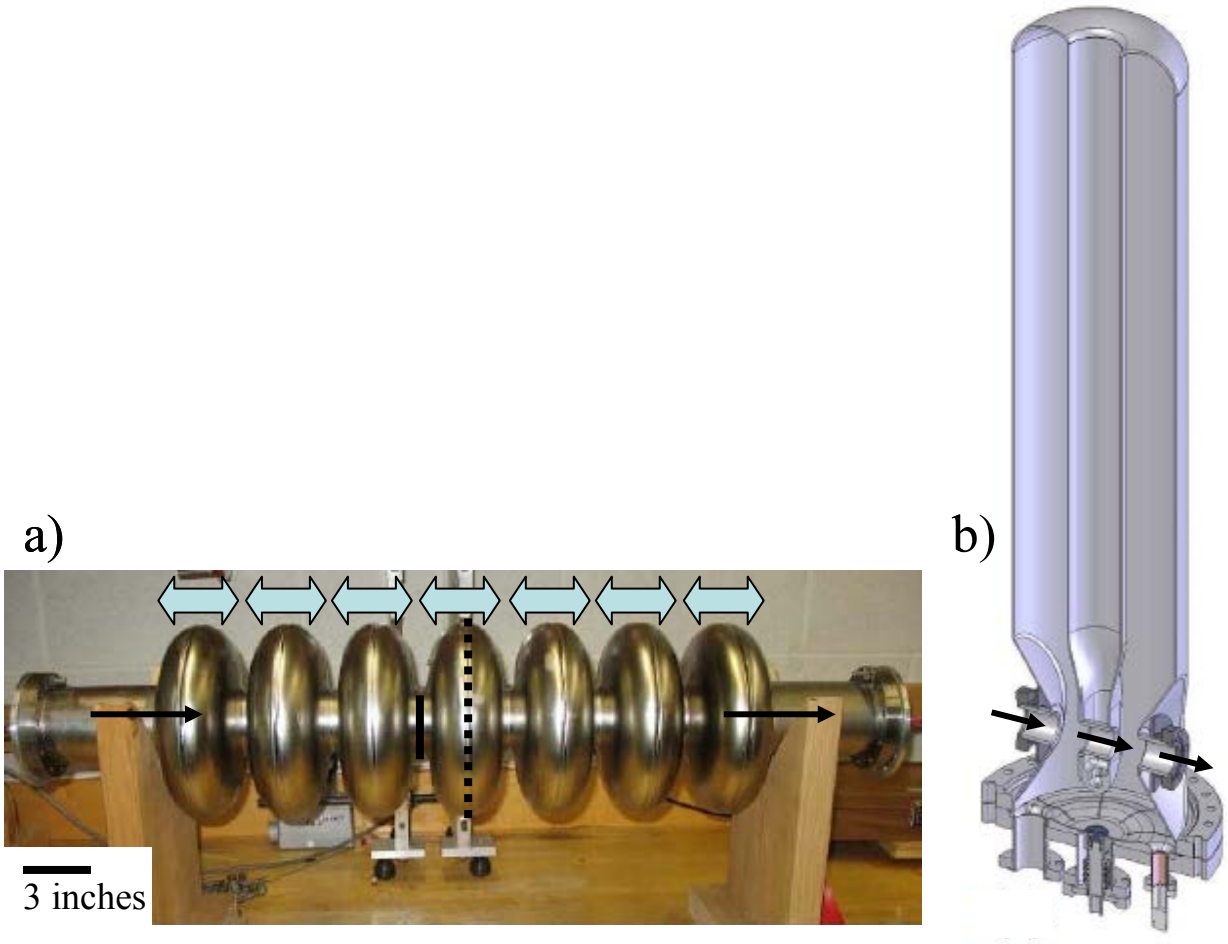

Figure I-1. Different shapes of niobium SRF cavities are motivated by different needs: a) a 7-cell 1.3 GHz β=0.81 elliptical cavity for a proton accelerator. The solid line is the iris and the dashed line is the equator of one of the cells. Block arrows indicate the oscillating EM field of each cell, which accelerates charged particles down the beam tube (black arrow). b) A niobium β=0.041 quarter-wave resonator cavity to be used for re-acceleration of exotic ion beams. For interpretation of the references to color in this and all other figures, the reader is referred to the electronic version of this dissertation.

B. A simplified overview of superconductivity in the context of SRF and niobium

High purity niobium (Nb) is often used as cavity material by the SRF community due to its high superconducting transition temperature (T_c = 9.2 K), ready availability in pure form, good ductility for ease of forming, and good thermal conductivity [1].

The cavities are cooled by surrounding them in liquid Helium to approximately 2-4K [1]. As the temperature drops below the superconducting transition temperature, electrons begin pairing off as Cooper pairs, transitioning to the superconducting ground state [1, 2]. The Cooper electron pairs cease to interact with the crystal lattice while the rest of the electrons remain normal conducting [1, 2]. The Cooper pairs still possess inertia, so when the time-varying electromagnetic fields used to accelerate the charged particles change direction, the Cooper pairs must also change direction [1, 2]. Because the Cooper pairs change direction, the time-varying surface magnetic field is not perfectly excluded from penetrating the inner rf surface of the cavity [1, 2]. The depth of penetration is called the skin depth, and is approximately 39 nm for niobium [1, 2]. This penetration induces a time-varying electric field in the skin depth, which causes the remaining normal conducting electrons to flow and change direction as well, including flowing through defects, and leading to the temperature-dependent BCS resistance [1, 2]. Chemical etching residue, sharp protrusions, foreign particles, and condensed gases on the rf surface of the cavity interact with the surface magnetic field, leading to the temperature-independent residual resistance [1]. The addition of the residual resistance to the BCS resistance gives the surface resistance [1]. Power dissipated by these resistances becomes heat that must be transported through the cavity wall and into the helium bath [1].

The quality factor (Q_0), which is the number of oscillations a resonator would take to dissipate its stored energy, is inversely proportional to the surface resistance (R_S) [1]. The electric field by which the charged particles are accelerated while passing through the cavity is often described as the average accelerating electric field (E_{acc}). Figure I-2 shows a plot of Q_0 versus E_{acc}, a common representation of cavity performance, which in this case shows the performance of a single crystal and polycrystalline niobium cavity are similar [3]. Higher values of Q_0 indicate more efficient power use, and higher values of E_{acc} result in higher particle velocities, which enable new physics to be explored [1]. While high E_{acc} is not always required by an application, e.g. medical equipment versus a particle collider, a high quality factor is always desired, as this can be directly related to lowering the cost of a cryogenic plant to keep the cavities at the desired temperature.

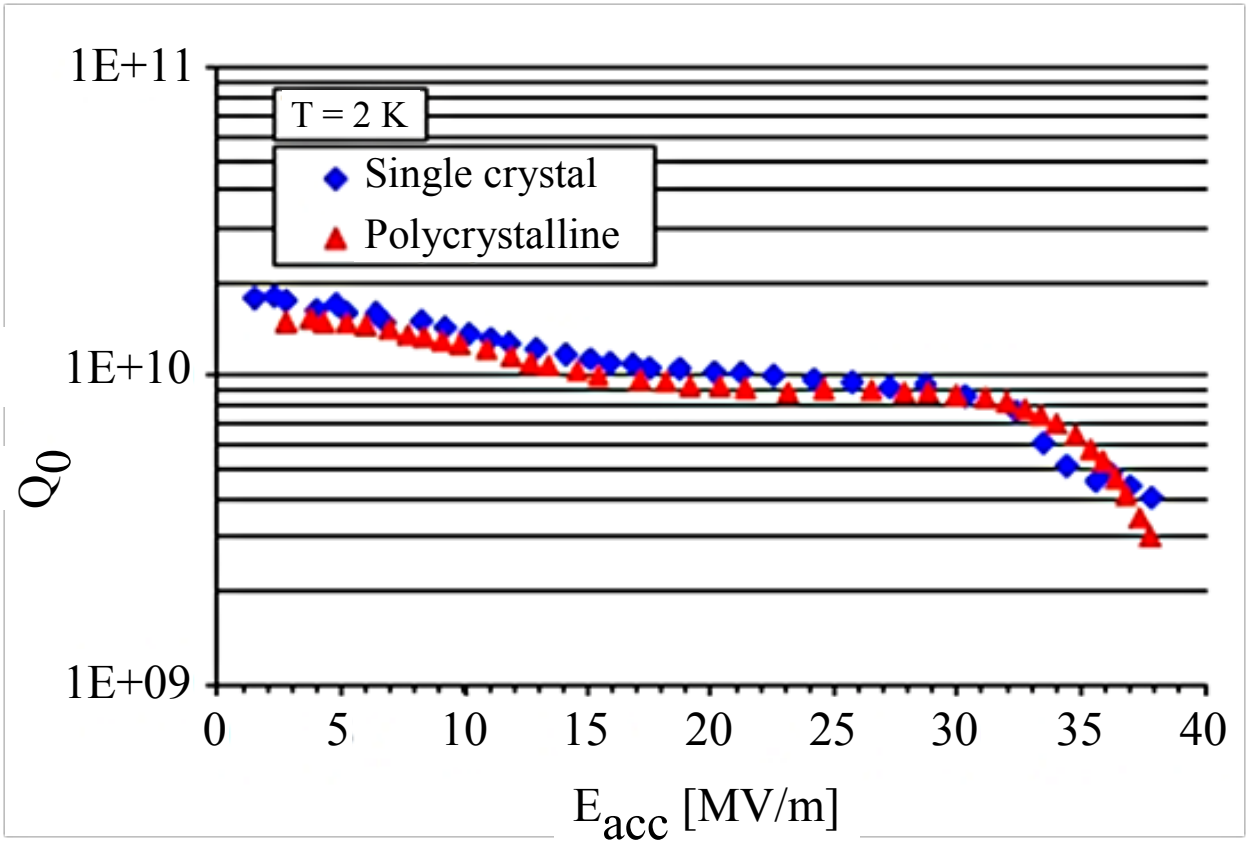

Figure I-2. Q_0 versus E_{acc} plot, used as a common representation of cavity performance [3].

C. Issues limiting cavity performance

A variety of defects can limit cavity performance. Broadly speaking, 'defects' are any sub-millimeter region of the cavity where the surface resistance is significantly higher than an ideal superconductor. Thermal breakdown at defects occurs when the temperature of a localized region of the cavity exceeds T_c and transitions out of the superconducting state lead to increasingly unstable power dissipation and eventual failure of the electric accelerating field, called a quench [4]. For this reason, high thermal conductivity is desired to quickly remove heat from the inner RF surface of the cavity to the outer helium bath [1]. At T_c, thermal conductivity is still dominated by the electron conductivity. At about 4 K there are enough remaining normal conducting electrons to effectively transport heat, even though there are many more Cooper pairs that are unavailable to transport heat. At about 3 K phonons (quantized lattice vibrations) dominate the thermal conductivity. The phonons also contribute to heat conduction above 3 K, though not significantly, because the number of phonons is inversely proportional to T^3, and the phonons are also scattered by the normal conducting electrons [1]. Interstitial impurities such as oxygen, nitrogen, hydrogen, and carbon scatter both electrons and phonons, and are especially detrimental to thermal conductivity.

Field emission is caused by foreign particles or sharp protrusions on the inner cavity surface that cause a build-up of locally high current density. These act as antennas off which electrons leave the cavity and re-impact the cavity wall, causing emission of x-rays and local heating that may lead to thermal breakdown, depending on the severity of the emission [1]. To prevent this,

cavities are cleaned by chemical etches at various stages of processing, and final assembly is done in clean rooms [1]. Field emission is considered the most common cause of cavity failures.

Multipacting is a resonant process that initially begins as a consequence of field emission, photoemission, or cosmic ray causing emission of an electron [1]. This electron is briefly accelerated by the rf fields and then impacts a nearby cavity wall, where secondary electrons are emitted off the rf surface [1]. These secondary electrons are accelerated and also impact a nearby cavity surface, and cause more secondary electron emission upon impact with the cavity wall, and so on, leading to thermal breakdown [1]. Multipacting has been reduced to a minor problem in most SRF cavity designs by changes to cavity shapes, and by pre-conditioning where pulsed-power processing vaporizes surface defects by a series of sharp increases and decreases in RF power [1].

Higher purity translates into better thermal conductivity, which removes the heat generated by defects and forestalls thermal breakdown, increasing the tolerance of the cavity for defects. The high purity is inextricably linked to overall cavity performance.

D. High purity leads to forming issues

To achieve the high purity needed for good thermal conductivity, niobium ingots are obtained using a high vacuum triple electron beam melting process [5]. The ingots are ~27cm in diameter, the cross-section of which typically consists of a few large grains occupying the center, with smaller grains (a few cm in diameter) at the edges where the temperature gradient was largest; occasionally only one grain occupies the center. The large grain size results from the lack of impurities that would otherwise pin the boundaries of growing grains, or act as nucleation sites for more grains; thus grain boundaries are highly mobile as the interior cools.

Ingots are then processed into sheet or tubes. Producing polycrystalline niobium sheet requires forging and rolling the ingots; however, the crystallographic texture of the rolled niobium sheets varies between batches, due in part to the difficulty of homogenizing deformation in such large grains, and leads to variability in forming properties [6]. Single or large grained discs cut directly from the cylindrical ingot are being considered as an alternative approach to the expense and problems of the polycrystalline sheet. The tradeoff is the mechanical deformation anisotropy, inherent in each of the few grain orientations of the disc, which must be taken into account when forming. Producing niobium tubes involves either bending sheet into a tube and welding, or forming a piece of a niobium ingot into a ring or a tube and then working it into a final tube shape.

Several popular options for forming niobium cavities are currently deep drawing, spinning, and a recent interest in hydroforming. Large-scale production will be needed for the proposed International Linear Collider (ILC), so that saving time and money are the major considerations behind the choices in forming path. The advantage of deep drawing is the conventionality of the fabrication path: (1) deep draw half-cells from sheets (either polycrystalline, large grain, or single crystal), (2) machine half-cell edges to tolerances, (3) electron-beam (e-beam) weld the half-cells together in series along with beam tube sections to assemble a multi-cell cavity (e-beam welding is most able to maintain the purity of Nb). The main drawback to deep drawing is the large number of expensive e-beam welds. Spinning and hydroforming both use tubes, and the advantage of both is a large reduction in the number of e-beam welds. The drawbacks of spinning are non-uniform thinning of the cavity wall and a deeper damage layer that requires more surface material removal by chemical etching [7]. The drawbacks with hydroforming have largely centered on poor formability due to poor quality tubes, whether welded, or extruded. A

common problem among all these forming processes, when using polycrystalline niobium, is a lack of texture homogeneity and grain size, which leads to variability in and problems with forming [8, 9].

Building an SRF accelerator such as the International Linear Collider, or other large scale application of SRF technology, would require producing cavities at an industrial scale, speed, and quality. The time and expense of e-beam welding (and the intrinsic difficulties with reproducibility in welding), and especially the large capital investment of purchasing many e-beam welding machines to finish cavity assembly in reasonable time frames, are weaknesses of the deep drawing manufacturing process. With proper texture control of tubes, or choice of crystal orientation, hydroforming should be more efficient than deep drawing. This problem was discussed during an open forum at the SRF 2009 conference in Berlin, where industry representatives complained: After a large project such as the International Linear Collider, to what project and to where would the excess capacity of e-beam machines go, and who would bear the capital investment cost? Investment in hydroforming machines may be better, as their utility for other manufacturing processes requires only changing the dies. To make this process viable, however, the ability to obtain tubes with sufficient forming properties requires much better understanding of how microstructure can be controlled, and hence, a better understanding of relationships between deformation processing, the activated slip systems, the dislocation substructure developed, and eventually recrystallization.

E. The need to first determine the active slip systems

Deliberate control of deformation and subsequent recrystallization is the basic method used by metallurgists to obtain a desired texture and microstructure in a polycrystalline metal. Before the relationship between the dislocation substructure and the recrystallization texture for SRF

purity niobium may be explored in detail, the active slip systems and resulting dislocation substructure must be investigated first. However, the nature of slip in BCC metals is complex. Prior studies investigating slip systems in single crystal niobium of many crystal orientations have been done using a higher purity than used for SRF cavities [10, 11]. The more recent studies assert that the elementary slip planes in niobium and other BCC metals depend on differences in the relaxation of screw dislocation cores affected by both temperature and purity [11]. Investigation of the slip systems of SRF purity niobium and comparison to these studies will help improve the understanding of the effect of crystal orientation and purity on slip systems.

In order to better understand the relationships between active slip systems, deformation substructure formed during processing, and recrystallization, this thesis will examine differently oriented niobium single crystals, deformed in the simpler case of uniaxial tension. The primary focus will be on determining the active slip systems and comparing results with prior studies of similar tests that used higher purity niobium [10, 11]. This examination is valuable for several reasons: it is a process that is under consideration for fabrication of cavities from slices of large grain or single crystals from ingots, expand the understanding of the effects of purity on the slip planes in niobium, provide a physical reference for computational modeling of large grain niobium deformation, and may be a simple enough experiment to permit fundamental study of the basic science of BCC slip systems.

II. Literature Review

A. Introduction

Greater understanding of the active slip systems in high purity niobium is desired, so foundational information about BCC slip systems is reviewed. First, a basic definition of dislocations is given. The role of dislocations and their motion to produce plastic deformation is explained using the example of uniaxial tension of a single crystal, which also introduces the effects of dislocation-dislocation interactions as deformation proceeds. These dislocation interactions lead to the formation of dislocation substructure, which often forms a large portion of the deformation substructure, so characteristics of dislocation substructure formation is also given. The failure of the Schmid law to adequately describe dislocation slip in high-purity body-centered cubic metals is exemplified in an early study on niobium, which is followed by the description of the relaxed screw dislocation core and other details that complicate slip in high-purity BCC metals. A recent theory describing the elementary slip planes of BCC metals and their dependency on temperature and purity is given. An overview of the orientation imaging microscopy (OIM) technique, which provides the crystal orientation at each point of a scanned area on a sample that are useful for calculating plane traces to examine slip traces and studying deformation substructure, completes the literature review.

B. Dislocation basics

The information in this section relies heavily on two standard works that describe dislocations [12, 13], and any information or diagrams that is not from those sources is referenced separately.

Dislocations are line defects within a crystal lattice with two 'pure' types, called edge or screw. Figure II-1a illustrates an edge dislocation, which is most easily thought of as an extra half-plane of atoms inserted into an otherwise perfect crystal lattice, much like inserting a half a sheet of paper into a stack of paper. Figure II-1b illustrates a screw dislocation as a block being sheared. In both cases the direction and amount of displaced lattice is the Burgers vector (b); for edge dislocations the Burgers vector is perpendicular to the line direction, while the Burgers vector is parallel to the line direction for screw dislocations. For either type, the slip plane is the plane of atoms that dislocation moves on, and contains the Burgers vector and line direction. In reality, dislocations are rarely straight and are mixed dislocations, where portions of their length have both edge and screw character. Dislocations may not end within an otherwise perfect crystal because they separate slipped and un-slipped crystal, and must terminate either on a free surface, grain boundary, or another dislocation. Dislocations may also terminate on themselves in the form of a dislocation loop. Dislocation loops form in a variety of ways and aid in the multiplication of dislocations that occurs during plastic deformation. One way that dislocations may be eliminated is by annihilation. Annihilation occurs when dislocations having opposite Burgers vectors, though are otherwise similar, meet and recombine into a whole plane.

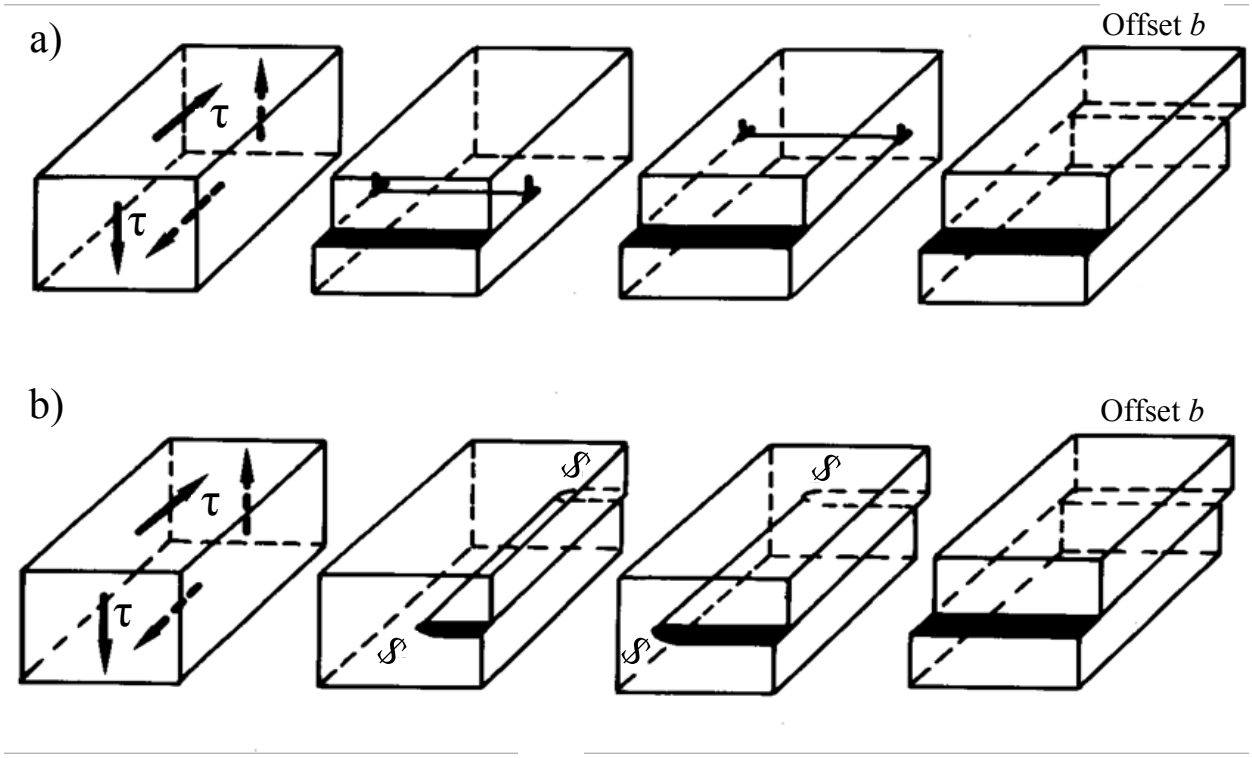

Figure II-1. Macroscopic deformation by glide of pure dislocations: a) Edge dislocation, b) Screw dislocation [14].

A dislocation may move, or 'glide', under an applied stress if a shear stress is resolved on the dislocation slip plane and in the direction of the Burgers vector. An edge dislocation, or a segment of a mixed dislocation having edge character, has a well-defined slip plane because of the necessary perpendicular relationship between the Burgers vector and line direction; the cross product of an edge dislocation Burgers vector and line direction equals the slip plane normal. A screw dislocation does not have a well defined slip plane because the Burgers vector and line direction are parallel, allowing screw dislocations or segments of screw character to 'cross-slip' onto any plane that contains the Burgers vector and a component of resolved shear stress.

Dislocations may also have steps along their length that have the same Burgers vector of the dislocation and behave according to the rules outlined above. A kink displaces the dislocation line within the same slip plane, so that for an edge dislocation the kink is of screw character, and for a screw dislocation the kink is edge character. In either case, the kink is highly mobile, as all motion is in the same slip plane. A jog moves the dislocation line to another parallel plane, so that for either an edge or screw dislocation the jog is of edge character, and now resides on a different slip plane than the rest of the dislocation. A jog on an edge dislocation may or may not be as mobile as the rest of the dislocation, because the resolved shear stress on the plane of the jog is almost certainly different than on the plane of the rest of the dislocation, and may not be sufficient to move the jog. A jog on a screw dislocation is not mobile with the rest of the dislocation unless assisted by a vacancy, a thermally activated process called 'climb'. The mobility, or lack thereof, of kinks and jogs help explain some of the non-intuitive deformation behavior of niobium and other BCC metals.

C. Tensile deformation of a single crystal

The thought experiment of an impurity-free single crystal deforming in uniaxial tension helps link the measured stress-strain curve, or more precisely the resolved shear stress-shear strain curve, to the motion and interactions of the dislocations that facilitate plastic deformation [14]. Dislocation interactions are governed by the interactions of stress fields, which surround a dislocation and are generated by the distortion of the crystal lattice caused by the dislocation; indeed all defects that distort the crystal lattice generate stress fields that govern interaction with each other [12, 13].

Figure II-2 shows a generalized resolved shear-stress-shear strain curve shows three different stages in the progression of dislocation interaction as shear strain increases, where changes in the slope of the curve indicate changes in dislocation interactions [14, 15]. The hypothetical single crystal tensile specimen is oriented such that a single slip system has a distinctly higher resolved shear stress than any of the other slip systems; this system will become the 'primary' slip system. Plastic deformation begins when the resolved shear stress equals the critical resolved shear stress (CRSS) on the primary slip system and causes dislocation glide. During Stage I, these dislocations glide through the crystal with little to no change in work hardening, or rate of increase of flow stress. As slip on the primary system proceeds, the sample becomes longer, causing the slip direction of the primary slip system to rotate toward the tensile axis. The distribution of resolved shear stresses on all the slip systems changes with this rotation, and eventually the resolved shear stress becomes great enough to cause dislocation glide on a secondary slip system. During Stage II, the work hardening increases as primary and secondary dislocations are halted by and pile up against each other. This occurs because the primary and secondary slip systems each have a different slip direction, causing the primary and secondary

dislocation lines to intersect and the stress fields of each slip system to interact with the other. During Stage III the resolved shear stress becomes high enough to force the primary and secondary dislocations to cut through each other, which is also a source of work hardening. However, the work hardening rate is often reduced in Stage III due to 'dynamical recovery', because the dislocations are more mobile again and annihilation may occur more often. The resolved shear stress required to activate the secondary slip system is typically greater than the CRSS of the primary system (for this simple example, the assumption that the CRSS of each slip system is the same is allowed), and is called 'latent hardening' because the prior activity of the primary slip system obstructs the activity of the secondary slip system.

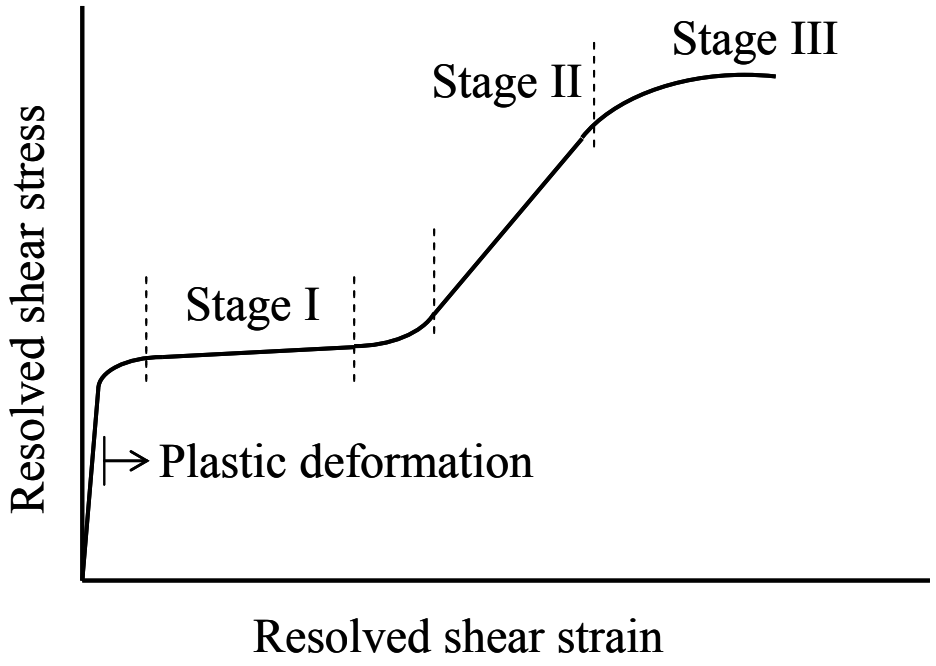

Figure II-2. Generalized shear stress-shear strain curve of a single crystal deformed in tension. Stage I consists of 'easy glide' with little work hardening (little increase in slope). In Stage II the large increase in work hardening results from piled-up dislocations. In Stage III work hardening results from dislocations cutting through each other [14, 15]

Frank loops are particularly strong sources of work hardening in BCC metals like niobium, and are formed by screw dislocations cutting through each other [14]. Figure II-3 illustrates the formation of Frank loops: a) Jogs form on intersecting screw dislocations as they cut through each other. These jogs are edge character and not mobile with the rest of the screw dislocation unless they gain additional thermal energy for climb. b) A screw dislocation pinned by jogs will bow out with increasing shear stress, and eventually the shear stress is great enough to force the jogs to move along the dislocation line and either annihilate, if of opposite sign, or combine with each other into superjogs (a jog of height greater than one plane spacing). c) Dislocation dipoles form due to the continued bowing of the screw dislocation. d) Eventually the bowed out screw dislocation reconnects with itself and breaks away from the jog, leaving behind a Frank loop (also called a prismatic loop). Frank loops are edge character and are a potent source of work hardening, because other passing dislocations may interact with the loop. Frank loops are very common in deformed BCC metals [14].

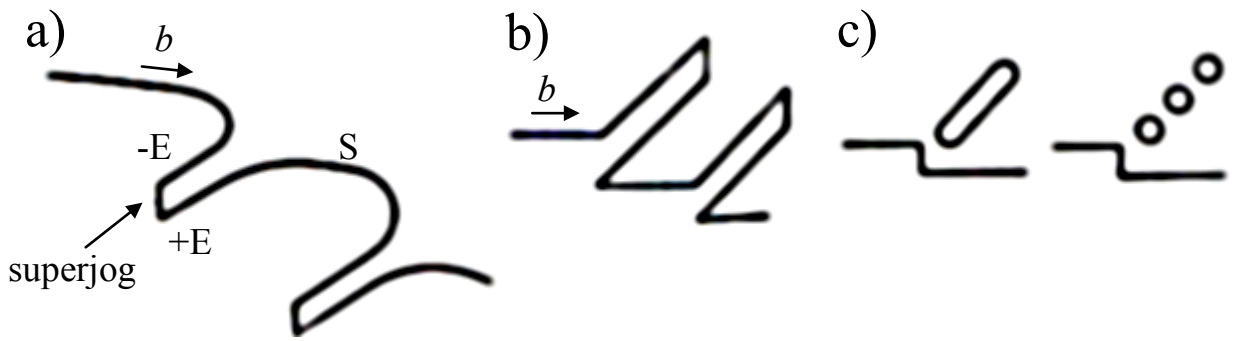

Figure II-3. Formation of Frank loops. a) a screw dislocation (S) of Burgers vector (*b*) bows out between superjogs and begins forming dislocation dipoles of edge character (+E, -E). b) Elongated dislocation dipoles. c) Frank loops may break into smaller loops (reproduced from [14]).

Dislocations that are pinned at one or both ends may become sources of dislocation multiplication, as increasing shear stress causes repeated cycles of dislocation lines or loops to form around and then break free of the source. Eventually an increasing back stress, due to the repulsion of the stress fields of dislocations crowded on the slip plane, disables the sources by sufficiently opposing the resolved shear stress [14].

The example above described the relatively simple case of a single crystal with a tensile axis oriented so that slip would occur on just one slip system at the beginning of deformation by tension. Slip on only one slip system is known as single slip, and in tension the slip direction of the active slip system will rotate toward the tensile axis [16]. The special case in which equal amounts of slip occurs on two slip systems simultaneously is called duplex slip [16]. The crystal direction that rotates toward the tensile axis is called the resultant slip direction, and is the vector sum of the slip directions of the two equally active slip systems [16]. For example, if the two slip directions were $[111]$ and $[1\bar{1}1]$, then the resultant slip direction would be $[101]$. The most general case of slip is called multiple slip, where two or more slip systems are active with unequal amounts of slip on each. The resultant slip direction still rotates toward the tensile axis during tension, and is still the vector sum of the active slip directions though each must be weighted according to the amount of slip contributed by each system [16]. An arbitrary shape change or deformation may require up to five independent slip systems operating together, so the dislocation interactions between slip systems are quite important [16].

Dislocation interactions with obstacles, mostly other dislocations in the case of high purity metals such as niobium, lead to the formation of dislocation substructure.

D. Dislocation substructure in single crystals

The deformed specimen has undergone a macroscopic shape change, and many dislocations remain within the deformed crystal lattice as tangled networks of dislocations, or dislocation substructure [17]. These remaining dislocations may be separated into two groups: statistically stored dislocations and geometrically necessary dislocations. Statistically stored dislocations are pairs of dislocations with opposite Burgers vectors that are near each other and would recombine into a whole plane, or annihilate, if they met. These pairs do not contribute to misorientation of the lattice, because the individual rotational contribution from one dislocation is cancelled by the opposite sign of the other dislocation in the pair. The new macroscopic shape is maintained by geometrically necessary dislocations, which are unpaired dislocations that accommodate the orientation gradient imposed by the macroscopic shape change. In a worked metal with no heat treatment, the statistically stored dislocation density is much greater than geometrically necessary dislocation density [17].

Dislocation substructures within a deformed single crystal tend to be planer, and are described as dislocation boundaries [18]. When slip is concentrated on one or two slip systems, dislocation boundaries tend to be oriented within 5° of the slip plane [18]. When slip is distributed onto many slip systems the dislocation boundaries tend to lie closer to the macroscopic highest stressed planes; for tension, the highest stressed planes are those tangent to a 45° cone about the tensile direction of the specimen [18].

These boundaries may be either geometrically necessary boundaries or incidental dislocation boundaries [19]. Geometrically necessary boundaries separate regions of the crystal that deformed via different sets of glide slip systems, and accommodate the difference in lattice rotations between those regions [19]. Geometrically necessary boundaries are arranged in

parallel families and have a special macroscopic orientation relative to the deformation axis [17]. Incidental dislocation boundaries further divide the regions between geometrically necessary boundaries into cells [20]. The cells are equiaxed regions of low misorientation relative to each other [17, 19]. The incidental dislocation boundaries consist of tangled glide and forest dislocations [19, 20]. As strain increases geometrically necessary boundaries increase in misorientation angle and decrease in spacing much more rapidly than incidental dislocation boundaries [17]. Incidental dislocation boundaries may eventually increase in misorientation enough that they become geometrically necessary boundaries [20]. Some of the geometrically necessary boundaries may already be or eventually become 'deformation induced' high-angle boundaries with additional strain, and are important later during recrystallization [17].

Depending on the relative orientations of the crystal and stress state, deformation may be homogeneously distributed with little or diffuse substructure formed, or heterogeneously localized such as deformation bands. Deformation bands are regions of rotated crystal lattice that form as different parts of the crystal deform and rotate via different sets of slip systems to particular end orientations in order to accommodate the applied strain [14]. The bands are often irregular in shape though elongated in the direction of principle strain [14]. Deformation bands are bounded by geometrically necessary dislocations, which accommodate the difference in orientation between the deformation band and surrounding lattice [14, 17]. The boundary is usually diffuse, indicating a gradual change in orientation (small orientation gradient) between the deformation band and the surrounding lattice [14].

The dislocations and dislocation boundaries, collectively called the dislocation substructure, evolve with and affect deformation of the niobium depending on the manufacturing process used (e.g. deep drawing, hydroforming) to produce an SRF cavity. A better understanding of

dislocation slip and dislocation substructure in niobium will be useful for more accurate modeling and predication of active slip systems for a given crystal orientation, and eventually, more accurate modeling of SRF cavity manufacturing processes.

E. An early study of the deformation of high purity single crystal niobium

Due to their close-packed atomic structure, dislocations in face-centered cubic (FCC) metals have a well-defined slip plane {111} and three <110> directions in which to move, and the active slip systems may be deduced from straight slip traces appearing on a properly polished sample. Yield by slip of FCC metals follows the Schmid law, that is, yield on a slip plane will occur at a critical resolved shear stress that is constant for a particular family of crystallographic slip planes [21]. The critical resolved shear stress is constant regardless of the slip system or sense (direction) of slip [21]. The Schmid law makes two assumptions that are not necessarily obvious though they are embedded in that definition [21, 22]. First, that the only component of the stress state causing dislocation motion is the resolved shear stress on the slip plane and in the slip direction [21, 22]. Second, the non-glide shear stress component, i.e. the normal stress perpendicular to the slip direction, does not affect dislocation motion [21, 22]. However, in niobium and other BCC metals the crystal lattice is not close-packed, and while the slip direction is defined as <111>, slip may occur on many planes, typically {110} and {112}. On polished samples of BCC metals, cross-slip of screw dislocations leads to wavy slip traces that roughly follow the plane trace of the maximum resolved shear stress (MRSS) plane [10, 23]. Previous studies investigating the active slip systems in high purity niobium using slip traces have shown that the Schmid law does not apply well to BCC metals, some of which are discussed next.

Early studies by Duesbery and Foxall investigated the deformation of high purity single crystal niobium, examining the effects of tension, compression, stress axis orientation,

temperature, and strain rate on the stress-strain behavior, slip line morphology, and active slip systems [10, 24]. Specimens were purified by electron beam zone-melting and by subsequent annealing above 2350 °C in a vacuum that never exceeded 2 x 10^{-10} Torr, to drive out impurities that have higher vapor pressures. Table II-1 lists the impurity contents reported for the specimens. While tension, compression, and ranges of temperature and strain rate were investigated, the data referred to in this section are restricted to that obtained in tension at room temperature (295 K) and a quasi-static strain rate (~10^{-4} s^{-1}), because those testing conditions are most similar to the testing conditions used in this thesis (see chapter III Materials and Methods).

Table II-1. The amount of impurities present in electron beam zone melted and vacuum annealed single crystal niobium tested by Duesbery and Foxall (impurity amounts were converted into atomic parts per million to ease comparison to Seeger [11])

Impurity	Amount (at ppm)
Tantalum	31
Tungsten	15
Oxygen	29
Nitrogen	33
Hydrogen	92
Carbon	85

Active slip systems were identified by plotting the rotation of the tensile axis due to deformation to determine the slip direction, and by slip trace analysis to determine the slip planes. The tensile axis was found by determining the crystal orientation from Laue back-scattered x-rays. Plotting the rotation of the tensile axis during deformation showed rotation toward the slip direction $[1\bar{1}1]$. The slip traces were observed with a light microscope using Nomarski interference contrast for fine lines, or oblique illumination when the lines became coarse, at progressive stages of deformation. Only long and straight slip traces were matched to slip planes, by comparing the angles of the observed slip traces to the tensile axis with those calculated using the crystal orientation. Only the angles calculated for {110} and {112} slip plane traces matched the observed slip trace angles.

Figure II-4 shows two stereographic projections containing possible tensile axis directions. In Figure II-4a the stereographic projection was divided into areas labeled according to the *theoretical* primary slip plane, assuming that slip should have occurred on the plane bearing the highest resolved shear stress and that the critical resolved shear stress was the same for all slip planes. The region near the [001] corner of the triangle is on the other side the [001]-[101] boundary because the authors wished to maintain a consistent $[1\bar{1}1]$ primary slip direction for all orientations. Figure II-4b shows a stereographic projection similar to Figure II-4a, though with the tensile axis of each of the specimens superimposed and labeled with the primary slip plane based on the *observed* slip traces; tensile axes of specimens resulting in observed {110} slip traces are indicated by black filled circles, {112} by open circles. Comparison of Figure II-4a with Figure II-4b shows a difference in the positions of the boundaries separating the calculated versus observed primary slip planes, which indicates that the critical resolved shear stress was different between the {110} and {112} family of planes, and even among the different {112}

planes. The ratios of the apparent critical resolved shear stresses (CRSS) in tension were 0.942 ± 0.003 τ_{CRSS} (121) = τ_{CRSS} (011) = 1.055 ± 0.008 τ_{CRSS} $(\bar{1}12)$. The dependence of the critical resolved shear stress on orientation among the {112} family of slip planes violates the stipulation in Schmid's law that the critical resolved shear stress be constant among a family of slip planes.

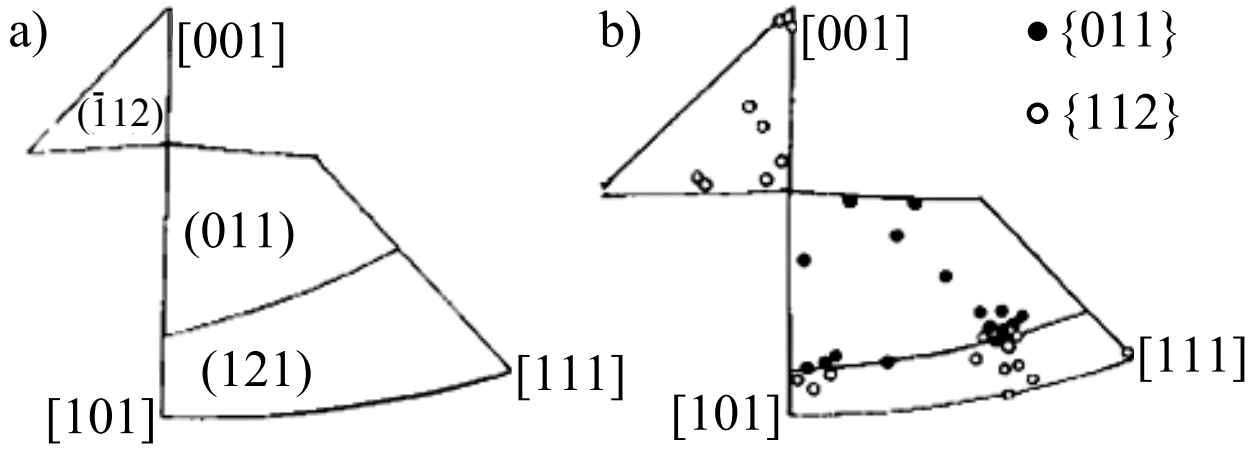

Figure II-4. Stereographic projections showing the dependence of: a) the theoretical primary slip planes and b) observed primary slip plane traces on the orientation of the tensile axis (reproduced and adapted from [10]).

The observed secondary slip systems were represented using stereographic projections similar to those used to represent the primary slip systems. Figure II-5 shows a stereographic projection with the tensile axes of the specimens plotted, each region labeled with the secondary slip system that matched the predominant observed slip traces[1]. If two or more slip systems matched an observed plane trace, the slip system possessing the highest resolved shear stress was chosen. While the presence of at least one other set of secondary slip traces for each specimen was mentioned, the details were not given. The observation of $[111](\bar{1}01)$ secondary slip was unexpected in the region near [001], because in this region the resolved shear stress is higher on a different {110} secondary slip system, $[111](0\bar{1}1)$.

[1] While not shown in this thesis, Figure 1(ii) in reference [24] also showed the expected operational secondary slip systems, depending on the position of a tensile axis within a similar stereographic projection, and based on the assumptions that the critical resolved shear stress was independent of slip system and that the operational system would have the highest resolved shear stress. However, that figure may contain a typo, as it gave the $[111](0\bar{1}1)$ slip system as having the highest resolved shear stress near the [001] corner of the projection, despite the $[111](\bar{1}\bar{1}2)$ slip system having the highest Schmid factors (and therefore highest resolved shear stresses) within that region of the projection. The boundary between the $[111](0\bar{1}1)$ and $[111](1\bar{2}1)$ slip systems near the $[101] - [1\bar{1}1]$ side of the projection also seemed to be inaccurate.

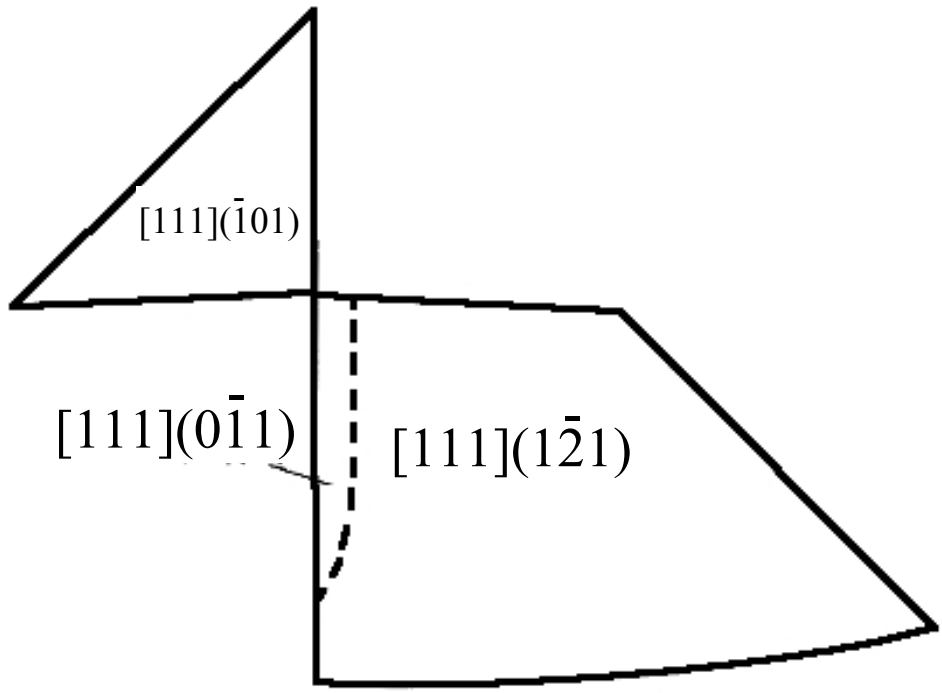

Figure II-5. Stereographic projection showing the dependence of the observed secondary slip plane traces on the orientation of the tensile axis (reproduced and adapted from [24]).

The stress-strain behavior was represented as shear stress-shear strain curves. The curves were calculated from the measured load-elongation data, according to single slip or multiple slip conditions based on the slip traces observed as shear strain increased.

Figure II-6 shows the shear stress-shear strain curves of specimens oriented such that the tensile axis was near the center of each region of differing primary slip. All the curves were similar to the generalized shear stress-shear strain curve having three stages of work hardening described earlier in Section II-C. Slip traces of these specimens were observed on two faces, the 'top' face from which the primary slip direction $[1\bar{1}1]$ emerged, and the 'side' face from which the secondary slip direction [111] emerged. The morphology of the slip traces, observed as the shear strain increased, was similar regardless of the primary slip plane family. During the transition from yielding into Stage I, the most distinct slip traces on the top face were long, only slightly wavy, and superimposed over other slip traces that were indistinct and homogenous. The more distinct slip traces of the top face were associated with slip traces on the side face that appeared straight and clustered as bands, leading the authors to suggest that those traces on each face were formed by the same screw dislocations. As Stage I progressed the slip traces on the top face became a much shorter and wavier network, as opposed to the long, mostly-straight appearance they had at the beginning of Stage I. Secondary slip traces were first observed on the side face at the end of Stage I. During the transition into Stage II, secondary slip traces formed an increasing number of bands at least 10-150 μm wide, often with another less intense band of a third slip plane nearby. During Stage II hills and valleys, which were roughly parallel to the primary slip trace, formed on the top face. The bands of secondary slip traces on the side faces corresponded with the valleys observed on the top face, while the spaces between secondary slip bands corresponded to the hills on the top face. Additional secondary bands continued to appear

during Stage II, and the bands became less distinct late in Stage II as the secondary traces began 'breaking out' or crossing the primary slip traces. Late in Stage II the hills of the top face developed a 'staircase' appearance and the slip traces corresponded to primary and secondary slip plane traces. During Stage III the secondary slip traces became coarser and covered the entirety of both faces.

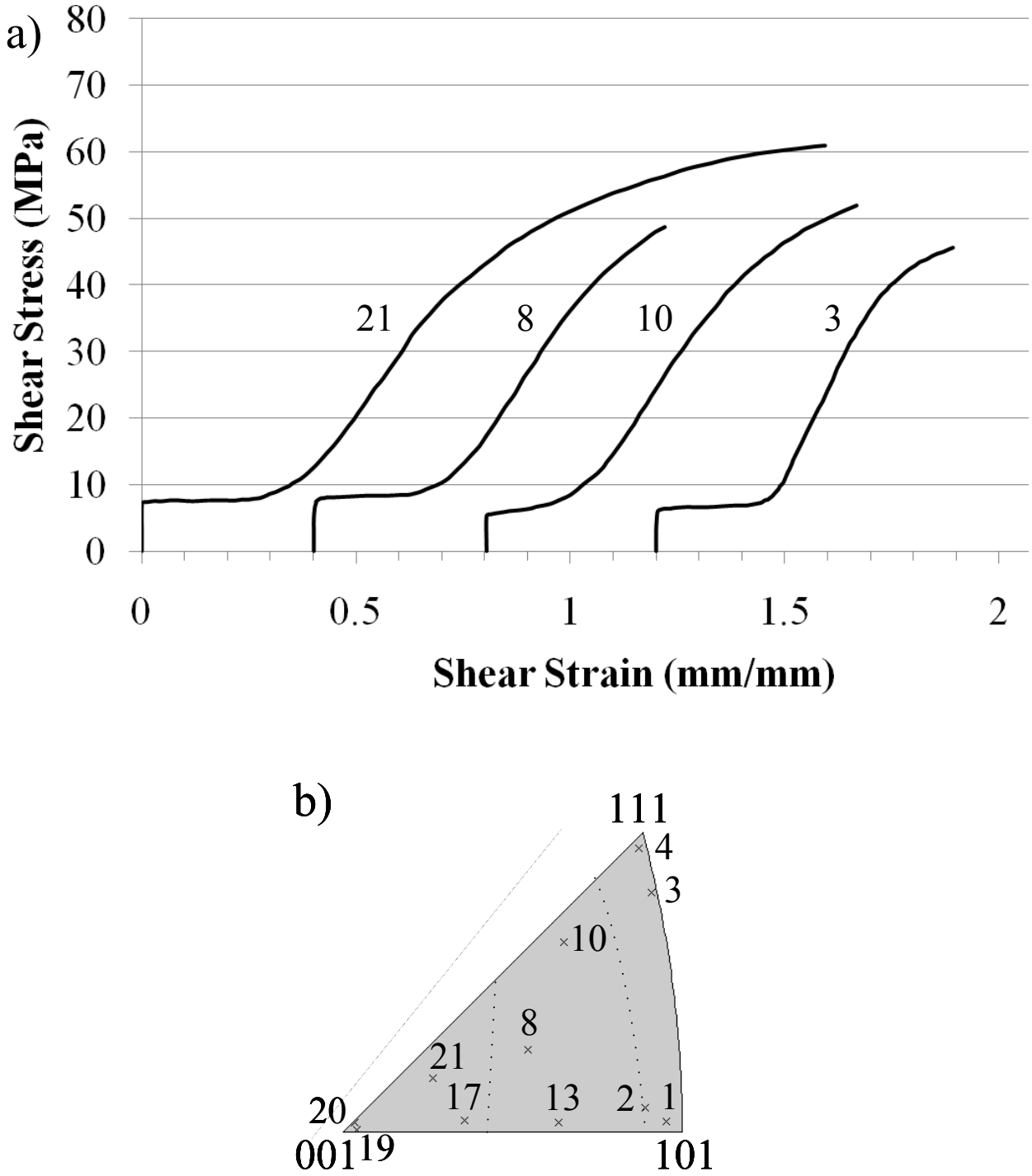

Figure II-6. a) The shear stress-shear strain curves for orientations away from symmetry boundaries. b) The reference triangle plots the tensile axis of D&F specimens to show the variation of shear stress-shear strain behavior with crystal orientation. The dashed lines are the boundaries between different observed primary slip planes from Figure II-4b (reproduced and adapted from [24]).

Figure II-7 shows the shear stress-shear strain curves of specimens oriented such that the tensile axis was near a multi-slip boundary or symmetry axes, that is, orientations for which multiple slip systems of different slip directions possess nearly equal resolved shear stresses. Specimens with the tensile axis close to a symmetry axis possessed high work hardening throughout deformation and no obvious linear stages. The work hardening rate depended on the number of equivalent systems; the highest work hardening rate belonged to specimen 19 oriented near [001] with four equivalent slip systems, followed by specimen 4 orientated near [111] with three equivalent slip systems, and then specimen 1 oriented near [101] with two equivalent slip systems. Specimens 20, 17, and 13 were oriented near the [001]-[101] symmetry boundary, along which the secondary slip system immediately possesses a resolved shear stress equal to that of the primary slip system. The slip traces observed for specimens with tensile axes oriented within 3° of the [001]-[101] boundary early in deformation consisted of bands approximately 150 μm wide of just one of the equally favored systems. At small strains, the slip traces consisted of crossing primary and secondary traces, and the discrete bands of a third slip plane observed for specimens with tensile axes oriented away from the boundary does not appear until later in deformation[2]. The slip traces for specimens oriented near the [001]-[111] boundary became very inhomogeneous, with different slip systems operating in different regions of the specimen.

[2] The description of the slip traces in reference [24] is occasionally vague, using terms such as "small" or "early" instead of referring to the three stages of deformation as the text had done elsewhere.

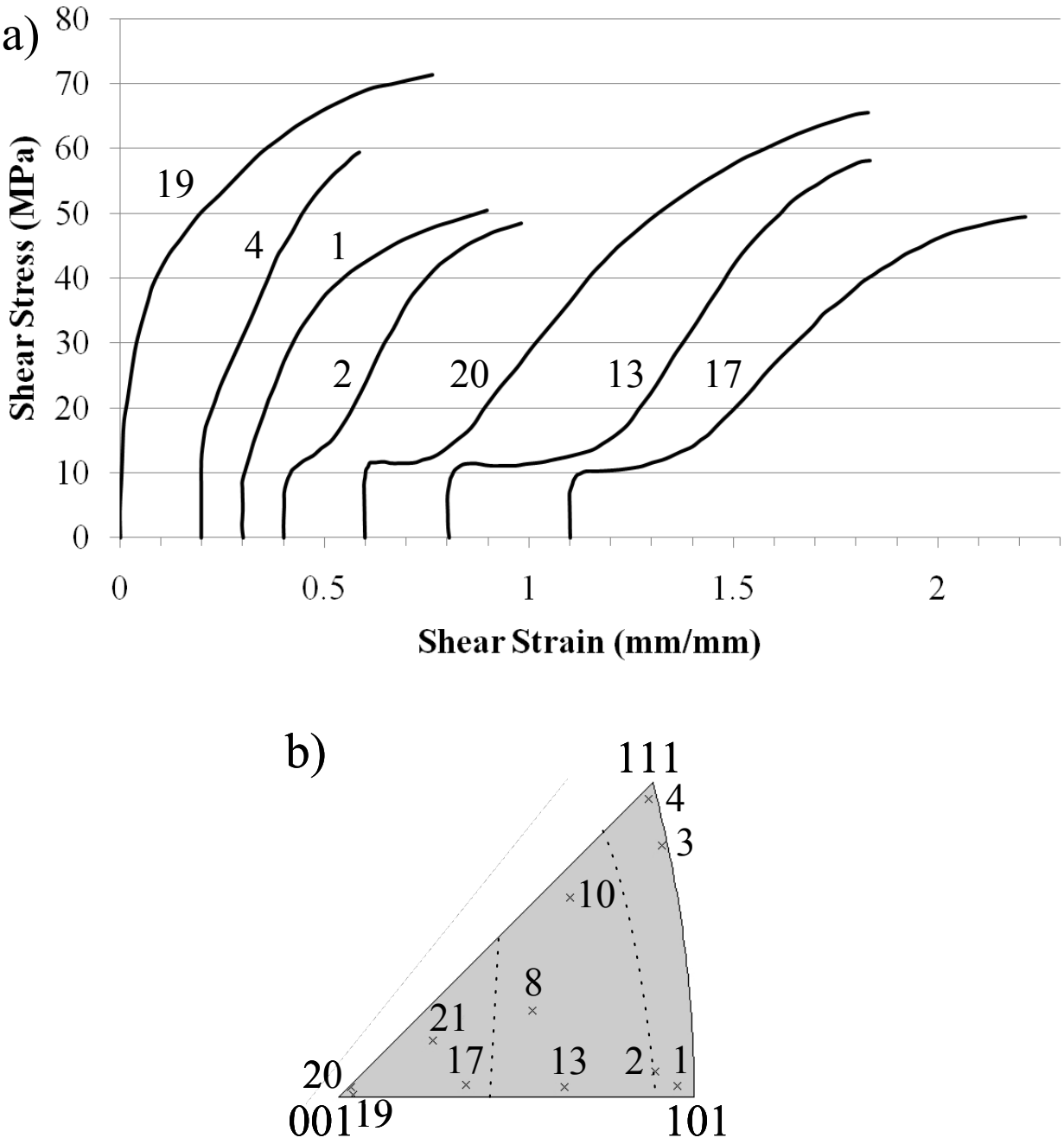

Figure II-7. The shear stress-shear strain curves for orientations near symmetry boundaries. Inset: The reference triangle plots the tensile axis of D&F specimens to show the variation of shear stress-shear strain behavior with crystal orientation. The dashed lines are the boundaries between different observed primary slip planes from Figure II-4b (reproduced and adapted from [24]).

This study demonstrated the failure of the Schmid law for BCC metals, and attributed the failure to the non-planer character of the BCC screw dislocation core. The 'anomalous' slip on a {110} plane having a resolved shear stress, which was only about half that of the primary {110} plane, would also be explained by the non-planer core of BCC screw dislocations in later studies discussed next [11, 25].

F. Recent theory of dislocations in high purity niobium and other BCC metals

The most important features of deformation in BCC metals are the rapid increase of the flow stress with decreasing temperature or increasing strain rate, the failure of the Schmid law, and dependence of the flow stress on orientation. These features are explained by the details of slip mechanisms in high purity BCC metals that are still emerging.

High voltage electron microscopy observations of dislocation motion during *in situ* strain tests indicate that edge dislocations are highly mobile in BCC metals, while screw dislocations have relatively low mobility [26, 27, 28]. Transmission electron microscopy observations show that this difference in mobility causes most edge dislocations to exit the crystal almost immediately after plastic deformation begins while leaving behind long drawn-out screw dislocations, and is further evidence that screw dislocations control the strain rate [25, 29].

In order to be mobile, straight dislocations must overcome Peierls barriers of the 1st kind, which are periodic energy potentials due to the atomic arrangement of the crystal lattice, and are different for dislocations of different character (i.e. edge versus screw) [25, 30]. The observed high mobility of the edge dislocations is due to the Peierls barrier being low, while screw dislocations have relatively lower mobility because the Peierls barrier is high [11, 25].

Two effects are thought to be responsible for the higher Peierls barrier: the twinning/anti-twinning asymmetry, and the non-planer screw dislocation core, which causes the screw dislocation to be influenced by non-glide shear stresses [31]. The twinning/anti-twinning asymmetry is the observation that less resolved glide shear stress is needed to move a screw dislocation in the twinning sense of slip than in the anti-twinning (opposite) sense. The twinning/anti-twinning asymmetry has been correlated to the energy required to displace an atom within a given slip plane in the direction of the Burgers vector. Figure II-8 visualizes this energy using a γ–surface, which is a contour map of the energy required to displace an atom from its unstressed equilibrium position to another location on the slip plane; in this case the energies were calculated using Finnis-Sinclair type central-force many-body potentials constructed and modified by Ackland, Thetford, and Vitek [32, 33]. Figure II-8 shows the γ–surfaces for the a) $(\bar{1}01)$ and b) $(\bar{1}2\bar{1})$ planes of molybdenum, and the c) $(\bar{1}01)$ and d) $(\bar{1}2\bar{1})$ planes of niobium. The upper x-axis and right-hand y-axis are ticked in terms of the lattice constant *a*, the contours are spaced every 200 mJ m^{-2}, every fifth contour is dashed to mark a J m^{-2} interval, and a solid-lined arrow represents the vector of a *a*/2[111] dislocation. The twinning sense of slip is in the [111] direction, and the anti-twinning sense in the opposite or $[\bar{1}\bar{1}\bar{1}]$ direction. A dashed-line arrow indicates the radius of dotted-lined circle. When a constant γ contour is closer to being circular, the less dependent the energy is on the direction of displacement, resulting in less asymmetry. The more centrosymmetric the surface, the less asymmetry there actually is on that slip plane between the twinning and anti-twinning sense of slip; in other words, the less of a twinning/anti-twinning effect is even present for that slip plane. Figure II-8a shows the $(\bar{1}01)$ plane of molybdenum, which happens to be the least centrosymmetric of the group VIB metals, while in Figure II-8c niobium shows that the $(\bar{1}01)$ plane is much more centrosymmetric,

implying that the twinning/anti-twinning asymmetry would be negligible should slip occur on the $(\bar{1}01)$ plane in niobium. Figures II-8b and II-8d show the $(\bar{1}2\bar{1})$ planes of molybdenum and niobium, respectively, and shows that the energy gradient for displacements in the [111] versus $[\bar{1}\bar{1}\bar{1}]$ direction is asymmetric in both molybdenum and niobium. However, while the asymmetry of the $(\bar{1}2\bar{1})$ plane is largest in molybdenum among the group VIB metals, the asymmetry for niobium is smaller than molybdenum, and is in fact the smallest among its own group, the group VB metals. That suggests that the twinning/anti-twinning effect in niobium should be small compared to molybdenum. Experiments on niobium at 77 K do claim that the critical resolved shear stress for an anti-twinning {112} plane is ~1.4-1.5 times that of a twinning {112} plane [34], while for molybdenum the critical resolved shear stress for an anti-twinning {112} plane is ~3 times that of a twinning {112} plane [33, 35, 36].

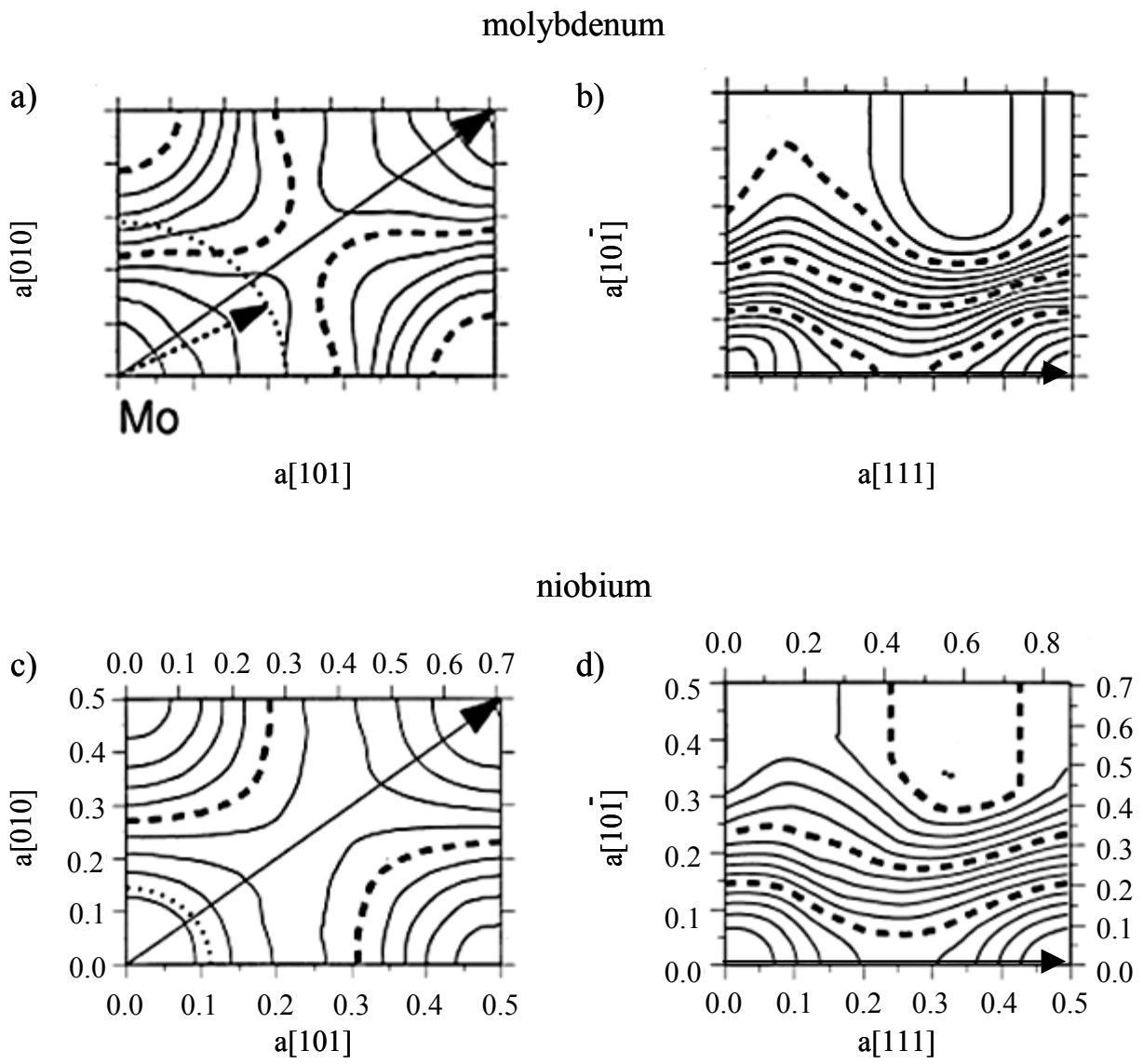

Figure II-8. The γ-surfaces for molybdenum a) $(\bar{1}01)$ and b) $(\bar{1}2\bar{1})$ planes, and for niobium c) $(\bar{1}01)$ and $(\bar{1}2\bar{1})$ planes. The upper x-axis and right-hand y-axis are ticked in terms of the lattice constant *a*, the contours are spaced every 200 mJ m^{-2}, every fifth contour is dashed to mark a J m^{-2} interval, and a solid-lined arrow represents the vector of a *a*/2[111] dislocation. The twinning sense of slip is in the [111] direction, and the anti-twinning sense in the $[\bar{1}\bar{1}\bar{1}]$ direction (reproduced and adapted from [31]).

The relationship between the crystal orientation and the stress state determines the sense of shear on the slip planes, which then determines whether slip on a {112} plane is in the twinning or anti-twinning sense. The rule dictated by the relationship between the crystal orientation and stress state is as follows [37]: Three {110} slip planes have a given <111> slip direction in common, and one of those three {110} planes will be closest to the maximum resolved shear stress plane; that is, the {110} plane with the highest resolved shear stress for the given <111> slip direction. Using the right-hand rule, the {112} plane normal rotated -30° about the given <111> slip direction relative to that {110} plane normal belongs to the twinning slip plane, and the {112} plane normal rotated +30° about the same <111> slip direction relative to that {110} plane normal is the anti-twinning slip plane normal. Table II-2 lists the possible combinations of twinning and anti-twinning {112} slip planes for a given slip direction and {110} plane with the highest resolved shear stress, based on the rule just described. The calculated relaxations of the screw dislocation cores that are described next do take the influence of the twinning/anti-twinning asymmetry (or lack thereof) on the {112} and {110} planes into account.

Table II-2. The twinning and anti-twinning {112} planes are listed according to slip direction and which {110} plane is closest the maximum resolved shear stress (MRSS) plane.

Slip Direction	{110} nearest MRSS	{112} nearest the {110}
$[111]$	$(1\bar{1}0)$	$(1\bar{2}1)$ Anti-Twinning $(\bar{2}11)$ Twinning
	$(\bar{1}01)$	$(\bar{1}\bar{1}2)$ Twinning $(\bar{2}11)$ Anti-twinning
	$(0\bar{1}1)$	$(\bar{1}\bar{1}2)$ Anti-twinning $(1\bar{2}1)$ Twinning
$[1\bar{1}1]$	(110)	(121) Twinning $(\bar{2}\bar{1}1)$ Anti-twinning
	$(\bar{1}01)$	$(\bar{1}12)$ Anti-twinning $(\bar{2}\bar{1}1)$ Twinning
	(011)	(-112) Twinning (121) Anti-twinning
$[\bar{1}\bar{1}1]$	$(1\bar{1}0)$	$(\bar{1}21)$ Anti-twinning $(2\bar{1}1)$ Twinning
	(101)	(112) Twinning $(2\bar{1}1)$ Anti-twinning
	(011)	(112) Anti-twinning $(\bar{1}21)$ Twinning
$[\bar{1}11]$	(110)	$(\bar{1}\bar{2}1)$ Twinning (211) Anti-twinning
	(101)	$(1\bar{1}2)$ Anti-twinning (211) Twinning
	$(0\bar{1}1)$	$(1\bar{1}2)$ Twinning $(\bar{1}\bar{2}1)$ Anti-twinning

The second cause for the higher Peierls barrier of the screw dislocation in high purity BCC metals is that the cores of the screw dislocations have relaxed onto symmetric planes of the <111> zone [11, 25]. Figure II-9 is an atomistic calculation of the screw dislocation core relaxation of niobium at 0 K with no external stress applied. The visualization method used is called differential displacements, which shows the relative displacements of neighboring atoms caused by: a) the screw components of the core, and b) the edge components of the core [31]. The [111] direction comes out of the page, and the atoms (dots) shown comprise three different layers separated by a distance of a/6[111], though the figure does not visually distinguish the different layers from each other. The plane traces of the {110} planes (solid lines) and {112} planes (dashed lines) belonging to the [111] zone are shown in the center of the figure, with the arrows on the dashed lines of the {112} planes indicating the twinning sense of slip; the displacement vectors are parallel to the plane trace of the plane the displacement occurs within. In Figure II-9a, the vectors indicate displacements caused by the screw component of the core relaxation, with the vectors parallel to the line between the two neighboring atoms. The direction of the vector represents the sign, and the length is normalized to the distance a/6[111]. In Figure II-9b the vectors indicate the direction of the relative displacements normal to the [111] Burgers vector caused by the edge components; the length is also normalized to a/6[111], though magnified by 15 times because otherwise the vectors would have been too small to see. The screw components shown in Figure II-9a are relaxed only on the three symmetric {110} planes; however, the non-glide stresses *do not* exert a force on the screw components of the core relaxation, and so *do not* affect the magnitude of the glide shear stress needed to move the screw dislocation [31]. The non-glide stresses *do* exert a force on the edge components of the core relaxation, and so *do* affect the glide shear stress needed to move the screw dislocation [31].

Figure II-9b shows that the edge components on the three symmetric {110} planes are very small; the edge components on the three symmetric {112} planes are also very small with little twinning/anti-twinning asymmetry, which is consistent with the minimal asymmetry of the {112} γ-surface of niobium shown previously in Figure II-8d [31].

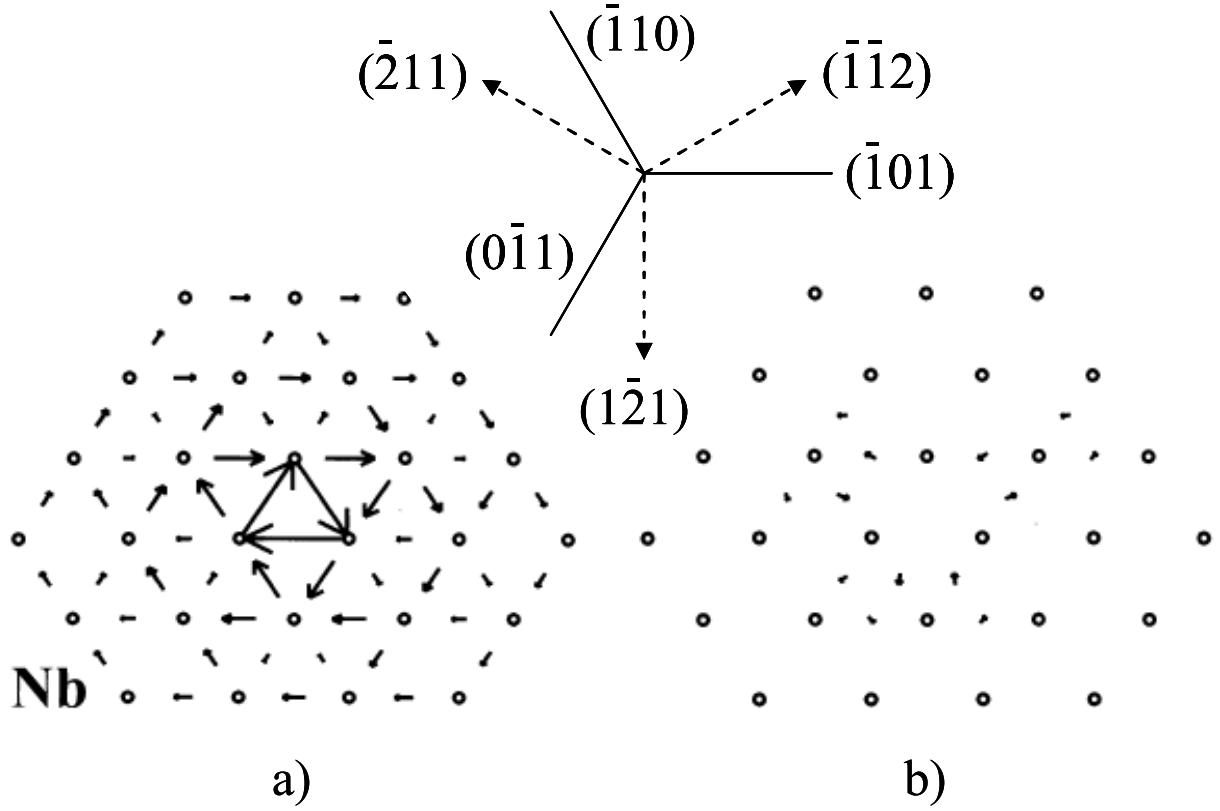

Figure II-9. The core structure of the a/2[111] screw dislocation in niobium as calculated at 0 K with no external stress applied. a) the screw components and b) the edge components. All the vectors shown were normalized to a/6 [111], though the vectors in b) were magnified 15 times by the original authors in order to be visible (reproduced and adapted from [31])

In order to move a dislocation, an external stress great enough to overcome the Peierls barrier must be applied. An external stress consists of several components: the glide shear stress, which can cause the dislocation to move, and the non-glide shear stresses, which cannot directly cause the dislocation to move [31]. The non-glide shear stresses do not usually affect the motion of dislocations with planer cores and thus may usually be ignored, i.e. typical dislocations in FCC metals that obey the Schmid Law (though there are special cases where the non-glide shear stresses are important for FCC metals) [31]. However, the edge components of the three-dimensional relaxed screw dislocation core in BCC metals do couple with the non-glide shear stresses, thereby distorting the core and changing the height of the Peierls barrier [31]. Depending on the relative orientation of the applied stress to the crystal orientation, the distortion may cause the Peierls barrier to become higher or lower, and thus the glide stress required to move the dislocation will become higher or lower. This helps explain the dependence of the flow stress on crystal orientation in BCC metals.

Figure II-10 is a differential displacement map of the relaxed niobium screw dislocation core at 0 K with a pure shear stress applied such that only a non-glide shear stress was produced, in order to observe the distortion of the core by the non-glide shear stress without causing the dislocation to glide; Figure II-10a shows the screw components and Figure II-10b shows the edge components [31]. The notation and visualization is similar to that used in Figure II-9, except that the location of the core has been moved one unit spacing to the left to better see the core rearrangement occurring to the right of the core, and is not a result of the external stress [31]. The non-glide stress only couples with the edge components of the relaxed screw dislocation core, and when comparing the un-stressed case and the purely non-glide shear stress case in Figure II-9b and Figure II-10b, respectively, the difference in niobium core relaxation

appears small [31]. The small difference implies that the effect of the non-glide shear stresses in niobium may also be small, at least for the core relaxation as calculated near 0 K [31].

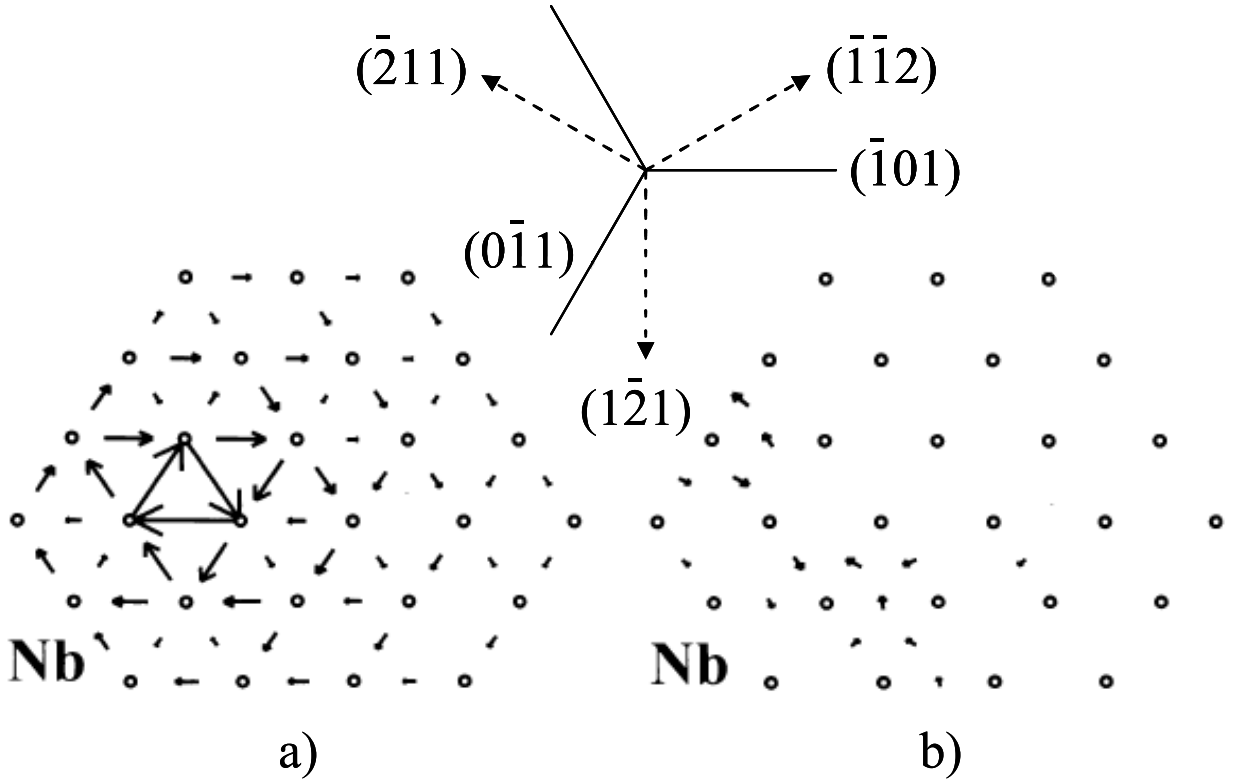

Figure II-10. The core structure of the a/2[111] screw dislocation in niobium as calculated at 0 K, distorted by an applied pure shear stress: a) the screw components and b) the edge components. All the vectors shown were normalized to a/6 [111], though the vectors in b) were magnified 15 times by the original authors in order to be visible (reproduced and adapted from [31]).

When a pure glide shear stress on the $(\bar{1}01)$ plane and [111] direction was computationally applied at 0 K in order to observe how the dislocation actually moved, the screw dislocation core moved by translation by successive steps on non-parallel {112} slip planes [31]. However, at finite temperatures higher than 0 K dislocations move by the kink-pair mechanism, and not by translation of the core as in the simplified case of 0 K [23]. Atomistic modeling of the screw core relaxation at finite temperatures has not been calculated at present, and the kink-pair mechanism is computationally intensive and does not appear to have been calculated yet either. Presently, the relaxation of the screw dislocation core at finite temperatures is assumed to occur in a qualitatively similar way, an assumption that appears to be acceptable given the results of the study examined later in this section, and other studies that examine dislocations using internal friction techniques [38, 39].

Figure II-11 is a simplified schematic showing how a screw dislocation moves via the thermally activated stress-assisted kink-pair mechanism in BCC metals. Figure II-11a shows the Peierls barriers of the 1^{st} kind as being asymmetrical hills to represent the twinning/anti-twinning asymmetry of {112} slip planes; Peierls barriers of the 1^{st} kind for {110} planes would be symmetric if the γ-surface was symmetric, and the twinning/anti-twinning asymmetry would be absent [25]. A resolved shear stress σ^* is able to shift the dislocation line up the side of the Peierls hill to position $\bar{u}$, though not enough to surmount the Peierls hill. Figure II-11b shows Figure II-11a viewed normal to the {112} plane, with the dislocation line shifted up the Peierls hill by the resolved shear stress. At finite temperatures pairs of kinks of opposite sign continuously form via thermal activation at locations along the length of the screw dislocation [25]. The distance between the kink pair at which they are in unstable equilibrium according to

elastic interaction is q_s and is determined in part by the resolved shear stress; if the resolved shear stress is too small the kink separation will be insufficient to keep the kinks from simply recombining (annihilating) [25]. A sufficient resolved shear stress, or critical resolved shear stress, provides enough separation to prevent the kinks from recombining [25]. The kinks separate further from each other at a velocity governed by diffusion, because the resolved shear stress has almost no effect on the remainder of the kink motion; the contribution to motion by the shear stress is very small because it is proportional to the very small length of the kink, so that the contribution to the kink motion by diffusion dominates [25]. The kinks are analogous to straight edge dislocations, so as the kinks move away from each other through the crystal lattice, the kinks still encounter Peierls barriers [25]. However, these are Peierls barriers of the 2^{nd} kind, also called 'kink potentials', and are low [25]. As the kinks continue to separate further from each other, the whole screw dislocation line will eventually surmount the Peierls hill (a Peierls barrier of the 1^{st} kind) and lie in the next Peierls valley [25].

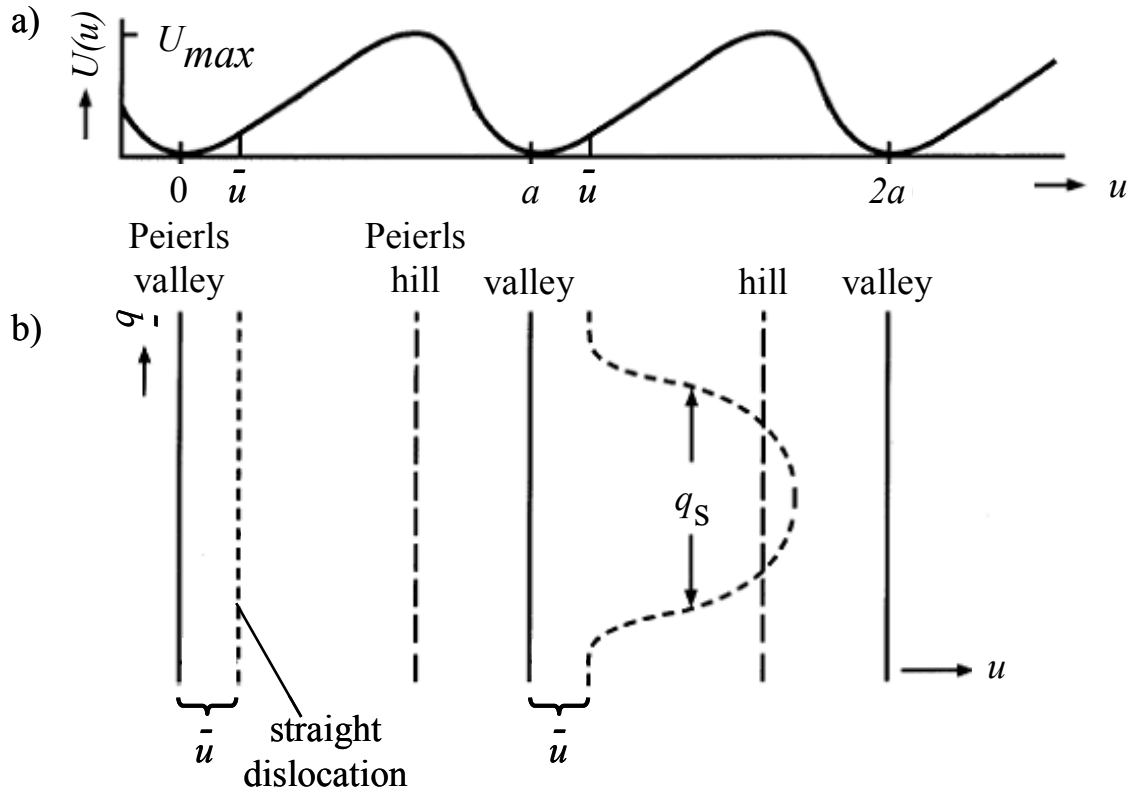

Figure II-11. A schematic of the kink pair mechanism: a) The Peierls barriers of the 1st kind U(u) with period a are shown as asymmetric hills to represent the twinning-anti-twinning asymmetry that is present on {112} planes in BCC metals; for {110} planes the barriers would be symmetric. The resolved shear stress moves the screw dislocation line up the Peierls hill by a distance $\bar{u}$. b) View normal to the {112} slip plane. At finite temperatures kink pairs form via thermal activation and surmount the Peierls hill. The distance between the kink pair at which they are in unstable equilibrium according to elastic interaction is q_s and is determined in part by the resolved shear stress; a sufficiently large resolved shear stress prevents the kink pair from annihilating, and allows the kinks to separate at a velocity controlled by diffusion (reproduced and adapted from [25]).

The observed increase in yield stress with decreasing temperature of BCC metals is attributed to the kink pair behavior in two ways. First, the frequency of kink pair formation is based on thermal activation and is therefore lower with decreasing temperature [25]. Second, the mobility of the kink pair is based on diffusion and is therefore lower with decreasing temperature [25].

In summary, the low-mobility screw dislocations in a high purity BCC metal control the strain rate because the height of the Peierls barrier is affected by the relaxed screw dislocation core, the twinning/anti-twinning effect, the non-glide shear stresses generated by the applied stress, and the available thermal energy.

G. Elementary slip planes in high purity niobium

Seeger sought to determine the elementary slip planes of the kink pairs in very high purity niobium by using careful cyclic-deformation technique experiments [11]. Very high purity niobium single crystals oriented such that the maximum resolved shear stress was resolved on the $[\bar{1}11](101)$ slip system were deformed in cycles of tension and compression in vacuum. Table II-3 lists an estimated maximum amount of each impurity present. A pre-deformation procedure, which consisted of cycling each specimen at 370 K with a resolved plastic shear-strain of 1.5×10^{-3} s^{-1} until a 'saturated' flow stress and stable hysteresis loop was obtained, ensured that a stable substructure was formed by large-scale motion of both screw and non-screw dislocations. Each specimen was then cooled in increments of 5 K, and cycled until a stable hysteresis loop was obtained and recorded for different plastic strain rates ranging from 6.5×10^{-5} to 3.5×10^{-3}. After about 50 cycles at different temperatures and strain rates, the substructure of each specimen was 'reset' using the pre-deformation process. Repeating these processes allowed hundreds of flow stress measurements to be done on each specimen while maintaining a

nearly constant substructure and crystallographic load axis. The resulting data are represented in Figure II-12 as curves for each strain rate in effective stress versus temperature space. Because the flow stress is controlled by screw dislocations, and screw dislocations move by the double kink mechanism, the appropriate models and equations of kink-kink interactions must be used to fit different portions of the curve to obtain the kink-pair formation enthalpy. At low temperatures and high effective stress the line tension approximation model is used (LT) [40], for moderate effective stress and temperature the elastic interaction with transition state approximation model is used (EI) [41, 42], and for low effective stress and high temperature the elastic interaction with adjustments taking kink diffusivity into account is used (D_k) [43]. The kink formation enthalpy may then be used to determine the kink height. The kink height determined by the cyclic deformation technique may be unambiguously matched to the slip plane on which the kinks must have formed, because the differences in spacing between the Peierls barriers for each slip plane family of the BCC crystal lattice are large enough. The kink height identified the {112} planes as the elementary slip planes in high purity niobium for the temperature range 120-350 K, which includes room temperature (300K) [11, 25].

Table II-3. The maximum possible impurity amounts for single crystal niobium used by Seeger *et. al* [11].

Impurity	Amount (at ppm)
Tantalum	<152
Oxygen	<8.5
Nitrogen	<7.3
Hydrogen	<47
Carbon	<8.5

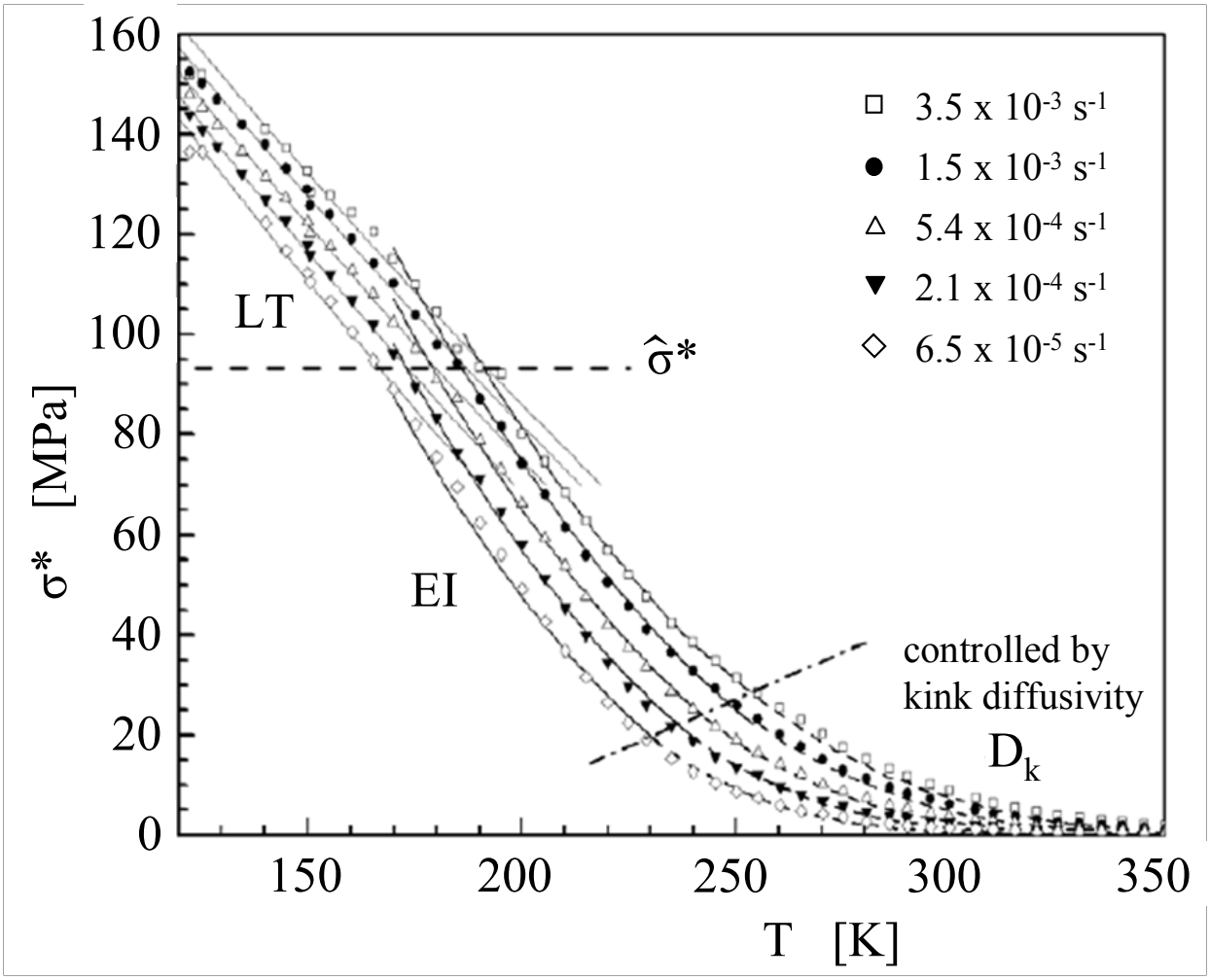

Figure II-12. Curves for each strain rate are plotted in effective stress (σ*) versus temperature (K) space. Each portion of the curve must be fit to the appropriate kink-kink- interaction model and equations, from which the kink formation enthalpy may be calculated that is in turn used to determine the kink height. The kink-kink interaction models are the line tension approximation (LT), the elastic interaction approximation (EI) where the transition state approximation holds, and finally the elastic interaction approximation where the kink diffusivity (D_k) must be taken into account. The boundaries between the models are indicated by dash-dotted lines. The ~93 MPa value of $\hat{\sigma}^*$ is the strain-rate-independent stress used as the transition between the line tension and elastic interaction approximation models (reproduced from [11]).

In summary: at room temperature, the structure of the a/2[111] screw dislocation core relaxation is not known. Relaxation is assumed to still occur, and in such a way that slip occurs on {112} planes [11, 25]. The literature refers to this the 'γ-relaxation', while this thesis will refer to it as the '{112} slip relaxation' simply to emphasize that this hypothetical relaxation results in slip on {112} planes. In order to move, the Peierls barrier is surmounted by the thermally activated, stress-assisted generation of a pair of kinks [44]. Because these kinks have an edge component, the kinks must have a well-defined slip plane. So-called elementary slip occurs on the {112} plane on which the kinks formed. Thus kinks locally determine the slip plane and enable a segment of the screw dislocation line to move and lie in the next energy valley [11, 25, 45]. Eventually the whole dislocation has moved by the action of the kinks moving in opposite directions along the rest of the screw dislocation line, causing it to surmount the Peierls barrier as they go [11, 25, 45]. As slip continues, kinks may form on one of the other {112} planes according to changes in the local stress state and thermal fluctuation. The distances over which elementary slip occurs between these cross slip events is unknown and may be as small as nanometers [11, 25]. The wavy appearance of slip traces is thought to be caused by frequent cross-slip [11, 25].

However, the relaxation of the screw dislocation core is dependent on temperature and on impurities. At a low enough temperature called the 'lower bend' temperature, for example less than about 70 K for molybdenum, the lack of thermal energy causes a change in the core relaxation, which restricts slip to {110} planes and causes the observed slip lines to become straight [11, 25]. The {110} slip relaxation (called β-relaxation in the literature) results in elementary slip on the {110} slip planes that is still controlled by the double kink mechanism. The low-temperature {110} slip relaxation is actually the ground state core relaxation, while the

{112} slip relaxation is the excited state that results from the increased thermal energy available above the lower bend temperature. However, because the transition of the screw dislocation core is a first order thermodynamic phase transition, the {110} slip relaxation may be stabilized and exist above the lower bend temperature [11, 25].

In niobium and other BCC metals, interstitial impurities may stabilize the {110} slip relaxation while the metal is above the lower bend temperature [11, 25]. In niobium of modest purity (<99.98 at%), interstitial impurities such as hydrogen or oxygen modify the screw core to the {110} slip relaxation [11, 25]. The {112} slip and {110} slip relaxations may coexist over a range of purities. At high purity, slip is dominated by elementary slip on {112} planes with frequent cross-slip among those {112} planes. At sufficiently low purities, slip is dominated by elementary slip on {110} planes with frequent cross-slip among those {110} planes. The precise range of impurity content is unclear, though in high purity iron 330 at. ppm nitrogen was sufficient to cause a significant amount of the {110} slip relaxation (β-relaxation) [46]. The impurity content necessary for significant {110} slip relaxation in niobium and therefore {110} elementary slip is not clear. Deforming high purity niobium in air may also lead to hydrogen contamination, because the normally protective thin surface oxide cracks repeatedly during deformation [11, 25].

The literature attributes the wavy slip traces observed on BCC metals to frequent cross slip [10, 23]. A reasonable extrapolation of the origin of wavy slip traces in the context of Seeger's elementary slip may be as follows: Figure II-13 is a schematic showing a screw dislocation with a) a [111] line direction (out of the page) and the 3 symmetric {112} planes (dashed lines) or {110} planes (solid lines). Elementary slip may occur on either type of plane, depending on whether the core relaxation is a {112} slip relaxation or {110} slip relaxation. Frequent cross-

slip among either b) the set of {112} planes or c) set of {110} planes would both lead to the wavy slip traces observed on niobium and other BCC metals deformed at room temperature, assuming the conditions were such that slip was possible on those elementary planes. The smaller the distance between cross-slip events, which may occur at the nanometer scale [11, 25], the more difficult to distinguish that a slip trace was actually formed by a combination of the individual slip traces.

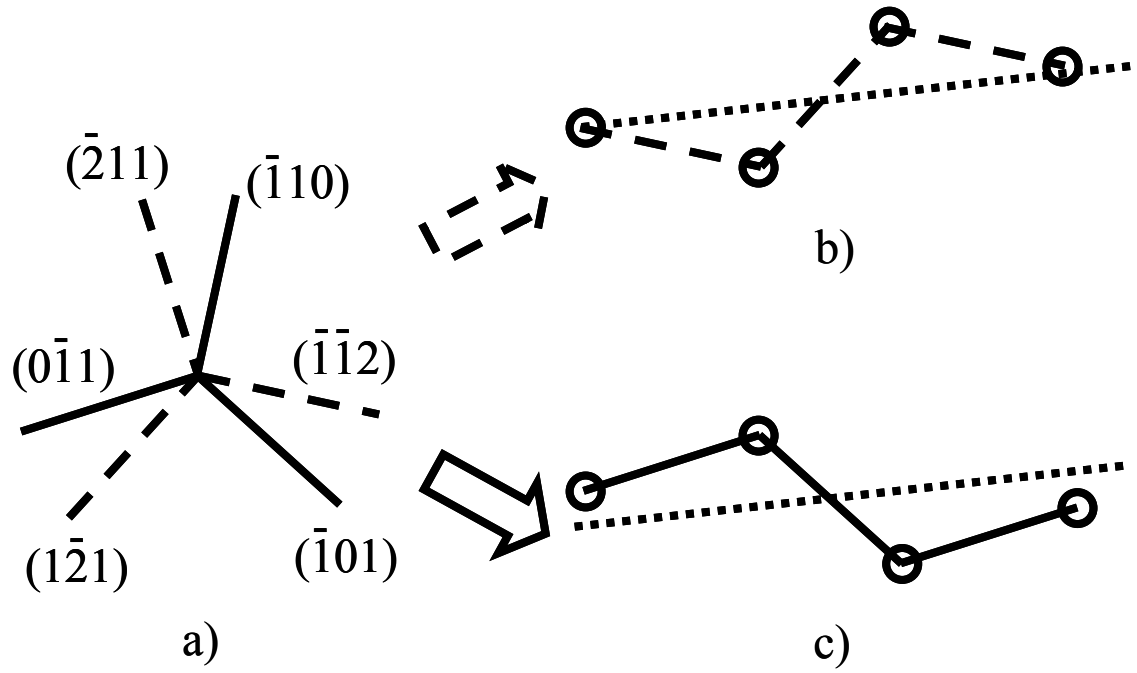

Figure II-13. A schematic diagram showing a [111] BCC screw dislocation with its Burgers vector and line direction out of the page, and the effect of core relaxation on a slip trace. a) The screw dislocation may move on either the 3 symmetric {112} planes (dashed lines) or the 3 symmetric {110} planes (solid lines), depending on the core relaxation. b) If the core is a {112} slip relaxation, the screw dislocation may glide from left to right over an arbitrary distance on a given {112} plane with frequent cross slip (each change in plane marked by a circle) among two of the three relaxation planes, while following a high resolved shear stress plane (fine dotted line). c) If the core is a {110} slip relaxation, the screw dislocation may glide from left to right over an arbitrary distance on a {110} plane with frequent cross slip (each change in plane marked by a circle) among two of the three relaxation planes, while following a high resolved shear stress plane (fine dotted line). Either case leads to a wavy slip trace that roughly follows the plane trace of a highly stressed plane. The smaller the distance between cross-slip events, which may occur at the nanometer scale [11, 25], the more difficult to distinguish that a slip trace was actually formed by a combination of individual slip traces.

The relaxation of the screw dislocation core in BCC metals leads to violation of Schmid's Law in two ways. Both violations break the definition that the critical resolved shear stress is constant for a family of slip systems regardless of the sense of slip. First, the screw dislocation core relaxation results in fractional edge components around the core (as seen in Figure II-9) that interact with the non-glide shear stress component of the stress tensor (the normal stress perpendicular to the slip direction), and causes the critical resolved shear stress to vary with the crystal direction of the stress axis even within the same family of slip planes [31].

Second, the critical resolved shear stress is different among the {112} family of slip planes in BCC metals because of the asymmetric energy gradient in the twinning vs. anti-twinning direction shown in Figure II-11. The twinning/anti-twinning asymmetry is thought to be relatively small in niobium because the asymmetry of the energy gradient on the {112} planes is small, in comparison to the other group VB metals (and group VIB metals such as molybdenum) [11, 25]. 'Small' does not mean 'almost none' however; in niobium, the twinning/anti-twinning asymmetry has been reported to cause the critical resolved shear stress to be 1.4-1.8 times higher in the anti-twinning direction than that in the twinning direction at 77 K [31, 34]. The non-glide shear stress effect may be small for the {110} slip relaxation if that relaxation is similar to the relaxation calculated at 0 K and shown in Figure II-9b, because the fractional edge components of the screw dislocation core that would interact with the non-glide stress are small, again 'small' does not mean 'almost none' and is relative to the other group VB and VIB metals [31]. Since the details of the {112} slip relaxation are unknown, it is unclear if the non-glide shear stress effect would be large or small at room temperature. In uniaxial tension both effects are present and the plastic anisotropy caused by the non-glide stress is typically twice as large as the twinning/anti-twinning asymmetry at 77K [31].

High purity BCC metals such as niobium may also exhibit 'anomalous slip', which is observed slip on a {110} plane with much less resolved shear stress rather than on another {110} slip plane with much more resolved shear stress, especially when certain crystal orientations are deformed at room temperature [47]. Figure II-14 is an inverse pole figure that represents all the possible stress axes. Anomalous slip is most likely when the stress axis of a crystal orientation is located between the <001> corner and the dash-dotted line near the center of the triangle [47]. Anomalous slip becomes rapidly less likely as the stress axis is located further toward the <011>-<111> boundary (indicated by the black arrows) [47]. For the orientations with a stress axis along the dash-dotted line, the highest resolved shear stress is on a pair of {112} planes, each in a different slip direction. However, slip is observed on a {110} plane having approximately half the resolved shear stress on the {112} planes, hence the label 'anomalous' [47]. A possible explanation for this behavior uses this example: if the $[111](\bar{2}11)$ and $[\bar{1}11](11\bar{2})$ slip systems were to operate simultaneously as expected, because both possess similar resolved shear stresses, then the resulting cutting of screw dislocations through each other would lead to many jogs; if the jogs were then forced to move with the screw dislocations the result would be many self interstitials, and extra thermal energy would be required to move the screw dislocations [47]. Instead, the dislocations of the $(\bar{2}11)$ and $(11\bar{2})$ planes cross-slip to the shared 'anomalous' $(0\bar{1}1)$ cross-slip plane, on which the screw dislocations may glide without the need for additional thermal energy [47]. The dislocations retain their Burgers vectors after cross slipping to the anomalous plane, so that coplaner slip as the $[111](0\bar{1}1)$ and $[\bar{1}11](0\bar{1}1)$ slip systems now occurs [47]. Minimization of the lattice energy is thus the driving force behind anomalous slip [47]. The condition most important for the occurrence of anomalous slip is a similar density of dislocations on the two {112} planes having different slip directions, because a

similar dislocation density would result in many screw dislocations cutting through each other [47]. While this condition is more likely when the resolved shear stress is similar on both {112} slip systems, the dislocation densities depend on the prior deformation history, so anomalous slip may be observed even if the resolved shear stresses are different due to dissimilar initial densities [47]. If the dislocation densities are sufficiently different due to dislocations present before deformation, anomalous slip may not be observed even if the resolved shear stresses are similar [47]. Anomalous slip is not typically observed at strains greater than 0.1 in uniaxial tests [47].

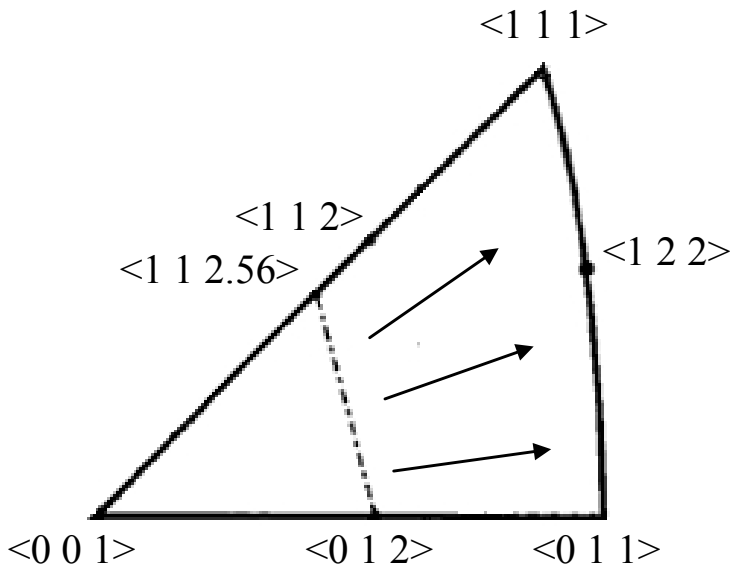

Figure II-14. Crystal orientations possessing a tensile axis located between the <001> corner and along the dash-dot dividing line are most susceptible to anomalous slip; the likelihood of anomalous slip decreases rapidly as the tensile axis is located further from the dividing line and toward the <011>-<111> boundary (black arrows) (reproduced and adapted from [47]).

H. Electron Backscatter Diffraction

Electron backscatter diffraction (EBSD) occurs as electrons from the incident beam in a scanning electron microscope inelastically scatter from a location on a sample. The Bragg scattering of these electrons results in diffraction patterns that may be used to determine the crystal orientation at the location interrogated by the electron beam [48]. Orientation imaging microscopy (OIM) automates the process of identifying the crystal orientation to produce maps of the crystal orientation over a scanned area, called EBSD maps or orientation maps [49-53]. Such data are used to establish relationships between crystallography and microstructure; for example, the relationship between grain orientation and fracture, oxidation, recrystallization, or the local average misorientation (LAM) of the crystal lattice that implies dislocation content [53]. Electron backscatter diffraction is also useful for determining relationships between grain boundary crystallography and boundary mobility, diffusivity, susceptibility to chemical attack, or mechanical properties [53].

Figure II-15 is a schematic of a basic hardware setup required for EBSD: 1) a scanning electron microscope (SEM) equipped with 2) a stage capable of tilting to at least 60-70° from horizontal or a similarly angled sample holder to optimize backscattering toward 3) a transmission phosphor screen that illuminates the diffraction pattern of the electrons and a sensitive CCD camera that records the diffraction pattern, and 4) an imaging processing system including acquisition software that calculates the crystal orientation of the data point based on the recorded diffraction pattern. Data analysis is typically done using software installed on a separate computer, so that previously collected data may be analyzed while acquiring new data [53].

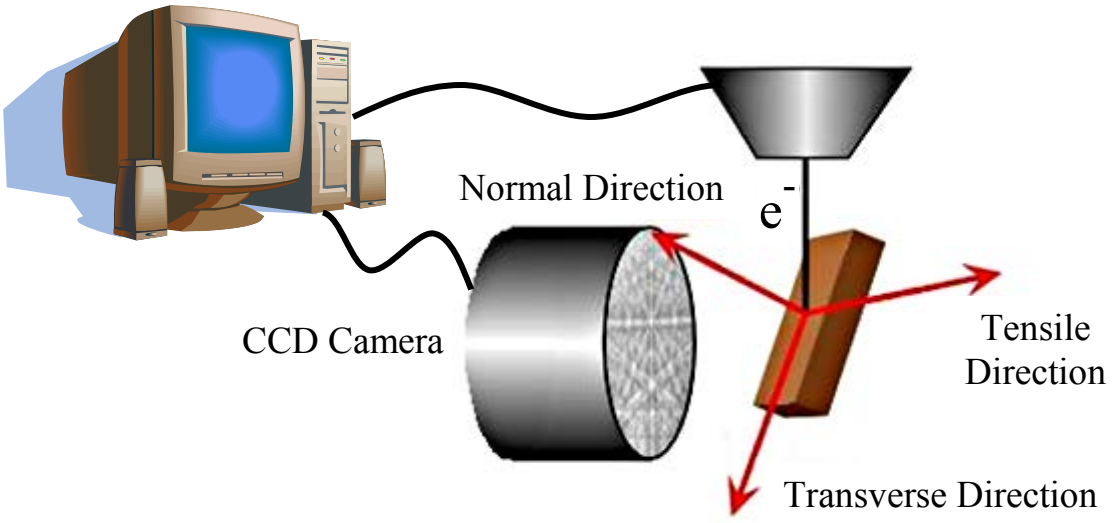

Figure II-15. The schematic shows an EBSD configuration. The electron beam interacts with a sample that is tilted 70°. Backscattered electrons form diffraction patterns on the phosphor screen that are imaged by CCD camera. A computer controls the electron beam, indexes the imaged diffraction pattern, and saves the orientation of each data point. Axes are defined directions on the sample: the transverse direction, tensile direction, and normal direction.

Given the large number of data points required to generate an orientation map, the most important parameters for data acquisition to consider are the speed, spatial resolution, and angular resolution. These depend on the method of operation, equipment, and sample material [53].

The method of operation consists of using either beam scanning or stage scanning to raster the electron beam over the desired area of the orientation map. Beam scanning is faster as only the beam is moved in a negligible amount of time. In terms of absolute orientation the inaccuracy is ~1° near the edges of a scan, and only becomes significant for very low magnifications [53, 54]. Beam defocusing is a potentially serious problem as the beam is deflected perpendicular to the tilt axis, and while this may be minimized if the SEM is equipped with dynamic focus correction, this is not always compatible with the external beam control required by the data acquisition software [53, 54]. Both these errors are minimized by high magnification and long working distances [53]. Stage scanning holds the electron beam on the optic axis and instead moves the stage [53]. This negates the beam defocus problem, assuming the x-y plane of the stage is parallel to the sample surface, but takes longer as stage motion is typically ~1s between points [53]. The positional accuracy of a normal SEM stage is not high, so stage scanning is usually only used when step size is larger than ~1μm [53].

Many factors affect the quality of the diffraction pattern. The backscattered electron signal and pattern quality increase with higher atomic number materials, and evidence suggests the spatial resolution may also increase with atomic number [53, 55, 56]. The diffraction pattern is formed from the surface layer, and so the surface must be carefully polished to avoid polishing artifact damage, such as embedded polishing media or dislocations introduced by shear during polishing. A mirror-like finish after mechanical polishing is sometimes adequate, though

electropolishing as the final polishing step is typical, especially for ductile metals such as high purity niobium. Dislocations and other defects reduce the clarity of the diffraction pattern because the disruption to the periodicity of the crystal lattice caused by these defects results in slightly shifted and superimposed diffraction patterns from that location [53]. Topography may be unavoidable, such as at edges where a softer material or phase meets a harder material or phase, which polishes unevenly and may lead to steps in the surface that shadow or obstruct the pattern. Determination of the orientation, called indexing, is most accurate when the diffraction pattern comes from a single crystallographic orientation [53]. If two or more patterns are imaged at the same time, such as when the beam straddles a grain boundary, the indexing process may solve the stronger of the patterns or simply fail to index [53]. Thus, the smallest grains or subgrains a given set of equipment may analyze are limited by the best achievable spatial resolution [53].

The spatial resolution is separated into the resolutions parallel Λ_A and perpendicular Λ_P to the tilt axis, since in the typical case of 70° tilt the area the beam interrogates is roughly elliptical, with the major axis perpendicular to the tilt axis, so that $\Lambda_P \approx 3\Lambda_A$ [53]. In addition to the tilt, the size of the area from which an EBSD pattern comes also depends on the probe (beam) size, beam accelerating voltage, and the atomic number of the material; the smaller the area the pattern comes from, the greater the spatial resolution [53]. Lower probe currents result in lower-quality patterns that are difficult to index, whereas high probe currents increase the beam size and spatial resolution suffers due to the subsequent increase in beam spread. The spatial resolution component Λ_A has been shown to be very dependent on the probe current for standard W-filament SEMs, while being much less dependent for field-emission gun SEMs

(FEGSEMs); FEGSEMs are typically capable of higher spatial resolutions than standard W-filament SEMs (for details, the reader is referred to [57]). Increasing the beam accelerating voltage also increases the beam spread, so the voltage used should be as low as possible. However, if the voltage is too low, pattern quality suffers due to lower efficiency of the transfer phosphor screen at low voltages, and indexing becomes difficult; a beam accelerating voltage of 20 kV is regarded as a good compromise [53]. If sizes of grains or subgrains are to be determined, experiments in aluminum indicate that for 10% accuracy at least 5 points need to 'land' in the feature, and 8 points for 5% [53].

While the absolute orientation may be measured to within ~2° depending on sample alignment and EBSD equipment, the angular precision is important when determining the relative misorientations between points within the same orientation map [53]. Even in an annealed single crystal, where ideally the orientation would be exactly the same at every point, there will be some amount of error simply due to the equipment, or 'orientation noise' [53]. Both orientation noise and real misorientation are measured simultaneously, making measurement of the smallest misorientations difficult, probably only as low as 0.5-1.5°, with the lower limit only achieved in a very well calibrated system. Orientation averaging may be used to sacrifice spatial resolution to push angular precision toward the lower limit, however, this is only most appropriate in annealed single-phase materials where the assumption of constant true orientation within the grains or subgrains is generally sound; in samples with many free dislocations and poorly developed boundaries orientation averaging is not appropriate [53]. Table II-4 gives some examples of metals of various atomic number and estimates of resolution and angular precision.

Table II-4. Summary of typical resolutions and speed of EBSD for different z materials [53].

Sample	SEM type	Spatial resolution (nm)		Angular precision	Time/pattern (s)	
		Λ_A	Λ_P		Beam scan	Stage scan
Aluminum	W	60	180	1°	0.2	1
	FEG	20	60	1°	0.2	1
Brass	W	25	75	1°	0.1-0.2	1
	FEG	9	27	1°	0.1-0.2	1
α-iron	W	30	90	1°	0.1-0.2	1
	FEG	10	30	1°	0.1-0.2	1

Data acquisition speed is limited by the slowest of three operations: 1) acquisition of an analyzable diffraction pattern, which depends on the material and operating conditions of the microscope, 2) indexing, which depends on the number of lines required for a solution, the pattern-solving algorithm, and the processing speed of the computer, and 3) repositioning to the next point (negligible for beam scanning, depends on speed of stage hardware for stage scanning) [53].

Important uses of EBSD data are determining crystallographic texture, boundary character, stored energy, and recrystallization, and relating these to orientation [53]. Bulk texture is often determined by using a representative sample cut along the reference direction-normal direction plane of the sheet, and 500-1500 orientation determinations made for sound statistical determination of the orientation distribution function (ODF), from which pole figures (PFs) may also be made. Before representing the data in orientation distribution functions or pole figures Gaussian smoothing of half width 1-5° is common to reduce noise [53]. The direct determination of the orientation distribution function from individual diffraction patterns is faster than by deconvolution from x-ray pole figures, and avoids problems associated with x-ray methods such as line broadening and ghost peaks [53].

Local average misorientation (LAM) maps highlight local gradients in lattice orientation over the mapped area. These maps are formed by comparing each data point to its immediate neighbors, and the difference in orientation, or misorientation, displayed using a color gradient scale. Local average misorientation maps are useful for highlighting features such as low-angle grain boundaries or deformation bands, which are sheet-like arrangements of dislocations arising from highly localized deformation [53]. The Local average misorientation data may also be represented as histograms, which have been shown to be correlated to geometrically necessary

dislocation (GND) density; peaks at higher average misorientations imply higher geometrically necessary dislocation content within the crystal lattice and therefore greater stored energy available for recovery and recrystallization [58]. This technique does not detect statistically stored dislocations (SSDs), as these pairs cancel each other's contribution to misorientation of the lattice. In a worked metal with no heat treatment, the statistically stored dislocations density is much greater than geometrically necessary dislocation density [17].

I. The opportunity for research

Careful examination of the active slip systems in niobium, made easier using single crystal crystals, has been done with very pure niobium. This very high purity was required to better understand the effects of screw dislocation core relaxation on: the dependence of the critical resolved shear stress on tensile axis orientation, the elementary slip planes, and possible mechanism for anomalous slip. However, the active slip systems of merely high purity niobium need to be investigated, in part because of being the primary material used for superconducting radio-frequency cavities, and to further evaluate the assertion that the elementary slip plane family depends on purity. Knowing which slip systems are active in high purity niobium will allow for proper crystal plasticity finite element models to be constructed to predict deformation and therefore improve cavity forming processes, and to understand how dislocation substructures form from the interactions of those active slip systems. In order to better understand the relationships between active slip systems and the deformation substructure formed during processing, this thesis will examine differently oriented high purity niobium single crystals, deformed in the simpler case of uniaxial tension. The primary focus will be on determining the active slip systems and comparing results with prior studies of similar tests that used higher purity niobium [10, 24]. Knowing the active slip systems and characterizing the dislocation

substructure formed by them will be useful to future studies that investigate the relationship between the dislocation substructure as a result of deformation, the recovered dislocation substructure after heat treatments, and the orientation of recrystallized grains.

III. Materials and Methods

A. The Tokyo-Denkai set of samples

Two sets of samples were used, and while prepared similarly, there were important differences such as source company, sample dimensions, surface polishing technique, and chemical etches.

One set of single crystal niobium samples was cut from the outer scrap rings that were left over after trimming a large grain niobium disc from Tokyo Denkai, for making a prototype 1.3 GHz, β=0.81 elliptical single cell cavity. While the samples were not tested for the exact impurity content, Table III-1 lists the specifications for the maximum allowed impurities used by Tokyo Denkai.

Table III-1. The maximum allowed impurity amounts used by Tokyo Denkai (values converted in order to compare to [11]).

Impurity	Specification (at ppm)
Tantalum	<93
Tungsten	<5
Titanium	<19
Iron	<17
Silicon	<33
Molybdenum	<9.7
Nickle	<16
Oxygen	<58
Nitrogen	<66
Hydrogen	<460
Carbon	<77

Portions of the ring were trimmed into dog-bone shape tensile coupons using electro-discharge machining (EDM). Figure III-1a shows the sample dimensions; the gage length was 18mm with 1mm fillets at the shoulders, 3.4mm wide, and 2.8mm thick; each grip section length was 10mm, 5mm wide, and 2.8mm thick. While the samples began as short arcs (dashed lines give a sense of the curvature), the gage length was made straight by EDM. Samples were then polished to mirror finish, first mechanically to 0.05μm colloidal silica, and then electropolished using 12V for 8 min using a 10% hydrofluoric, 90% sulfuric acid solution indirectly cooled by a -30°C methanol bath. Electropolishing was done using a Tungsten wire cathode (diameter 1mm) and the sample as anode, which were held approximately 25mm apart from each other using a stand and clamps. The sample was immersed with its long axis vertical, with less than the length of the grip section out of the electrolyte so as not to corrode the connecting alligator clip; the length of Tungsten wire immersed was approximately 40mm. The sample surface to be polished faced the Tungsten wire. A stir bar on a low setting (speed 3 or 4) slowly stirred the electrolyte. The temperature was monitored with an electronic thermometer immersed in the methanol bath, and liquid nitrogen added to the bath as needed to maintain the temperature. Any time a sample was electropolished (including the Ningxia samples described in the next section), the current needed to maintain the 12V potential typically dropped to about a third of the starting current by the end of electropolishing.

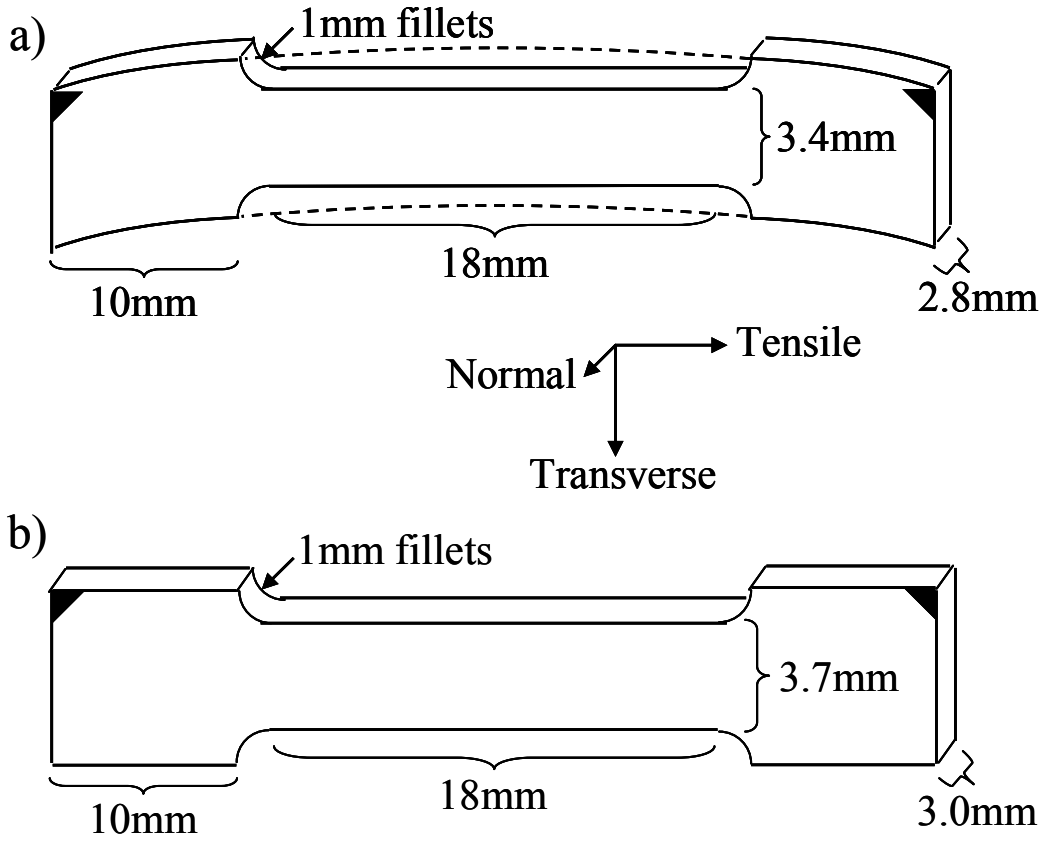

Figure III-1. A schematic of the sample dimensions for a) the Tokyo-Denkai set (dashed lines give the sense of the arc of the scrap ring from which the straightened samples were cut), and b) the Ningxia set. The black triangles mark the filed-down corners used to mount the samples in the SEM consistently.

Orientation imaging microscopy (OIM) was conducted on a Camscan 44FE SEM using a TSL(Link) hardware and software system to find the crystal orientation of each grain in the slice, using Bunge Euler angle notation (φ_1 Φ φ_2). Euler angles can be converted to equivalent Miller indices representations using the orientation matrix [59]. After OIM measurements were completed, three samples with orientations close to $[\bar{1}10][001]$ (referred to as A), $[\bar{1}01][101]$ (referred to as C), and $[\bar{1}11][101]$ (referred to as F), were chosen for study, i.e. [crystal direction parallel to the surface normal of the sample][crystal direction parallel to the tensile axis of the sample]. These three samples were selected because each had either a surface normal or a tensile direction within the same family as another specimen within the set. Table III-2 lists the four slip systems possessing the highest four Schmid factors in the initial orientation for each sample.

Table III-2. The initial order of Schmid factors on slip systems in single crystal tensile samples from Tokyo Denkai scrap rings.

Name	Initial order of Schmid factors on slip systems
A	0.49 $[1\bar{1}1](\bar{1}12)$, 0.49 $[111](\bar{1}\bar{1}2)$, 0.46 $[111](0\bar{1}1)$, 0.45 $[1\bar{1}1](011)$
C	0.48 $[1\bar{1}1](121)$, 0.48 $[1\bar{1}1](011)$, 0.44 $[111](0\bar{1}1)$, 0.43 $[111](1\bar{2}1)$
F	0.48 $[1\bar{1}1](121)$, 0.47 $[1\bar{1}1](011)$, 0.43 $[111](1\bar{2}1)$, 0.43 $[111](0\bar{1}1)$

Prior to tensile testing, a grid was put onto the unpolished back of each sample by spray painting through a wire mesh, and the resulting grid of paint squares on each sample was digitally photographed before and after deformation. Samples were mounted in a tensile testing machine (Instron 4302, controlled using Instron's Bluehill software), and each sample was deformed to 40% engineering strain. Digital photographs were compared with the previous image to estimate local tensile strains. The estimated local tensile strains were found by calculating the length in the tensile direction between the upper left-hand corner of adjacent paint squares in both the undeformed and deformed images. The undeformed length was subtracted from the deformed length and the result divided by the undeformed length to give an engineering strain in the tensile direction between each pair of paint squares. Finally, the engineering strain between each pair of paint squares was averaged with the engineering strains found between the paint square pairs adjacent to it (that is, to the left and right the paint square in the tensile direction) to give the estimated local tensile strain.

Each sample was then cut in half with a diamond saw and etched with a buffered-chemical polish (BCP) for 10min, with no temperature control of the acid. The BCP solution was a mixture of 1 part 49% hydrofluoric, 1 part 69.3% nitric, and 2 parts 85% phosphoric acid. The BCP solution removes approximately 2.5μm/min of niobium at room temperature, so about 25 μm was removed from the surfaces of the sample halves. The sample halves were rinsed in ultra-pure water, dried, and sealed into nitrogen filled bags while in a clean room. Halves of differing crystal orientation were e-beam welded together under vacuum at Sciaky (Chicago, IL) a few days later. The cut ends were butted together and each half held in place by a metal clip near the shoulder on the gripping area, which acted as heat sinks. The electron beam dwelt for 1-2 seconds, heating the gage length of the samples such that they were red hot at the shoulder

(~600-700°C). The sample cooled quickly, and was below red-hot a few seconds after welding. Welded samples are referred to using the corresponding two letters that had labeled each initial crystal orientation; the letter of the initial crystal orientation is also used to refer to the appropriate half or side of the welded sample. In order to make OIM measurements possible, the welded samples were then electropolished, using 12V for 10min at -30°C.

OIM scans of 10μm step size were made in and adjacent to the weld, at suspected recrystallization fronts, and relatively far from the weld, near the shoulder. Composite inverse pole figure OIM maps were assembled, with prisms superposed to show crystal orientation based on the original sample surface normal, as deformation caused the original surface normal to rotate or twist in response to the activated deformation systems. Local average misorientation maps (LAM) highlighted small changes in lattice rotation over larger areas of approximately $4mm^2$. These maps are formed by comparing each data point to its neighbors, and the difference in rotation displayed using a 0° (blue) to 5° (red) gradient scale, which highlights low-angle grain boundaries and geometrically necessary dislocation boundaries.

Slip trace analysis was done near recrystallization fronts to identify possible active slip systems using secondary and backscattered electron images taken while the sample surface was not tilted (a complete description of slip trace analysis follows later in this chapter). While this analysis was done after welding, the surface topography should not have been changed significantly by the heating. However, the samples had been BCP etched after deformation, and then electropolished again after welding to enable OIM, both of which diminished the topographic visibility of the slip lines, before the images were taken (a mistake *not* repeated for the Ningxia set of samples). Despite this, many slip lines were still visible and useful.

B. The Ningxia set of samples

Samples comprising another set of single crystal niobium samples were cut from a disc that had been sliced from an ingot obtained from Ningxia. While the samples were not tested for the exact impurity content, Table III-3 lists the specifications of maximum allowed amounts of impurities, and the actual impurity content from a batch Ningxia niobium ordered according to those specifications. OIM was used to find the crystal orientation of each grain in the slice. Tensile samples having any rotation about the surface normal of the plate could be cut from these grains. When representing the grain orientation in Bunge Euler angle notation, rotation about the surface normal of the plate is equivalent to changing φ_1 while holding Φ and φ_2 fixed. Uniaxial tension stress was computationally applied to each possible sample orientation by adding or subtracting increments in 1° steps so that φ_1 had values between 0 and 259°. Schmid factors on all slip systems were computed at each value of φ_1. For example, Figure III-2 shows how the Schmid factors varied with 1° increments of φ_1, giving the range of available slip system combinations to choose from using the parent grain orientation of 198 87 248 (solid black line). The orientation of sample S3 was chosen to have the highest Schmid factor on a {112} slip plane, the next highest Schmid factor being on a {110} plane, with both planes having the same <111> slip direction; this condition was found at 148 87 248, indicated by the dashed line in Figure III-2. The difference between the desired and parent orientation was -50° φ_1. Figure III-3 shows the equivalent rotation of 50° about the surface normal of the plate (black spot) from the parent reference orientation (black arrow) to the desired tensile axis orientation (dashed black arrow). Also note the necessary sign change of the rotation, which preserves the right handed convention used for rotations. Thus each of the tensile specimen orientations was chosen to

favor particular slip systems or combinations of slip systems. The grey numbers were working labels for the parent grains, however, within this dissertation the parent grains are labeled directly with their Euler angles instead. The grey letters label samples that were not used in this dissertation. The grey labels are provided here for clarity if the plate is used for further experiments, though do not need to be considered within this dissertation.

Table III-3. The maximum allowed impurity amounts specified to Ningxia, and the impurities present in an ingot of Ningxia niobium supplied according to those specifications.

Impurity	Specification (at ppm)	Ingot (at ppm)
Tantalum	<257	51
Tungsten	<35	8
Titanium	<97	10
Iron	<50	8
Silicon	<99	33
Molybdenum	<48	10
Nickel	<47	8
Oxygen	<58	29
Nitrogen	<66	33
Hydrogen	<184	276
Carbon	<77	77

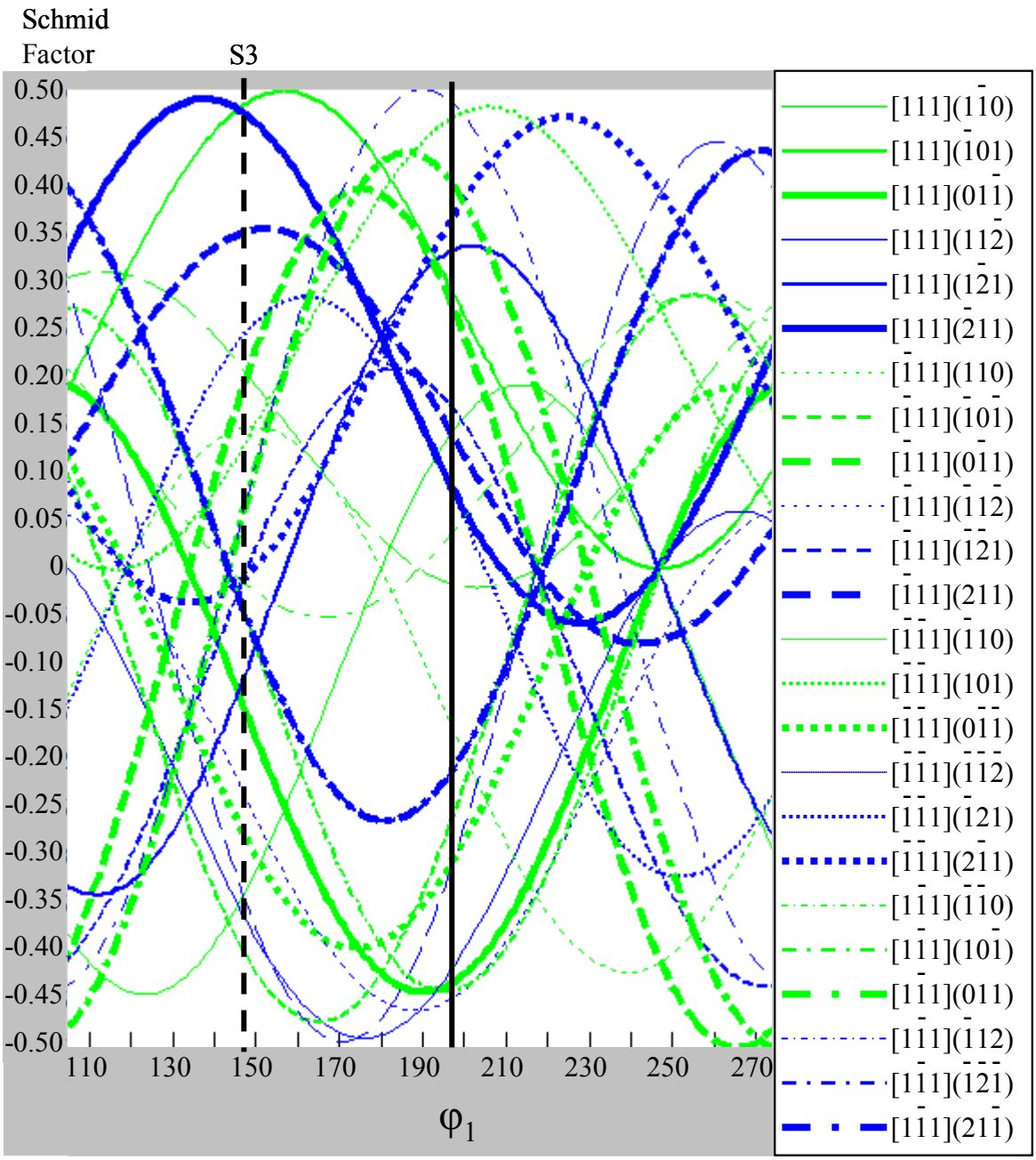

Figure III-2. The Schmid factors on slip systems as a function of orientation, computed using in-plane tensile stress. For example, rotating the parent grain orientation 198 87 248 (solid vertical line) to the desired 148 87 248 orientation of sample S3 (dashed vertical line) requires a -50° change in φ_1. Slip systems of the {110} family are green, while those of the {112} family are blue. Similar figures showing the selection of the other desired orientations of the Ningxia samples are in the Appendix.

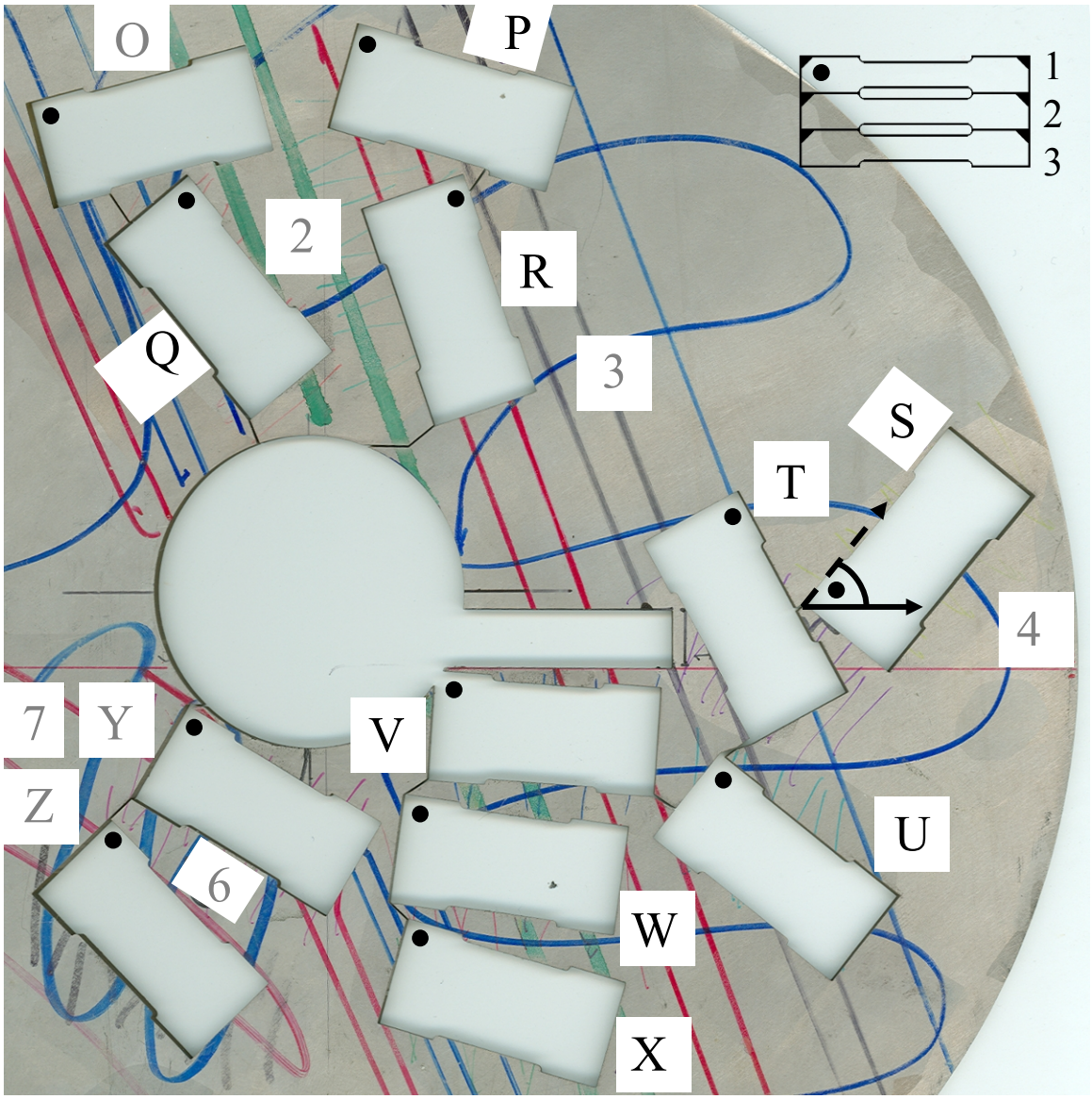

Figure III-3. A Ningxia ingot disc showing the locations of the Ningxia samples. Samples were cut as blocks of three samples (the schematic in the upper right corner). Each block of samples was rotated based on the previously determined difference in φ_1 found similarly to Figure III-2. For example, the computed -50° change in φ_1, required rotating the sample block template by +50° about the sheet normal (indicated by black dots, out-of-page) for the parent grain 198 87 248 (solid arrow is the reference direction of the parent grain), so the sample orientation has the desired 148 87 248 for Sample S3 (dotted arrow is tensile axis of desired orientation). Grey text labels samples and notation that were not used in this dissertation, though is provided for clarity if the plate is used in further experiments.

Dog-bone shaped tensile coupons were cut from individual grains using electro-discharge machining (EDM). Three samples were cut for each chosen orientation (i.e. S1, S2, S3), though only one sample of the three was prepared and deformed; the remaining samples are available for further experiments by others. Figure III-1b shows the sample dimensions; the gage length was 18mm with 1mm fillets at the shoulders, 4mm wide, and 2.8mm thick; each grip section length was 10mm, 6mm wide, and 2.8mm thick. The samples were then polished to mirror finish by alternating between chemical etching (80% Nitric and 20% Hydrofluoric acid for 4 minutes) and mechanical polishing steps. The last mechanical polish was to 0.05μm using colloidal silica, followed by electropolishing with 12V at -30°C for 8 min. Orientation imaging microscopy (OIM) was conducted on a Camscan 44FE SEM using a TSL(Link) system to confirm that the initial orientation at the center of each specimen would indeed resolve the desired shear stress onto the desired slip systems as shown in Table III-4. The Euler angles used to decide how to cut the Ningxia samples were convenient to that purpose, however, these needed to be changed to an Euler angle set that would label the desired slip systems in a similar manner to the prior experiments described in section II-E of the Literature Review, to make comparison between the studies easier. Due to cubic crystal symmetry, there are 24 Euler angle variants possible that describe the 'same' orientation, giving 24 sets of ways the slip systems can be labeled in order of descending Schmid factor, with the order of each set depending on the stereographic triangle containing the tensile axis of that orientation. Therefore the Euler angle variant used to describe each sample's orientation was selected such that the tensile axis was similar to those used in the prior experiments; that is, within the regions of the [001]-[101]-[111] and$[001]-[101]-[1\bar{1}1]$ stereographic triangles that insured the slip system with the highest Schmid factor had a $[1\bar{1}1]$ slip direction.

Table III-4. Intended slip system activation in single crystal tensile specimens cut from the Ningxia ingot slice.

Name	Initial order of Schmid factors on slip systems
U3	0.38 $[1\bar{1}1](121)$, 0.37 $[\bar{1}11](211)$, 0.36 $[1\bar{1}1](011)$, 0.36 $[\bar{1}11](101)$
P3	0.49 $[1\bar{1}1](\bar{1}12)$, 0.49 $[111](\bar{1}\bar{1}2)$, 0.47 $[111](0\bar{1}1)$, 0.47 $[1\bar{1}1](011)$
V3	0.47 $[1\bar{1}1](011)$, 0.46 $[1\bar{1}1](121)$, 0.46 $[111](0\bar{1}1)$, 0.45 $[111](1\bar{2}1)$
W3	0.48 $[1\bar{1}1](121)$, 0.47 $[1\bar{1}1](011)$, 0.44 $[111](1\bar{2}1)$, 0.44 $[111](0\bar{1}1)$
X3	0.50 $[1\bar{1}1](121)$, 0.46 $[1\bar{1}1](011)$, 0.41 $[1\bar{1}1](110)$, 0.38 $[111](1\bar{2}1)$
R2	0.48 $[1\bar{1}1](121)$, 0.48 $[1\bar{1}1](011)$, 0.42 $[111](0\bar{1}1)$, 0.40 $[111](1\bar{2}1)$
Q2	0.48 $[1\bar{1}1](011)$, 0.48 $[1\bar{1}1](121)$, 0.41 $[111](0\bar{1}1)$, 0.38 $[111](1\bar{2}1)$
S3	0.49 $[1\bar{1}1](011)$, 0.47 $[1\bar{1}1](121)$, 0.43 $[111](0\bar{1}1)$, 0.38 $[111](1\bar{2}1)$
T3	0.49 $[1\bar{1}1](011)$, 0.44 $[1\bar{1}1](121)$, 0.42 $[111](0\bar{1}1)$, 0.41 $[111](\bar{1}\bar{1}2)$

After OIM, samples were mounted in a tensile testing machine (Instron 4302, Instron's Bluehill software) and deformed to 40% engineering strain in uniaxial tension at a quasi-static strain rate (~10^{-3} s^{-1}). After deformation, OIM scans were made at no fewer than four locations within a few mm of the center of the gage length, in regions with apparent slip traces. OIM scan step sizes were either 10μm for full width scans, 1μm step for 112x327 μm maps, or 0.2μm for 22x65μm maps; the long axis of all the scans was parallel to the transverse direction. The smallest 0.2 μm step size was chosen based on the limit of EBSD spatial resolution in iron of 90 nm (under ideal conditions); while niobium is higher atomic weight than iron and the limit should be lower, 0.2 μm (200 nm) was chosen to be conservative (see section II-H). Secondary electron images (which show surface topography) and backscatter electron (which form contrast based on electrons backscattering out of the crystal lattice) images were taken after each OIM scan, leaving the sample in tilted position so as to not disturb the careful alignment achieved for the OIM scans.

EBSD data was also represented as local average misorientation (LAM) maps to highlight local gradients in lattice orientation. The LAM data were also represented as histograms, in which peaks at higher average misorientations imply higher geometrically necessary dislocation content within the crystal lattice [58]. As this technique only detects geometrically necessary dislocations, and does not detect the statistically stored dislocations (SSDs), the LAM represents an estimate of the lower bound of total dislocation density; the actual density is likely much higher as the samples had not yet been welded or heat treated.

Because the sample normal rotated due to deformation on most specimens due to the activity of slip, this change in the surface normal needed to be identified in OIM data acquisition, and

corrected for this rotation to allow proper interpretation of the OIM data. OIM scans require that the normal surface being interrogated be tilted to 70° so that electron backscatter diffraction patterns go toward the camera, which results in the rotation due to deformation being 'left-out' of the raw deformed orientation data. Accurately representing the relative changes in orientation due to deformation required the 'left-out' tilt to be reintroduced into the deformed orientation data. The amount of 'left-out' tilt needed to correct the raw deformed orientation data was found as follows. Each sample was mounted on the sample stage such that the tilting axis of the surface normal required for OIM occurred about the tensile direction. The samples were mounted in a small vise such that the normal surfaces of *ends* of the sample were parallel to the surface of the sample stage, because the ends had not rotated during deformation due to being fixed in the grips. Hence, the normal surface of the gage length was not parallel to the sample stage surface, rotated about the tensile direction equal to the amount of left-out tilt.

Figure III-4 shows a schematic of how the left-out tilt was found: a) While the sample stage was at 0° tilt, the apparent width of the sample was measured on the SEM monitor at 20x magnification. The apparent width was approximately equal to the actual width because the rotations due to deformation were small (less than 10°). Multiplying the apparent width by the cosine of 70° gave a new apparent width that would mean the normal surface was properly tilted to 70°. b) The sample was then tilted while the width was measured on the SEM monitor until this new apparent width was achieved, at the same 20x magnification as for 0° sample stage tilt. The stage tilt was recorded from the dial on the SEM, as the left-out tilt would be the difference of 70° and the sample stage tilt. The left-out tilt was then added as a rotation about the tensile direction to the raw deformed orientation data, thereafter referred to as 'tilt corrected' OIM data. The aspect ratios of the secondary and backscattered electron images were also corrected by

adding the left-out tilt to 70°, taking the cosine, and multiplying the result by the transverse direction (height) of the image; the tensile direction (width) of the images was not distorted and remained the same. Thus an image that was consistent with the tilt corrected deformed orientation data was obtained, and the slip traces were correctly measured.

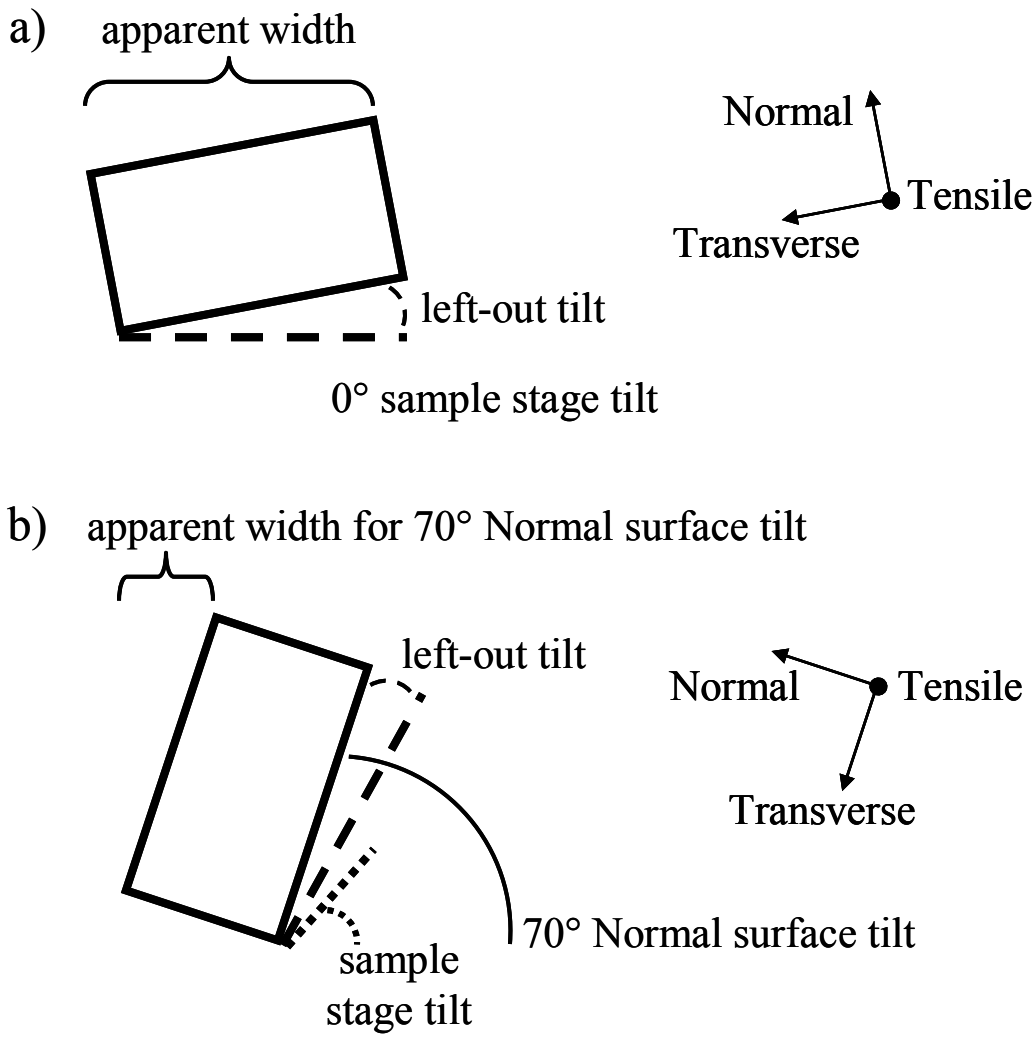

Figure III-4. A schematic of the cross-section of the deformed gage length used to determine the left-out tilt. a) the sample at 0° stage tilt, and b) the sample tilted such that the deformed surface was properly tilted to 70° to enable OIM.

A crystal plasticity finite element modeling (CPFEM) approach was used to predict active slip systems based on each single crystal specimen's initial orientation, assuming that slip on {110} and {112} planes had similar critical resolved shear stresses (CRSS), and {123} slip was not activated (this work was performed by Amir Zamiri as a part of his Ph.D. dissertation [60, 61]). A fine-meshed dog-bone model of the same dimensions as the physical samples was uniaxially deformed using ABAQUS. The boundary conditions were such that one end was held fixed while the other was displaced a set distance at each time step. For each time step, the orientation, stress, and work hardening parameters of each slip system were updated. Predictions of activated slip systems are based on a combined constraints method, which identifies the yield function. By minimizing the yield function, the active slip systems are chosen. The finite element model is updated to satisfy its requirements, and then proceeds to the next time step [62]. The simulations were conducted to a final engineering strain of 40%. Activation of different slip systems in different crystals was predicted. Some material parameters had already been determined by trial and error to obtain a close fit to previous studies of experimental stress-strain curves [63]. Further details of the finite element modeling are the subject of Amir Zamiri and Aboozar Mapar's dissertations [61, 64].

C. Slip trace analysis

Slip trace analysis is a method of inferring the active slip systems in a deformed sample. Slip traces are formed as dislocations exit the surface of a crystal, leaving a step on the surface that increases in height as more dislocations of that system exit; each dislocation increases the height of the step by one Burgers vector. The slip trace is the line of intersection of the surface and the slip plane of the dislocation that formed it. A slip trace indicates the slip plane of a slip system, but does not necessarily indicate the slip direction; this is true for the {110} family of slip planes

in a BCC metal such as niobium. For example, the slip trace of the $(\bar{1}01)$ slip plane could be made by dislocation activity of the $[111](\bar{1}01)$ or $[1\bar{1}1](\bar{1}01)$ slip systems; every {110} slip plane possesses two possible <111> slip directions because both are perpendicular to a particular {110} slip plane. However, in a BCC metal the {112} planes are also possible slip planes, and each of the slip planes in the {112} family of slip planes possesses only one possible <111> slip direction; this is because only one <111> slip direction is perpendicular to a particular {112} slip plane (this is also true of the {123} family of planes, though these are not considered slip planes in this work). Figure III-5 shows examples of how slip traces may appear, depending on the intersection each set of planes makes with the sample surface: a) slip traces belonging to the same slip system operating over a given volume of crystal appear as parallel lines on the surface, while b) different slip systems operating in the same volume would appear as other sets of parallel lines, and c) the lines being indistinguishable from each other despite belonging to different planes, due to a crystal orientation that happens to cause the slip traces to be similar to each other.

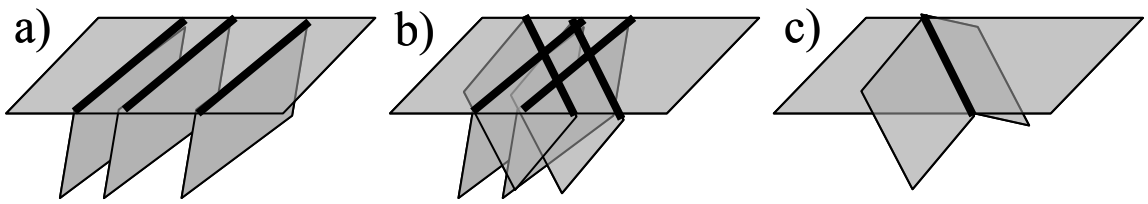

Figure III-5. Examples of slip traces. a) Slip traces of the same slip system are parallel, b) Intersecting slip traces of two different slip systems, c) Two different slip systems that produce a very similar slip trace.

Care must be taken when interpreting slip traces. Figure III-5c illustrates a case for which a slip trace may belong to multiple slip systems, so that additional criteria must be used to determine which slip system is more likely to have produced the slip trace, or if both slip systems may have contributed. Frequent cross-slip in BCC metals such as niobium leads to wavy slip traces, due to the frequent change in slip plane of screw dislocations while moving in the same slip direction, so only relatively short straight portions of the slip traces were used. Slip traces may also be rendered difficult to detect due to changes in active slip systems. For example, if a system becomes much less active, and other systems much more active, then the slip traces of the less active system may become obscured by the slip traces caused by the second slip system. The surface examined must also be as flat as possible, or the apparent angle of the slip traces across the surface will be inaccurate. An image of a tilted surface may be corrected later by adjusting the aspect ratio to approximate how the surface should appear, provided the angle and axis of the tilt are known; this was necessary for the images of the Ningxia set of samples, though not for the images of the Tokyo-Denkai set of samples.

Identifying the slip systems for a given visible trace is illustrated in Figure III-6, and proceeded as follows: a) Secondary and backscatter electron images of likely slip traces on the Normal (polished) surface were taken while the sample was tilted immediately before or after OIM scans. The image aspect ratio of these images was adjusted to compensate for the tilt. A line was drawn along a feature thought to be a slip trace (solid white lines). The visible trace was copied and compared to similar features nearby (dashed white lines) to establish that it was a repeating feature, as would be expected of real slip traces that had formed on the surface due to the motion of dislocations on the separate though parallel planes of an active slip system. b) The visible traces (now green lines instead of white) were compared to the calculated plane traces

(many colors) of the crystal orientation in which the visible trace originated. A calculated plane trace and visible trace were considered to match if within ±5° of rotation of each other (green lines bounded by dashed black lines). This allowed for a combination of unaccounted-for tilt of the sample surface, as the deformed surface was likely not quite planar any longer, and for slight differences in rotation between the image and the orientation measured by OIM.

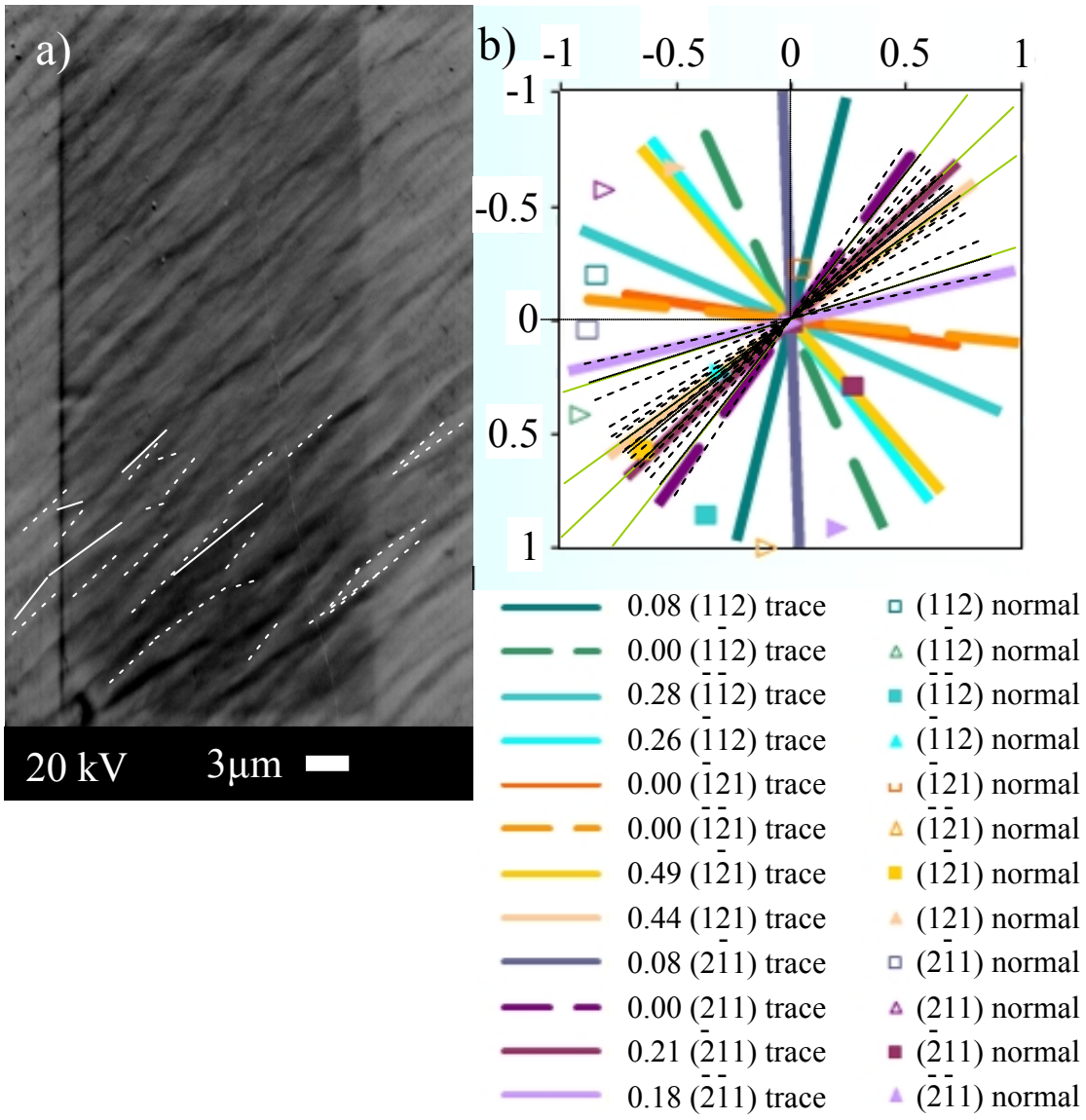

Figure III-6. Example of matching a) visible traces (white lines) to b) {112} calculated slip traces (colored lines). A visible trace (green line) matched a calculated slip trace if within ±5° of each other, marked by dashed lines to either side of possible traces. Also note how a single possible trace may match multiple calculated traces, or the average of two, or possibly, none. The Schmid factor of the <111>{112} slip system each trace belongs to is also given for the deformed orientation of sample X3 shown.

Secondary and backscattered electron images were also taken of the transverse surface; these were done after the OIM scans and required removing and remounting the sample to view the transverse surface. These images were not necessarily taken at the same exact position along the gage length as the normal surface images taken immediately before or after the OIM scans, although all the images from either surface were taken within a few millimeters of the center of the gage length. The samples were remounted carefully so that the same crystal orientations found from OIM of the normal surface could be used in the slip trace calculations for the transverse surface images, assuming that the crystal orientation did not vary much near the center of the gage length. Identification of likely slip traces and matching to calculated slip traces was done for the transverse surface images of the Ningxia samples in a similar manner as that of the normal surface images.

D. Glide and Non-glide shear stress calculations

The cores of screw dislocations in niobium are non-planer, and so the non-glide stresses may affect the magnitude of the glide stress required to move those dislocations and cause a slip system to be active by distorting the relaxed screw dislocation core. The familiar glide stress is simply the resolved shear stress acting on the slip plane in the slip direction, obtained by multiplying the 0.2% offset yield stress by the Schmid factor of the slip system. There are 3 non-glide stresses: The 1^{st} non-glide stress is a shear stress parallel to the slip direction though on the non-glide stress plane, and the 2^{nd} and 3^{rd} non-glide stresses are both shear stresses perpendicular to the slip direction on the slip plane and non-glide stress plane, respectively. The non-glide stresses are calculated by multiplying the 0.2% offset yield stress by the non-glide factors of the slip system. Details for the calculating of the Schmid and non-glide factors are given elsewhere [65, 66]. Table III-5 lists the slip systems and the non-glide stress planes for each. The non-glide stress planes for {110} slip systems were determined by [65, 66] through atomistic calculations. These planes appear to follow a pattern: the non-glide stress plane normal happens to be the first <110> direction that is rotated to the slip plane normal direction's original position when rotating about the slip direction in the *left-handed* sense (that is, a negative right-handed rotation). While the details of the screw core relaxation that results in {112} elementary slip are not known at present, this thesis assumes that the same pattern observed for the {110} non-glide stress planes holds in order to determine the {112} non-glide stress planes shown in Table III-5. This assumption is based on both the {110} and {112} slip planes having a similar 3-fold symmetry about the <111> slip directions, and is at least a starting point in the absence of a detailed description of the {112} slip relaxation. It is also important to point out that the non-glide stresses given in this thesis are *maximum* values. In practice each of the 3 non-glide

stresses must be multiplied by a correction factor ('non-glide stress coefficient') that is determined through atomistic simulations for that metal; the correction factor was estimated to be 0.6 in molybdenum for slip on {110} slip planes [65, 66], and not known at present for niobium. It seems reasonable to expect the correction factor is different for {110} slip planes versus {112} slip planes because of the twinning/anti-twinning nature of the {112} slip planes. In the literature, each non-glide stress is multiplied by its respective correction factor, then summed with the glide stress to give an 'effective resolved shear stress' that is somewhat similar to the idea of a critical resolved shear stress. Thus the correction factor indicates how much influence each non-glide stress has on the effective resolved shear stress, and therefore on the activity of the slip system; the larger the correction factor is the larger the influence the non-glide stresses have on the effective yield stress of a slip system.

Table III-5. The list of slip systems and the non-glide stress planes for each. The non-glide stress planes for {110} slip systems were determined by [65, 66] through atomistic calculations. This thesis assumes that the same pattern observed for the {110} non-glide stress planes holds in order to determine the {112} non-glide stress planes shown. Slip System numbers match those in "Schmid and non-glide shear for 24 Equiv Eulers.m" MATLAB file.

Slip System	Slip Direction	Slip Plane	Non-Glide Stress Plane
α	$\mathbf{m}^{\alpha}$	$\mathbf{n}^{\alpha}$	$\mathbf{n}_1{}^{\alpha}$
1	$[111]$	$(01\bar{1})$	$(\bar{1}10)$
2	$[111]$	$(\bar{1}01)$	$(0\bar{1}1)$
3	$[111]$	$(1\bar{1}0)$	$(10\bar{1})$
4	$[\bar{1}11]$	$(0\bar{1}1)$	(101)
5	$[\bar{1}11]$	$(\bar{1}0\bar{1})$	$(\bar{1}\bar{1}0)$
6	$[\bar{1}11]$	(110)	$(01\bar{1})$
7	$[\bar{1}\bar{1}1]$	(101)	(011)
8	$[\bar{1}\bar{1}1]$	$(0\bar{1}\bar{1})$	$(1\bar{1}0)$
9	$[\bar{1}\bar{1}1]$	$(\bar{1}10)$	$(\bar{1}0\bar{1})$
10	$[1\bar{1}1]$	$(10\bar{1})$	(110)
11	$[1\bar{1}1]$	(011)	$(\bar{1}01)$
12	$[1\bar{1}1]$	$(\bar{1}\bar{1}0)$	$(0\bar{1}\bar{1})$
49	$[111]$	$(11\bar{2})$	$(\bar{1}2\bar{1})$
50	$[111]$	$(1\bar{2}1)$	$(2\bar{1}\bar{1})$
51	$[111]$	$(\bar{2}11)$	$(\bar{1}\bar{1}2)$
52	$[\bar{1}11]$	$(\bar{1}1\bar{2})$	$(\bar{2}\bar{1}\bar{1})$
53	$[\bar{1}11]$	$(\bar{1}\bar{2}1)$	$(1\bar{1}2)$
54	$[\bar{1}11]$	(211)	$(12\bar{1})$
55	$[\bar{1}\bar{1}1]$	$(\bar{1}\bar{1}\bar{2})$	$(1\bar{2}\bar{1})$
56	$[\bar{1}\bar{1}1]$	$(\bar{1}21)$	$(\bar{2}1\bar{1})$
57	$[\bar{1}\bar{1}1]$	$(2\bar{1}1)$	(112)
58	$[1\bar{1}1]$	$(\bar{1}12)$	$(\bar{2}\bar{1}1)$
59	$[1\bar{1}1]$	$(\bar{1}\bar{2}\bar{1})$	$(1\bar{1}\bar{2})$
60	$[1\bar{1}1]$	$(21\bar{1})$	(121)

Finally, some important notes on slip system notation should be addressed. The slip systems given in Table III-5 do have different though equivalent notation that is not explicitly shown in the table. For example, $[111](01\bar{1})$ in the first row could be written as $[111](0\bar{1}1)$. This means that in order to be consistent with the rule of determining the non-glide stress plane, the signs of the non-glide stress plane must also be reversed, changing from $(\bar{1}10)$ to $(1\bar{1}0)$. The sign of the resolved glide shear stress and the 1st non-glide stress then reverse because the signs of their respective planes have been reversed, while the signs of the other non-glide stresses are not affected. That alternate notation is equivalent to the original notation because it describes the other half of a glide loop. For example, if $[111](01\bar{1})$ were the positive half then $[111](0\bar{1}1)$ describes the negative half of the same glide loop, which is really all the same dislocation, and either half of the glide loop results in the same shear strain. Choosing which notation to use amounts to whichever notation is convenient. This thesis uses the notation that gives a positive resolved glide shear stress, and so slip systems will occasionally be given with reversed slip planes. On a cautionary note, the table in the literature [65, 66] from which the non-glide stress planes for the slip systems with {110} slip planes are reproduced also included slip systems with the same {110} slip plane, though with a reversed Burgers vector and different non-glide stress plane. For example, on the same row as the $[111](01\bar{1})$ slip system with a $(\bar{1}10)$ non-glide stress plane, a second slip system is given as $[\bar{1}\bar{1}\bar{1}](01\bar{1})$ with a $(10\bar{1})$ non-glide stress plane. The first slip system is appropriate for tension, and the second slip system is for compression; the authors in [65, 66] assert that the difference in non-glide stress plane helps explain why the effective yield stress is different in tension versus compression, since the magnitude of the stress on each is not necessary the same even for the same load axis. However, this thesis only uses the

simplification of uniaxial tension, and so Table III-5 only includes slip systems appropriate for tension.

IV. Results

A. Introduction

Local regions of each specimen from both the Tokyo-Denkai and Ningxia sample sets were investigated using electron microscopy methods to identify evidence for activated slip systems. Orientation imaging microscopy (OIM) was used to identify grain orientations and orientation gradients of the samples after sample preparation (chemical etches and polishing), after deformation, and for the Tokyo-Denkai samples also after welding. The resolved shear stresses on each slip system were calculated using the crystal orientation of the sample. Tables were made listing the slip systems of each sample with resolved shear stresses great enough to suggest activation of that slip system was possible. Secondary electron and backscattered electron images of the deformed samples were used to observe possible slip traces. The visible traces were then identified by matching them to slip traces that had been calculated from the crystal orientations of the deformed samples, and the results listed as tables. The OIM data were also used to generate pole figures, which showed how the crystal lattice of each sample rotated due to deformation.

The Tokyo-Denkai and Ningxia sample sets complement one another in that both sets provide the opportunity to investigate the deformed state in niobium of different purities. The Tokyo-Denkai set of samples were welded and recrystallized before a more detailed investigation of the dislocation substructure could be done. The Ningxia set of samples systematically varied the initial resolved shear stress on slip systems to investigate {110} versus {112} slip, and the effect of various combinations of slip systems on dislocation substructure, forming a foundation of data for future investigation of recrystallization. The results for Tokyo-Denkai samples C, F, and A provide stress-strain curves, slip trace observations, orientation

maps, and pole figures used to gather evidence for later discussion of which slip systems were most likely to have been active. Representative locations on the Ningxia sample set are discussed in detail, and a table summarizing observations of all of the Ningxia sample set is provided.

B. Tensile tests of the Tokyo-Denkai and Ningxia single crystal samples

Engineering stress-strain curves represent the collective effects of purity, pre-existing dislocations, and interactions of different slip systems as tensile deformation proceeded in each sample. Figure IV-1 shows the engineering stress-strain curves of all the Tokyo-Denkai and Ningxia single crystal samples to the final engineering strain of approximately 40%. The changes in slope in the stress-strain curve of each sample indicate changes in the resistance to deformation resulting from dislocation accumulation and/or changes in crystal orientation. Figure IV-2 shows the true stress-strain curves calculated from the same load and elongation data that the engineering stress-strain curve had been calculated from. The difference between the engineering and true stress-strain curves is that the cross-sectional area of the sample is assumed to be constant throughout deformation when calculating the engineering stress, while the true stress and true strain calculations assume a continuously reduced cross-sectional area that maintains a constant volume throughout deformation. The true stress-strain curves for samples A and U3 are truncated at the true strain where each sample reached ultimate tensile strength, because the true stress and true strain calculations are inaccurate beyond the ultimate tensile strength. The softening observed in the engineering stress-strain curves is absent in the true stress-strain curves, indicating that the softening observed in the engineering stress-strain curves is an artifact of the constant cross-sectional area assumption. Softening is still observed in the true stress-strain curve for sample T3, and may not be wholly due to this artifact.

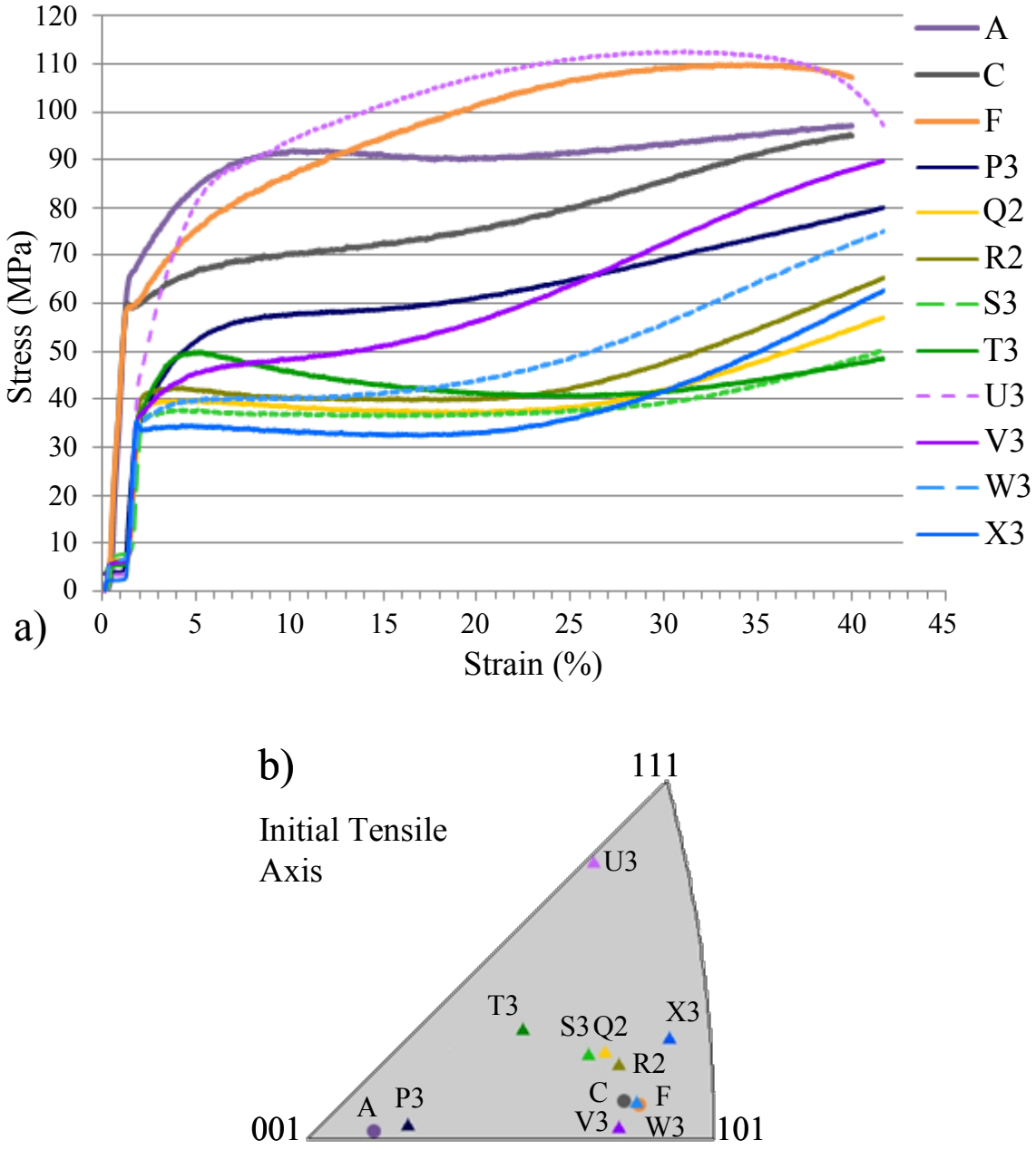

Figure IV-1. a) The engineering stress-strain curves for both sets of samples. Note the plateau that indicates easy glide just after yield (e.g. samples Q2, R2, S3, W3, X3), and the changes in slope indicating changes in hardening behavior. b) The inverse pole figure shows the crystal direction of the initial tensile axis for each of the Tokyo-Denkai (circle) or Ningxia (triangle) samples.

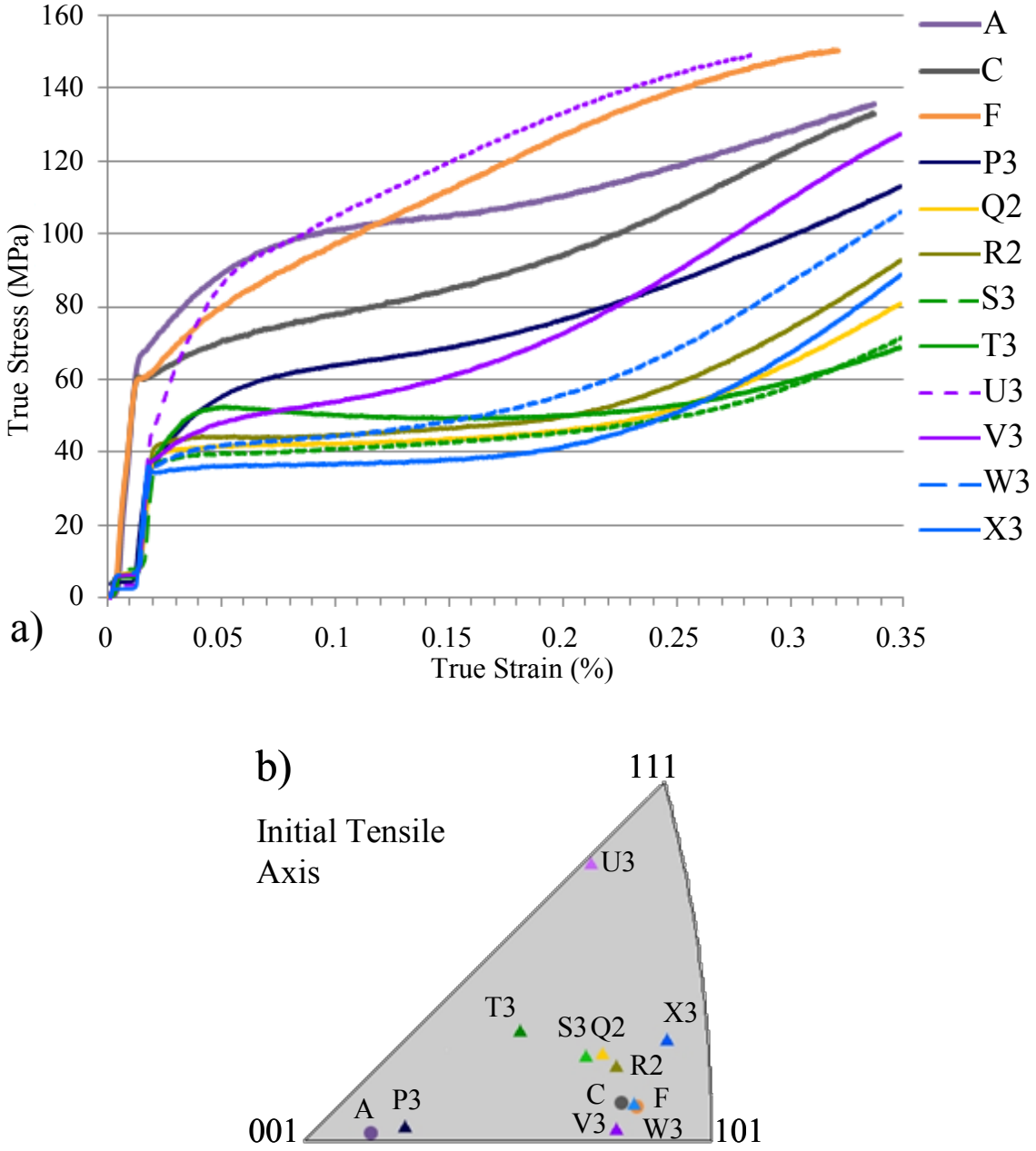

Figure IV-2. a) The true stress-strain curves for both sets of samples. b) The inverse pole figure shows the crystal direction of the initial tensile axis for each of the Tokyo-Denkai (circle) or Ningxia (triangle) samples.

Table IV-1 lists the slip systems initially oriented to have high Schmid factors that would result in a high resolved shear stress on those slip systems, the yield stress, and a brief description of the work hardening behavior immediately following yield for each sample. The orientations of samples Q2, R2, S3, W3, and X3 were selected to promote slip in a single <111> direction, and all possess a plateau of little or no work hardening in the stress-strain curves, or easy glide, up to a strain of about 20%; the plateau is expected because these samples were initially oriented for single slip. Sample T3 was also oriented such that slip was promoted in a single <111> direction; instead of the expected plateau, the hardening rate increased immediately upon yield and was followed by slight softening. Samples C and F from the lower purity Tokyo-Denkai ingot were also oriented such that slip was promoted in a single <111> direction; however the expected plateau does not occur in the stress-strain curves. Samples A, P3, U3, and V3 were oriented so that two or more slip systems of differing slip directions had nearly the same resolved stress so that hardening was expected immediately upon yield; the hardening rate of the stress-strain curves for these samples did increase immediately upon yielding.

Table IV-1. The slip systems with the highest 4 Schmid factors (direction with highest is in **bold type**) in single crystal tensile specimens from the Tokyo-Denkai sample set (A,C,F) and the Ningxia sample set (P3,Q2,R2,S3,T3,U3,V3,W3,X3). Twinning (T) and anti-twinning (A) planes are noted.

Name	Initial order of Schmid factors on slip systems	0.2% strain offset Yield Stress (MPa), Initial hardening behavior; other notes
A	0.49 [**1$\bar{1}$1**]($\bar{1}$12)T, 0.49 [111]($\bar{1}\bar{1}$2)A, 0.46 [111](0$\bar{1}$1), 0.45 [**1$\bar{1}$1**](011)	66.0 high hardening then softening; 4 slip systems with high Schmid factor
C	0.48 [**1$\bar{1}$1**](121)A, 0.48 [**1$\bar{1}$1**](011), 0.44 [111](0$\bar{1}$1), 0.43 [111](1$\bar{2}$1)T	59.1 moderate hardening
F	0.48 [**1$\bar{1}$1**](121)A, 0.47 [**1$\bar{1}$1**](011), 0.43 [111](1$\bar{2}$1)T, 0.43 [111](0$\bar{1}$1)	59.2 high hardening
U3	0.38 [**1$\bar{1}$1**](121)A, 0.37 [$\bar{1}$11](211)T, 0.36 [**1$\bar{1}$1**](011), 0.36 [$\bar{1}$11](101)	46.3 extremely high hardening; 4 slip systems with low Schmid factors
P3	0.49 [**1$\bar{1}$1**]($\bar{1}$12)T, 0.49 [111]($\bar{1}\bar{1}$2)A, 0.47 [111](0$\bar{1}$1), 0.47 [**1$\bar{1}$1**](011)	34.8 high hardening; 4 slip systems with high Schmid factor
V3	0.47 [**1$\bar{1}$1**](011), 0.46 [**1$\bar{1}$1**](121)A, 0.46 [111](0$\bar{1}$1), 0.45 [111](1$\bar{2}$1)T	37.1 moderate hardening; 4 slip systems with high Schmid factor
W3	0.48 [**1$\bar{1}$1**](121)A, 0.47 [**1$\bar{1}$1**](011), 0.44 [111](1$\bar{2}$1)T, 0.44 [111](0$\bar{1}$1)	34.7 moderate-low hardening
X3	0.50 [**1$\bar{1}$1**](121)A, 0.46 [**1$\bar{1}$1**](011), 0.41 [1$\bar{1}$1](110), 0.38 [111](1$\bar{2}$1)T	34.1 upper yield point, slight softening
R2	0.48 [**1$\bar{1}$1**](121)A, 0.48 [**1$\bar{1}$1**](011), 0.42 [111](0$\bar{1}$1), 0.40 [111](1$\bar{2}$1)T	40.7 slight hardening then softening
Q2	0.48 [**1$\bar{1}$1**](011), 0.48 [**1$\bar{1}$1**](121)A, 0.41 [111](0$\bar{1}$1), 0.38 [111](1$\bar{2}$1)T	39.1 slight softening
S3	0.49 [**1$\bar{1}$1**](011), 0.47 [**1$\bar{1}$1**](121)A, 0.43 [111](0$\bar{1}$1), 0.38 [111](1$\bar{2}$1)T	36.4 slight softening
T3	0.49 [**1$\bar{1}$1**](011), 0.44 [**1$\bar{1}$1**](121)A, 0.42 [111](0$\bar{1}$1), 0.41 [111]($\bar{1}\bar{1}$2)A	37.6 high hardening then softening, ends deformation with lowest flow stress

The Tokyo-Denkai samples (samples A, C, and F) exhibited subtle upper-lower yield point behavior, and possessed a significantly higher yield stress than the Ningxia sample set. Sample C, the upper dark gray curve in Figure IV-1, had the lowest yield stress of the three Tokyo-Denkai specimens, and a modest initial hardening rate that decreased to a low rate after about 5% strain, and then increased again at about 17% strain. In contrast, the upper orange curve of sample F possessed an initially high hardening rate that decreased gradually until reaching an ultimate strength near 40% strain. Sample A, the upper purple curve, was a hard orientation that had the highest yield stress immediately followed by a high hardening rate. The flow stress of sample A peaked soon after yield near 9% followed by modest softening, after which hardening developed again at approximately 18% strain; by the end of deformation the flow stress was slightly greater than the peak stress that had occurred at 9% strain. Sample A shows a distinct upper yield point effect; samples C and F show a similar effect but without the stress decrease upon yielding.

C. Evidence for activated slip systems in the Tokyo-Denkai samples

1. Side C of welded sample FC

Figure IV-3 is a secondary electron image (SEI) of side C of welded sample FC. The grain boundaries of the recrystallization front (white arrows) divided the recrystallized grains to the left and the recovered orientations to the right; the nominal tensile strain at the imaged location was 40%. A rough estimate of the local Engineering strain in the tensile direction is also given for each imaged location, as this varied even within the same sample. The recovered orientations had sufficient heat to allow many dislocations to find nearby annihilation partners, but there was not enough grain boundary mobility for the growing recrystallized grains to change the crystal orientation. Thus, geometrically necessary dislocations associated with slip bands were preserved. Dislocations exiting the surface due to recovery probably did not significantly affect the visibility of the slip traces that had formed during deformation. The short solid white lines indicate the visible traces observed on the surface of the sample. Each visible trace (solid white lines) was copied and compared to similar features nearby (dashed white lines) to establish that it was a repeating feature, as would be expected of real slip traces that had formed on the surface due to the motion of dislocations on the separate though parallel planes of an active slip system. The long, labeled white lines are the plane traces calculated from the orientation data to which the visible traces were matched. Figure IV-4 shows the same area and uses the same notation as Figure IV-3, for a backscattered electron image (BEI). Visible traces are apparent in both Figure IV-3 and Figure IV-4 for four slip planes: (121), (110), $(1\bar{1}2)$, and $(2\bar{1}1)$.

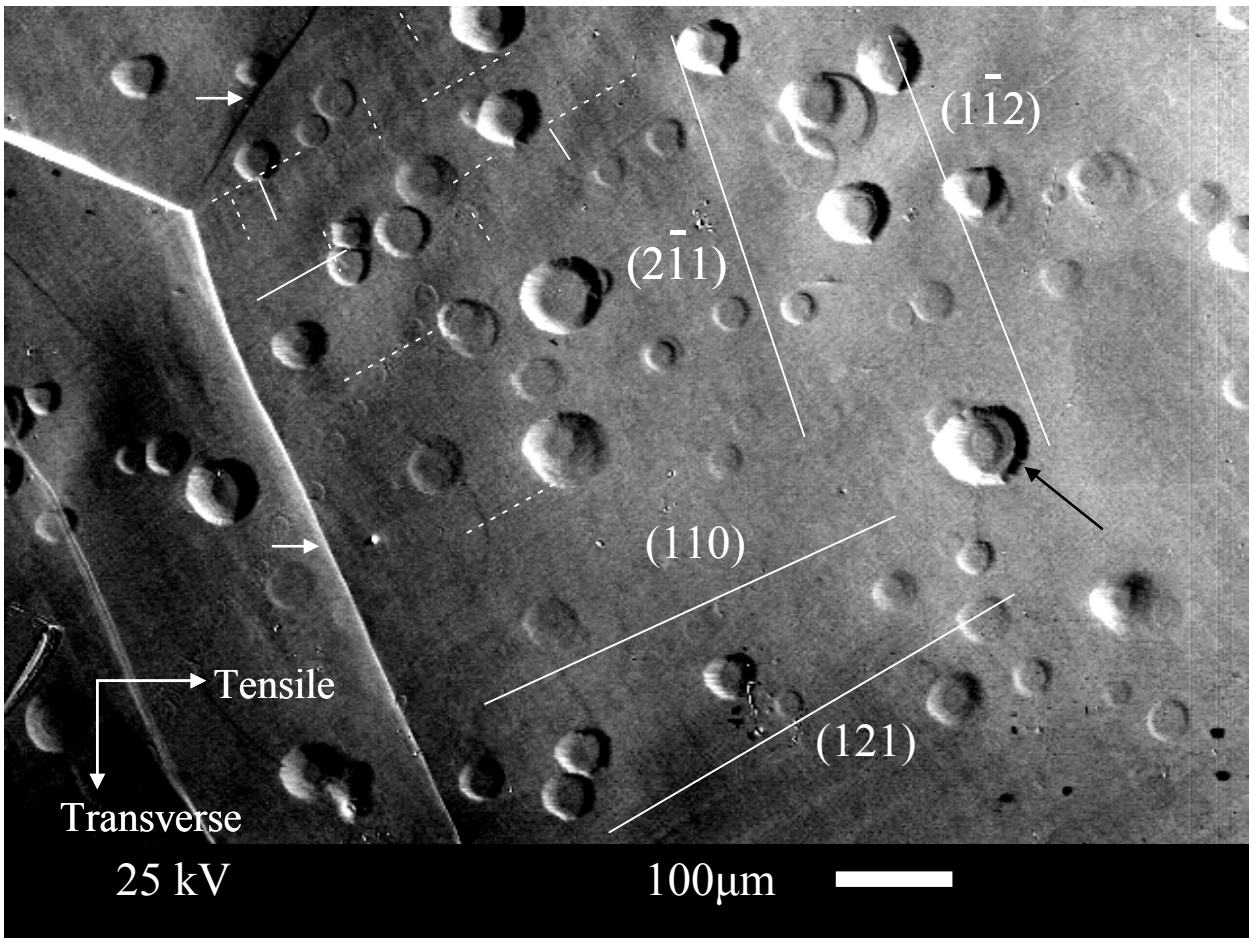

Figure IV-3. Slip traces on side C of welded sample FC (SEI image). The grain boundaries of the recrystallization front (white arrows) divided the recrystallized grains on the left from the recovered region on the right where there slip traces are drawn. The visible traces (short solid white lines) were matched to the calculated slip traces (labeled, longer solid white lines). Copies of the visible traces show that the trace repeats itself (short dashed white lines). One of many pits that formed due to a 10min BCP etch after deformation (black arrow). The estimated local tensile strain was 40%.

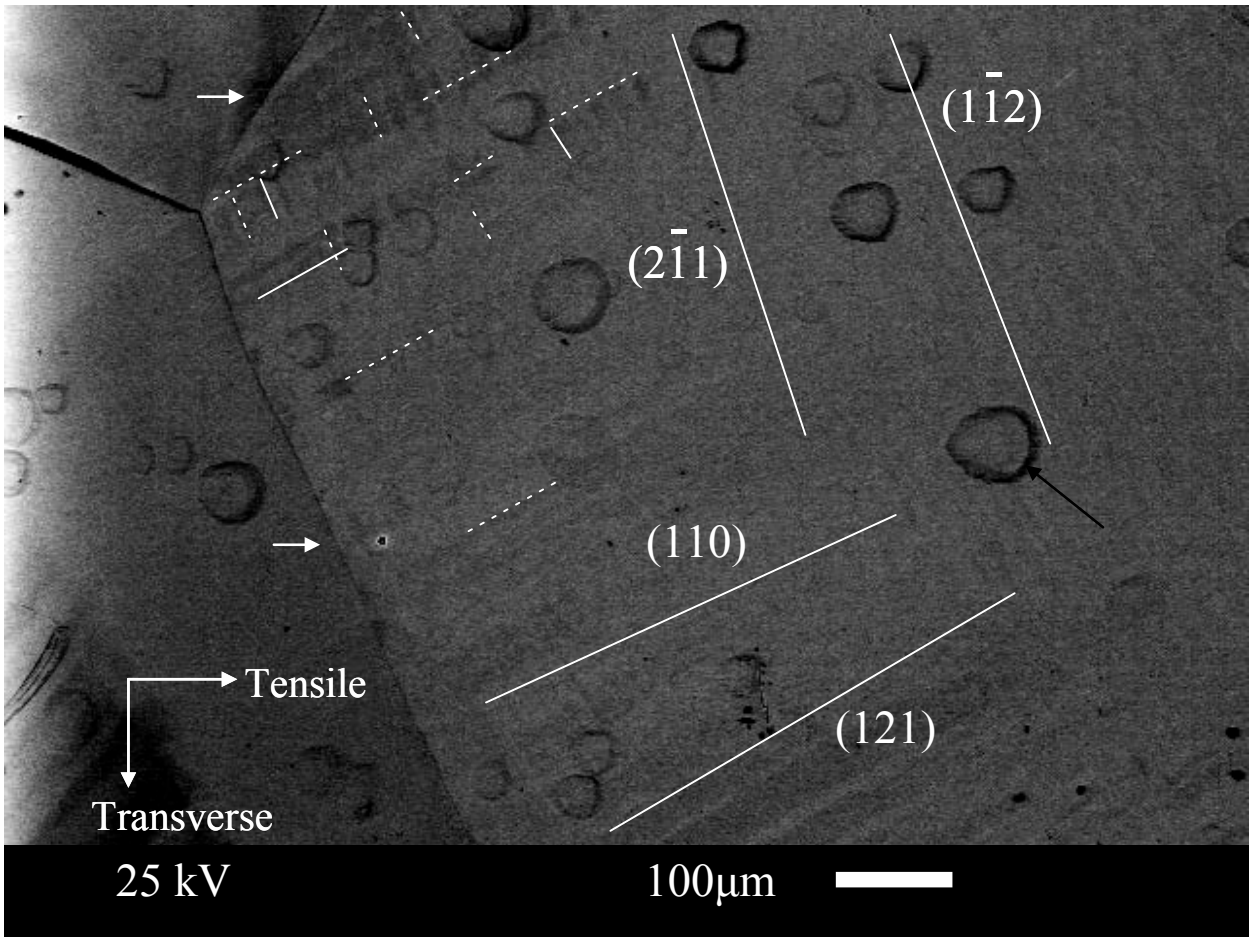

Figure IV-4. Slip traces on side C of welded sample FC. The location and notation is identical to Figure IV-2, though imaged instead in BEI mode. The grain boundaries of the recrystallization front (white arrows) divided the recrystallized grains on the left from the recovered region on the right where the slip traces are drawn. The estimated local tensile strain was 40%.

While both secondary and backscattered electron images were taken and used to identify visible traces on the normal (polished) surface, only the images in which the visible traces are most apparent will be shown for the remaining samples. Images not shown in the main text are provided in the Appendix. Because a BCP etch is normally done to clean a cavity surface before welding two halves of a cavity together by electron beam welding, a similar 10min buffered-chemical 'polish' (BCP) was made on the Tokyo-Denkai samples after deformation. The etching caused some pitting seen in Figure IV-3 and Figure IV-4, with an example pit indicated by a black arrow. Pitting is also visible on some of the other Tokyo-Denkai samples.

Figure IV-5 shows three discrete pole figures made from EBSD data that compare the orientations of crystal C in sample FC before deformation, after deformation, and after welding. The black data are from the initial crystal orientation, collected from the center of the gage length before deformation[3]. The gray data are from the deformed crystal orientation, collected from a location about 3 millimeters from the center of the gage length after deformation. The white data are from the recovered crystal orientation, collected near the recrystallization front 3-4 millimeters from the weld. By overlaying these data, each pole figure illustrates the rotation of a particular family of crystal directions (i.e. poles) in relation to the laboratory coordinate axes: the

[3] The fuzziness of the poles indicates a distribution of orientations and/or orientation gradients. A higher spread could imply more pre-existing dislocations, but the geometry of their arrangement is not known. There is no correlation between spread with initial hardening rates, and in fact, the spread in most of the samples is similar, around half a degree. Thus, the relationship between these implied dislocations and those activated during the tensile test are examined in the discussion.

normal direction points to the right, the transverse direction points down the page, and the tensile direction points into the page from the center of the pole figure; the positions of the laboratory axes will change for each sample in order to consistently show the similar primary and secondary slip directions that were chosen to ease comparison of slip systems between samples. These data are presented in a stereographic projection, such that 90° from the center represents the transverse-normal plane that is perpendicular to the tensile axis. White circles in the pole figures of Figure IV-5 mark the loci of orientations 45° from the tensile direction, because for the case of uniaxial tension, the maximum resolved shear stress possible on a slip system occurs when the slip direction and slip plane normal are both exactly 45° from the tensile direction.

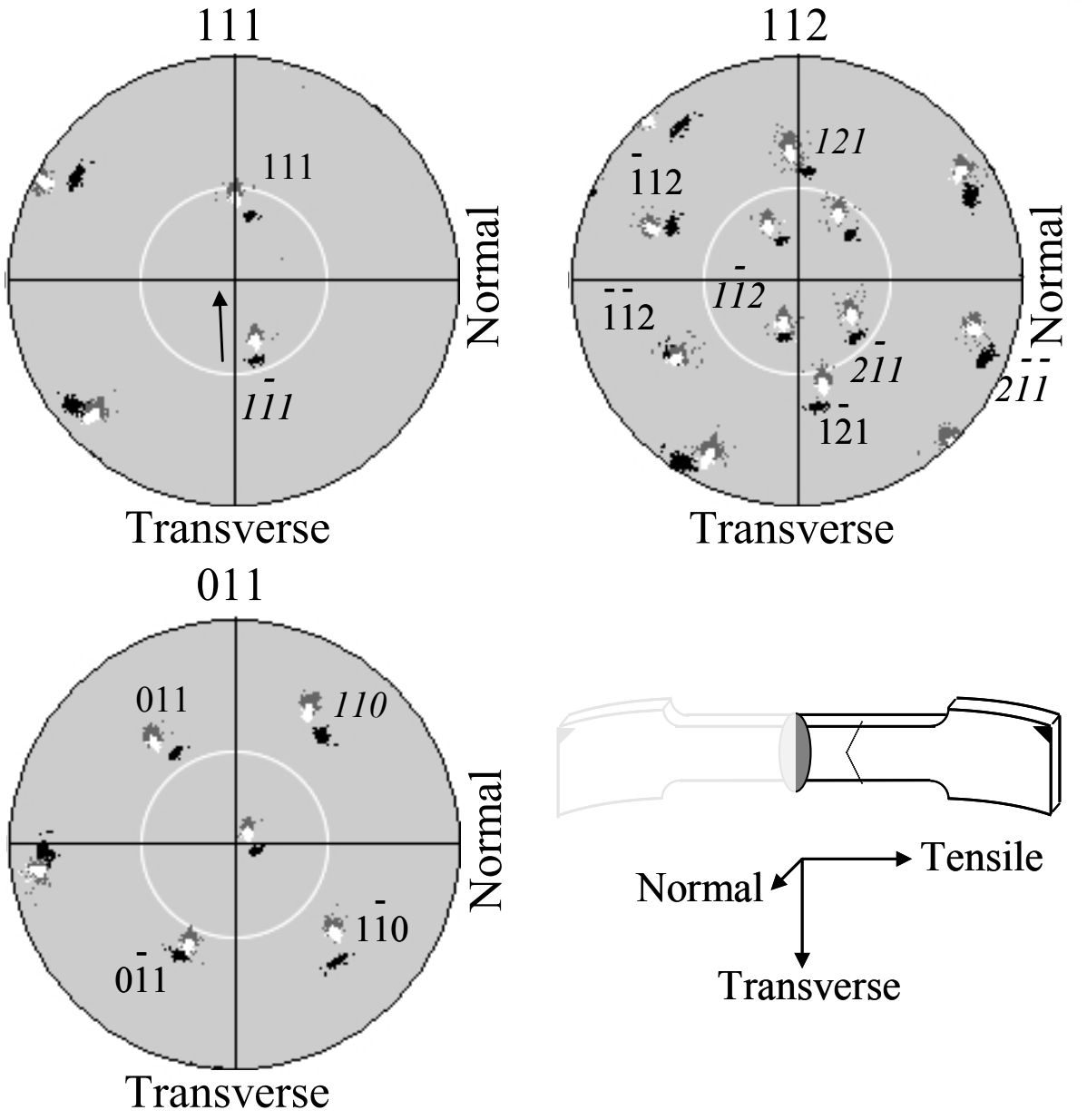

Figure IV-5. Pole figures collected from side C of welded sample FC and a schematic of the sample; the dotted line is the recrystallization front. The center of each plot is the tensile axis. Initial (black), deformed (grey), and recovered (white) orientations are overlaid. Labeled directions describe all three orientations. The slip plane normals of observed plane traces (italic text), and slip plane normals with no observed plane traces for slip systems that acquired enough resolved shear to possibly be active (plain text), are also labeled. Upper Left <111> PF: Note that the primary $[1\bar{1}1]$ slip direction (italic text) rotated toward the tensile axis, and that the secondary [111] slip direction (plain text) rotated closer to being 45° from the tensile axis (white circle).

The <111> pole figure in the upper left of Figure IV-5 shows how the <111> slip directions have rotated in response to deformation. The primary $[1\bar{1}1]$ slip direction (labeled in italic text) rotated toward the tensile direction, while the secondary [111] slip direction (labeled in plain text) rotated closer to 45° from the tensile direction. The slip plane normals also rotate due to deformation. The <110> pole figure in the lower left of Figure IV-5 shows that the (011) slip plane normal had initially been near 45° to the tensile axis (black spot near white circle) and then rotated away (white spot). Conversely, the $(0\bar{1}1)$ slip plane normal was initially away from and then rotated toward 45° from the tensile direction. Similarly, the <112> pole figure in the upper right of Figure IV-5 shows that the (121) slip plane normal had initially been near and then rotated away from being 45° to the tensile direction. Conversely, the $(1\bar{2}1)$ slip plane normal was initially away from and then rotated toward 45° from the tensile direction. Therefore, the slip direction and slip plane normals that were further from the 45° orientation resulted in less resolved shear on the $[1\bar{1}1](011)$ and $[1\bar{1}1](121)$ slip systems, while the rotation of the slip direction and slip plane normals closer to 45° from the tensile direction resulted in increased resolved shear stress on the $[111](0\bar{1}1)$ and $[111](1\bar{2}1)$ slip systems. The pole figures give a visual sense of the rotation of the crystal, the spreading of the orientation as deformation proceeded (increasing size and smearing of the spots), and the changes in resolved shear on the various slip systems, while tables provide quantitative data the quantitative distribution of the Schmid factors and resolved shear stresses on the various slip systems.

Table IV-2 summarizes the evidence for active slip systems for both sides of sample C of the Tokyo-Denkai sample set. In order to be listed in Table IV-2, a slip system must meet either of two criteria: 1) A slip system must possess either an initial or final resolved glide shear stress that was at least half that of the highest initial resolved glide shear stress of that slip plane family.

For example, because the initial resolved glide shear stress was 28.2 MPa for the $[1\bar{1}1](121)$ slip system, any other slip systems with a {112} slip plane and either an initial or final resolved glide shear stress equal to or greater than 14.1 MPa are listed. 2) If a visible slip trace matched a slip system's calculated slip plane trace, that slip system is listed regardless of resolved glide shear stress. The reasoning for these criteria are that 1) the non-glide shear stress effect alone is theorized to enable slip systems with half the highest glide shear stress to be active, and 2) the physical evidence of a plane trace matching a visible slip trace must be examined closely and the resolved shear stresses are evidence that will be used to argue for or against activity. Table IV-2 lists the slip systems meeting the criteria for both sides of sample C. Those slip systems with visible traces that matched calculated slip traces are marked '*'. Table IV-2 gives the initial resolved glide and non-glide shear stresses at yield and the final glide and non-glide resolved shear stress at the end of deformation for each slip system, and notes the twinning planes (T) and the anti-twinning (A) planes for the slip systems possessing {112} slip planes, the 0.2% offset yield stress and final flow stress, hardening rate immediately after yield, the crystal directions that moved toward the tensile direction, and the initial and final Euler angles used to calculate the resolved stresses. Tables containing similar data for the other Tokyo-Denkai samples are given in subsequent sections, and were assembled in the same manner as Table IV-2 was for sample C (Table IV-3 for sample F and Table IV-4 for sample A).

Table IV-2. A list of evidence considered for potentially active slip systems for both sides of sample C of the Tokyo-Denkai sample set. The 0.2% strain offset yield stress and final flow stress are given under the sample name, in that order. Slip systems with matching possible and calculated slip traces are marked '*', and the greatest initial and final resolved glide shear stresses for the {110} and {112} slip system families are given in bold. Twinning (T) and anti-twinning (A) {112} planes are also indicated.

Sample, stresses (MPa), Hardening slope at yield, Slip direction that rotated toward TD, Initial Euler angles, Final Euler angles	Potentially active system	Initial resolved shear stress at yield (MPa): glide, non-glide 1, 2, 3	Final resolved shear stress (MPa): glide, non-glide 1, 2, 3
FC side C 59.1, 94.7 Slight $[1\bar{1}1]$ 6 125 93 2 128 101	$[1\bar{1}1](121)$*	**28.2** 20.4 -6.0 12.4 A	40.9 29.3 -6.1 12.9 A
	$[1\bar{1}1](011)$	**28.1** 7.3 6.4 6.0	40.6 10.2 6.9 6.1
	$[111](0\bar{1}1)$	26.1 18.0 -3.6 8.4	**44.2** 35.1 -12.1 19.7
	$[111](1\bar{2}1)$	25.5 5.8 4.9 3.6 T	**45.8** 15.0 7.6 12.1 T
	$[1\bar{1}1](110)$*	20.8 28.1 -12.4 6.4	30.4 40.6 -12.9 6.9
	$[1\bar{1}1](\bar{1}12)$	20.4 -7.8 12.4 -6.4 T	29.3 -11.6 12.9 -6.9 T
	$[111](\bar{1}\bar{1}2)$	19.7 25.5 -8.4 4.9 A	30.8 45.8 -19.7 7.6 A
	$[111](1\bar{1}0)$	18.0 -8.0 8.4 -4.9	35.1 -9.1 19.7 -7.6
	$[\bar{1}11](1\bar{1}2)$*	8.9 8.5 -23.8 25.8 A	5.1 4.3 -32.9 45.7 A
	$[111](2\bar{1}\bar{1})$	5.8 -19.7 3.6 -8.4 N/A	15.0 -30.8 12.1 -19.7 N/A
	$[\bar{1}11](110)$*	4.7 -5.3 23.8 -25.8	2.1 -3.4 32.9 -45.7
	$[\bar{1}\bar{1}1](2\bar{1}1)$*	4.1 4.9 -28.6 19.8 A	12.0 12.1 -40.5 39.7 A
CA side C 59.1, 94.7 Slight $[1\bar{1}1]$ 6 125 93 1 128 99	$[1\bar{1}1](121)$*	**28.2** 20.4 -6.0 12.4 A	41.1 29.6 -6.3 13.2 A
	$[1\bar{1}1](011)$	**28.1** 7.3 6.4 6.0	40.8 10.5 6.9 6.3
	$[111](0\bar{1}1)$	26.1 18.0 -3.6 8.4	**44.3** 34.9 -11.7 19.5
	$[111](1\bar{2}1)$	25.5 5.8 4.9 3.6 T	**45.7** 14.7 7.8 11.7 T
	$[1\bar{1}1](110)$*	20.8 28.1 -12.4 6.4	30.4 40.8 -13.2 6.9
	$[1\bar{1}1](\bar{1}12)$	20.4 -7.8 12.4 -6.4 T	29.6 -11.5 13.2 -6.9 T
	$[111](\bar{1}\bar{1}2)$	19.7 25.5 -8.4 4.9 A	31.0 45.7 -19.5 7.8 A
	$[111](1\bar{1}0)$	18.0 -8.0 8.4 -4.9	34.9 -9.4 19.5 -7.8
	$[\bar{1}11](1\bar{1}2)$*	8.9 8.5 -23.8 25.8 A	5.6 4.8 -33.0 45.7 A
	$[111](\bar{1}01)$*	8.0 26.1 -4.9 -3.6	9.4 44.3 -7.8 -11.7
	$[1\bar{1}1](\bar{1}01)$*	7.3 -20.8 6.0 -12.4	10.5 -30.4 6.3 -13.2
	$[111](2\bar{1}\bar{1})$	5.8 -19.7 3.6 -8.4 N/A	14.7 -31.0 11.7 -19.5 N/A
	$[\bar{1}11](110)$*	4.7 -5.3 23.8 -25.8	2.3 -3.7 33.0 -45.7
	$[\bar{1}\bar{1}1](2\bar{1}1)$*	4.1 4.9 -28.6 19.8 A	11.9 12.1 -40.8 39.4 A

The results for side C of welded sample FC may then be summed up as follows, and the remaining samples are presented in a similar manner: The visible traces were identified as the (121), (110), $(1\bar{1}2)$, and $(2\bar{1}1)$ slip planes by matching them to calculated plane traces. The $[1\bar{1}1]$ slip direction was identified as the primary slip direction because it was observed to rotate toward the tensile axis, which suggests that at least one slip system with a $[1\bar{1}1]$ slip direction was active. The changes in resolved shear stress caused by the crystal rotation are quantified in Table IV-2. Table IV-2 indicates that the $[1\bar{1}1](121)$ and $[1\bar{1}1](110)$ slip systems, whose slip direction and slip planes match both the $[1\bar{1}1]$ slip direction rotation and visible trace observations, possessed high initial and final resolved glide shear stresses. While the (110) slip trace also corresponds to the $[\bar{1}11](110)$ slip system, Table IV-2 indicates that the initial and final resolved glide shear stress on that system was relatively low. Visible traces matching slip systems of the secondary [111] slip direction were not observed despite Table IV-2 indicating that high final resolved glide shear stresses were present on those systems at the end of deformation. However, the <111> pole figure in Figure IV-5 shows that the recovered [111] secondary slip direction has almost no component in the normal direction, meaning that the slip steps formed by dislocations of the [111] slip direction would not have emerged on the surface examined for slip traces, and this may account for the lack of observed slip traces of those slip systems. The component of the primary $[1\bar{1}1]$ direction in the normal direction is small, so the slip traces may also be faint; because secondary electron imaging relies on topography for contrast, so these slip traces may be less clear, which may account for the lack of observed slip traces of $[1\bar{1}1]$ slip systems. On the other hand, the plane traces of active slip systems are often visible in the backscattered electron image, because the rotations of the crystal lattice caused by

dislocations near the surface affect the intensity of the backscattering electrons and thus generate contrast. Further analysis regarding crystal rotations appear in the Discussion.

2. Side C of welded sample CA

The observations for side C of welded sample CA are similar to side C of Sample FC. The estimated local tensile strain was 21%. The backscattered electron image in Figure IV-6 shows the grain boundaries of the recrystallization front (white arrows) dividing the recrystallized grains to the right and the recovered orientation to the left, where a visible trace matched both the (121) and (110) calculated slip traces. Another visible trace matched both the $(1\bar{1}2)$ and $(2\bar{1}1)$ calculated slip traces. Another visible trace matched only the $(\bar{1}01)$ calculated slip trace. The <111> pole figure in Figure IV-7 shows that the primary $[1\bar{1}1]$ slip direction rotated toward the tensile axis (black arrow). Table IV-2 indicates that the slip traces of the $[1\bar{1}1](121)$ and $[1\bar{1}1](110)$ slip systems, whose slip direction and slip planes match both the $[1\bar{1}1]$ slip direction rotation and visible trace observations, were initially oriented for high resolved shear stress and still possessed high final resolved glide shear stresses at the end of deformation. Table IV-2 indicates that both the initial and final resolved shear stress was relatively low on the slip systems corresponding to the other slip traces. Side C of sample CA has the same slip trace visibility problems as side C of sample FC, and for similar reasons as described above for side C of sample FC.

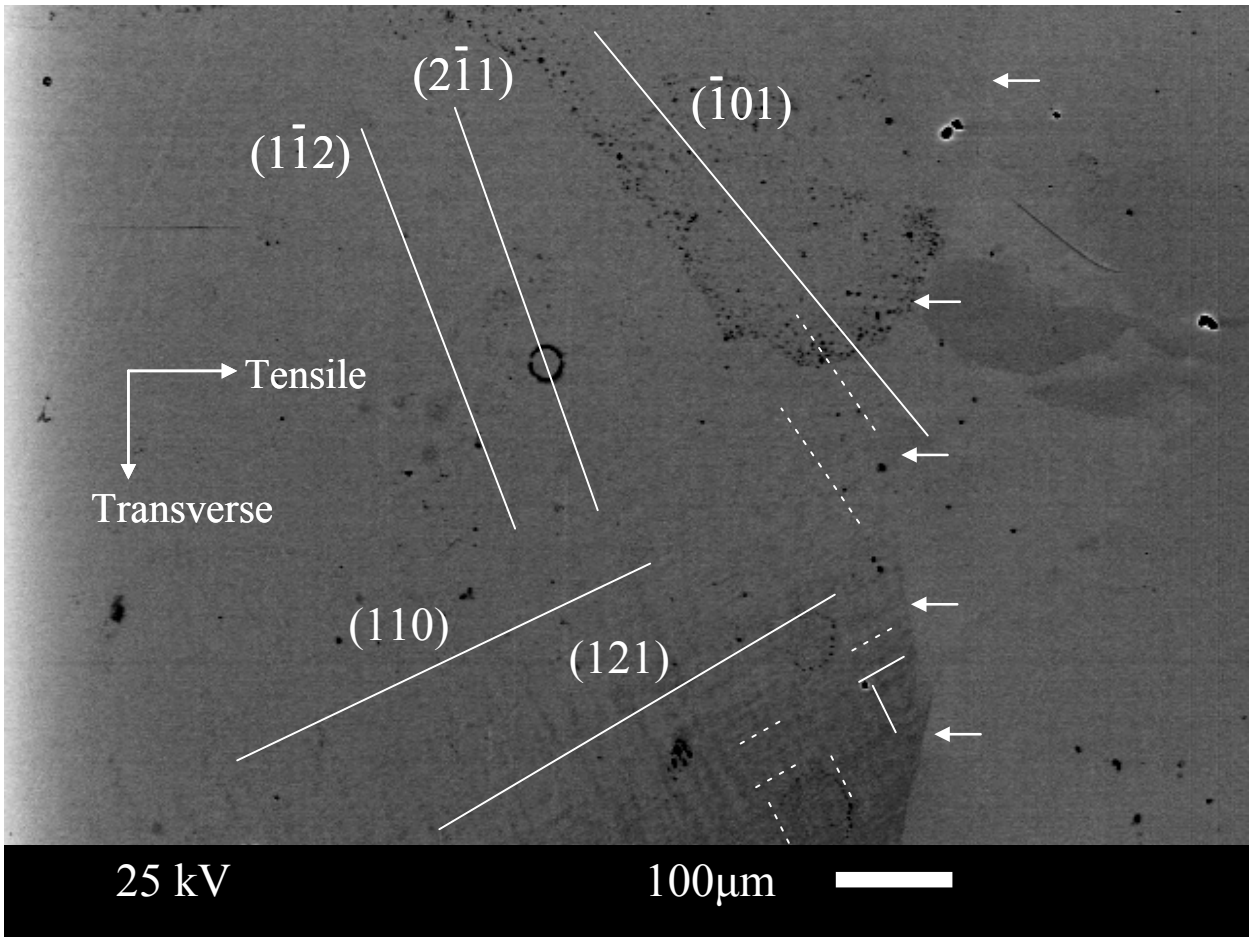

Figure IV-6. Slip traces on side C of welded sample CA (BEI). The grain boundaries of the recrystallization front (white arrows) divided the recrystallized grains to the right from the recovered region on the left, where the slip traces are drawn. The estimated local tensile strain was 21%.

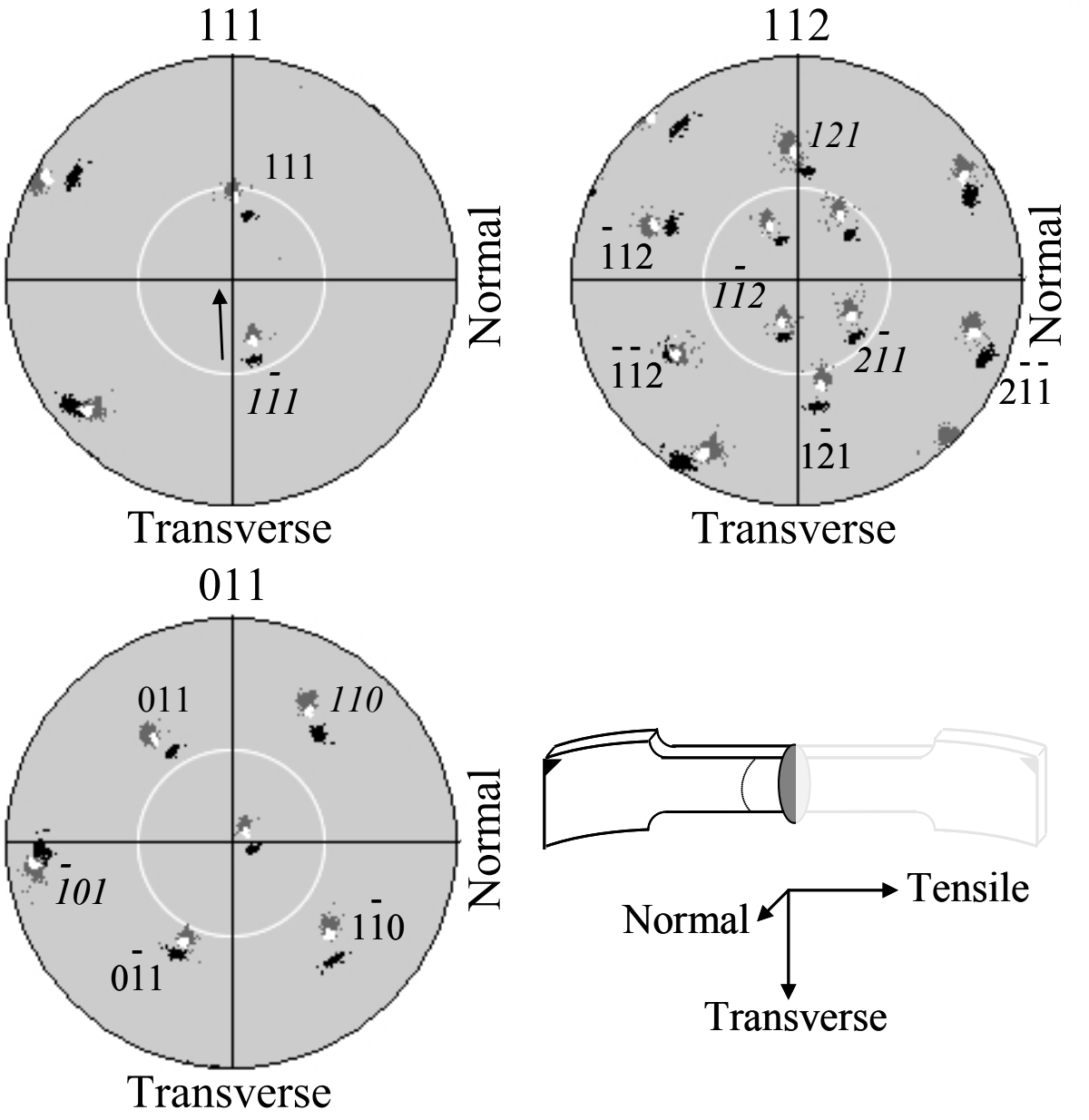

Figure IV-7. Pole figures collected from side C of welded sample CA and a schematic of the sample; the dotted line is the recrystallization front. The center of each plot is the tensile axis. Initial (black), deformed (grey), and recovered (white) orientations are overlaid. Labeled directions describe all three orientations. The slip plane normals of observed plane traces (italic text), and slip plane normals with no observed plane traces for slip systems that acquired enough resolved shear to possibly be active (plain text), are also labeled. Upper Left <111> PF: Note the rotation of the primary $[1\bar{1}1]$ slip direction (italic text) toward the tensile axis, and the rotation of the secondary slip direction (plain text) closer to 45° from the tensile axis (white circle).

Sample C is summarized as follows: The estimated local tensile strains for each half of sample C were not similar, with 40% for side FC and 21% for side CA. Despite the difference in local strain, both sides possessed visible traces that matched the calculated slip traces of the $[1\bar{1}1](121)$ and $[1\bar{1}1](110)$ slip systems, which possessed high resolved glide shear stresses. Both sides also showed the $[1\bar{1}1]$ primary slip direction rotating toward the tensile axis.

3. Side F of welded sample AF

Side F of welded sample AF is described in a similar manner as sample C: The SEI image in Figure IV-8 shows the grain boundaries of the recrystallization front (white arrows) dividing the recrystallized grains to the left and the recovered orientation to the right, where a visible trace that matched both the (121) and $(\bar{2}11)$ calculated slip traces and another visible trace matched the (211) calculated slip trace. The estimated local tensile strain at the image location was 27%. The <111> pole figure in Figure IV-9 shows that the primary $[1\bar{1}1]$ slip direction moved indirectly closer to the tensile axis (black arrow). Table IV-3 summarizes the evidence for active slip systems for both sides of sample F. Table IV-3 indicates that the highest initial and high final resolved glide shear stresses were present on the $[1\bar{1}1](121)$ slip system, whose slip direction and slip planes match both the $[1\bar{1}1]$ slip direction rotation and visible trace observations. Table IV-3 indicates that the initial and final glide shear stresses on the $[\bar{1}11](211)$ and $[111](\bar{2}11)$ slip systems were relatively low, though the slip planes match visible slip traces.

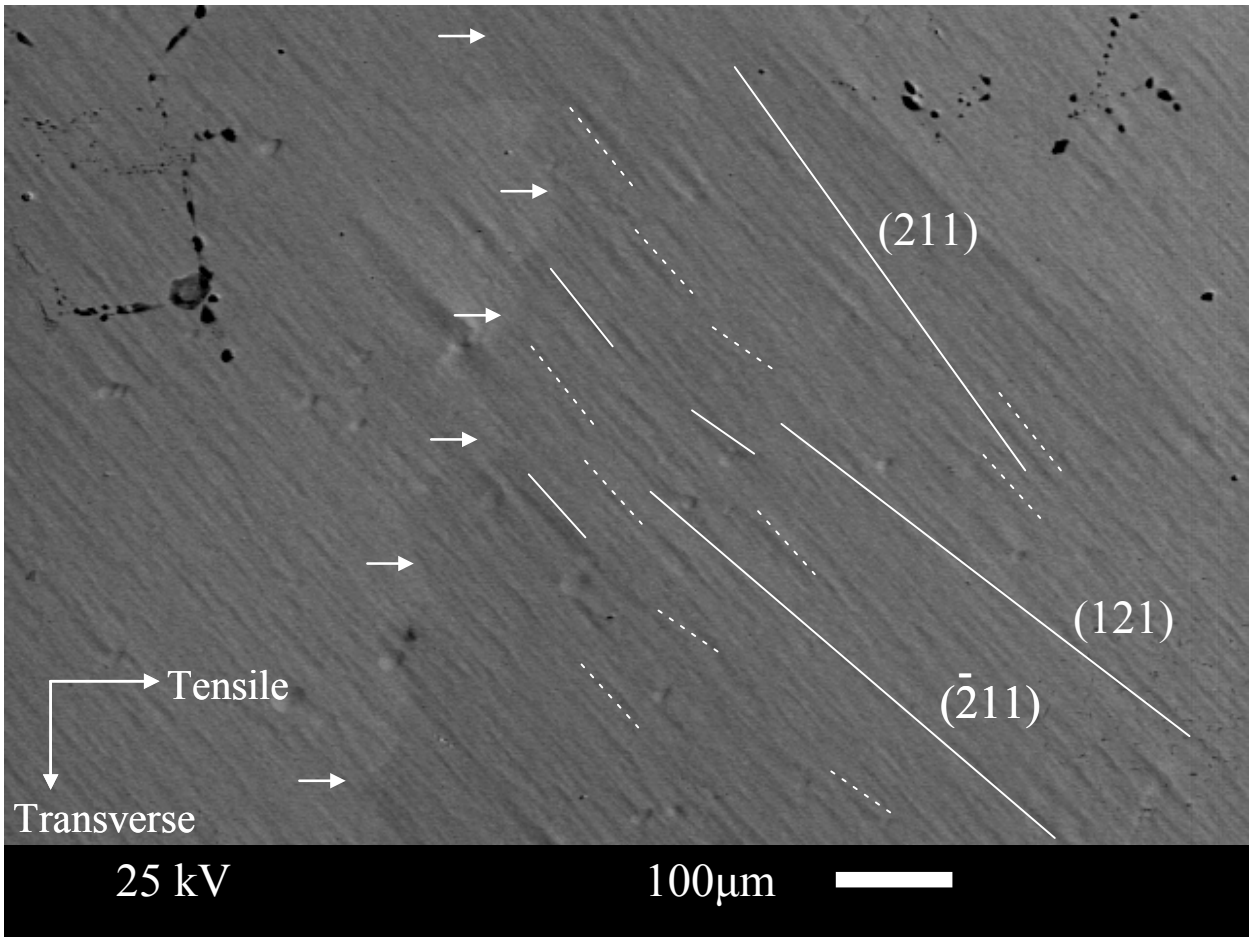

Figure IV-8. Slip traces on side F of welded sample AF (SEI). The grain boundaries of the recrystallization front (white arrows) divided the recrystallized grains on the left from the recovered region on the right where there slip traces are drawn. The estimated local tensile strain was 27%.

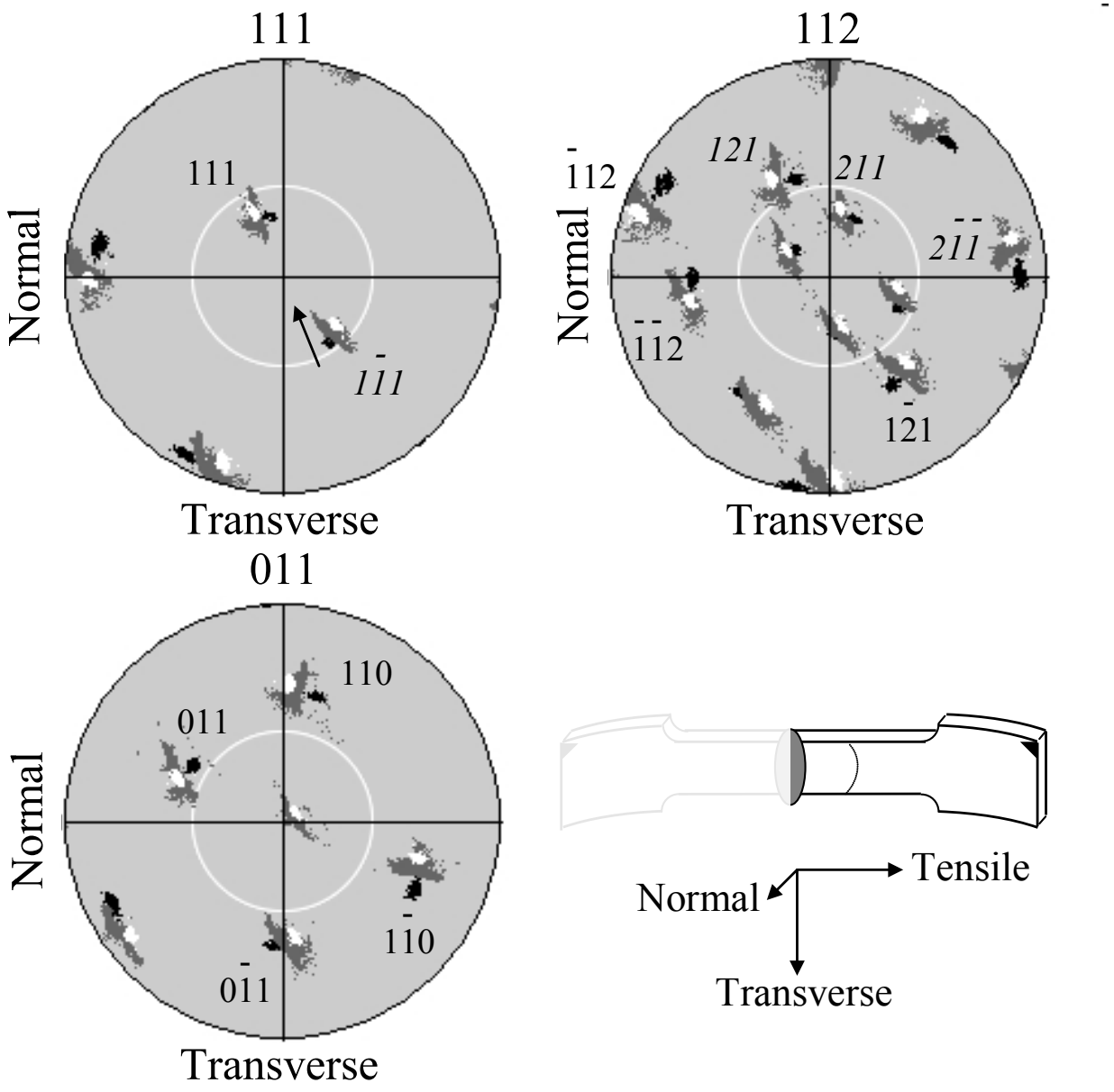

Figure IV-9. Pole figures collected from side F of welded sample AF and a schematic of the sample; the dotted line is the recrystallization front. Initial (black), deformed (grey), and recovered (white) orientations are overlaid. The slip plane normals of observed plane traces (italic text), and slip plane normals with no observed plane traces for slip systems that acquired enough resolved shear to possibly be active (plain text), are also labeled. Upper Left <111> PF: The primary $[1\bar{1}1]$ (italic text) slip direction moves indirectly toward the tensile axis, and [111] secondary (plain text) slip direction stays in place.

Table IV-3. A list of evidence considered for potentially active slip systems for both sides of sample F of the Tokyo-Denkai sample set. The 0.2% strain offset yield stress and final flow stress are given under the sample name, in that order. Slip systems with matching possible and calculated slip traces are marked '*', and the greatest initial and final resolved glide shear stresses for the {110} and {112} slip system families are given in bold. Twinning (T) and anti-twinning (A) {112} planes are also indicated.

Sample, stresses (MPa), Hardening slope at yield, Slip direction that rotated toward TD, Initial Euler angles, Final Euler angles	Potentially active system	Initial resolved shear stress at yield (MPa): glide, non-glide 1, 2, 3	Final resolved shear stress (MPa): glide, non-glide 1, 2, 3
FC side F 59.2, 107.3 Moderate $[1\bar{1}1]$ 159 58 300 154 57 319	$[1\bar{1}1](121)$*	**28.5** 19.5 -4.9 12.0 A	46.5 29.3 -4.1 13.6 A
	$[1\bar{1}1](011)$	**27.7** 6.1 7.1 4.9	43.8 7.0 9.4 4.1
	$[111](1\bar{2}1)$*	25.9 7.1 4.1 4.4 T	**52.6** 20.9 5.3 16.4 T
	$[111](0\bar{1}1)$	25.8 19.1 -4.4 8.4	**48.7** 42.4 -16.4 21.6
	$[1\bar{1}1](110)$	21.6 27.7 -12.0 7.1	36.7 43.8 -13.6 9.4
	$[1\bar{1}1](\bar{1}12)$*	19.5 -9.0 12.0 -7.1 T	29.3 -17.2 13.6 -9.4 T
	$[111](1\bar{1}0)$	19.1 -6.7 8.4 -4.1	42.4 -6.2 21.6 -5.3
	$[111](\bar{1}\bar{1}2)$	18.7 25.9 -8.4 4.1 A	31.7 52.6 -21.6 5.3 A
	$[1\bar{1}1](21\bar{1})$	9.0 28.5 -7.1 -4.9 N/A	17.2 46.5 -9.4 -4.1 N/A
	$[\bar{1}11](1\bar{1}2)$*	7.6 7.4 -24.4 25.7 A	1.2 1.1 -39.2 51.3 A
	$[\bar{1}11](211)$*	7.4 -0.2 25.7 -1.4 T	1.1 -0.2 51.3 -12.2 T
	$[111](2\bar{1}\bar{1})$*	7.1 -18.7 4.4 -8.4 N/A	20.9 -31.7 16.4 -21.6 N/A
AF side F 59.2, 107.3 Moderate $[1\bar{1}1]$ 159 58 300 158 60 311	$[1\bar{1}1](121)$*	**28.5** 19.5 -4.9 12.0 A	48.9 35.7 -8.9 17.9 A
	$[1\bar{1}1](011)$	**27.7** 6.1 7.1 4.9	48.8 13.0 9.0 8.9
	$[111](1\bar{2}1)$	25.9 7.1 4.1 4.4 T	**50.0** 14.0 9.3 10.2 T
	$[111](0\bar{1}1)$	25.8 19.1 -4.4 8.4	**49.7** 36.9 -10.2 19.5
	$[1\bar{1}1](110)$	21.6 27.7 -12.0 7.1	35.8 48.8 -17.9 9.0
	$[1\bar{1}1](\bar{1}12)$	19.5 -9.0 12.0 -7.1 T	35.7 -13.2 17.9 -9.0 T
	$[111](1\bar{1}0)$	19.1 -6.7 8.4 -4.1	36.9 -12.7 19.5 -9.3
	$[111](\bar{1}\bar{1}2)$	18.7 25.9 -8.4 4.1 A	36.0 50.0 -19.5 9.3 A
	$[\bar{1}11](211)$*	7.4 -0.2 25.7 -1.4 T	9.7 -1.2 50.2 -10.5 T
	$[111](2\bar{1}\bar{1})$*	7.1 -18.7 4.4 -8.4 N/A	14.0 -36.0 10.2 -19.5 N/A

4. Side F of welded sample FC

On side F of welded sample FC, the BEI image in Figure IV-10 shows the grain boundaries of the recrystallization front (white arrows) dividing the recrystallized grains to the right and the recovered orientation to the left, where visible traces matched the (121), $(1\bar{2}1)$, $(1\bar{1}2)$, (211) and $(\bar{2}11)$ calculated slip traces. The estimated local tensile strain at the image location was 33%. The <111> pole figure in Figure IV-11 shows that the primary $[1\bar{1}1]$ slip direction moved toward the tensile axis (black arrow). The <111> pole figure also shows that the secondary [111] slip direction moved closer to being 45° from the tensile axis (white circle), which would help increase the resolved glide shear stresses on slip systems of the $[1\bar{1}1]$ slip direction. Table IV-3 indicates the $[1\bar{1}1](121)$ and $[111](1\bar{2}1)$ slip systems, whose slip directions and slip planes match both the slip direction rotations and visible trace observations, had high initial and final resolved glide shear stresses. The $[1\bar{1}1](\bar{1}12)$ and $[111](\bar{2}11)$ slip systems, whose slip directions and slip planes match both the slip direction rotations and visible trace observations, had relatively high final resolved glide shear stresses. Table IV-3 indicates that the initial and final glide shear stresses on the $[\bar{1}11](1\bar{1}2)$ and $[\bar{1}11](211)$ slip systems were relatively low, though the slip planes match visible slip traces.

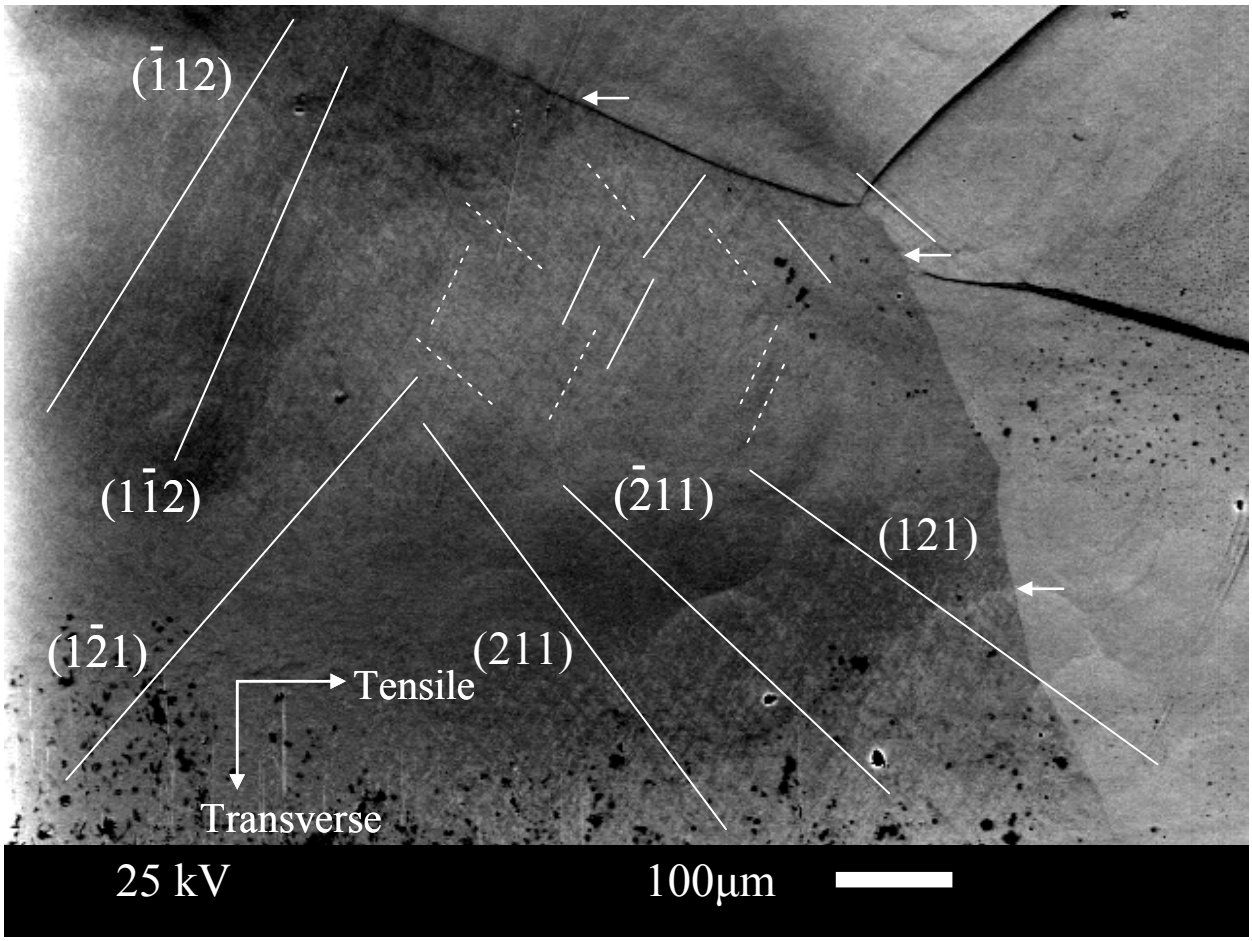

Figure IV-10. Slip traces on side F of welded sample FC (BEI). The grain boundaries of the recrystallization front (white arrows) divided the recovered region on the left where the slip traces are drawn from the recrystallized grains to the right. The estimated local tensile strain was 33%.

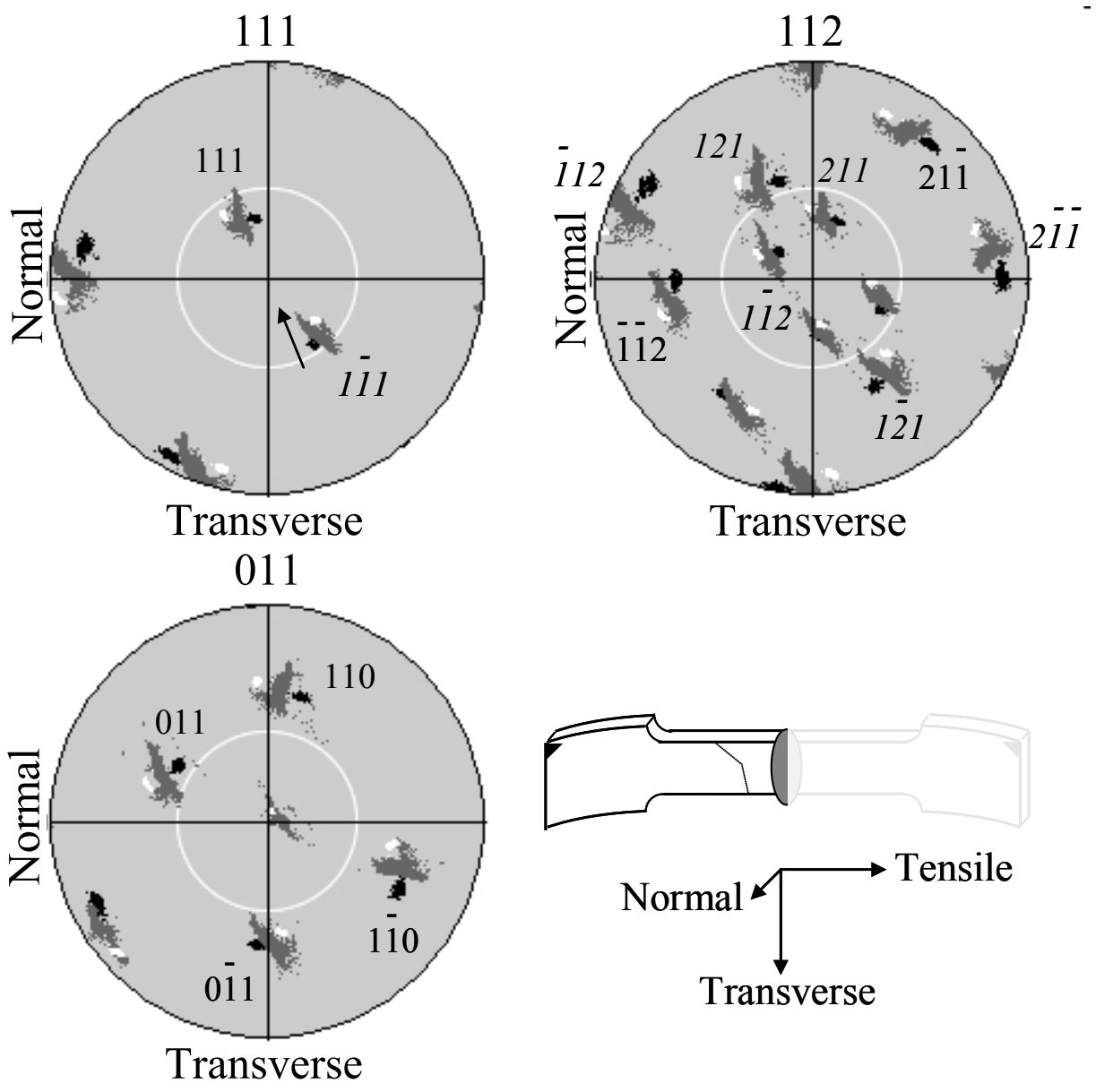

Figure IV-11. Pole figures collected from side F of welded sample FC pole figures and a schematic of the sample; the dotted line is the recrystallization front. Initial (black), deformed (grey), recovered (white) orientations are overlaid. The slip plane normals of observed plane traces (italic text), and slip plane normals with no observed plane traces for slip systems that acquired enough resolved shear to possibly be active (plain text), are also labeled. Upper Left <111> PF: The primary $[1\bar{1}1]$ (italic text) slip direction moves indirectly toward the tensile axis. The secondary slip direction [111] secondary (plain text) slip direction moves away from the tensile axis.

Sample F is summarized as follows: The estimated local tensile strains for each half of sample F were fairly similar, with 27% for side AF and 33% for side FC. Both sides possessed visible traces that matched the calculated slip trace of the $[1\bar{1}1](121)$ slip system, which possessed the highest initial resolved glide shear stress. Both sides also showed the $[1\bar{1}1]$ primary slip direction rotating toward the tensile axis.

5. Side A of welded sample AF

While sample A initially had a tensile axis close to the [001] direction so that many slip systems had a high resolved shear stress at yield, sample A possessed the highest yield stress of the Tokyo-Denkai sample set. The SEI image in Figure IV-12 shows the slip traces near the recrystallization front on side A of welded sample AF, where the recrystallization front divided the recovered region to the left and the recrystallized grains to the right (white arrows). Despite all the slip traces being faint, the visible traces each matched one or more calculated slip traces: $(\bar{1}\bar{1}2)$, $(2\bar{1}1)$, $(\bar{2}\bar{1}1)$, $(\bar{1}21)$, and $(1\bar{1}0)$. The estimated local tensile strain at the image location was 60%. The <111> pole figure in Figure IV-13 shows that only the $[1\bar{1}1]$ slip direction rotated toward the tensile axis (black arrow), but the rotation was small, indicating that other slip systems were also operating in a manner that maintained the orientation, while the [111] and $[\bar{1}11]$ directions moved slightly away. Table IV-4 summarizes the evidence for active slip systems for both sides of sample A. Table IV-4 indicates that the initial and final resolved glide shear stresses on the $[111](\bar{1}\bar{1}2)$ slip system were high, while the initial and final resolved glide shear stresses on the $[1\bar{1}1](\bar{2}\bar{1}1)$ slip system were moderate. The final resolved glide shear stresses on the $[\bar{1}\bar{1}1](2\bar{1}1)$, $[\bar{1}\bar{1}1](\bar{1}21)$, $[111](1\bar{1}0)$, and $[\bar{1}\bar{1}1](1\bar{1}0)$ slip systems were relatively high, while the initial resolved glide shear stresses on those systems were relatively low. Although Table IV-4 indicated that slip systems of $[1\bar{1}1]$ slip directions possessed high

initial and final resolved glide shear stresses, slip traces matching those systems were not observed; noting the recovered orientation, all four of the <111> slip systems have a slip component out of the sample normal surface, but the $[\bar{1}11]$ should cause the greatest topography.

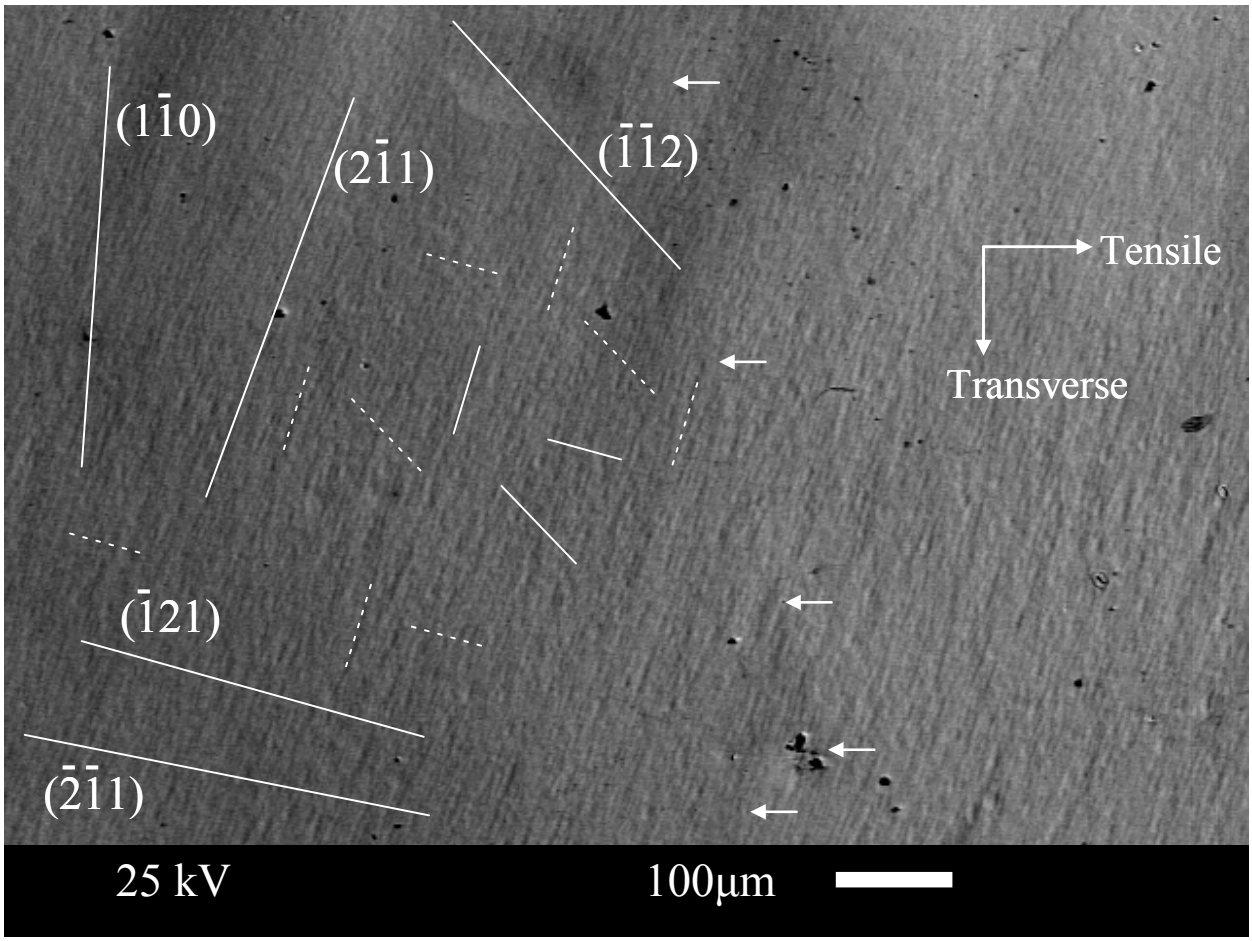

Figure IV-12. Slip traces on side A of welded sample AF (SEI). The grain boundaries of the recrystallization front (white arrows) divided the recovered region on the left where the slip traces are drawn from the recrystallized grains to the right. The estimated local tensile strain was 60%.

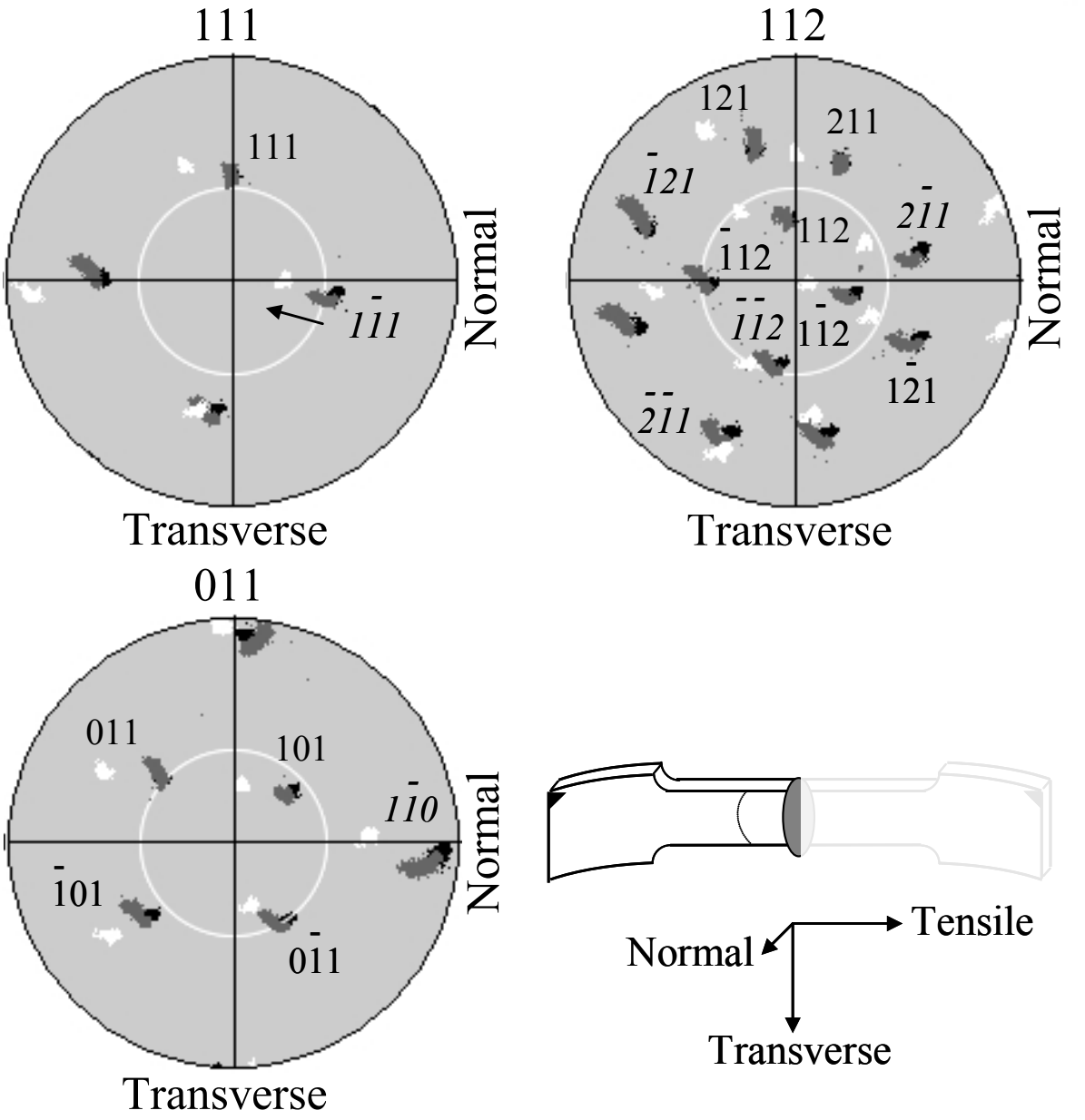

Figure IV-13. Pole figures collected from side A of sample AF and a schematic of the sample; the dotted line is the recrystallization front. The localized strain was high at 60%. Initial (black), deformed (grey), and recovered (white) orientations are overlaid. The slip plane normals of observed plane traces (italic text), and slip plane normals with no observed plane traces for slip systems that acquired enough resolved shear to possibly be active (plain text), are also labeled. Upper Left <111> PF: Note rotation of the $[1\bar{1}1]$ (Italic text) slip direction toward the tensile axis. The [111] and $[\bar{1}11]$ slip directions move slightly away from the tensile axis.

Table IV-4. A list of evidence considered for potentially active slip systems for both sides of sample A of the Tokyo-Denkai sample set. The 0.2% strain offset yield stress and final flow stress are given under the sample name, in that order. Slip systems with matching possible and calculated slip traces are marked '*', and the greatest initial and final resolved glide shear stresses for the {110} and {112} slip system families are given in bold. Twinning (T) and anti-twinning (A) {112} planes are also indicated.

Sample, stresses (MPa), Hardening slope at yield, Slip direction that rotated toward TD, Initial Euler angles, Final Euler angles	Potentially active system	Initial resolved shear stress at yield (MPa): glide, non-glide 1, 2, 3	Final resolved shear stress (MPa): glide, non-glide 1, 2, 3
AF side A 66.0, 97.0 Moderate $[1\bar{1}1]$ 5 96 133 4 120 139	$[1\bar{1}1](\bar{1}12)$	**32.4** 13.0 4.3 13.7 T	37.0 15.8 1.4 6.7 T
	$[111](\bar{1}\bar{1}2)$*	32.2 19.8 -5.1 18.7 A	35.3 39.7 -33.2 26.1 A
	$[111](0\bar{1}1)$	**30.1** 4.3 13.6 5.1	**43.3** 25.5 -7.1 33.2
	$[1\bar{1}1](011)$	30.0 26.2 -13.7 18.0	33.5 30.5 -6.7 8.1
	$[\bar{1}\bar{1}1](112)$	28.4 11.3 5.8 17.9 T	33.3 -3.1 35.1 -5.7 T
	$[\bar{1}11](1\bar{1}2)$	28.0 16.4 -5.0 23.8 A	9.1 4.8 -3.4 43.2 A
	$[\bar{1}\bar{1}1](101)$	26.3 22.9 -17.9 23.7	40.2 17.5 5.7 29.4
	$[1\bar{1}1](\bar{1}01)$	26.2 -3.8 18.0 -4.3	30.5 -3.1 8.1 -1.4
	$[111](\bar{1}01)$	25.7 30.1 -18.7 13.6	17.8 43.3 -26.1 -7.1
	$[\bar{1}11](101)$	25.7 2.8 18.8 5.0	8.0 0.3 39.8 3.4
	$[\bar{1}\bar{1}1](011)$	22.9 -3.4 23.7 -5.8	17.5 -22.8 29.4 -35.1
	$[\bar{1}11](0\bar{1}1)$	22.9 25.7 -23.8 18.8	7.7 8.0 -43.2 39.8
	$[111](1\bar{2}1)$	19.8 -12.4 18.7 -13.6 T	**39.7** 4.5 26.1 7.1 T
	$[1\bar{1}1](121)$	19.5 32.4 -18.0 4.3 A	21.1 37.0 -8.1 1.4 A
	$[\bar{1}\bar{1}1](2\bar{1}1)$*	17.1 28.4 -23.7 5.8 A	36.4 33.3 -29.4 35.1 A
	$[\bar{1}11](211)$	16.4 -11.6 23.8 -18.8 T	4.8 -4.3 43.2 -39.8 T
	$[1\bar{1}1](\bar{2}\bar{1}1)$*	13.0 -19.5 13.7 -18.0 N/A	15.8 -21.1 6.7 -8.1 N/A
	$[\bar{1}\bar{1}1](\bar{1}21)$*	11.3 -17.1 17.9 -23.7 N/A	-3.1 -36.4 -5.7 -29.4 N/A
	$[111](1\bar{1}0)$*	4.3 -25.7 5.1 -18.7	25.5 -17.8 33.2 -26.1
	$[\bar{1}\bar{1}1](1\bar{1}0)$*	3.4 26.3 -5.8 -17.9	22.8 40.2 -35.1 5.7

Table IV-4 (cont'd)

CA side A 66.0, 97.0 Moderate $[1\bar{1}1]$ 5 96 133 4 105 128	$[1\bar{1}1](\bar{1}12)$*	**32.4** 13.0 4.3 13.7 T	**47.4** 17.1 6.5 13.8 T
	$[111](\bar{1}\bar{1}2)$	32.2 19.8 -5.1 18.7 A	45.3 35.8 -17.2 28.3 A
	$[111](0\bar{1}1)$	**30.1** 4.3 13.6 5.1	**46.8** 15.2 11.1 17.2
	$[1\bar{1}1](011)$	30.0 26.2 -13.7 18.0	44.9 37.2 -13.8 20.4
	$[\bar{1}\bar{1}1](112)$	28.4 11.3 5.8 17.9 T	38.8 9.7 20.0 17.6 T
	$[\bar{1}11](1\bar{1}2)$	28.0 16.4 -5.0 23.8 A	32.2 19.2 -9.4 40.4 A
	$[\bar{1}\bar{1}1](101)$*	26.3 22.9 -17.9 23.7	39.1 28.0 -17.6 37.7
	$[1\bar{1}1](\bar{1}01)$	26.2 -3.8 18.0 -4.3	37.2 -7.6 20.4 -6.5
	$[111](\bar{1}01)$	25.7 30.1 -18.7 13.6	31.6 46.8 -28.3 11.1
	$[\bar{1}11](101)$*	25.7 2.8 18.8 5.0	29.7 3.6 31.0 9.4
	$[\bar{1}\bar{1}1](011)$	22.9 -3.4 23.7 -5.8	28.0 -11.2 37.7 -20.0
	$[\bar{1}11](0\bar{1}1)$	22.9 25.7 -23.8 18.8	26.1 29.7 -40.4 31.0
	$[111](1\bar{2}1)$	19.8 -12.4 18.7 -13.6 T	35.8 -9.5 28.3 -11.1 T
	$[1\bar{1}1](121)$	19.5 32.4 -18.0 4.3 A	30.3 47.4 -20.4 6.5 A
	$[\bar{1}\bar{1}1](2\bar{1}1)$*	17.1 28.4 -23.7 5.8 A	29.1 38.8 -37.7 20.0 A
	$[\bar{1}11](211)$	16.4 -11.6 23.8 -18.8 T	19.2 -13.0 40.4 -31.0 T
	$[1\bar{1}1](\bar{2}\bar{1}1)$	13.0 -19.5 13.7 -18.0 N/A	17.1 -30.3 13.8 -20.4 N/A
	$[111](1\bar{1}0)$	4.3 -25.7 5.1 -18.7	15.2 -31.6 17.2 -28.3

Figure IV-14 is digital photographs that show that strain had become localized on the left side, which would become side A of welded sample AF, both a) thinning from ~3mm to ~2mm (black arrows), and b) some areas (black arrows) were locally strained as much as ~60% in the tensile (horizontal) direction. This large amount of localized strain may have obscured the slip traces of the most highly stressed slip systems and contributed to their not being observed.

a)

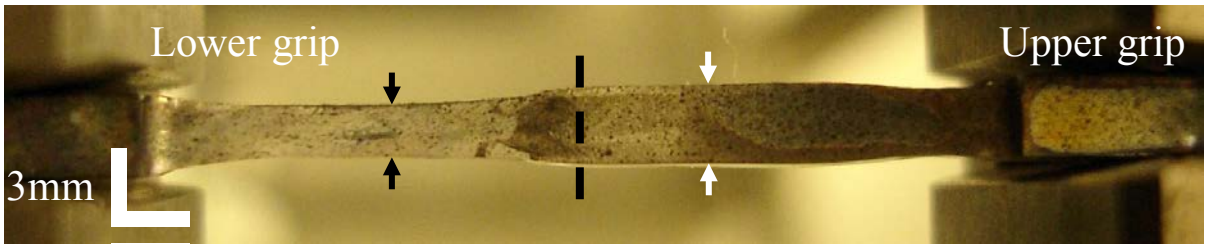

b)

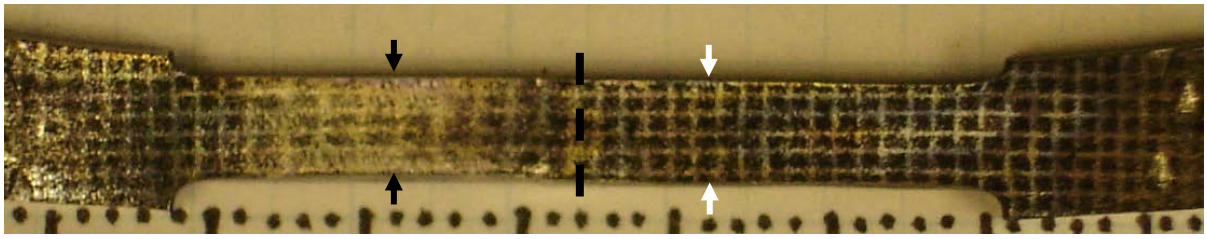

Figure IV-14. a) Side view of Sample A after deformation. The sample was cut in half (dashed line). The left side became welded sample AF side A, and had thinned from ~3mm to ~2mm (black arrows). The right side became welded sample CA side A, and remained ~3mm thick (white arrows). b) Back of Sample A after deformation with fiducial spots. Areas of the left side had upwards of 60% local strain (black arrows) along the long axis, while the right side had around 7% (white arrows).

6. Side A of welded sample CA

The digital photographs in Figure IV-14 show that side A of welded sample CA had only been locally strained to about 7%, due to the strain having been concentrated on the opposite side. The secondary electron image in Figure IV-15 shows that visible traces matched the $(\bar{1}12)$, (101), and $(2\bar{1}1)$ calculated slip traces. The <111> pole figure in Figure IV-16 shows a little rotation of the primary $[1\bar{1}1]$ slip direction toward the tensile axis (black arrow), and little rotation of the other {111} slip directions. Table IV-4 indicates that the $[1\bar{1}1](\bar{1}12)$, whose slip direction and slip plane match both the slip direction rotation and visible trace observations, possessed both the highest initial and highest final resolved glide shear stresses. The $[\bar{1}\bar{1}1](101)$ slip system, whose slip plane matched a visible trace, possessed initial and final resolved glide shear stresses that were relatively high. The resolved glide shear stresses for other slip systems whose slip plane matched a visible trace were mixed: the initial resolved glide shear stress was relatively high and the final resolved glide shear stress was relatively moderate for the $[\bar{1}11](101)$ slip system, while the initial and final resolved glide shear stresses were relatively moderate for the $[\bar{1}\bar{1}1](2\bar{1}1)$ slip system. The highest resolved shear stresses remained on slip systems of the $[1\bar{1}1]$ and [111] slip directions. The <111> pole figure in Figure IV-16 shows that the recovered [111] secondary slip direction has almost no component in the normal direction, meaning that the slip steps formed by dislocations of the [111] slip direction would not have emerged on the surface examined for slip traces, and may account for the lack of observed slip traces of those slip systems.

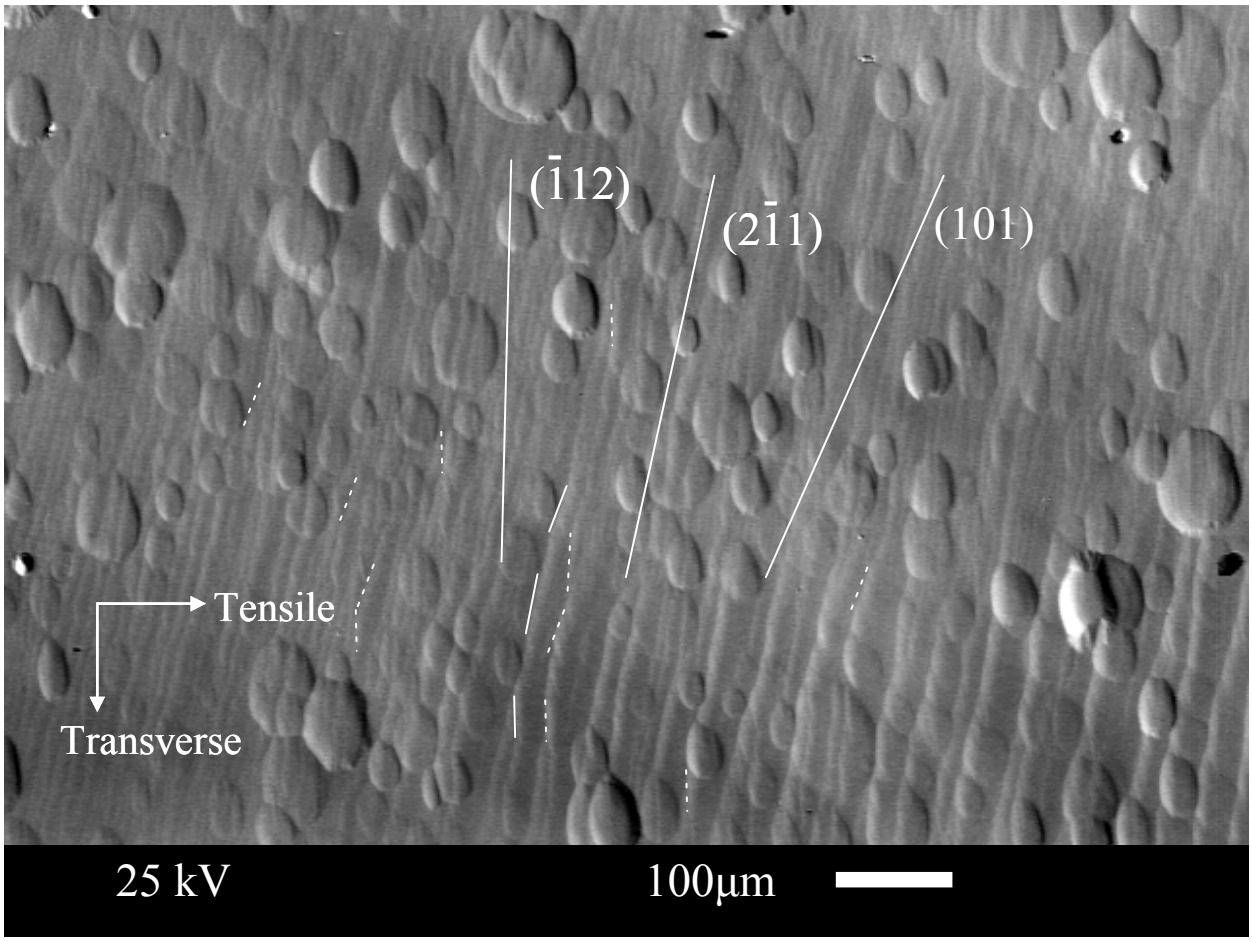

Figure IV-15. Slip traces on side A of welded sample CA (SEI). Recrystallized grains are not visible and located out of frame near the upper and lower left corners. The estimated local tensile strain was 7%.

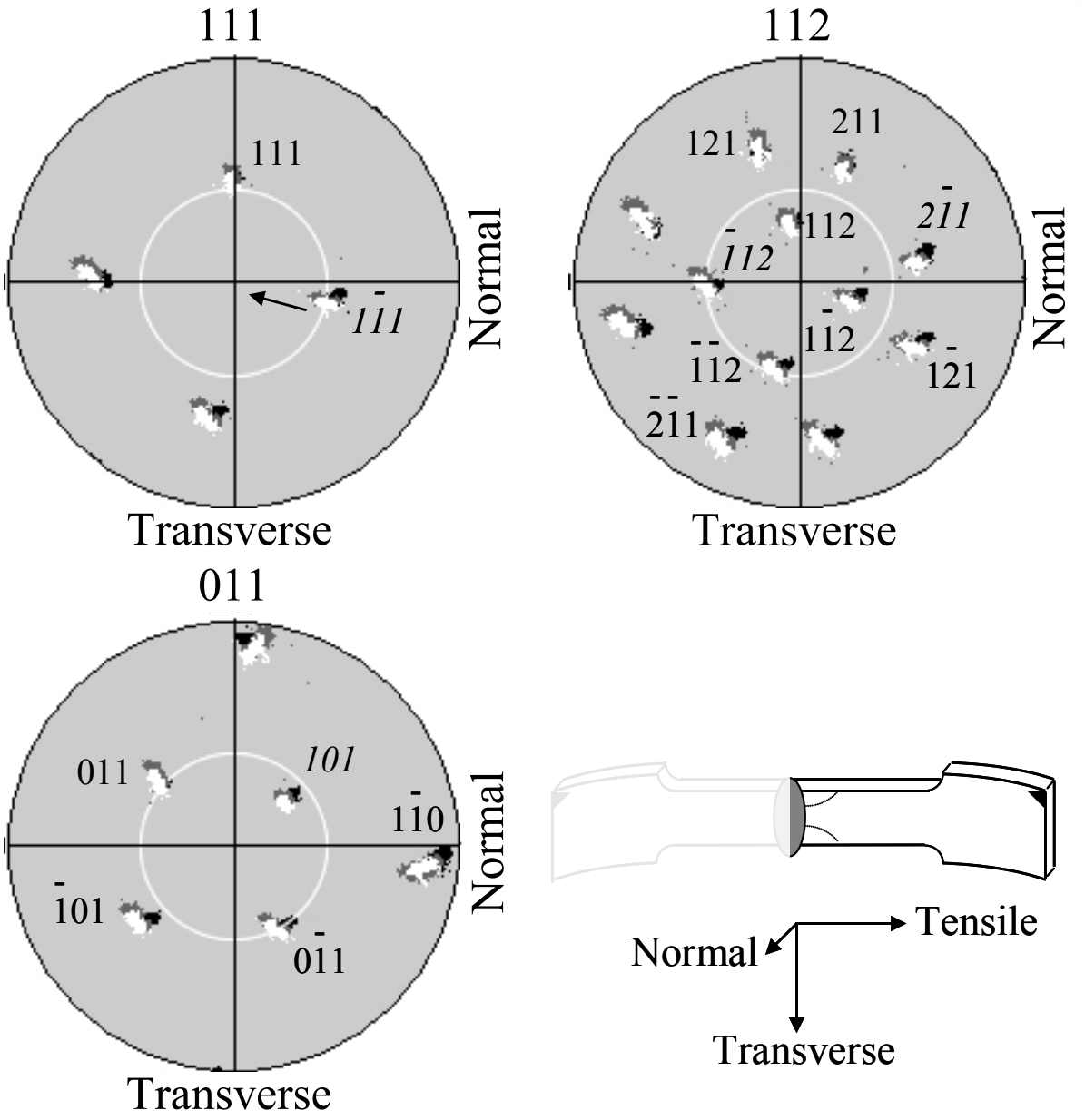

Figure IV-16. Pole figures collected from side A of sample CA pole figures and a schematic of the sample; the dotted line is the recrystallization front. The localized strain was low at 7%. Initial (black), deformed (grey), and recovered (white) orientations are overlaid. The slip plane normals of observed plane traces (italic text), and slip plane normals with no observed plane traces for slip systems that acquired enough resolved shear to possibly be active (plain text), are also labeled. Upper Left <111> PF: The primary [111] (Italic text) slip direction rotated slightly toward the tensile axis, $[\bar{1}11]$ moved slightly away, and $[1\bar{1}1]$ remained in place.

Sample A is summarized as follows: The estimated local tensile strains for each half of sample C were very different, with 60% for side AF and 7% for side CA. Slip trace analysis resulted in matches to slip systems that possessed high initial and high final resolved glide shear stresses for each side of sample A. Both sides showed that the $[1\bar{1}1]$ primary slip direction rotated slightly toward the tensile axis.

D. Evidence of active slip systems in the Ningxia set of samples

The deliberately chosen orientations of the second set of samples provided the opportunity to compare differences in dislocation activity and combinations of various slip systems. Detailed descriptions of three samples are provided to illustrate different types of deformation: X3, T3, and P3. Samples X3 and T3 were oriented for preferred single slip and easy glide on {112} and {110} planes, respectively. Sample P3 was oriented to have nearly the same resolved slip on two {112} planes with different <111> directions.

1. Sample X3

The initial orientation of sample X3 was chosen such that the resolved glide shear stress of 17.0 MPa on the $[1\bar{1}1](121)$ slip system was greater than the 15.5 MPa resolved glide shear stress on the $[1\bar{1}1](011)$ slip system (about 8.5% greater). The stress-strain curve of sample X3 in Figure IV-1 shows an initial plateau of easy glide (a period of no increase in flow stress, due to no increase in work hardening), until about 18% strain where the hardening rate increased and became high for the remainder of deformation. Figure IV-17 shows an SEI and BEI image of the same location on the normal surface, and both images show visible traces that each matched the (121), $(21\bar{1})$, (211), and $(2\bar{1}\bar{1})$ calculated plane traces. The <111> pole figure in Figure IV-18 shows that the primary $[1\bar{1}1]$ slip direction rotated toward the tensile direction (black arrow),

indicating that at least one slip system having a $[1\bar{1}1]$ slip direction was active; the secondary slip direction [111] moved closer to 45° from the tensile direction, which would help increase the resolved shear stress on slip systems of the [111] slip direction as deformation proceeded.

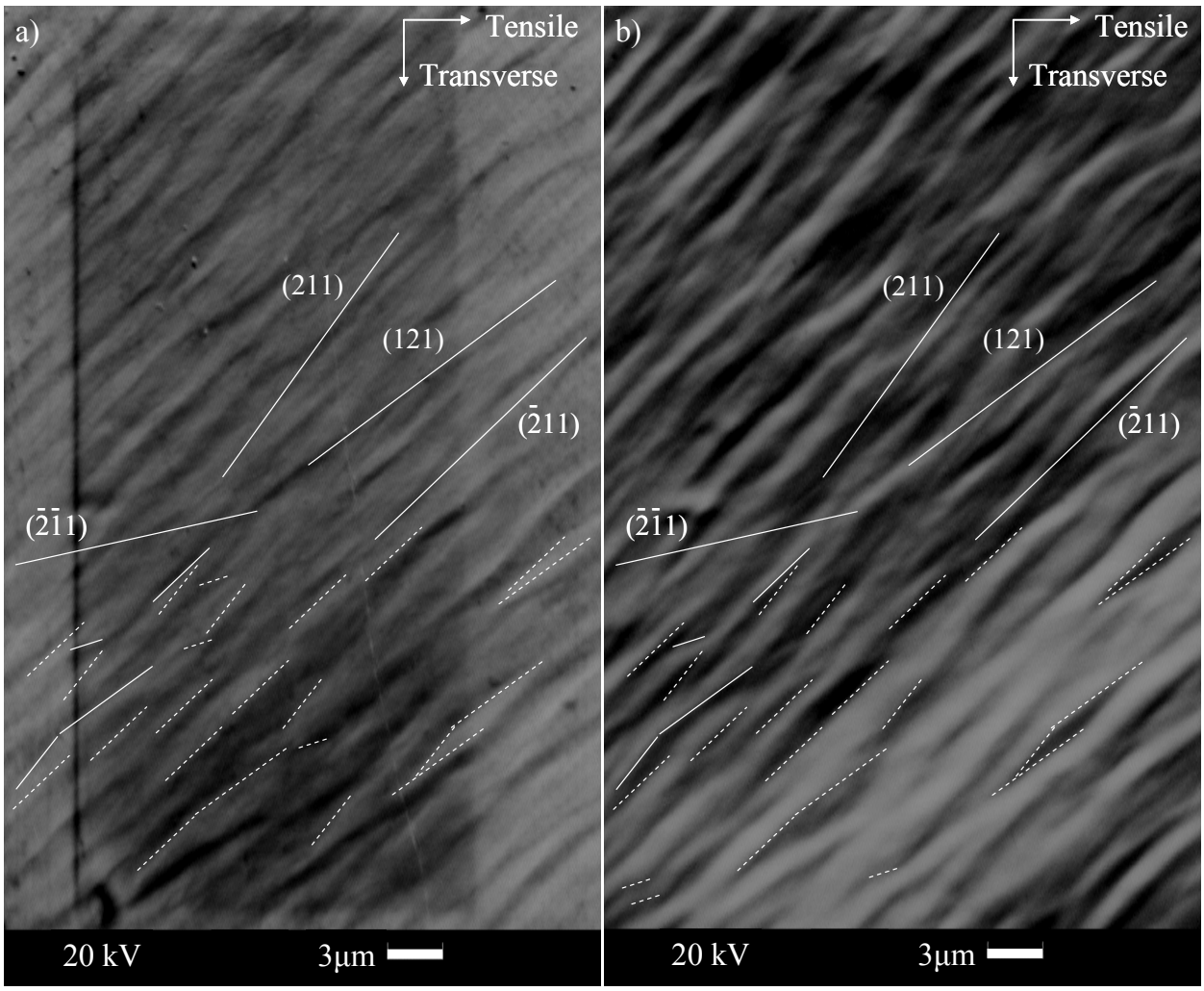

Figure IV-17. Slip traces on sample X3 after deformation. The same location was imaged in both a) SEI and b) BEI. The visible traces (short white lines) match the calculated slip traces (labeled long white lines).

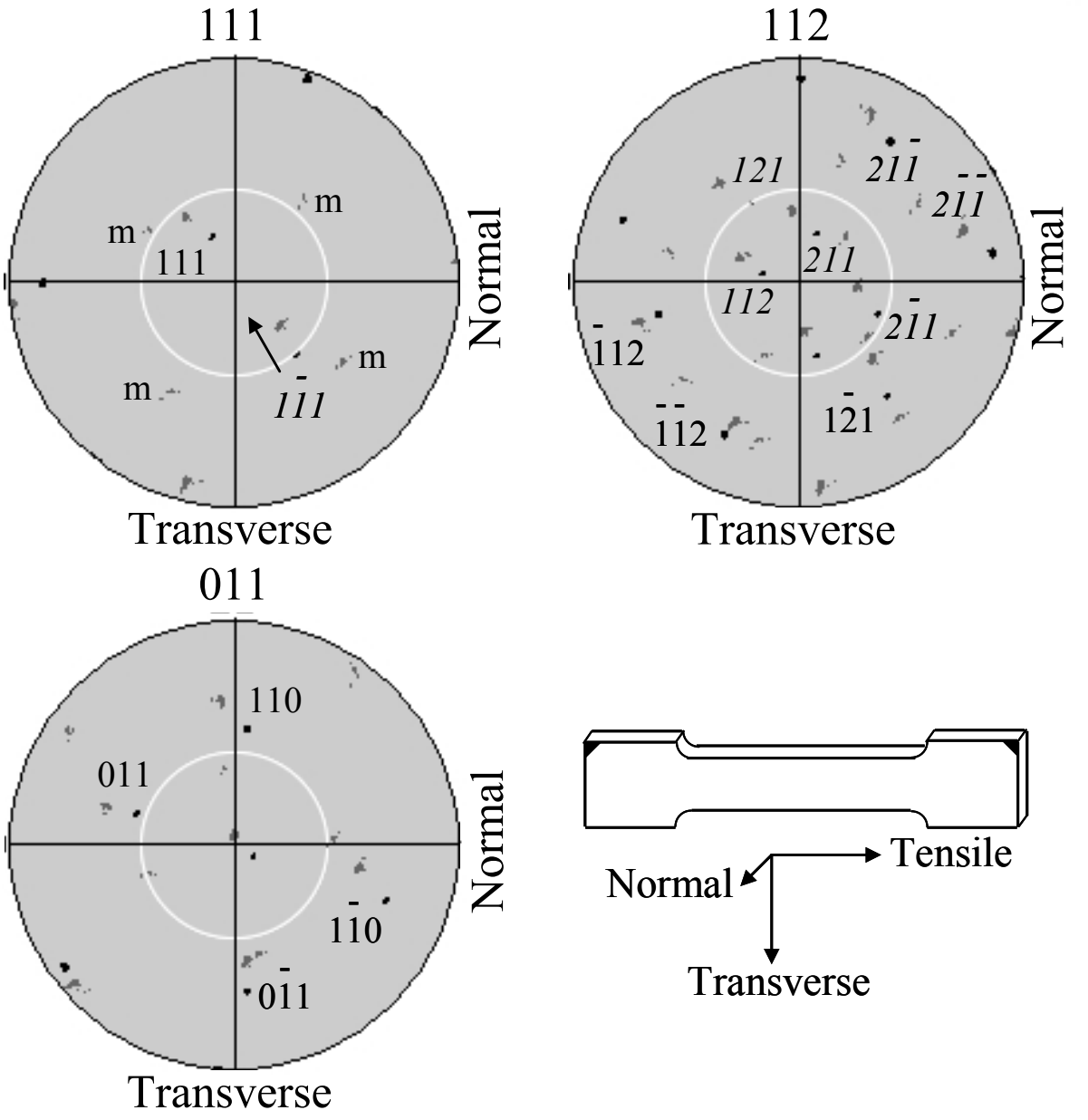

Figure IV-18. Pole figures collected from sample X3, with the tensile axis in the center of each pole figure. Initial orientation (black) and deformed orientation (grey) are overlaid. The primary (Italic text) and secondary (plain text) slip directions are labeled in the <111> pole figure. The slip plane normals of observed plane traces (italic text), and slip plane normals with no observed plane traces for slip systems that acquired enough resolved shear to possibly be active (plain text), are also labeled. Note the rotation of the primary $[1\bar{1}1]$ slip direction toward the tensile axis. A minority orientation noted by 'm' on the <111> pole figure appeared due to deformation.

Table IV-5 summarizes the evidence for active slip systems for sample X3 of the Ningxia sample set. Table IV-5 lists only the slip systems that met the same final glide shear stress criterion given earlier in Section IV-C-3 for the Tokyo-Denkai samples. Slip systems with visible traces that matched calculated slip traces are also listed regardless of the resolved glide shear stress values. Since the Ningxia samples were examined for slip traces on two surfaces, matches from the normal (polished) surface are marked '*', matches from the transverse surface marked '†', so slip systems with matches on both surfaces are marked '*†'. The initial resolved glide and non-glide shear stresses at yield and the final resolved glide and non-glide shear stresses at the end of deformation are given for each slip system. The twinning planes are labeled 'T' and the anti-twinning planes 'A' for the slip systems possessing {112} slip planes. Table IV-5 also gives the 0.2% strain offset yield stress and final flow stress (in that order) below the sample name, the hardening rate immediately after yield, the crystal directions that moved toward the tensile direction for each sample, and the initial and final Euler angles used to calculate the resolved stresses. Tables containing similar data for the other Ningxia samples are given in subsequent sections, and were assembled in the same manner as Table IV-5 was for sample X3 (Table IV-6 for sample T3, Table IV-7 for sample P3, and the tables for the remaining Ningxia samples in the Appendix).

Table IV-5. A list of evidence considered for potentially active slip systems for sample X3 of the Ningxia sample set. The 0.2% strain offset yield stress and final flow stress are given under the sample name, in that order. Slip systems with matching possible and calculated slip traces are marked '*'if observed on the Normal surface, and marked '†' if observed on the Transverse surface. The greatest initial and final resolved glide shear stresses for the {110} and {112} slip system families are given in bold. Twinning (T) and anti-twinning (A) {112} planes are also indicated.

Sample, stresses (MPa), Hardening slope at yield, Slip direction that rotated toward TD, Initial Euler angles, Final Euler angles	Potentially active slip system	Initial resolved shear stress at yield (MPa): glide, non-glide 1, 2, 3	Final resolved shear stress (MPa): glide, non-glide 1, 2, 3
X3 34.1, 62.5 Slight $[1\bar{1}1]$ 33 117 130 28 123 141	$[1\bar{1}1](121)$*†	**17.0** 9.9 -1.7 8.3	27.2 16.2 -1.7 7.7 A
	$[1\bar{1}1](011)$	**15.5** 1.6 6.6 1.7	25.0 3.0 6.0 1.7
	$[1\bar{1}1](110)$	13.9 15.5 -8.3 6.6	22.1 25.0 -7.7 6.0
	$[111](1\bar{2}1)$	13.0 4.6 1.0 2.0 T	**30.7** 13.1 2.2 10.0 T
	$[111](0\bar{1}1)$	12.3 10.2 -2.0 3.0	**27.9** 25.3 -10.0 12.2
	$[111](1\bar{1}0)$	10.2 -2.1 3.0 -1.0	25.3 -2.6 12.2 -2.2
	$[1\bar{1}1](\bar{1}12)$	9.9 -7.1 8.3 -6.6 T	16.2 -11.0 7.7 -6.0 T
	$[111](\bar{1}\bar{1}2)$	8.3 13.0 -3.0 1.0 A	17.6 30.7 -12.2 2.2 A
	$[1\bar{1}1](21\bar{1})$*†	7.1 17.0 -6.6 -1.7 N/A	11.0 27.2 -6.0 -1.7 N/A
	$[\bar{1}11](211)$*	4.9 0.6 12.3 3.6 T	-0.2 0.0 29.7 -6.3 T
	$[111](2\bar{1}\bar{1})$*	4.6 -8.3 2.0 -3.0 N/A	13.1 -17.6 10.0 -12.2 N/A
	$[\bar{1}1\bar{1}](\bar{1}\bar{1}2)$†	1.5 0.3 10.6 6.2 T	-5.0 0.2 27.9 -2.3 T
	$[\bar{1}1\bar{1}](\bar{2}1\bar{1})$†	1.2 1.5 -16.8 10.6 A	-5.2 -5.0 -25.6 27.9 A

Table IV-5 indicates that the $[1\bar{1}1](121)$ slip system, whose slip direction and slip plane matches the observations of the $[1\bar{1}1]$ slip direction and visible traces, possessed the highest initial resolved glide shear stress at yield and a high final resolved glide shear stress at the end of deformation. While the $(21\bar{1})$, (211), and $(2\bar{1}\bar{1})$ slip traces also each correspond to the $[1\bar{1}1](21\bar{1})$, $[\bar{1}11](211)$, and $[111](2\bar{1}\bar{1})$ slip systems, Table IV-5 indicates that the initial and final resolved shear stresses on those systems were relatively low.

Figure IV-19 shows an SEI image at a location on the Transverse surface that shows visible traces that each matched the (121), $(21\bar{1})$, (112), and $(\bar{2}1\bar{1})$ calculated plane traces. Table IV-5 indicates that the $[1\bar{1}1](121)$ slip system, whose slip direction and slip plane matches the observations of the $[1\bar{1}1]$ slip direction and visible traces, possessed the highest initial resolved glide shear stress at yield and a high final resolved glide shear stress at the end of deformation. While the $(21\bar{1})$, (112), and $(\bar{2}1\bar{1})$ slip traces also each correspond to the $[1\bar{1}1](21\bar{1})$, $[\bar{1}11](211)$, and $[111](2\bar{1}\bar{1})$ slip systems, Table IV-5 indicates that the initial and final resolved shear stresses on those systems were relatively low.

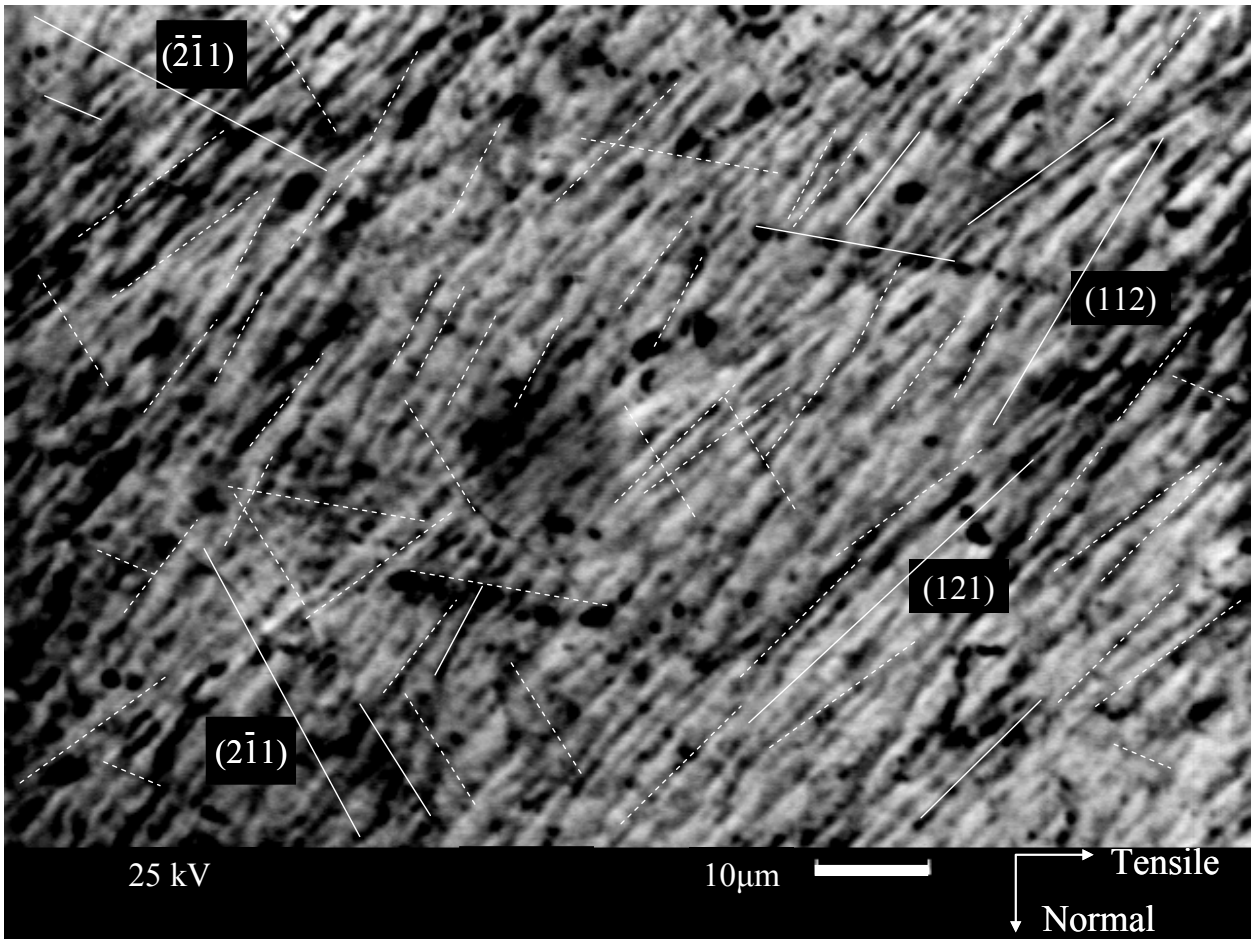

Figure IV-19. SEI of slip traces on the Transverse surface of sample X3 after deformation. The visible traces (short white lines) match the calculated slip traces (labeled long white lines).

The pole figures in Figure IV-18 also show a minority orientation (32 pixels total in groupings no larger than 10, average grouping of 4) that appeared after deformation that is very different from the vast majority of the deformed orientation (41,930 pixels); the {111} poles belonging to the minority orientation are labeled 'm'. Whether this is genuinely portions of the crystal lattice rotated by the combined action of different slip systems and resulting dislocation substructure or simply an artifact is unclear; the very small number of pixels in an observed average grouping, given a step size of 0.2 μm between pixels, would mean that genuinely rotated areas would be approximately 1 μm in diameter or less.

The orientation imaging microscopy data (OIM) with the crystal orientation of each pixel over the scanned area both before and after deformation enabled the dislocation substructure to be examined. The aspect ratio of these maps was adjusted in a similar manner as the slip trace images to match the 'tilt-corrected' orientation data (see Materials & Methods section III-K), a consequence of which is the need for vertical and horizontal scale bars of different lengths to represent the same real distance in these images. Figure IV-20 shows two different representations of the deformed sample X3 in the same 112 x 327 μm area with a step size of 1 μm. Figure IV-20a shows a map of the relative difference in orientation from 0 (blue) to 17° (red) that compared the deformed orientation of each pixel to the initial undeformed orientation of sample X3 (a single average orientation obtained from sample X3 before deformation), and was used to estimate the width of deformation bands when present. This area of sample X3 did not possess deformation bands, only a homogeneous difference in deformed to undeformed orientation of approximately 15-17° across the whole area. Figure IV-20b shows a local average misorientation map, which gives the average difference in orientation of each pixel with respect to its immediate neighbors from 0 (blue) to 5° (red). Local crystal rotations imply the presence

of geometrically necessary dislocation structures that formed during deformation; this was examined because geometrically necessary dislocation boundaries tend to be aligned within 5° of the slip plane if one or two slip systems dominate deformation, while tending to lie closer to the macroscopically most-stressed plane for multiple slip (see Literature Review II-D) [19]. Figure IV-20b shows that the local average misorientation was about 1° and appeared homogeneously distributed in the deformed sample X3. This implies that geometrically necessary dislocation content was distributed with no apparent heterogeneity at the 1 μm length scale. Figure IV-21 presents orientation maps in the same manner as Figure IV-20, though examined on a smaller length scale of 22 x 65 μm area with step size of 0.2 μm that was found within the larger area examined in Figure IV-20. Figure 21a again shows that the difference between the deformed and undeformed orientation was homogeneous and approximately 15-17°. Figure 21b shows approximately homogeneously distributed intersecting geometrically necessary dislocation boundaries about 1 μm apart from each other. The plane traces shown are calculated from the point at which they cross; the twinning (T) or anti-twinning (A) nature of {112} planes is also labeled. Geometrically necessary dislocation boundaries are aligned with the (121) plane trace, which belongs to the most-stressed $[1\bar{1}1](121)$ slip system, though the boundaries intersecting those are not clearly aligned with particular slip plane traces.

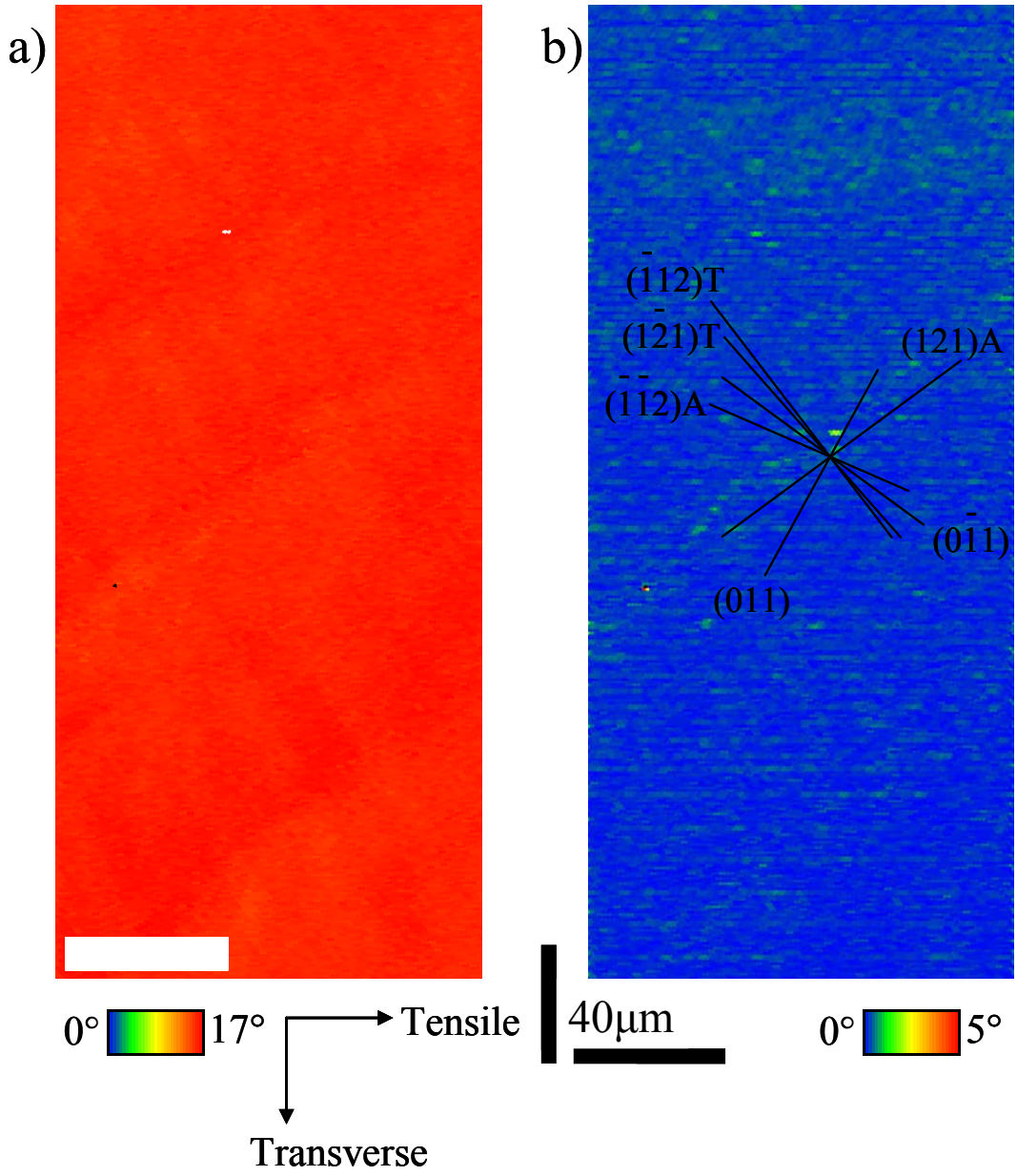

Figure IV-20. Two different representations of the same orientation data obtained after deformation of sample X3 from an 112x327µm area with 1µm step size. The scale bars are common to both images. a) A map of relative difference between the deformed and initial orientations with a range from 0°(blue) to 17°(red). b) A local average misorientation map based on first neighbors with a range of average misorientation from 0°(blue) to 5°(red).

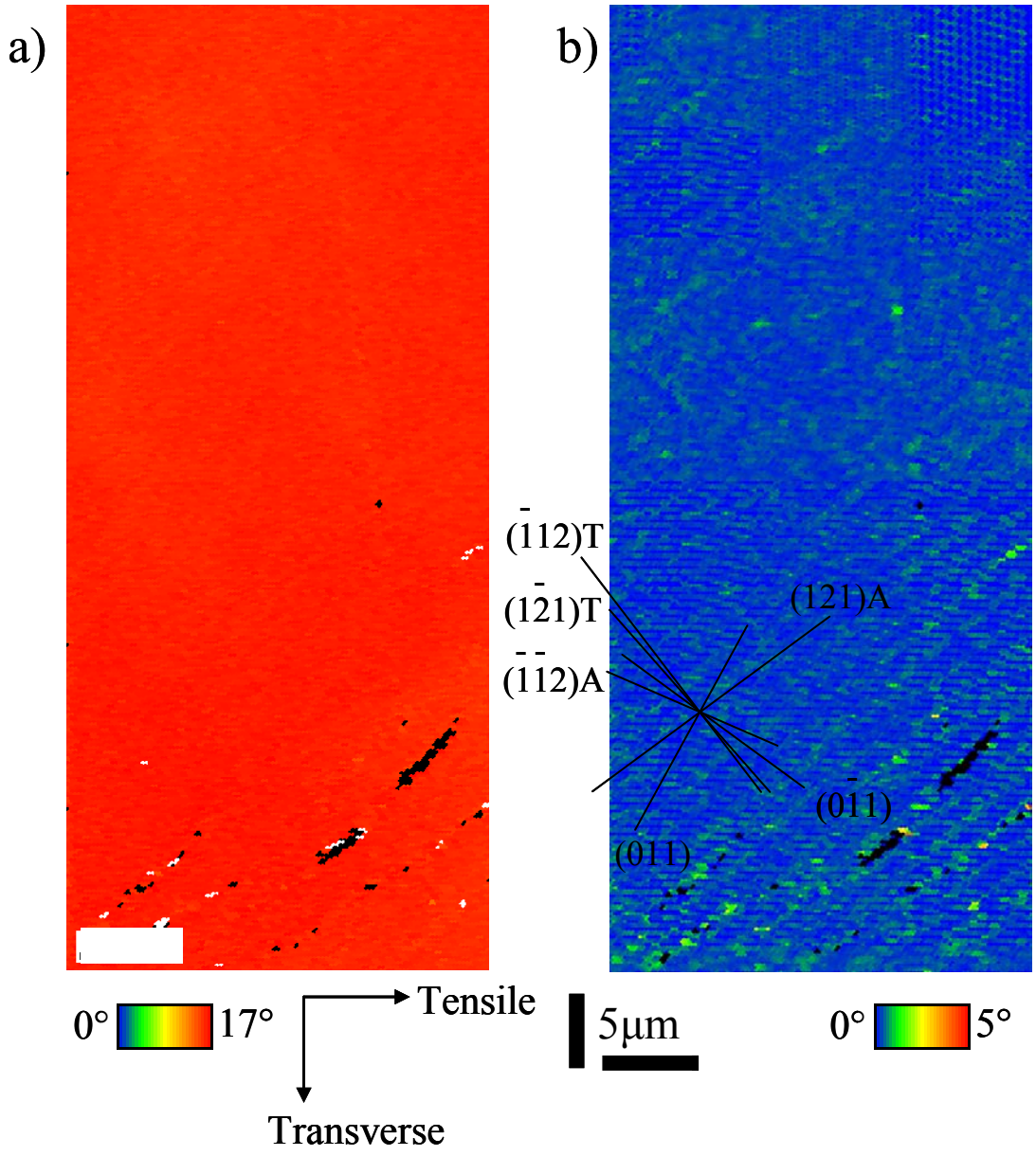

Figure IV-21. Two different representations of the same orientation data obtained after deformation of sample X3 from a 22x65µm area with 0.2 µm step size. The scale bar is common to both images. a) A map of relative difference between the deformed and initial orientations with a range from 0°(blue) to 17°(red). b) A local average misorientation map based on first neighbors with a range of average misorientation from 0°(blue) to 5°(red).

Sample X3 is summarized as follows: The engineering stress-strain curve shows initial Stage I easy glide after yield indicating at least one active primary slip system (frequent cross slip on different slip planes sharing the same slip direction would still result in easy glide, so multiple active slip systems cannot be ruled out), followed by Stage II linear work hardening indicating at least two active slip systems with different slip directions. The slip trace corresponding to the initial most highly stressed {112} slip system, $[1\bar{1}1](121)$, was observed on both the normal and transverse surface of the sample. Slip traces corresponding to the initial most highly stressed {110} slip system, $[1\bar{1}1](011)$, were not observed on either surface. The $[1\bar{1}1]$ direction rotated toward the tensile direction, suggesting at least one primary $[1\bar{1}1]$ slip system was active. The geometrically necessary dislocation substructure that developed appeared homogeneous at both length scales, with no obvious organization visible at the 1μm length scale. At the 0.2 μm length scale, boundaries aligned with the (121) plane trace that belongs to the most-stressed $[1\bar{1}1](121)$ slip system were visible, with boundaries intersecting them that were not clearly aligned with slip plane traces.

Table IV-6 summarizes the observations of the geometrically necessary dislocation substructure from the orientation maps, similarly obtained from all the Ningxia samples; the corresponding orientation maps for all samples are found in the Appendix.

Table IV-6. The summary of shear band and geometrically necessary dislocation boundary morphologies was found by representing the OIM data two different ways for two different length scales.

Sample	Area of map (μm), step size (μm)	Map of relative difference in orientation between deformed and initial orientations	Local average misorientation map
P3	112x327, 1	Heterogeneous intersecting bands, ~8-54 μm wide, ~4-17° within bands.	Heterogeneous intersecting boundaries, ~3-16 μm apart, ~1-3°. Boundaries aligned with (112) and between calculated traces.
	22x65, 0.2	Heterogeneous intersecting bands, ~4-17 μm wide, ~3-12° within bands.	Heterogeneous intersecting boundaries, ~1-19 μm apart, ~2°. Boundaries aligned with (112) and between calculated traces.
Q2°	112x327, 1	Homogeneous ~14-16°	Homogeneous, ~1-2°
	22x65, 0.2	Homogeneous ~14-16°	Homogeneous intersecting boundaries, ~1-5 μm apart, ~1-2°. Boundaries aligned between calculated traces.
R2°	112x327, 1	Homogeneous ~16-19°	Homogeneous, 1-2°
	22x65, 0.2	Homogeneous ~16-19°	~Homogeneous intersecting boundaries, ~1-2 μm apart, ~1-2°. Boundaries aligned with (110) and between calculated traces.
S3°	112x327, 1	Homogeneous ~14-16°	Heterogeneous intersecting boundaries, ~5-22 μm apart, ~1-3°. Boundaries aligned with (121) and between calculated traces.
	22x65, 0.2	Homogeneous ~9-18°	~Homogeneous intersecting boundaries, ~1-3 μm apart, ~1-3°. Boundaries aligned with $(0\bar{1}1)$, (110), and between calculated traces.
T3°	112x327, 1	Homogeneous ~24-26°	~Homogeneous parallel boundaries, ~5-10 μm apart, 1-2°. Boundaries aligned between calculated traces.
	22x65, 0.2	Homogeneous ~24-26°	~Homogeneous intersecting boundaries, ~1-2 μm apart, ~1-2°. Boundaries aligned between calculated traces.

Table IV-6 (cont'd)

U3 °	112x327, 1	Heterogeneous intersecting bands, ~6-124 μm wide, ~6-21° within bands.	Heterogeneous intersecting boundaries, ~13-124 μm apart, ~1-3°. Boundaries aligned with $(2\bar{1}1)$ and between calculated traces.
	22x65, 0.2	Heterogeneous intersecting bands, ~1-5 μm wide, ~6-16° within bands. Another large band's width extended out-of-frame, ~10-20° within band.	Heterogeneous intersecting boundaries, ~1-2 μm apart, ~1-2°. Boundaries aligned with (011) and between calculated traces.
V3 °	112x327, 1	Mostly homogeneous ~12-16° with few intersecting bands of ~8-12° ~3-12 μm wide.	Heterogeneous with few boundaries, ~1-3°. Boundaries aligned with $(1\bar{2}1)$, $(\bar{1}12)$ and between calculated traces.
	22x65, 0.2	Heterogeneous intersecting bands, ~1-8 μm wide, ~8-12° within bands.	~Homogeneous intersecting boundaries, ~1-2 μm apart, ~1-2°. Boundaries aligned with (121) and between calculated traces.
W3 °	112x327, 1	Homogeneous ~15-17°	Homogeneous, ~1°
	22x65, 0.2	Homogeneous ~15-17°	~Homogeneous intersecting boundaries, ~1-2 μm apart, ~1-2°. Boundaries aligned with (121), $(\bar{1}12)$, $(1\bar{2}1)$, and between calculated traces.
X3 °	112x327, 1	Homogeneous ~15-17°	Homogeneous, ~1°
	22x65, 0.2	Homogeneous ~15-17°	~Homogeneous intersecting boundaries, ~1 μm apart, ~1°. Boundaries aligned with (121), $(\bar{1}12)$, $(1\bar{2}1)$, and between calculated traces.

2. Sample T3

Sample T3 was initially oriented such that the resolved glide shear stress of 18.3 MPa resolved on the $[1\bar{1}1](011)$ slip system was greater than the 16.6 MPa resolved glide shear stress on the $[1\bar{1}1](121)$ slip system (about 9.3% greater). The stress-strain curve in Figure IV-1 indicated a high initial hardening process that peaked at about 5% strain followed by an extended period of softening to a flow stress only barely above that of the yield stress. Slight hardening resumed at about 26% strain, and by the end of deformation the final engineering flow stress was just under the highest value reached at the initial hardening peak shortly after yield.

Figure IV-22 shows a SEI and BEI image of the same location on the normal surface, and both images show a visible trace that matched calculated slip traces for both (011) and (211), and another visible trace that matched (112). The <111> pole figure in Figure IV-23 shows that the primary $[1\bar{1}1]$ slip direction became closer to the tensile axis (black arrow), indicating that at least one slip system with a $[1\bar{1}1]$ slip direction was active. The <111> pole figure in Figure IV-23 shows that the secondary slip direction [111] moved closer to 45° from the tensile direction (white circle), which would help increase the resolved shear stress on slip systems of the [111] slip direction as deformation proceeded. Table IV-7 summarizes the evidence for active slip systems for sample T3. Table IV-7 indicates that the slip system $[1\bar{1}1](011)$, whose slip direction and slip plane match the secondary [111] slip direction rotation and visible trace observations, possessed the highest initial resolved glide shear stress at yield and remained high at the end of deformation. Two other slip systems had slip planes that matched the same visible trace as $[1\bar{1}1](011)$: the $[\bar{1}11](211)$ slip system only possessed moderate initial glide shear stress at yield that became relatively low at the end of deformation, and the $[\bar{1}\bar{1}1](011)$ slip system whose glide shear stress was relatively low at the beginning and end of deformation. The

other visible trace matched the $[\bar{1}\bar{1}1](112)$ slip system, whose glide shear stress was relatively low at the beginning of deformation and became moderate at the end of deformation.

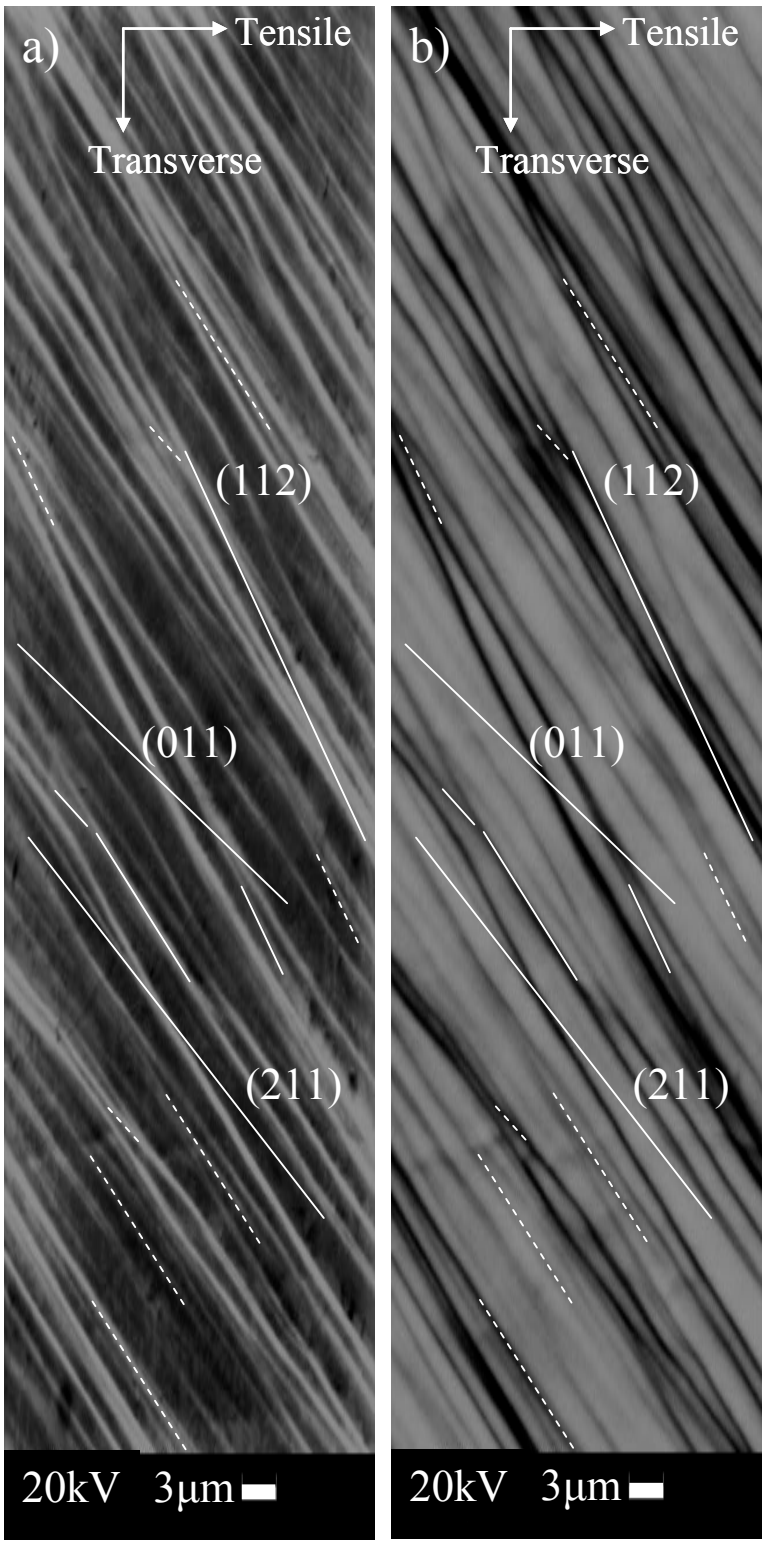

Figure IV-22. Slip traces on sample T3 after deformation, a) SEI and b) BEI. The calculated slip traces are the long labeled lines to which the visible traces (shorter white lines) were matched.

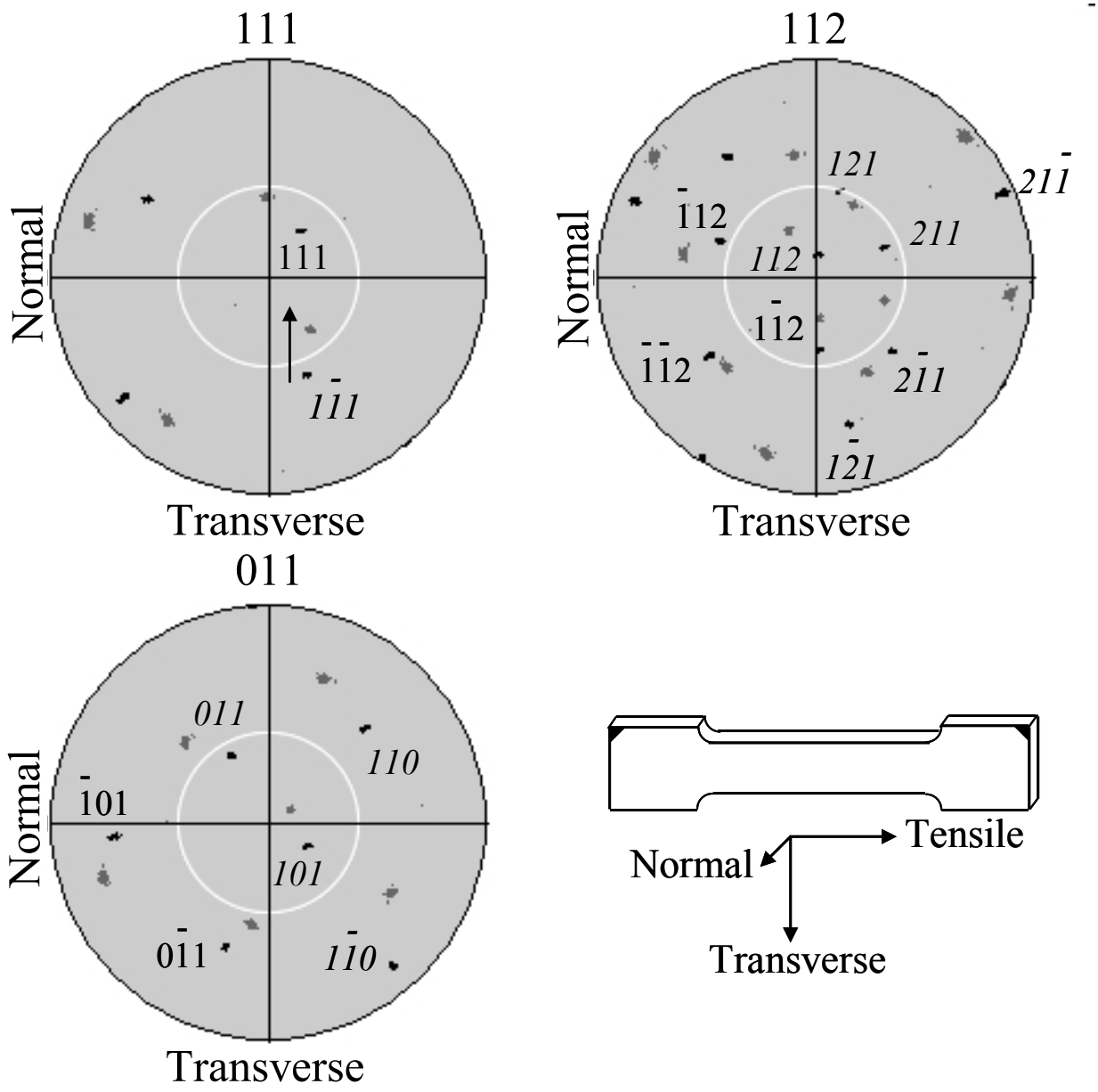

Figure IV-23. Pole figures collected from sample T3, with the tensile axis in the center of each pole figure. Initial orientation (black) and deformed orientation (grey) are overlaid. The primary (Italic text) and secondary (plain text) slip directions are labeled in the <111> pole figure. The slip plane normals of observed plane traces (italic text), and slip plane normals with no observed plane traces for slip systems that acquired enough resolved shear to possibly be active (plain text), are also labeled. Note the rotation of the $[1\bar{1}1]$ primary slip direction toward the tensile axis, which implies activity of at least one $[1\bar{1}1]$ slip system.

Table IV-7. A list of evidence considered for potentially active slip systems for sample T3 of the Ningxia sample set. The 0.2% strain offset yield stress and final flow stress are given under the sample name, in that order. Slip systems with matching possible and calculated slip traces are marked '*'if observed on the Normal surface, and marked '†' if observed on the Transverse surface. The greatest initial and final resolved glide shear stresses for the {110} and {112} slip system families are given in bold. Twinning (T) and anti-twinning (A) {112} planes are also indicated.

Sample, stresses (MPa), Hardening slope at yield, Slip direction that rotated toward TD, Initial Euler angles, Final Euler angles	Potentially active slip system	Initial resolved shear stress at yield (MPa): glide, non-glide 1, 2, 3	Final resolved shear stress (MPa): glide, non-glide 1, 2, 3
T3 37.6, 48.6 High $[1\bar{1}1]$ 168 65 270 171 59 292	$[1\bar{1}1](011)$*†	**18.3** 7.9 1.8 8.8	22.4 8.8 1.8 5.5
	$[1\bar{1}1](121)$†	**16.6** 15.1 -8.8 10.6 A	20.7 18.0 -5.5 7.3 A
	$[111](0\bar{1}1)$	15.7 4.8 1.9 2.6	**23.6** 15.5 -3.6 10.1
	$[111](\bar{1}\bar{1}2)$	15.3 11.8 -2.6 4.5 A	18.3 22.6 -10.1 6.5 A
	$[1\bar{1}1](\bar{1}12)$	15.1 -1.5 10.6 -1.8 T	18.0 -2.7 7.3 -1.8 T
	$[\bar{1}11](101)$†	13.6 6.5 0.7 13.4	6.9 2.4 8.3 15.2
	$[\bar{1}11](1\bar{1}2)$	11.9 11.6 -13.4 14.1 A	6.6 5.3 -15.2 23.5 A
	$[111](1\bar{2}1)$†	11.8 -3.5 4.5 -1.9 T	**22.6** 4.3 6.5 3.6 T
	$[\bar{1}11](211)$*†	11.6 -0.3 14.1 -0.7 T	5.3 -1.2 23.5 -8.3 T
	$[111](\bar{1}01)$	10.9 15.7 -4.5 1.9	8.1 23.6 -6.5 -3.6
	$[1\bar{1}1](110)$†	10.5 18.3 -10.6 1.8	13.5 22.4 -7.3 1.8
	$[\bar{1}11](110)$†	6.5 -7.0 13.4 -14.1	2.4 -4.5 15.2 -23.5
	$[\bar{1}\bar{1}1](112)$*†	5.5 2.1 5.4 12.5 T	9.1 0.8 18.0 3.7 T
	$[\bar{1}\bar{1}1](101)$†	5.2 4.4 -12.5 17.9	10.1 5.7 -3.7 21.7
	$[111](1\bar{1}0)$†	4.8 -10.9 2.6 -4.5	15.5 -8.1 10.1 -6.5
	$[\bar{1}\bar{1}1](011)$*	4.4 -0.8 17.9 -5.4	5.7 -4.3 21.7 -18.0
	$[\bar{1}\bar{1}1](2\bar{1}1)$†	3.5 5.5 -17.9 5.4 A	8.3 9.1 -21.7 18.0 A
	$[1\bar{1}1](21\bar{1})$†	1.5 16.6 -1.8 -8.8 N/A	2.7 20.7 -1.8 -5.5 N/A
	$[\bar{1}\bar{1}1](1\bar{1}0)$†	0.8 5.2 -5.4 -12.5	4.3 10.1 -18.0 -3.7

Figure IV-24 shows an SEI image at another location on the Transverse surface, and shows visible traces that matched the (011), (121), (101), $(1\bar{2}1)$, (211), (110), (112), $(1\bar{1}0)$, $(2\bar{1}1)$, and $(21\bar{1})$ calculated plane traces. Table IV-7 indicates several slip systems whose slip directions and slip planes match the primary $[1\bar{1}1]$ slip direction rotation and visible trace observations: the slip systems $[1\bar{1}1](011)$ and $[1\bar{1}1](121)$ possessed high resolved glide shear stresses at the beginning and end of deformation, the $[1\bar{1}1](110)$ slip system possessed moderate resolved glide shear stress at the beginning and end of deformation, while the $[1\bar{1}1](21\bar{1})$ slip system possessed very low resolved glide shear stress at the beginning and end of deformation. Table IV-7 also indicates two slip systems whose slip directions and slip planes match the secondary [111] slip direction rotation and visible trace observations: the $[111](1\bar{2}1)$ slip system possessed a resolved glide shear stress that was moderate at the beginning of deformation and then high at the end of deformation, while the $[111](1\bar{1}0)$ slip system possessed a resolved glide shear stress that was relatively low at the beginning of deformation and then moderate at the end of deformation. While visible traces were matched to other slip systems, Table IV-7 indicates that the initial and final resolved glide shear stress on those systems were never greater than moderate or relatively low.

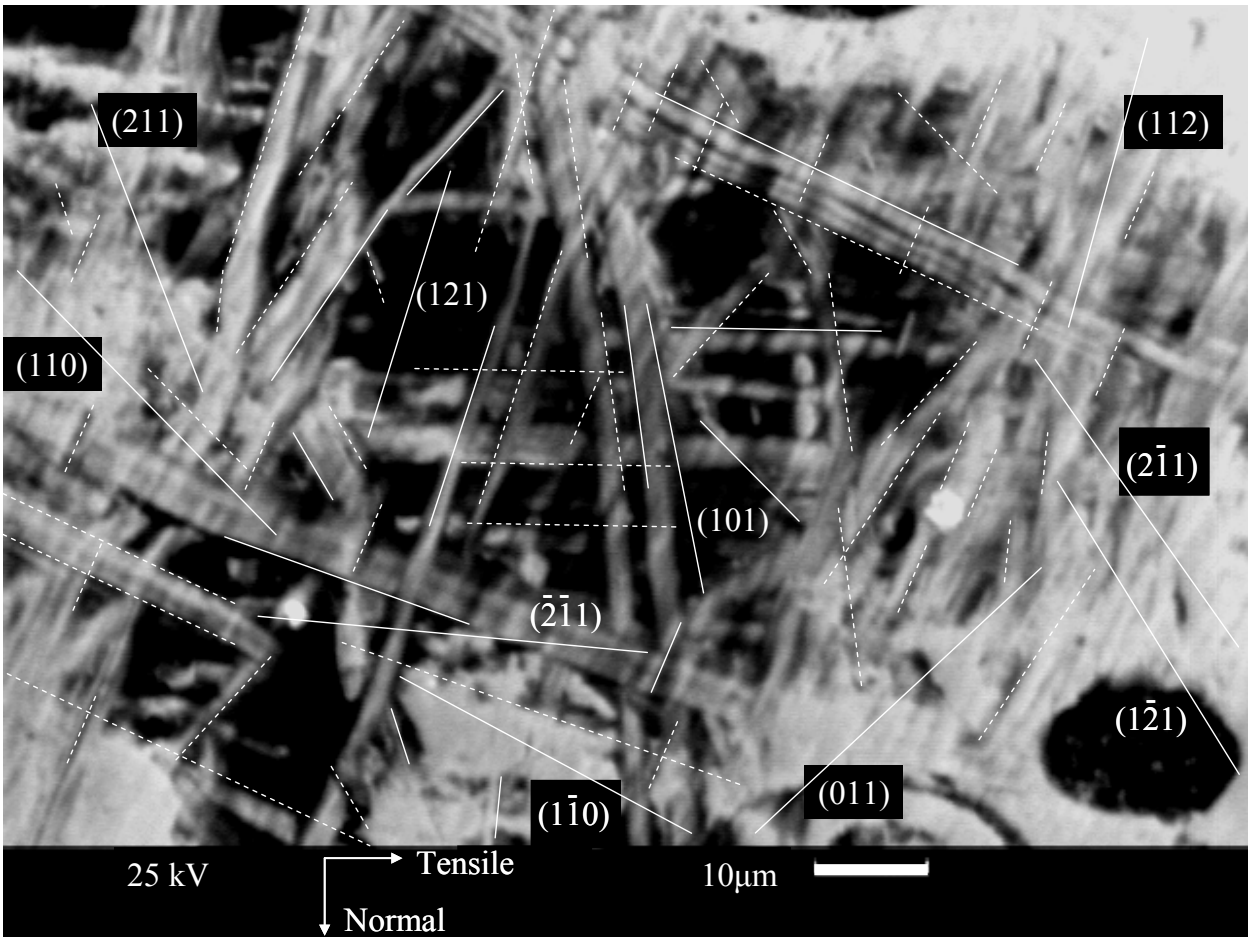

Figure IV-24. SEI of slip traces on the Transverse surface of sample T3 after deformation. Calculated slip traces are the long labeled lines which matched the visible traces (shorter white lines).

Figure IV-25 shows two different representations of the same orientation data obtained from a 112 x 327 μm area and a step size of 1 μm from the deformed sample T3. Figure IV-25a is a map of the relative difference in orientation and shows that this area of sample T3 did not possess deformation bands, only a homogeneous difference in deformed to undeformed orientation of approximately 24-26° across the whole area. Figure IV-25b shows that for the deformed sample T3, homogeneously distributed parallel boundaries of about 1-2° local average misorientations and 5-10 μm apart from each other were present, implying similarly distributed geometrically necessary dislocation boundaries at the 1 μm length scale; the boundaries are not aligned with particular slip plane traces. Figure IV-26 presents orientation maps in the same manner as Figure IV-25 though examined on a smaller length scale, a 22 x 65 μm area with step size of 0.2 μm found within the larger area examined by Figure IV-25. Figure VI-26a again shows that the difference between the deformed and undeformed orientation was homogeneous and approximately 24-26°. Figure IV-26b shows approximately homogeneously distributed intersecting geometrically necessary dislocation boundaries, about 1-2 μm apart from each other and with local average misorientations of about 1-2°; the boundaries are not aligned with particular slip plane traces. Table IV-6 summarizes the observations of the orientation maps of sample T3, along with similar observations of the orientation maps for the rest of the Ningxia samples.

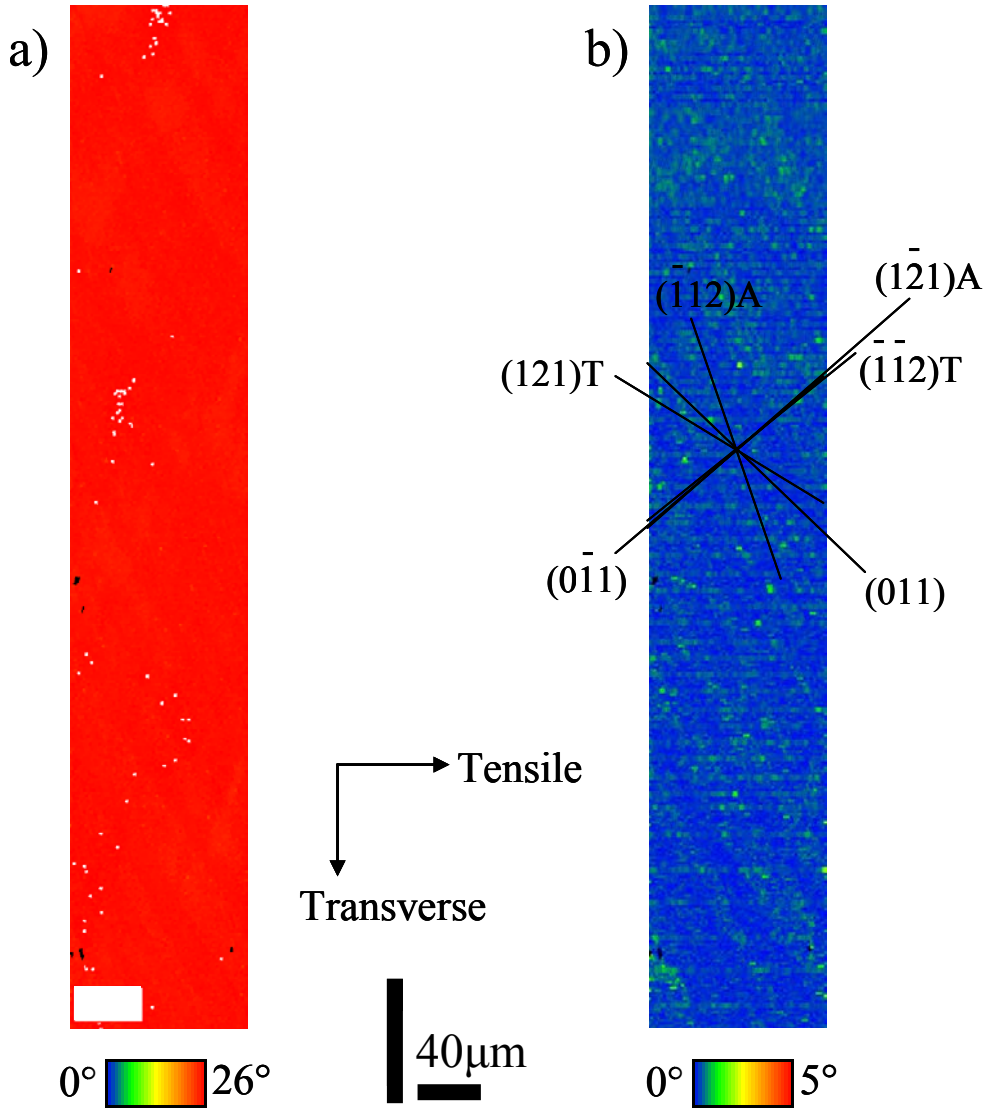

Figure IV-25. Two different representations of the same orientation data obtained after deformation of sample T3 from an 112x327µm area with 1µm step size. The scale bars are common to both images. a) A map of relative difference between the deformed and initial orientations with a range from 0°(blue) to 26°(red). b) A local average misorientation map based on first neighbors with a range of average misorientation from 0°(blue) to 5°(red).

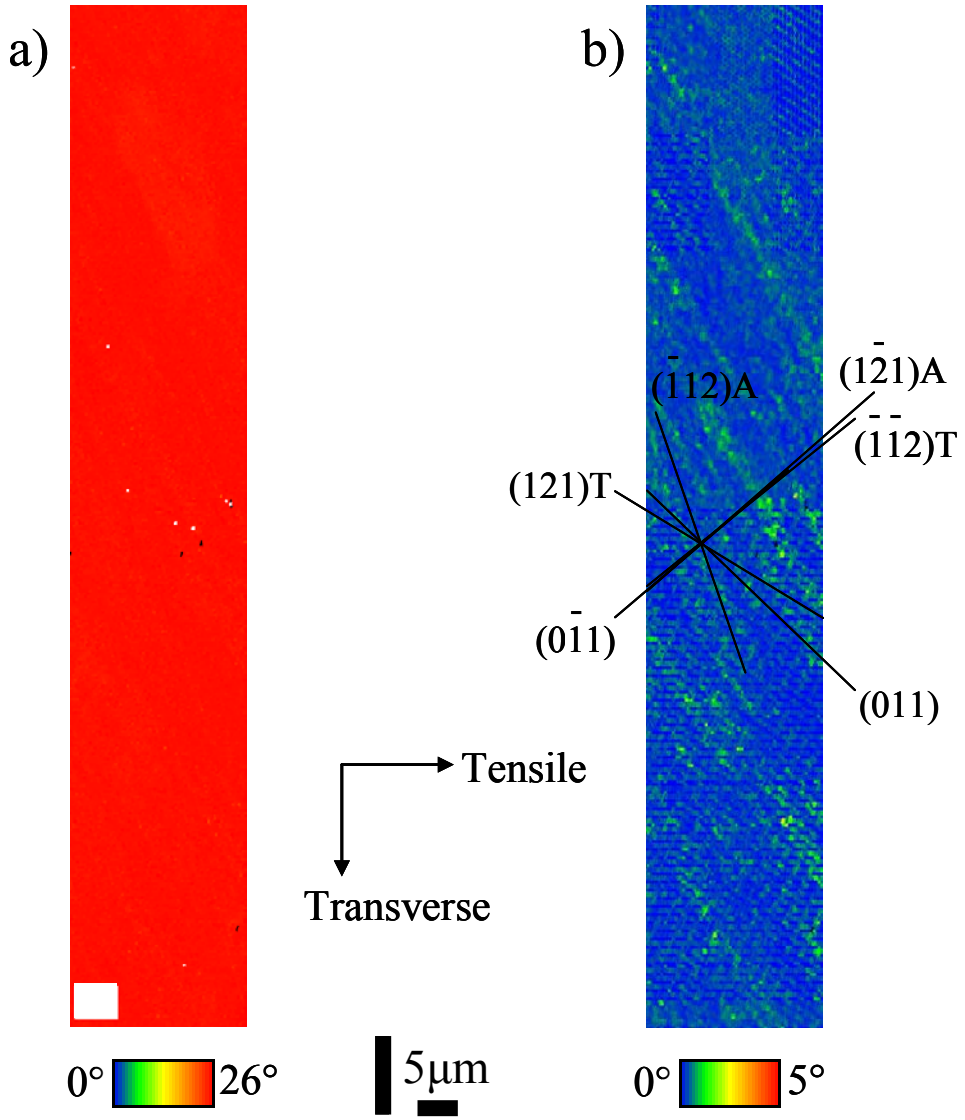

Figure IV-26. Two different representations of the same orientation data obtained after deformation of sample T3 from a 22x65μm area with 0.2 μm step size. The scale bars are common to both images. a) A map of relative difference between the deformed and initial orientations with a range from 0°(blue) to 26°(red). b) A local average misorientation map based on first neighbors with a range of average misorientation from 0°(blue) to 5°(red).

3. Sample P3

Sample P3 was initially oriented such that four slip systems possessed similar high resolved glide shear stresses: 17.1 MPa on $[1\bar{1}1](\bar{1}12)$, 17.0 MPa on $[111](\bar{1}\bar{1}2)$, 16.4 MPa on $[111](0\bar{1}1)$, and 16.4 MPa on $[1\bar{1}1](011)$. The stress strain curve for P3 in Figure IV-1 shows a high initial hardening rate that decreased after about 4% strain, becoming slight at about 8% strain, and then began increasing again at about 14% strain.

Figure IV-27 shows an SEI and BEI image of the same location on the Normal surface, and both show several visible traces that matched the $(\bar{1}\bar{1}2)$, (112), $(1\bar{1}2)$, $(\bar{1}01)$, and $(2\bar{1}1)$ calculated slip traces. The <111> pole figure in Figure IV-28 shows that the [111] slip direction rotated toward the tensile axis, suggesting that at least one slip system with a [111] slip direction was active; thus between the two essentially equally stressed $[1\bar{1}1]$ and [111] slip directions, [111] behaved as the primary slip direction. The <111> pole figure in Figure IV-28 also shows that the secondary slip direction $[1\bar{1}1]$ remained close to 45° from the tensile direction (white circle), which would help increase the resolved shear stress on slip systems of the $[1\bar{1}1]$ slip direction throughout deformation. Table IV-8 summarizes the evidence for active slip systems for sample P3. Table IV-8 indicates two slip systems whose slip direction and slip plane match the primary [111] slip direction rotation and visible trace observations: the $[111](\bar{1}\bar{1}2)$ slip system possessed a resolved glide shear stress that was high at the beginning of deformation and the highest of any slip system at the end of deformation, and the $[111](\bar{1}01)$ slip system that possessed a high resolved glide shear stress at the beginning and end of deformation . Table IV-8 indicates that the slip system $[1\bar{1}1](\bar{1}01)$, whose slip direction and slip plane also matches the secondary $[1\bar{1}1]$ slip direction rotation and visible trace observations, possessed a moderate resolved glide shear stress at the beginning and end of deformation. While visible traces were

matched to other slip systems, Table IV-8 indicates that the initial and final resolved glide shear stress on those systems were never greater than moderate. The pole figures in Figure IV-31 also show scattered minority orientations that appeared as a result of deformation.

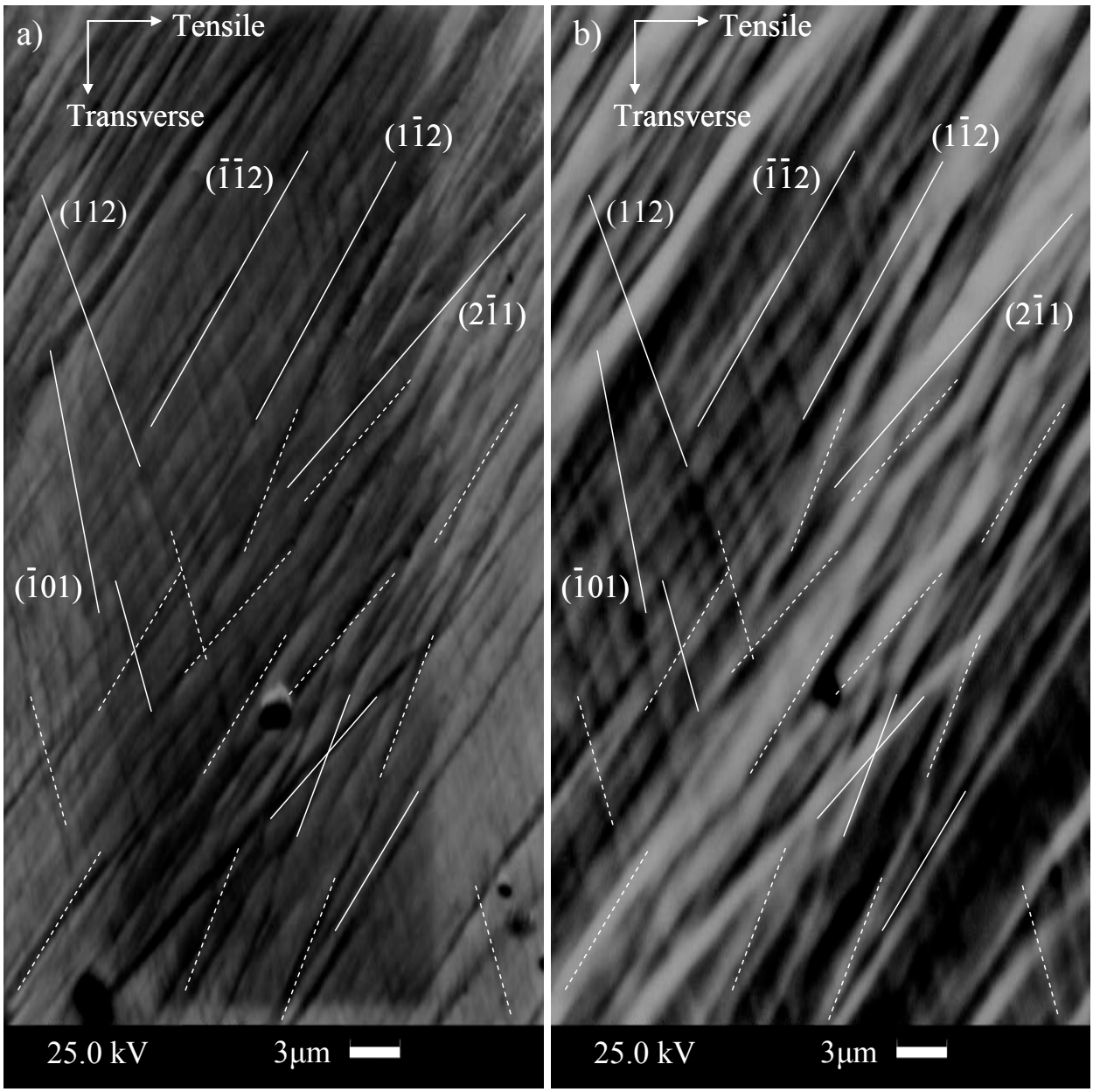

Figure IV-27. Slip traces on sample P3 after deformation, a) SEI and b) BEI. Calculated slip traces are the long labeled lines to which the visible traces (small white lines) were matched.

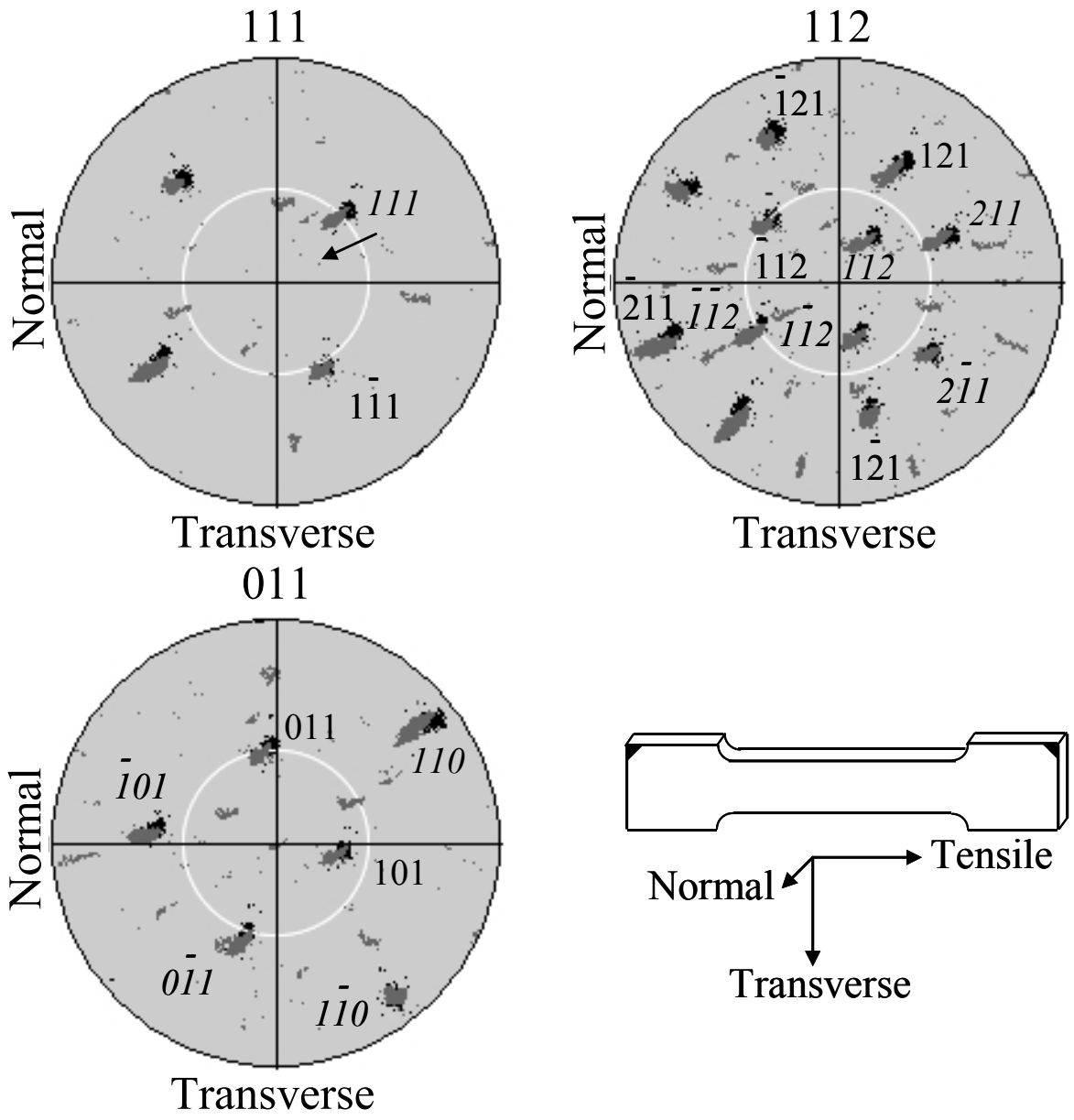

Figure IV-28. Pole figures collected from sample P3, with the tensile axis in the center of each pole figure. Initial orientation (black) and deformed orientation (grey) are overlaid. The primary (Italic text) and secondary (plain text) slip directions are labeled in the <111> pole figure. The slip plane normals of observed plane traces (italic text), and slip plane normals with no observed plane traces for slip systems that acquired enough resolved shear to possibly be active (plain text), are also labeled. Note slight rotation of [111] slip direction towards the tensile axis. Several minority orientations appeared as a result of deformation.

Table IV-8. A list of evidence considered for potentially active slip systems for sample P3 of the Ningxia sample set. The 0.2% strain offset yield stress and final flow stress are given under the sample name, in that order. Slip systems with matching possible and calculated slip traces are marked '*'if observed on the Normal surface, and marked '†' if observed on the Transverse surface. The greatest initial and final resolved glide shear stresses for the {110} and {112} slip system families are given in bold. Twinning (T) and anti-twinning (A) {112} planes are also indicated.

Sample, stresses (MPa), Hardening slope at yield, Slip direction that rotated toward TD, Initial Euler angles, Final Euler angles	Potentially active slip system	Initial resolved shear stress at yield (MPa): glide, non-glide 1, 2, 3	Final resolved shear stress (MPa): glide, non-glide 1, 2, 3
P3 34.8, 80.0 High [111] 182 79 263 179 73 262	$[1\bar{1}1](\bar{1}12)$	**17.1** 5.9 3.2 5.8 T	37.5 7.0 13.6 7.3 T
	$[111](\bar{1}\bar{1}2)$*	17.0 11.5 -3.8 9.5 A	**38.4** 27.8 -8.4 17.3 A
	$[111](0\bar{1}1)$†	**16.4** 3.5 5.7 3.8	38.2 10.0 8.9 8.4
	$[1\bar{1}1](011)$	**16.4** 13.3 -5.8 9.0	**39.3** 25.7 -7.3 20.9
	$[\bar{1}\bar{1}1](112)$*	14.0 4.9 4.6 8.9 T	25.7 8.9 12.2 22.4 T
	$[\bar{1}11](1\bar{1}2)$*	13.7 8.6 -4.0 13.6 A	29.1 21.7 -17.3 33.1 A
	$[\bar{1}\bar{1}1](101)$	13.3 10.9 -8.9 13.5	24.6 20.0 -22.4 34.6
	$[1\bar{1}1](\bar{1}01)$*†	13.3 -3.1 9.0 -3.2	25.7 -13.6 20.9 -13.6
	$[111](\bar{1}01)$*†	12.9 16.4 -9.5 5.7	28.2 38.2 -17.3 8.9
	$[\bar{1}11](101)$	12.9 2.0 9.6 4.0	29.4 8.2 15.7 17.3
	$[111](1\bar{2}1)$	11.5 -5.4 9.5 -5.7 T	27.8 -10.5 17.3 -8.9 T
	$[1\bar{1}1](121)$	11.2 17.1 -9.0 3.2 A	30.6 37.5 -20.9 13.6 A
	$[\bar{1}\bar{1}1](011)$	10.9 -2.4 13.5 -4.6	20.0 -4.6 34.6 -12.2
	$[\bar{1}11](0\bar{1}1)$†	10.9 12.9 -13.6 9.6	21.1 29.4 -33.1 15.7
	$[\bar{1}\bar{1}1](2\bar{1}1)$*†	9.1 14.0 -13.5 4.6 A	16.9 25.7 -34.6 12.2 A
	$[\bar{1}11](211)$†	8.6 -5.1 13.6 -9.6 T	21.7 -7.4 33.1 -15.7 T
	$[111](\bar{2}11)$	5.4 17.0 -5.7 -3.8 N/A	10.5 38.4 -8.9 -8.4 N/A
	$[\bar{1}\bar{1}1](\bar{1}21)$	4.9 -9.1 8.9 -13.5 N/A	8.9 -16.9 22.4 -34.6 N/A
	$[111](1\bar{1}0)$†	3.5 -12.9 3.8 -9.5	10.0 -28.2 8.4 -17.3
	$[1\bar{1}1](110)$†	3.1 16.4 -3.2 -5.8	13.6 39.3 -13.6 -7.3
	$[\bar{1}\bar{1}1](1\bar{1}0)$†	2.4 13.3 -4.6 -8.9	4.6 24.6 -12.2 -22.4
	$[\bar{1}11](110)$†	2.0 -10.9 4.0 -13.6	8.2 -21.1 17.3 -33.1

Figure IV-29 shows an SEI image at another location on the Transverse surface, and shows visible traces that matched the $(0\bar{1}1)$, $(\bar{1}01)$, $(2\bar{1}1)$, (211), $(1\bar{1}0)$, and (110) calculated plane traces. Table IV-8 indicates several slip systems whose slip directions and slip planes matched the primary [111] slip direction rotation and visible trace observations: the $[111](0\bar{1}1)$ slip system possessed a resolved glide shear stress that was the highest at yield for the {110} family of slip systems, and remained high at the end of deformation. While visible traces were matched to other slip systems, Table IV-8 indicates that the initial and final resolved glide shear stress on those systems were never greater than moderate.

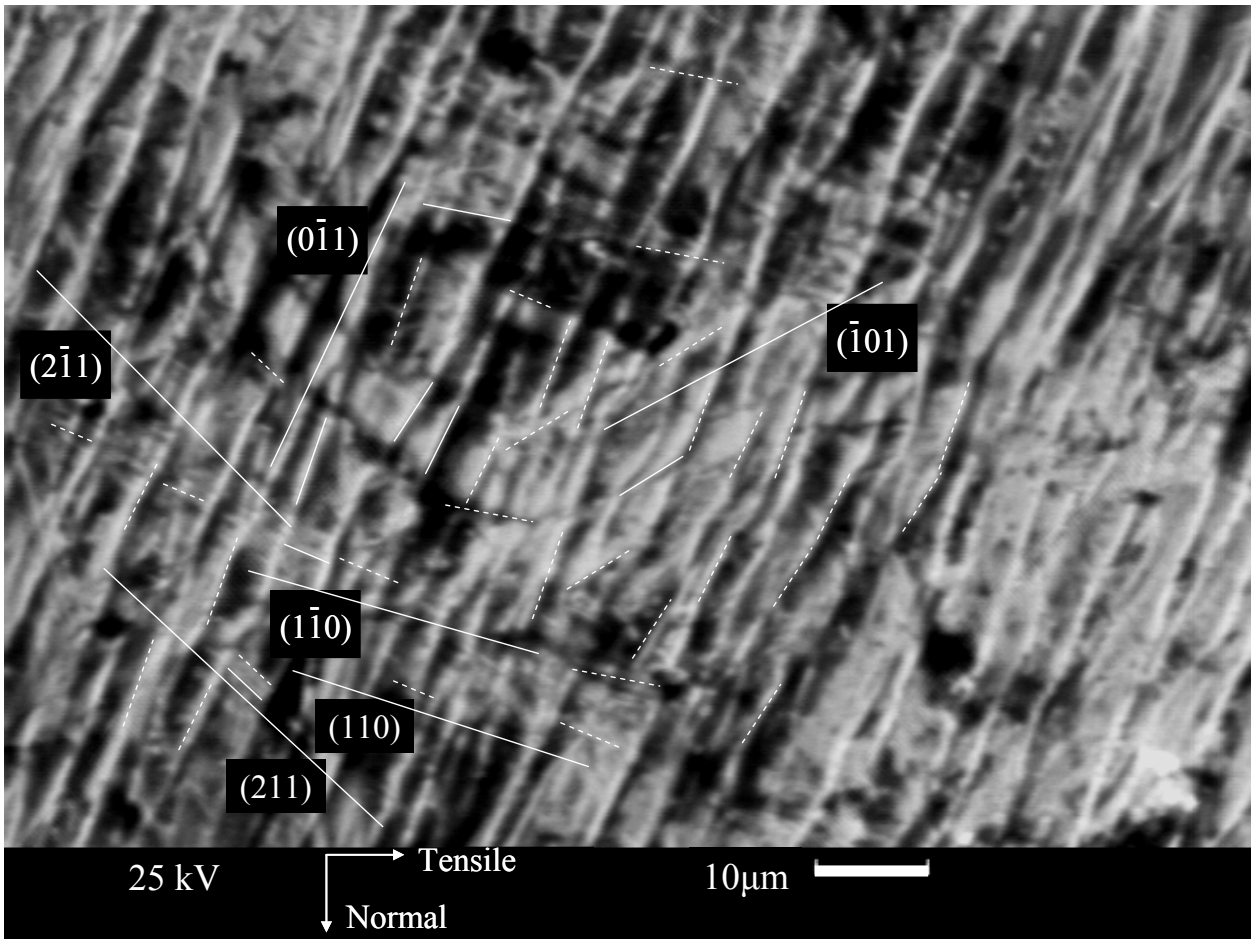

Figure IV-29. SEI of slip traces on the Transverse surface of sample P3 after deformation. Calculated slip traces are the long labeled lines to which the visible traces (shorter white lines) were matched.

Figure IV-30 shows two representations of the same orientation data obtained from a 112 x 327 μm area and a step size of 1 μm from the deformed sample P3. Figure IV-30a is a map of the relative difference in orientation and shows that this area of sample P3 did possess heterogeneously intersecting deformation bands, about 8-54 μm wide and rotated about 4-17° relative to the undeformed orientation. Figure IV-30b shows that for the deformed sample P3, heterogeneously distributed intersecting boundaries of about 1-3° local average misorientations and 3-16 μm apart from each other were present, implying similarly distributed geometrically necessary dislocation boundaries at the 1 μm length scale. Slip plane traces were calculated for two different points, one near the top of the image within a deformation band, and another near the center of the image in a region that was more similar to the initial undeformed orientation. Within the deformation band near the top of the image, the boundaries are not aligned with particular slip plane traces. In the region more similar to the initial undeformed orientation, some boundaries are aligned with the (112) plane trace, which belongs to the $[\bar{1}\bar{1}1](112)$ slip system that Table IV-8 indicates had moderately high resolved glide shear stress at the end of deformation; the other boundaries are not aligned with particular slip planes. Figure IV-31 presents orientation maps in the same manner as Figure IV-30 though examined a smaller length scale, a 22 x 65 μm area with step size of 0.2 μm found within the larger area examined by Figure IV-30. Figure IV-31a shows heterogeneously intersecting deformation bands, about 4-17 μm wide and rotated about 3-12° relative to the undeformed orientation. Figure IV-31b shows heterogeneously distributed intersecting geometrically necessary dislocation boundaries, about 1-19 μm apart from each other and with local average misorientations of about 2°. Plane traces are again calculated for two points, and though the boundaries are not aligned with particular slip plane traces at either point, some of the boundaries are again aligned with the (112) plane trace.

Table IV-6 summarizes the observations of the orientation maps of sample P3, along with similar observations of the orientation maps for the rest of the Ningxia samples.

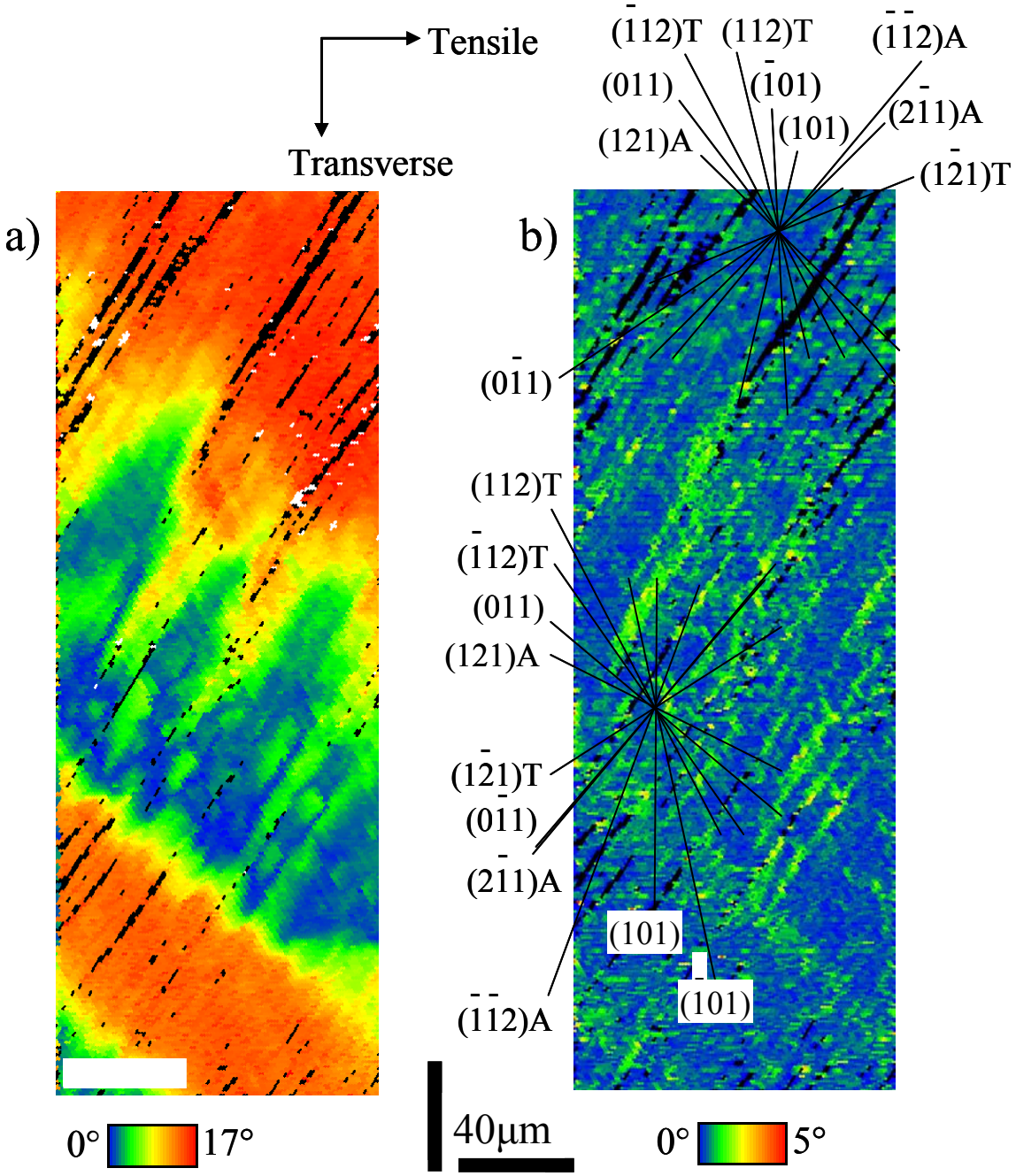

Figure IV-30. Two different representations of the same orientation data obtained after deformation of Sample P3 from an 112x327µm area with 1µm step size. The scale bar is common to both images. a) A map of relative difference between the deformed and initial orientations with a range from 0°(blue) to 17°(red). b) A local average misorientation map based on first neighbors with a range of average misorientation from 0°(blue) to 5°(red).

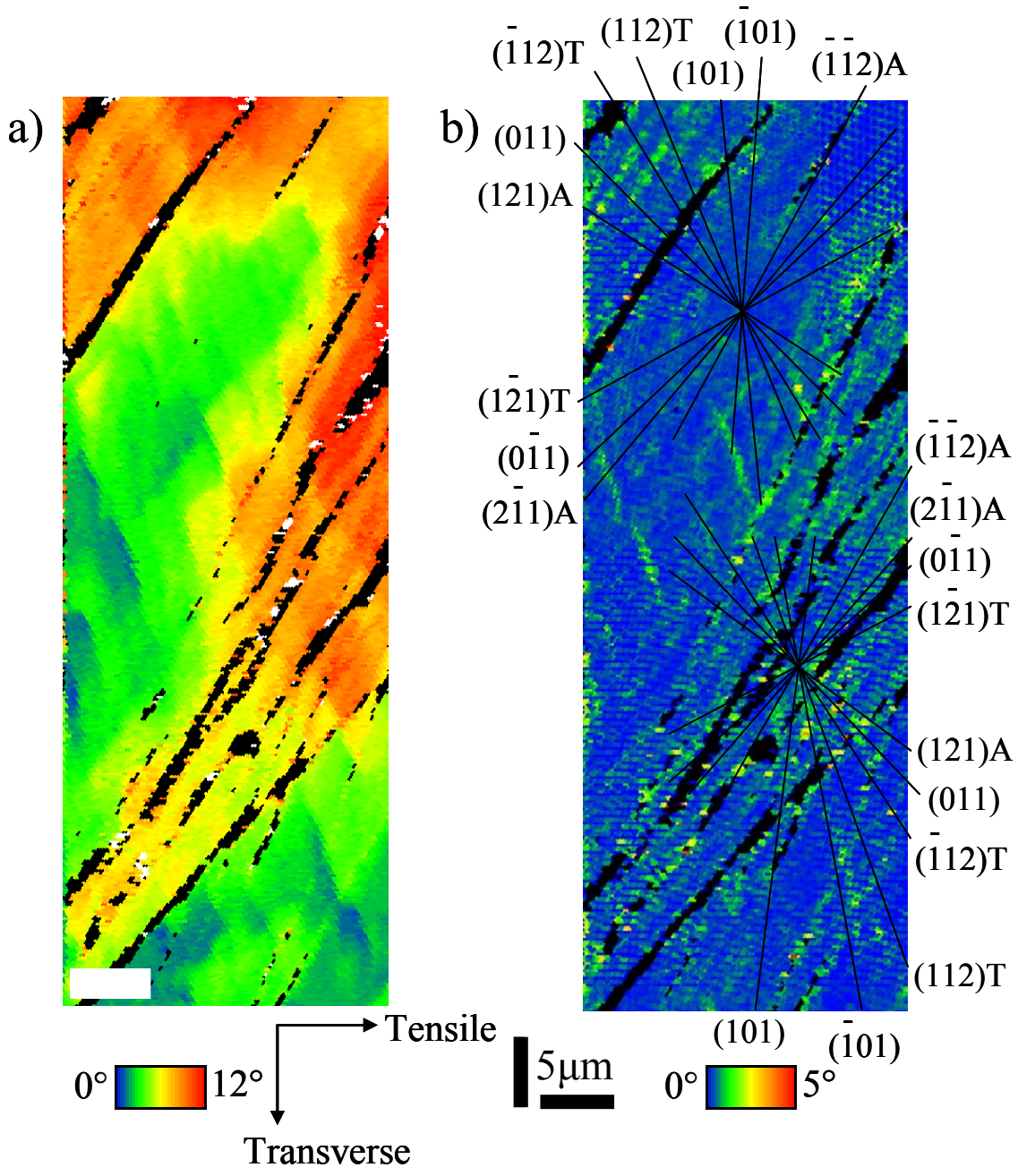

Figure IV-31. Two different representations of the same orientation data obtained after deformation of Sample P3 from a 22x65μm area with 0.2 μm step size. The scale bar is common to both images. a) A map of relative difference between the deformed and initial orientations with a range from 0°(blue) to 17°(red). b) A local average misorientation map based on first neighbors with a range of average misorientation from 0°(blue) to 5°(red).

Summarizing, Tables IV-5, 7, 8 list the evidence for possibly active slip systems for samples X3, T3, and P3, respectively. Table IV-6 lists the observations of deformation bands and geometrically necessary dislocation boundaries for all the samples in the Ningxia set, obtained in a similar manner as demonstrated for samples X3, T3, and P3. The images of visible traces, pole figures, orientation maps, and a table listing the evidence for possibly active slip systems for the other samples in the Ningxia set are in the Appendix.

V. Discussion

A. Introduction

The Discussion will follow the order of the processing steps, from the initial state of the prepared niobium samples, through the uniaxial deformation. The whole processing history of the material is important, because each subsequent step depends on the prior state of the material. The initial state of the prepared samples with regard to the purity and the presence of pre-existing dislocations, and the consequences of both, are discussed first. The stress-strain curves provide the yield stresses and show the changes in work hardening as deformation proceeded for each sample. Having obtained yield stresses from the stress-strain curves, the resolved shear stresses at yield and the hardening behavior immediately following yield are used to explore the complexities of the orientation-dependent critical resolved shear stress of BCC niobium. The most direct physical evidence of activity of a slip system is when a visible trace is matched to a calculated plane trace, though there are complications to that analysis, as described in Materials and Methods section III-C, with further complications due to interstitial impurities changing the screw core relaxation and the elementary slip plane. Other supporting evidence is needed to determine which slip systems were active: The slip direction of an active slip system rotates toward the tensile direction during uniaxial tension and is determined from the pole figures. While that rotation is also indirect physical evidence of slip system activity, the rotation only indicates that at least one slip system having that slip direction was active, and does not directly identify the slip plane. High resolved shear stress on a slip system was also evidence for slip system activity, though it is indirect evidence because the critical resolved shear stresses of BCC slip systems change depending on the orientation of the tensile direction and because the resolved shear stresses were calculated assuming an ideal uniaxial tension stress state. The

activity of both {112} and {110} slip planes in the Tokyo-Denkai and Ningxia sample sets is asserted, and would be enabled by the preexisting interstitial impurities as received from the manufacturer and/or additional hydrogen contamination absorbed during sample preparation and deformation. Based on the evidence gathered in the Results section and subsequently carefully examined in the Discussion, the most likely active slip systems are determined for the Tokyo-Denkai and Ningxia sample sets. Finally, a detailed comparison between the behavior of the Ningxia sample set and that of a similar earlier study is done (from section II-E, a Duesbery and Foxall sample set [24]).

B. Initial state of the prepared samples

Deformation does not only depend on the orientation of the tensile axis, but also on the purity of the samples and any pre-existing dislocations. Higher impurity content results in a higher yield stress, because dislocations are pinned by the impurities until the resolved shear stress is high enough to allow the dislocation to break away. Impurities in BCC metals may even affect the slip planes of screw dislocations. The theory explained in section II-F of the Literature Review asserts that in very high purity niobium deformed at room temperature, screw dislocation cores are relaxed such that elementary slip occurs on {112} planes, so that the screw dislocations may cross slip easily and often among the set of 3 {112} planes having the same <111> slip direction, according to the stress state at any given moment during deformation [11]. The theory also asserts that sufficient interstitial impurity content would lead to a screw core relaxation for which elementary slip occurs on {110} planes, and consequently slip and frequent cross-slip on a set of 3 {110} planes in a similar manner [11]. Table V-1 summarizes the interstitial impurity content of several sets of single crystal niobium samples, and shows that both the Tokyo-Denkai and Ningxia sample sets did possess greater interstitial impurity levels than the niobium used in

the study by Seeger *et. al.* that asserted elementary slip on {112} planes [11]. While the amount of interstitial impurities needed to cause significant numbers of screw dislocations to change from the {112} to {110} slip relaxation in niobium at room temperature is unclear, another study did indicate that 330 ppm nitrogen in high purity iron caused a measurable increase in the {110} screw core relaxation [46]; while niobium is not iron, this provides at least some idea as to the interstitial impurity levels needed for {110} slip to become noticeably favored.

Table V-1. The list summarizes the interstitial impurity content of different sets of single crystal niobium samples, given in atomic parts per million (at ppm).

Interstitial Impurity	Seeger et al maximum amount of each [11]	Duesbery & Foxall 1969 measured amounts [25]	Ningxia ingot measured amounts	Ningxia specification	Tokyo-Denkai specification
Oxygen	<8.5	29	29	<58	<58
Nitrogen	<7.3	33	33	<66	<66
Hydrogen	<47	92	276	<184	<460
Carbon	<8.5	85	77	<77	<77
Total	<71.3	239	415	<385	<661

The specified total interstitial impurity levels for both the Tokyo-Denkai and Ningxia niobium sample sets used in this thesis imply that the amount of interstitial impurities exceeds 330 ppm, so the possibility of slip on {110} planes must be considered even if sample preparation issues were not also a potential source of additional impurities. The Tokyo-Denkai and Ningxia sets of samples may also have absorbed additional interstitial hydrogen from the chemical etches or electropolishing used during sample preparation. Simple calculations indicate that hydrogen could diffuse in niobium 1mm during each one of the multiple 4 min chemical etchings, or 1.3mm during each one of multiple 8min electropolishings, despite being done at 0 and -30°C respectively [67]. With a 10min room temperature chemical etch, hydrogen could diffuse 6.5mm. Given that the Tokyo-Denkai and Ningxia samples were only approximately 3mm thick, all of those distances represent full penetration of hydrogen from the surface to the center of the samples. Hydrogen could also enter during deformation as the thin surface oxide cracks. Etching and deformation were also explicitly referred to in the literature as possible sources of hydrogen contamination [11]. Indeed, the experiments that identified {112} as the elementary slip planes in high purity niobium were done under vacuum, specifically to avoid an order of magnitude increase in sample hydrogen content that occurred during preliminary tests and had been attributed to deformation [11]. Though the amount is not known, there was ample opportunity for the Tokyo-Denkai and Ningxia samples to absorb additional hydrogen during sample preparation and deformation, in addition to the impurities already present, so {110} slip must be considered in addition to {112} slip.

The presence of pre-existing dislocations in the prepared samples would affect deformation and needed to be examined. Transmission electron microscopy (TEM) of specimens taken from the same grains as the samples might have provided a means of examining any pre-existing

dislocations in the source niobium, and several TEM specimens were made. However, complications with the TEM specimen preparation cast doubt as to whether the dislocations observed would be representative of those in the prepared tensile samples for the following reasons: Niobium is very ductile, due to being single crystal with no grain boundaries and high purity with little impurity drag, either to pin or slow dislocation slip. TEM specimens must be very thin, so blanks were cut with a diamond saw, thinned mechanically using successively finer diamond grit paper (similar to the sample preparation for OIM), round specimens punched out, their centers mechanically dimpled using diamond slurry, and finally perforated using a double-sided jet electropolisher. Experience showed that after careful mechanical polishing of the niobium sample surface in preparation for orientation imaging microscopy (OIM), the electron backscatter diffraction patterns were still not clear enough to index, while after electropolishing the patterns were very clear. This was attributed to a 'damage layer' of dislocations that was introduced during mechanical polishing, which was subsequently removed by the electropolishing. The concern was that, despite the final perforation by electropolishing, the thin TEM specimens would retain dislocations that had been introduced into the thin sample due to the stresses produced during the mechanical polishing steps.

Instead, the presence of pre-existing geometrically necessary dislocations in the prepared samples was investigated using local average misorientation data. Greater geometrically necessary dislocation (GND) density is correlated to greater degrees of local average misorientation (LAM), because the presence of geometrically necessary dislocations rotates the crystal lattice. Figure V-1 shows the number average and standard deviation of the local average misorientation for each Tokyo-Denkai sample in the initial state with a step size of 30 μm. The graphs were made by taking the average and standard deviation of the LAM map data (computed

by the software), similar to Figure IV-20 of sample X3 except taken after sample preparation though still undeformed, as a representation of the number average LAM from each sample. Similarly, Figure V-2 shows the same for the Ningxia samples though with a step size of 1 μm. Comparison of LAM data taken at different step sizes is not accurate. The inaccuracy was confirmed using two LAM maps of the same area, one with a larger step size than the other (data not shown). The smaller step size was coarsened (the software simply removes every other pixel) until its step size was similar to the larger step size; this was done for several of the Ningxia samples. The LAM data were compared and found that the coarsened data set tended to have a larger LAM than the data set that started with the larger step size, even though the data is from the same area and same lattice rotations. Thus no direct comparison between the initial state of the Tokyo-Denkai and Ningxia LAM data should be made. Among the undeformed Tokyo-Denkai samples, sample A possesses the highest number average LAM (0.71±0.39) and implies a greater initial geometrically necessary dislocation density relative to samples C and F; the number average LAM for samples C (0.57±0.35) and F (0.61±0.37) is similar and implies a similar initial geometrically necessary dislocation density. Among the undeformed Ningxia samples, sample P3 possess the highest number average LAM (0.36±0.27) and implies a greater initial geometrically necessary dislocation density than the other Ningxia samples, while sample T3 has the lowest LAM (0.12±0.10), which implies it has the lowest dislocation density. The initial number average local average misorientation is similar among the other Ningxia samples: Q2 0.24±0.18, R2 0.23±0.14, S3 0.22±0.11, U3 0.17±0.13, V3 0.34±0.21, W3 0.24±0.13, and X3 0.24±0.10, which implies that the initial geometrically necessary dislocation density was similar among the Ningxia samples. Within the Tokyo-Denkai and Ningxia sets, the variation in the local average misorientation is smaller than the standard deviation among the samples in the

set, so the variations are not statistically significant. That implies that the variations in the initial dislocation density of each sample within each of the sets are also not significant.

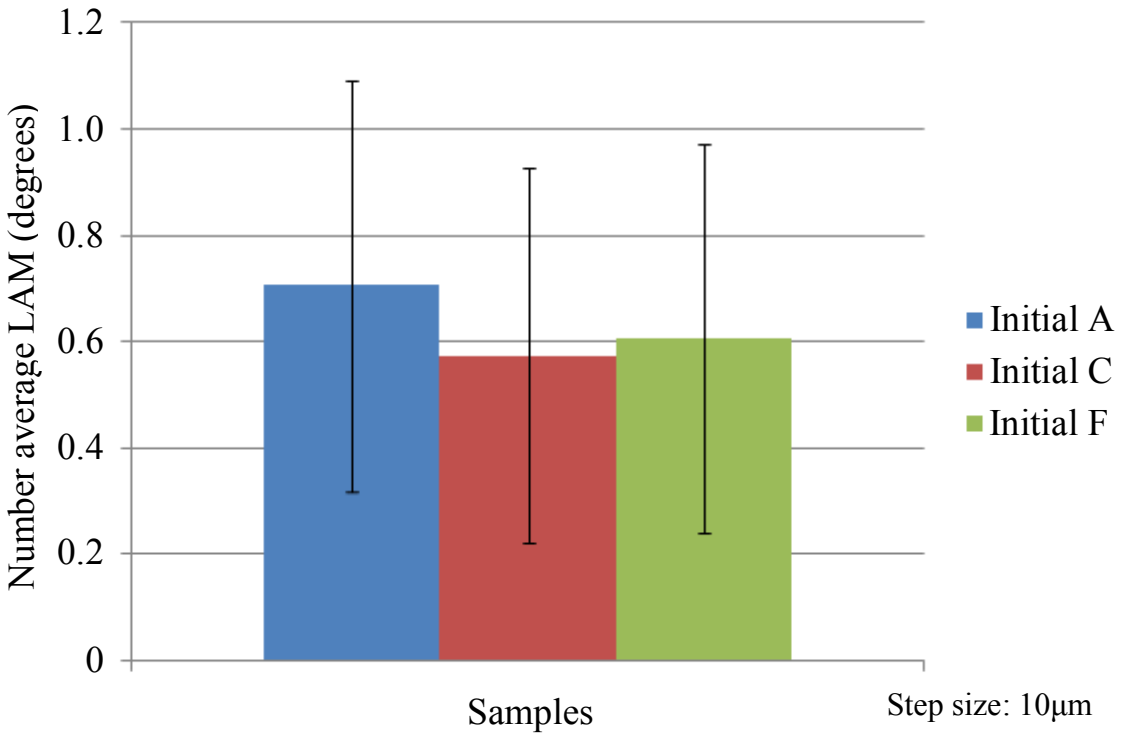

Figure V-1. The number average local average misorientation and standard deviation is given for the initial state of each prepared Tokyo-Denkai sample. Local average misorientations were determined using 1st nearest neighbors.

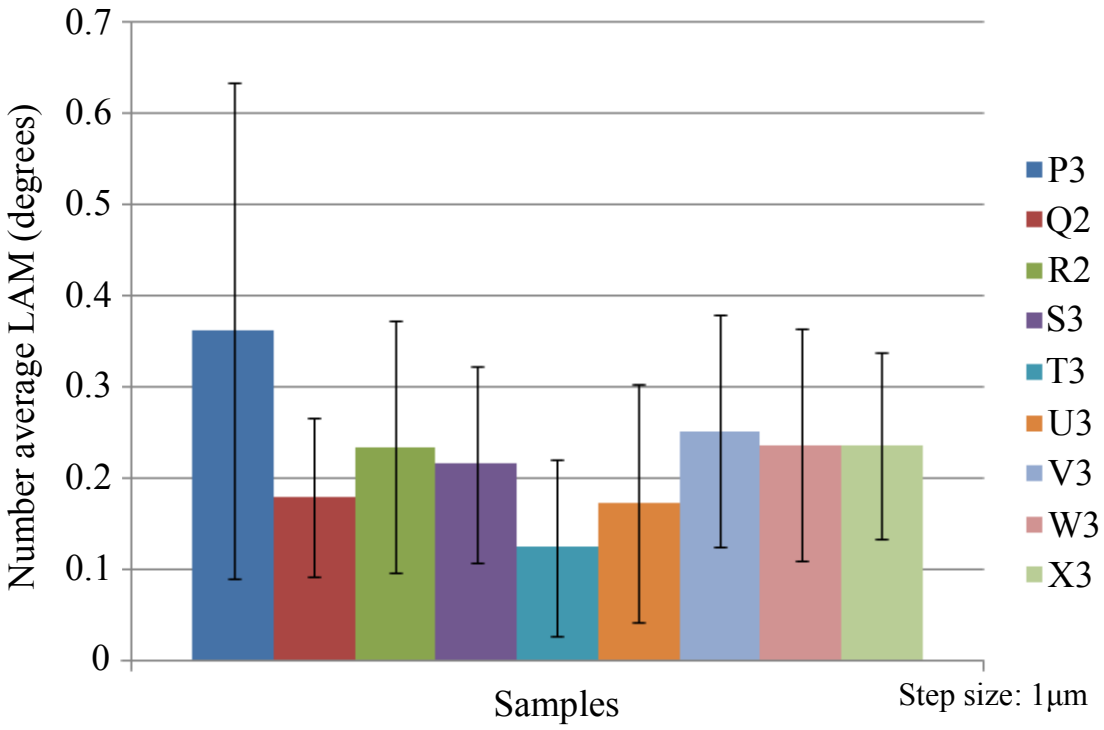

Figure V-2. The number average local average misorientation and standard deviation is given for the initial state of each prepared Ningxia sample. Local average misorientations were determined using 1st nearest neighbors.

A possible source of pre-existing dislocations may be those compensating for the stress caused by the thermal contraction that occurred as the ingot cooled during purification. The molten niobium was cooled by a water jacket that established the radius of the ingot while near the 2750 K melting temperature; the solidified niobium is supported below the water jacket and moves downward as more niobium solidifies, making the ingot an elongated cylinder. As the ingot solidified the volume occupied by the niobium shrank due to thermal contraction, but the outer radius constrained the shrinkage, as it solidified first. The thermal contraction with constraint would lead to internal stress and strain that would generate dislocations. The stress state is complicated and may be similar to that of tempered glass, in which the stress state transitions from compression on the outer surface to tension in the center [68]. A simplified stress state is assumed in this work. Given the thermal expansion of niobium 7.3 μm/m/K, the 2450K temperature range (from the melting temperature to room temperature, 300K), and the known 126.7 mm radius of the ingot, the radius would contract approximately 2.3 mm if not for the solidified edge. A rough estimate of the radial strain caused by thermal contraction is approximately 1.8%, and the strain caused by the thermal contraction in the circumferential direction is also 1.8%. This stress state of contraction in both the circumference and radius of the ingot may be further simplified to uniaxial tension along the long axis of the ingot. The slip systems that may have produced dislocations to compensate for the thermal strain would be those with a high Schmid factor when uniaxial tension was applied along the long axis of the ingot, which became the Normal direction of the Tokyo-Denkai and Ningxia samples once they were prepared.

The Schmid factors on slip systems due to the thermal stress were found for several of the samples, using the simplifying assumption of uniaxial tension in the Normal direction of the

sample. Table V-2 lists the samples, the two {112} and {110} slip systems with the highest Schmid factors due to the thermal stress in the sample Normal direction, the two {112} and {110} slip systems with the highest Schmid factors later imposed by uniaxial tension in the sample tensile direction, and the relationship between the pre-existing dislocations that may have formed due to the thermal stress and the primary slip system(s) from the uniaxial tension test. Dislocations due to thermal stress will be assumed to exist on the slip systems with the highest Schimd factor due to the thermal stress, because the Tokyo-Denkai and Ningxia samples were not annealed prior to deformation to be consistent with SRF cavity forming procedure; annealing would have diminished the density of pre-existing dislocations. The local average misorientation data only implies the geometrically necessary dislocation content for each sample, and may only be used to compare the content *relative* to other samples within the same set, and thus cannot be used to assert there are no pre-existing dislocations. If the slip direction of the pre-existing dislocations intersects with the slip direction of the primary slip system(s) of the uniaxial tension test, then their relationship is 'Forest'. Then the pre-existing dislocations should interfere with the primary slip system(s) of the uniaxial tension test. Any observed immediate hardening at yield may be due in part to those forest dislocations generated by the thermal stress that intersect high Schmid factor slip systems. If the slip direction of the pre-existing dislocations is the same as the slip direction of the primary slip system(s) of the uniaxial tension test, then the relationship is 'Primary'. Then the pre-existing dislocations are not oriented as forest dislocations and do not interfere with the primary slip system(s) of the uniaxial tension test (e.g. Samples Q2, R2, U3, V3 and X3). In that case, no hardening immediately following yield due to pre-existing dislocations is expected. Whether pre-existing dislocations actually affect the

hardening immediately after yield depends on their relationship to the primary slip system(s) of the uniaxial tension test.

Table V-2. The slip systems with the highest Schmid factors due to a possible thermal stress (tension in the normal direction), the highest Schmid factors due to the uniaxial tensile test (tension in the tensile direction), and the relationship between those two at yield are listed for selected samples.

Sample name, initial hardening	Potentially active system	Schmid factor due to radial thermal stress (Tension in normal direction)	Schmid factor at yield (Tension in tensile direction)	Relationship to primary if present at yield
C Slight	$[\bar{1}\bar{1}1](\bar{1}10)$	0.47	0.03	Forest
	$[\bar{1}\bar{1}1](\bar{1}21)$	0.47	0.01	Forest
	$[\bar{1}11](110)$	0.45	0.08	Forest
	$[\bar{1}11](\bar{1}\bar{2}1)$	0.44	0.01	Forest
	$[1\bar{1}1](\bar{1}2\bar{1})$	0.01	0.48	Primary
	$[1\bar{1}1](011)$	0.07	0.48	Primary
	$[111](01\bar{1})$	0.04	0.44	Forest
	$[111](1\bar{2}1)$	0.01	0.43	Forest
F Moderate	$[\bar{1}\bar{1}1](\bar{1}21)$	0.42	0.01	Forest
	$[\bar{1}\bar{1}1](\bar{1}10)$	0.40	0.03	Forest
	$[1\bar{1}1](\bar{1}12)$	0.33	0.33	Primary
	$[1\bar{1}1](10\bar{1})$	0.33	0.10	Primary
	$[1\bar{1}1](\bar{1}\bar{2}\bar{1})$	0.10	0.48	Primary
	$[1\bar{1}1](011)$	0.25	0.47	Primary
	$[111](1\bar{2}1)$	0.05	0.43	Forest
	$[111](01\bar{1})$	0.01	0.43	Forest
A Moderate	$[1\bar{1}1](\bar{1}12)$	0.50	0.49	Primary
	$[1\bar{1}1](10\bar{1})$	0.44	0.40	Primary
	$[\bar{1}11](\bar{1}1\bar{2})$	0.43	0.42	Forest
	$[1\bar{1}1](011)$	0.41	0.45	Primary
	$[111](11\bar{2})$	0.00	0.49	Forest
	$[111](01\bar{1})$	0.01	0.46	Forest
S3 Barely	$[1\bar{1}1](011)$	0.50	0.49	Primary
	$[\bar{1}11](0\bar{1}1)$	0.48	0.13	Forest
	$[\bar{1}11](\bar{1}\bar{2}1)$	0.45	0.00	Forest
	$[1\bar{1}1](\bar{1}\bar{2}\bar{1})$	0.45	0.47	Primary
	$[1\bar{1}1](\bar{1}12)$	0.42	0.37	Primary
	$[111](01\bar{1})$	0.22	0.43	Forest
	$[111](1\bar{2}1)$	0.31	0.38	Forest

Table V-2 (cont'd)

T3 High	$[\bar{1}\bar{1}1](\bar{1}10)$	0.49	0.02	Forest
	$[\bar{1}11](110)$	0.49	0.17	Forest
	$[\bar{1}11](211)$	0.44	0.31	Forest
	$[\bar{1}\bar{1}1](2\bar{1}1)$	0.43	0.09	Forest
	$[1\bar{1}1](011)$	0.09	0.49	Primary
	$[1\bar{1}1](\bar{1}\bar{2}\bar{1})$	0.05	0.44	Primary
	$[111](01\bar{1})$	0.08	0.42	Forest
	$[111](11\bar{2})$	0.20	0.41	Forest
X3 Barely	$[1\bar{1}1](\bar{1}12)$	0.41	0.29	Primary
	$[1\bar{1}1](\bar{1}01)$	0.37	0.05	Primary
	$[1\bar{1}1](011)$	0.33	0.46	Primary
	$[\bar{1}\bar{1}1](\bar{1}21)$	0.31	0.01	Forest
	$[1\bar{1}1](121)$	0.17	0.50	Primary
	$[1\bar{1}1](110)$	0.04	0.41	Primary
	$[111](1\bar{2}1)$	0.11	0.38	Forest
	$[111](0\bar{1}1)$	0.01	0.36	Forest
Q2 Barely	$[1\bar{1}1](121)$	0.50	0.48	Primary
	$[\bar{1}\bar{1}1](\bar{1}21)$	0.47	0.02	Forest
	$[\bar{1}\bar{1}1](1\bar{1}0)$	0.45	0.02	Forest
	$[1\bar{1}1](110)$	0.45	0.35	Primary
	$[1\bar{1}1](011)$	0.42	0.48	Primary
	$[111](0\bar{1}1)$	0.35	0.41	Forest
	$[111](1\bar{2}1)$	0.40	0.38	Forest
R2 Slight	$[1\bar{1}1](121)$	0.50	0.48	Primary
	$[\bar{1}11](\bar{1}\bar{2}1)$	0.48	0.00	Forest
	$[\bar{1}11](0\bar{1}1)$	0.46	0.10	Forest
	$[1\bar{1}1](011)$	0.45	0.48	Primary
	$[111](0\bar{1}1)$	0.33	0.42	Forest
	$[111](1\bar{2}1)$	0.40	0.40	Forest

Table V-2 (cont'd)

P3 High	$[\bar{1}\bar{1}1](2\bar{1}1)$	0.50	0.26	Forest
	$[\bar{1}11](110)$	0.47	0.06	Forest
	$[\bar{1}11](211)$	0.46	0.25	Forest
	$[\bar{1}\bar{1}1](1\bar{1}0)$	0.45	0.07	Forest
	$[1\bar{1}1](\bar{1}12)$	0.19	0.49	Forest
	$[111](\bar{1}\bar{1}2)$	0.32	0.49	Primary
	$[111](0\bar{1}1)$	0.12	0.47	Primary
	$[1\bar{1}1](011)$	0.02	0.47	Forest
V3 Moderate	$[1\bar{1}1](\bar{1}12)$	0.39	0.35	Primary
	$[1\bar{1}1](\bar{1}01)$	0.36	0.14	Primary
	$[\bar{1}\bar{1}1](\bar{1}21)$	0.33	0.01	Forest
	$[1\bar{1}1](011)$	0.32	0.47	Primary
	$[1\bar{1}1](121)$	0.16	0.46	Primary
	$[111](0\bar{1}1)$	0.01	0.46	Forest
	$[111](1\bar{2}1)$	0.10	0.45	Forest
U3 Very High	$[1\bar{1}1](\bar{2}\bar{1}1)$	0.41	0.13	Primary
	$[1\bar{1}1](\bar{1}01)$	0.38	0.07	Primary
	$[1\bar{1}1](110)$	0.34	0.29	Primary
	$[\bar{1}11](\bar{1}\bar{2}1)$	0.31	0.12	Forest
	$[1\bar{1}1](121)$	0.17	0.38	Primary
	$[\bar{1}11](211)$	0.10	0.37	Forest
	$[1\bar{1}1](011)$	0.04	0.36	Primary
	$[\bar{1}11](101)$	0.06	0.35	Forest
W3 Moderate-Low	$[1\bar{1}1](\bar{1}12)$	0.39	0.33	Primary
	$[1\bar{1}1](\bar{1}01)$	0.36	0.11	Primary
	$[\bar{1}\bar{1}1](\bar{1}21)$	0.32	0.01	Forest
	$[1\bar{1}1](011)$	0.32	0.47	Primary
	$[1\bar{1}1](121)$	0.16	0.48	Primary
	$[111](1\bar{2}1)$	0.11	0.44	Forest
	$[111](0\bar{1}1)$	0.01	0.44	Forest

There are several other considerations of how the initial condition of the sample may influence the behavior at yield and immediately following yield. A greater amount of impurities, pre-existing dislocations, or combination of both would be expected to increase the yield stress of a sample. Impurities do not cause hardening immediately after yield because once the shear stress is great enough to break the dislocation away from the pinning impurity, those impurities do not continuously distort the dislocation lines the way dislocation-dislocation interactions do. Samples oriented such that two intersecting slip systems possess similar resolved shear stresses during the uniaxial tension test are expected to show immediate hardening at yield due to the interaction of those two systems, and so any hardening due to pre-existing dislocations that had formed because of a thermal stress would contribute to the observed hardening at yield. The stress-strain curves are examined next with these perspectives in mind.

C. The Tensile Tests

The engineering stress-strain curves of the Tokyo-Denkai samples in Figure IV-1 possessed high yield stresses that may have been due to dislocations being pinned by greater impurity content, and/or by pre-existing dislocations of intersecting slip systems acting as forest dislocations. While samples C and F do exhibit some upper-lower yield point behavior that is a symptom of impurity pinning, the effect is very small. The yield stresses of the Ningxia samples are lower than those of the Tokyo-Denkai samples and suggests that the Ningxia samples contained fewer impurities than the Tokyo-Denkai samples, which is consistent with the amounts of impurities given for each set in Table V-1.

Hardening immediately following yield is expected from two sources: pre-existing forest dislocations formed by the thermal stress, and when two intersecting slip systems are both active at yield due to the orientation of the sample tensile direction. The Tokyo-Denkai and Ningxia samples give the opportunity to separate these two sources of hardening, and estimate how much hardening is dominated by each source. Hardening from pre-existing forest dislocations is not expected in samples A, U3, V3, W3, and X3, because Table V-2 indicates that the slip systems with highest Schmid factors due to the assumed thermal stress have the same slip direction as the primary slip direction of the most highly stressed slip systems during the tensile test; slip systems with the same slip direction interfere with each other very little. Only slight hardening at yield was observed for sample X3, which is consistent with the lack of pre-existing forest dislocations and being initially oriented for single slip for the uniaxial tension test. Moderately low hardening at yield was observed for sample W3, which is not consistent with the lack of pre-existing forest dislocations and expected easy glide; this interesting result will be explored more later in this section. In the cases of sample A, U3, and V3, the observed hardening immediately

following yield in Figure IV-1 may be attributed to the intersecting slip systems at yield. The very high hardening observed for sample U3 may be due in part to the dislocation reaction made possible by the intersecting $[\bar{1}11]$ and $[1\bar{1}1]$ slip directions; driven by a reduction in strain energy, the Burger's vectors of those dislocations may combine $[\bar{1}11]+[1\bar{1}1] = [001]$ to form dislocations that lie on (001) planes. These [001](001) dislocations cannot move, and so act as forest dislocations to the other active slip systems [69]. The moderate hardening at yield observed for sample A and sample V3 is thus representative of hardening dominated by intersecting slip systems with $[1\bar{1}1]$ and [111] slip directions for the Tokyo-Denkai set (sample A) and the Ningxia set (sample V3).

Hardening immediately following yield dominated by pre-existing forest dislocations is expected for samples C, F and T3, because Table V-2 indicates the pre-existing dislocations are forest dislocations, while the tensile axes of the samples were oriented for single slip. The high hardening observed for sample T3 may be due in part to pre-existing forest dislocations, though a more complete answer will emerge with further discussion in this section. Figure IV-1 shows that the hardening immediately after yield is different for each of those samples. This may be due to differing amounts of pre-existing forest dislocations in each sample, especially samples C and F, which should behave similarly to each other since their tensile axes are nearly identical. The local average misorientation data only implies differences in total geometrically necessary dislocation density among samples within each set, and does not directly differentiate between differently *oriented* pre-existing dislocations (forest or primary); however, the local average misorientation indirectly correlates with forest or primary pre-existing dislocations because the highest Schmid factor slip systems due to thermal stress are most likely to be the dominant source of pre-existing dislocations. Figure V-1 shows that the local average misorientation is

similar between samples C and F and implies the amount of pre-existing forest dislocations in each is similar, yet the hardening at yield in sample F is higher than sample C. That difference in hardening may be related to the variation in the local average misorientation, but it is inconclusive at this point (a more complete answer will emerge later in this section). Hardening may diminish as the forest dislocation barrier is broken down by the repeated intersection of the dislocations generated by the tensile stress (since no new forest dislocations form while the other dislocations are continuously formed during the tensile test); that may explain some of the diminishing initial hardening observed in Samples C, F, and T3. However, the breaking down of the barrier would occur concurrently with the changing crystal direction of the tensile axis as the sample rotated while deformation proceeded, and the resulting changes in favored slip systems dominate the later hardening behavior.

Hardening immediately following yield is expected from both pre-existing forest dislocations and intersecting slip systems due to the tensile axis orientation in Sample P3, and indeed, Figure IV-1 shows high hardening immediately following yield.

Up to this point, no differentiation has been made between slip systems with {110} or {112} slip planes, because the amount of impurities that were present to begin with or may have been introduced into the Tokyo-Denkai and Ningxia sample sets is large enough that slip on both {112} and {110} slip planes must be considered. Samples Q2, S3, and R2 all have tensile axes orientated for single slip: Table V-2 shows that samples Q2 and R2 possess equally highly stressed slip systems possessing {112} and {110} slip planes and the same <111> slip direction. For sample S3, the most highly stressed slip system is a <111>{110} slip system. Table V-2 shows that the probable pre-existing forest dislocations for samples Q2 and R2 are on {110} slip planes, while the likely pre-existing forest dislocations for sample S3 are on {112} slip planes.

Thus hardening immediately following yield is dominated by pre-existing forest dislocations, if present, since the {110) and {112} slip systems with the same slip direction in sample Q2 and R2 do not interfere with each other. Figure IV-1 shows that all these samples possess slight hardening immediately following yield, regardless of whether only {112} slip, only {110} slip, or both {112} and {110} slip are allowed. The slight hardening observed for all these samples suggests that the hardening from pre-existing forest dislocations is not significant in samples Q2, R2, and S3, though it may account for the slight rounding of the stress-strain curves observed at yield. If the hardening due to pre-existing forest dislocations were significant in these samples, significant hardening should have been observed in at least one of those samples, no matter which slip planes slip actually occurred on. Samples Q2 and R2 were taken from one grain of the ingot slice centimeters apart from each other, and sample S3 from another grain entirely. Also, all of the Ningxia samples were taken from locations some distance from the rim of the ingot slice, so the initial dislocation content may be lower. This suggests that even if pre-existing forest dislocations were present in these samples taken far from each other, the effect on hardening was not significant, and by extension suggests that hardening due to pre-existing dislocations in the whole Ningxia sample set may not be significant.

Because the Tokyo-Denkai samples came from the rim, where thermal contraction strains are likely to be higher, due to larger thermal gradients imposed by the chilled mold, it is more plausible that a significant portion of the observed hardening (in C, F), immediately after yield could be attributed to pre-existing forest dislocations. Since hardening from pre-existing forest dislocations is not significant in the Ningxia sample set, which may be due to the samples being extracted from the middle of the ingot, the hardening immediately following yield in sample T3 is the most unexpected, and it must come from intersecting slip systems other than pre-existing

dislocations, though how, considering that sample T3 was supposed to be oriented for easy glide?

The high initial work hardening of sample T3 is interesting because the initial orientation of the tensile axis highly favored a single {110} slip system above all the other slip systems, and easy glide would be expected if screw dislocations of the {110} core relaxation were numerous enough to make the {110} slip systems dominant. The absence of easy glide in sample T3 suggests that {110} slip was not dominant at the time of yield, though it does not rule out activity of {110} slip systems sometime after yield; this is consistent with the possibility of further hydrogen contamination during deformation, and the uncertain amount of impurities needed in niobium to change enough screw dislocation cores to the {110} slip relaxation and cause noticeable {110} slip. Figure IV-1 shows that the initial hardening slope of samples T3 and P3 are very similar, which suggests that the dislocation interaction mechanisms could be similar in these two samples. While the contribution of pre-existing forest dislocations to the initial hardening may not be significant, Table V-2 shows that both sample P3 and T3 had similar pre-existing forest dislocation conditions, so that even if the contribution really were significant it would be similar in both samples. The tensile axis of sample P3 was initially oriented to favor two {112} slip systems with different slip directions with similarly high resolved shear stresses that would favor slip system interference with each other. While a single {110} slip system was most favored in sample T3, the initial orientation of the tensile direction also favored two {112} slip systems having different slip directions that intersect, and therefore interfere with each other, to also have similar high initial resolved shear stresses. The similarity between samples P3 and T3, both in initial hardening slope and presence of high shear stresses on a pair of {112} slip

systems with intersecting slip directions, suggests that the initial hardening of sample T3 was predominantly caused by the two intersecting {112} slip systems interfering with each other.

Attributing a high initial hardening rate to intersecting {112} slip systems to all the Ningxia samples and not just sample T3 is supported by Table V-3, which shows that samples with larger differences between the initial resolved glide shear stresses acting on intersecting {112} slip systems have a lower initial hardening slope, while those samples with a small difference tend to have a high initial hardening slope. The numerical values of the initial hardening slope were found with a linear curve fit of the engineering stress-strain data points that comprised the initial hardening; only slopes with a fit of $R^2 > 0.9$ are shown numerically, while 'N/A' indicates that there were not enough data points to give a sufficiently accurate fit. Table V-3 also shows that if the ratio of the two highest intersecting {112} slip systems is taken (rather than simply taking the difference), then a ratio of ~1.1 or less correlates with the initial hardening being at least moderately low or greater; a ratio greater than ~1.1 correlates with little to no immediate hardening. This correlation occurs in both the Ningxia (beginning with sample W3) and Tokyo-Denkai (beginning with sample C) sample sets. That suggests that the pre-existing forest dislocations may not be the only source of hardening at yield in the Tokyo-Denkai sample set, since the intersecting {112} systems would contribute to the hardening as well if the intersecting {112} systems were operating at the same time. The difference in these initial resolved glide shear stresses on the intersecting {112} slip systems may be accounted for by the twinning/anti-twinning and non-glide shear stress effects, because those effects change the amount of resolved glide shear stress required for slip on those systems for that particular tensile direction. Table V-3 also shows the other slip system combinations that were checked but they are not able to correlate differences in initial resolved shear stress to the observed hardening behavior at yield.

Table V-3. Samples listed in order of decreasing difference between the two highest resolved glide shear stress {112} slip systems with intersecting slip directions, which correlates to increasing initial hardening rate.

Sample	Hardening slope immediately after yield (R^2>0.9)	Highest slip systems with intersecting slip directions	Initial resolved shear stress at yield of imitating slip systems (MPa): glide, non-glide 1, 2, 3	Difference in rgrss between two highest slip systems with intersecting slip directions		
				{112}	Either slip plane	{110}
Ningxia						
Q2	Slight N/A	$[1\bar{1}1](121)$	18.8 13.9 -5.1 10.0 A	4.0, 1.270	2.8	2.8
		$[111](1\bar{2}1)$	14.8 1.8 3.2 0.9 T			
		$[1\bar{1}1](011)$	18.9 5.2 4.9 5.1			
		$[111](0\bar{1}1)$	16.1 9.6 -0.9 4.1			
X3	Slight N/A	$[1\bar{1}1](121)$	17.0 9.9 -1.7 8.3 A	4.0, 1.308	4.0	3.2
		$[111](1\bar{2}1)$	13.0 4.6 1.0 2.0 T			
		$[1\bar{1}1](011)$	15.5 1.6 6.6 1.7			
		$[111](0\bar{1}1)$	12.3 10.2 -2.0 3.0			
R2	Slight N/A	$[1\bar{1}1](121)$	19.7 14.2 -4.7 9.8 A	3.6, 1.216	2.7	2.6
		$[111](1\bar{2}1)$	16.2 2.8 3.1 1.6 T			
		$[1\bar{1}1](011)$	19.6 5.0 5.2 4.7			
		$[111](0\bar{1}1)$	17.0 11.0 -1.6 4.7			
S3	Slight N/A	$[1\bar{1}1](121)$	17.3 13.6 -5.5 9.2 A	3.5, 1.254	2.3	2.3
		$[111](1\bar{2}1)$	13.8 0.7 3.5 0.4 T			
		$[1\bar{1}1](011)$	17.8 5.7 3.7 5.5			
		$[111](0\bar{1}1)$	15.5 8.4 -0.4 3.9			
W3	Moderate-low 2.7	$[1\bar{1}1](121)$	16.6 11.5 -3.0 7.0 A	1.5, 1.092	1.4	1.1
		$[111](1\bar{2}1)$	15.2 4.1 2.5 2.5 T			
		$[1\bar{1}1](011)$	16.3 3.7 4.1 3.0			
		$[111](0\bar{1}1)$	15.2 11.1 -2.5 5.0			
T3	High 7.0	$[1\bar{1}1](121)$	16.6 15.1 -8.8 10.6 A	1.3, 1.085	2.7	2.7
		$[111](\bar{1}\bar{1}2)$	15.3 11.8 -2.6 4.5 A			
		$[1\bar{1}1](011)$	18.3 7.9 1.8 8.8			
		$[111](0\bar{1}1)$	15.7 4.8 1.9 2.6			
U3	Very high 13.9	$[1\bar{1}1](121)$	17.5 11.4 -6.4 18.7 A	0.6, 1.036	0.6	0.5
		$[\bar{1}11](211)$	16.9 5.8 6.9 12.2 T			
		$[1\bar{1}1](011)$	16.7 3.0 12.3 6.4			
		$[\bar{1}11](101)$	16.2 13.1 -12.2 19.1			

Table V-3 (cont'd)

V3	Moderate 3.9	$[1\bar{1}1](121)$	17.2 12.9 -3.7 6.8 A	0.4, 1.024	0.3	0.3
		$[111](1\bar{2}1)$	16.8 3.9 3.5 2.7 T			
		$[1\bar{1}1](011)$	17.4 5.0 3.2 3.7			
		$[111](0\bar{1}1)$	17.1 11.9 -2.7 6.2			
P3	High 7.2	$[1\bar{1}1](\bar{1}12)$	17.1 5.9 3.2 5.8 T	0.1, 1.006	0.1	0.1
		$[111](\bar{1}\bar{1}2)$	17.0 11.5 -3.8 9.5 A			
		$[1\bar{1}1](011)$	16.4 13.3 -5.8 9.0			
		$[111](0\bar{1}1)$	16.4 3.5 5.7 3.8			
Tokyo-Denkai						
C	Moderate-Low 2.7	$[1\bar{1}1](121)$	28.2 20.4 -6.0 12.4 A	2.8, 1.106	2.1	2.0
		$[111](1\bar{2}1)$	25.5 5.8 4.9 3.6 T			
		$[1\bar{1}1](011)$	28.1 7.3 6.4 6.0			
		$[111](0\bar{1}1)$	26.1 18.0 -3.6 8.4			
F	Moderate 5.1	$[1\bar{1}1](121)$	28.5 19.5 -4.9 12.0 A	2.6, 1.100	2.6	1.9
		$[111](1\bar{2}1)$	25.9 7.1 4.1 4.4 T			
		$[1\bar{1}1](011)$	27.7 6.1 7.1 4.9			
		$[111](0\bar{1}1)$	25.8 19.1 -4.4 8.4			
A	Moderate 5.5	$[1\bar{1}1](\bar{1}12)$	32.4 13.0 4.3 13.7 T	0.2, 1.006	0.2	0.1
		$[111](\bar{1}\bar{1}2)$	32.2 19.8 -5.1 18.7 A			
		$[1\bar{1}1](011)$	30.0 26.2 -13.7 18.0			
		$[111](0\bar{1}1)$	30.1 4.3 13.6 5.1			

D. The critical resolved shear stress is complicated in BCC metals

The activity of a slip system in a BCC metal depends on non-glide shear stresses that affect both the {110} and {112} slip relaxations of screw dislocation cores, and the twinning/anti-twinning asymmetry of the {112} planes. The observations in the previous section suggest that the {112} slip relaxation is dominant, at least at yield, for the Ningxia sample set. However, the {112} slip relaxation has not yet been modeled and has simply been inferred to exist by previous studies in molybdenum [11, 47, 70]. The inference is based on combining the observations from both the kink height study and the atomistic calculations of the relaxed screw cores. The molybdenum kink height study observed that below a certain temperature the measured kink height matched that of {110} planes, and then above that temperature the kink heights matched {112} planes. The atomistic studies of a molybdenum screw core at 0 K indicated relaxation onto the three symmetric {110} planes that share a given <111> slip direction (in other words, the {110} planes of that <111> zone); there is some secondary relaxation onto the {112} planes of that slip direction. So the inference is: if at low temperatures the screw core relaxation on {110} planes results in {110} kink heights and thus {110} elementary slip, then the observation of {112} kink heights at higher temperatures implies that the screw core transforms in such a way that results in elementary slip on {112} planes at higher temperatures [11, 47, 70]. Whether the {112} slip relaxation would actually be spread predominantly onto the three symmetric {112} planes is unclear; if it did, the twinning/anti-twinning asymmetry would distort the screw dislocation core even without an external stress.

While a detailed description of the inferred {112} slip relaxation does not exist, some characteristics provide a basis for plausible speculation. A screw core relaxed on the three symmetric {112} planes that share a given slip direction would probably not be spread equally

on each of those planes, given the twinning/anti-twinning asymmetry intrinsic to the {112} planes; the relaxed core would not be symmetric even in an unstressed state. The non-glide shear stress planes would also be {112} planes, and so the non-glide shear stress would also be influenced by the twinning/anti-twinning effect. Given these complications, the critical resolved shear stress required to activate a {112} slip system may vary in non-trivial ways with the crystal orientation of the sample.

Furthermore, the term 'critical resolved shear stress' is closely associated with the Schmid law, and is a fixed value if the Schmid law holds, as is generally true in FCC metals. The Schmid law does not hold in BCC metals like niobium (see section II-G of the Literature Review), and so this thesis defines the critical resolved shear stress as the resolved glide shear stress necessary to cause dislocation slip, with the understanding that it is not a fixed value and depends on the crystallographic direction of the tensile axis because of the twinning/anti-twinning and non-glide shear stress effects. The criteria used for identifying possibly active slip systems for the Tokyo-Denkai samples in Tables IV-2 through IV-4, and for the Ningxia samples in Tables IV-3 through IV-, were not attempting to assert values for the critical resolved shear stress. The objective was to set an inclusive standard for slip systems to be considered possibly active, since this was an inference rather than a physical observation. Slip systems that corresponded to a visible trace were given the benefit of the doubt and included in those tables even if the final resolved glide shear stress was too low to meet the criteria, because the non-glide stresses can affect the amount of resolved glide shear stress needed for slip and should be available to future investigations.

Determining the critical resolved shear stress for BCC slip systems at room temperature is therefore complicated by the non-glide shear stresses that affect both the screw dislocation core

relaxations and the twinning/anti-twinning asymmetry of the {112} slip planes. These screw dislocation core relaxations result in elementary slip occurring preferentially on {110} or {112} slip planes, according to the sample purity. These collectively cause the critical resolved shear stress of a slip system or family of slip systems to depend on the direction of the tensile axis. The resolved glide shear stress required to activate a slip system after yield typically increases, due mostly to latent hardening and eventually with self hardening. However, the crystallographic direction that corresponds to the tensile axis changes throughout deformation, so the critical resolved shear stress for any given slip system also changes throughout deformation and the hardening effects further complicate prediction of the resolved glide shear stress required for beginning and maintaining slip activity on a slip system after yield.

Still, a critical resolved shear stress must exist for each slip system, if only as an outcome of aggregated complicated details, but it may be valid only for a particular tensile direction at some point in time. That is, the critical resolved shear stress for each BCC slip system is potentially unique, depending on how much the twinning/anti-twinning asymmetry and non-glide stresses cause variation in the critical resolved shear stress. For the {110} slip systems, only the non-glide stresses would affect any variation in critical resolved shear stress. While neither the Tokyo-Denkai nor Ningxia sample set contains enough samples for rigorous statistical analysis of the resolved stresses, the prior section suggests that preexisting forest dislocations in the Ningxia set do not provide a significant complication to initial hardening. The initial resolved stresses at yield of the highly stressed slip systems of the Ningxia sample set are investigated to enable at least qualitative comparison to physical evidence of slip system activity. Figure V-3 shows a stereographic projection section that shows the initial tensile direction of each sample in the Ningxia set. Each sample lists the following slip planes that share the $[1\bar{1}1]$ slip direction:

the twinning {112} slip plane (noted with a 'T'), the anti-twinning {112} slip plane (noted with a 'A'), and the {110} slip plane with highest resolved glide shear stresses. The slip system with the highest resolved glide shear stress that has a slip direction that intersects $[1\bar{1}1]$ and a {112} slip plane is also listed (noted with an 'I'; whether the system is twinning 'T' or anti-twinning 'A' is also noted). The initial values at yield from left to right are: the resolved glide shear stress, 1^{st} non-glide stress, and the sum of the 2^{nd} and 3^{rd} non-glide stresses (summation is consistent with [71]). Because the non-glide stress coefficients (correction factors) of the non-glide stresses are not known for niobium, the maximum values are shown and will be considered in a qualitative manner. The 1^{st} non-glide stress is a shear stress parallel to the slip direction though on the non-glide stress plane, and the 2^{nd} and 3^{rd} non-glide stresses are both shear stresses perpendicular to the slip direction; while the non-glide stresses cannot cause the screw dislocation to slip, they do distort the relaxed core and change the amount of glide shear stress needed to cause slip. The effective yield (Peierls) stress for a slip system is the glide shear stress plus the product of each non-glide stress and its respective correction factor. Thus a positive 1^{st} non-glide stress decreases the resolved glide shear stress needed for dislocations to slip on that slip system, while a negative value increases it. When the sum of the 2^{nd} and 3^{rd} non-glide stresses is positive the resolved glide shear stress needed for dislocations to slip on that slip system also decreases; if the sum of the 2^{nd} and 3^{rd} non-glide stresses is negative and is large enough, slip on one of the other two slip planes in the zone of the slip direction becomes favored [65, 66, 71]. For the slip systems with {112} planes, the resolved glide shear stress needed for slip decreases for the twinning plane, and increases for the anti-twinning plane. Figure V-3

shows that the 1st non-glide shear stress tends to be positive for the anti-twinning {112} slip system and would lower the glide shear stress needed for slip, while the anti-twinning nature of that same slip system would increase the glide shear stress needed for slip. Figure V-3 shows that for the twinning slip system with a $[1\bar{1}1]$ slip direction in all the samples (except sample P3), a negative though small 1st non-glide shear stress would increase the glide shear stress needed for slip, while the twinning nature of that same slip system would decrease the glide shear stress needed for slip. This exemplifies the complex interactions between the twinning/anti-twinning asymmetry and non-glide stress effects.

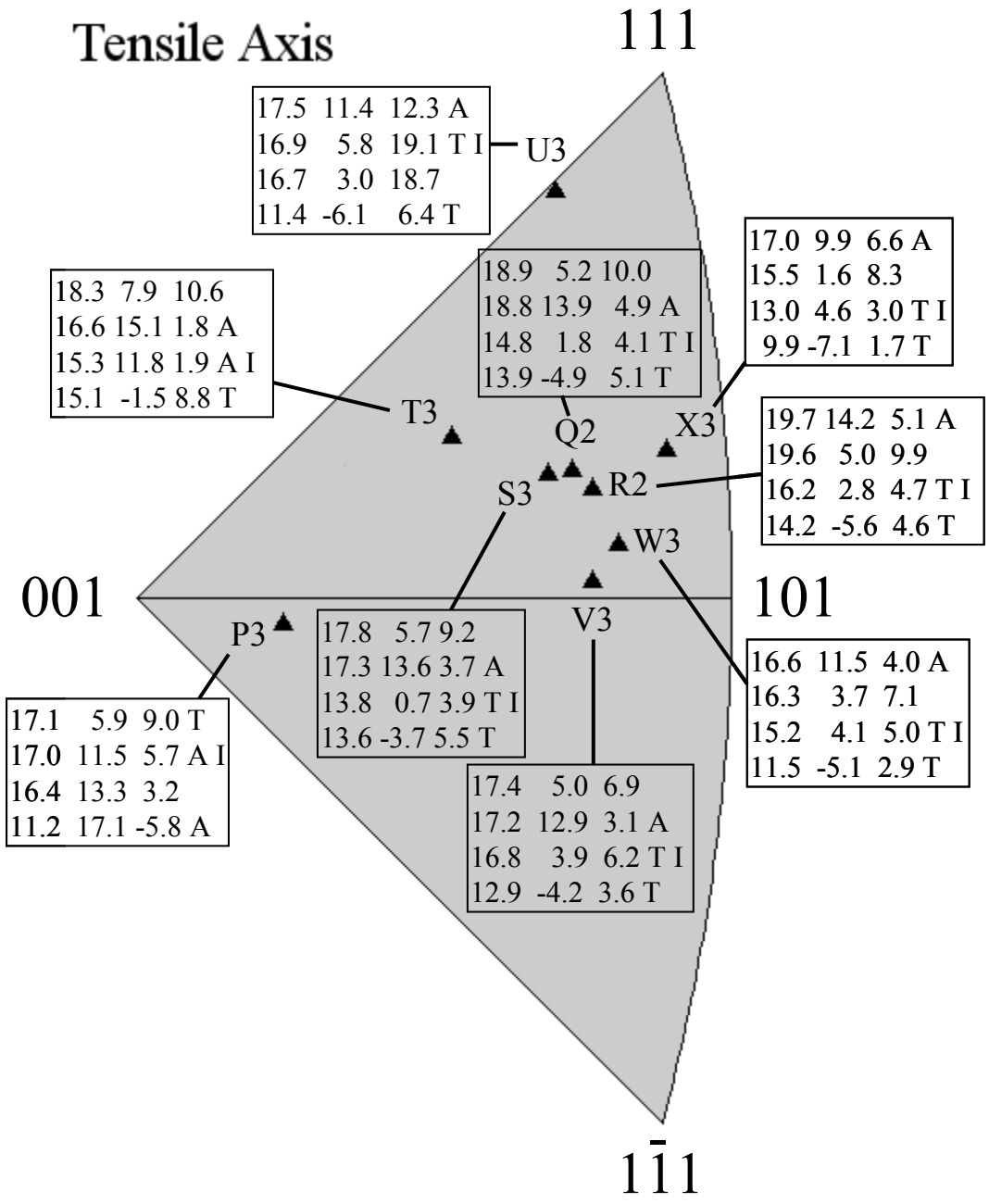

Figure V-3. This stereographic projection section figure shows the initial tensile direction of each Ningxia sample. Each sample lists the following slip planes that share the $[1\bar{1}1]$ slip direction: the twinning {112} slip plane 'T', the anti-twinning {112} slip plane 'A', and the {110} slip plane with highest resolved glide shear stress. The slip system with a slip direction that intersects $[1\bar{1}1]$, a {112} slip plane, and the next highest resolved glide shear stress is also listed (noted with an 'I', and whether the system is twinning 'T' or anti-twinning 'A'). The initial values at yield from left to right are: the resolved glide shear stress, 1st non-glide stress, and the sum of the 2nd and 3rd non-glide stresses.

Finding patterns in the initial resolved shear stresses at yield is complicated because yield may occur on either a twinning {112} slip system, anti-twinning {112} slip system, or {110} slip system, whose critical resolved shear stresses may all be different depending on the tensile direction. According to the literature, in a sufficiently pure niobium sample at room temperature, slip should occur on {112} planes only, and should require a lower resolved glide shear stress to yield on a twinning {112} slip system than an anti-twinning {112} slip system [31]. . Because the details of the inferred {112} slip relaxation are not known, it is unclear how large an effect the non-glide shear stresses have on {112} slip. The effect would have to be large enough to enable slip on the intersecting {112} slip systems at yield if the explanation for the hardening observed at yield discussed in the previous section (V-C) is accurate. The ratio of near 1.1 or below between the highest resolved glide shear stresses of intersecting slip systems with {112} slip planes that correlates to hardening at yield may be a rough indicator of the how much the combined twinning/anti-twinning and non-glide shear stress effects affect the value of the critical resolved shear stress. Easy glide does not necessarily require equal amounts of single slip on two systems with the same slip direction, though easy glide does exclude activity of slip systems that intersect the slip systems that are active (during easy glide). At this point in time, it is not possible to assess non-glide shear stresses because there is no model established yet for evaluating the non-Schmid effects required for activating glide in niobium (though a model for molybdenum has recently been published [71]). Since the extent to which the twinning/anti-twinning effect and non-glide shear stress effect interact and change the amount of resolved glide shear stress needed to cause dislocation slip (activate slip systems) in niobium is unclear, being dependent on three variables, quantifying the critical resolved shear stresses is simply too complex in the context of this thesis.

E. Rotation of the tensile axis

The rotation axis of a tensile sample is useful because it may be used to determine the slip direction of the slip system(s) that dominate the rotation, because the crystallographic direction of the tensile axis becomes closer to the dominant slip direction. However, the rotation does not directly identify slip planes. Assuming that the rotation occurs all at once about a single axis, the rotation axis of a tensile sample may be found by directly measuring both the crystal direction parallel to the tensile axis after the deformation and the crystal direction parallel to the tensile axis before deformation, and taking the cross product of the two. A sample rotating due to only one active slip direction (or one resultant slip direction) will have a *calculated* rotation axis that is the cross product of that slip direction and the crystal direction parallel to the tensile direction before deformation. If both the measured and calculated rotation axes are very similar, then rotation of the sample was dominated by the slip direction used to determine the calculated rotation axis. The assumptions that the rotation occurs all at once about a single rotation axis due to only one active slip direction means that this method is most accurate when comparing the undeformed orientation to a deformed orientation found while the sample deformed via easy glide, or at least the deformed orientation of a region within the sample that was rotated by only one active slip direction. However, the deformed orientations of the Tokyo-Denkai and Ningxia samples were taken after samples had already been deformed into at least early stage II as indicated by the stress-strain curves in Figure IV-1. That means that a second slip direction had become active, and that all samples had deformed via at least two rotation axes, one after the other. The measured rotation axes of the Tokyo-Denkai and Ningxia samples are actually an amalgamation of all the sequential rotations caused by all activated slip systems as deformation proceeded. However, if both the measured and calculated rotation axes are still similar despite

this difficulty, then rotation of the sample was still dominated by the slip direction used to determine the calculated rotation axis. That does not imply inactivity of other slip systems, only that they did not dominate rotation of the sample. Table V-4 summarizes this analysis for the Tokyo-Denkai sample set, and Table V-5 summarizes this analysis for the Ningxia sample set. The measured rotation axis and the rotation axis calculated based on the $[1\bar{1}1]$ slip directions differ by less than 5° for side C of welded sample FC, side A of sample AF, side C of sample FC, and samples Q2, R2, S3, T3, W3, X3, providing strong evidence that slip systems having $[1\bar{1}1]$ slip directions were active. The $[1\bar{1}1]$ slip direction is not dominant in the remaining Tokyo-Denkai and Ningxia samples evidenced by the 8° or larger differences between the measured and calculated rotation axes; that is expected in side A of sample CA, sample P3, U3, and V3, because those samples were oriented such that slip systems with intersecting <111> slip directions had similar resolved glide shear stresses. The large difference was unexpected for both side F of sample FC and side F of sample AF, because sample F had been thought to be oriented for easy glide; however, the intersecting {112} slip systems explanation given earlier accounts for both the moderate initial hardening observed at yield (see section V-C) and the large difference between the measured and calculated rotation axes.

Table V-4. Comparison of calculated and measured rotation axes found by assuming single slip and by direct measurement for the Tokyo-Denkai sample set. The estimated local strain at the recrystallization (Rx) front is also given.

Welded Sample	Slip direction that moved toward TD:	Calculated rotation axis if single slip:	Measured rotation axis	Difference between axes in degrees	Local Strain at Rx front
AF Side A	$[1\bar{1}1]$	$[\overline{75}\ \overline{66}\ 9]$	$[\overline{77}\ \overline{63}\ 10]$	2°	~60%
CA Side A	$[1\bar{1}1]$	$[\overline{75}\ \overline{66}\ 9]$	$[\overline{61}\ \overline{79}\ 7]$	11°	~7%
CA Side C	$[1\bar{1}1]$	$[\overline{79}\ \overline{20}\ 58]$	$[\overline{78}\ \overline{21}\ 58]$	1°	~21%
FC Side C	$[1\bar{1}1]$	$[\overline{79}\ \overline{20}\ 58]$	$[\overline{78}\ \overline{23}\ 58]$	1°	~40%
FC Side F	$[1\bar{1}1]$	$[\overline{78}\ \overline{17}\ 61]$	$[\overline{73}\ \overline{36}\ 58]$	11°	~33%
AF Side F	$[1\bar{1}1]$	$[\overline{79}\ \overline{20}\ 58]$	$[\overline{79}\ 18\ 59]$	20°	~27%

Table V-5. Comparison of calculated and measured rotation axes found by assuming single slip and by direct measurement for the Ningxia sample set.

Sample	Slip direction that moved toward TD:	Calculated rotation axis if single slip:	Measured rotation axis and degrees of rotation	Difference between calculated and measured axes
P3	$[111]$	$[78\ \overline{61}\ \overline{17}]$	$[58\ \overline{80}\ \overline{13}]$	16°
Q2	$[1\bar{1}1]$	$[\overline{79}\ \overline{22}\ 57]$	$[\overline{80}\ \overline{14}\ 57]$	5°
R2	$[1\bar{1}1]$	$[\overline{79}\ \overline{20}\ 59]$	$[\overline{76}\ \overline{28}\ 58]$	5°
S3	$[1\bar{1}1]$	$[\overline{80}\ \overline{26}\ 54]$	$[\overline{80}\ \overline{24}\ 54]$	1°
T3	$[1\bar{1}1]$	$[\overline{81}\ \overline{35}\ 46]$	$[\overline{81}\ \overline{36}\ 47]$	1°
U3	$[1\bar{1}1]$	$[\overline{77}\ \overline{14}\ 63]$	$[\overline{86}\ 36\ 36]$	33°
V3	$[1\bar{1}1]$	$[\overline{79}\ \overline{23}\ 56]$	$[\overline{76}\ \overline{37}\ 54]$	8°
W3	$[1\bar{1}1]$	$[\overline{78}\ \overline{18}\ 60]$	$[\overline{78}\ \overline{15}\ 60]$	1°
X3	$[1\bar{1}1]$	$[\overline{74}\ \overline{8}\ 66]$	$[\overline{75}\ \overline{5}\ 66]$	1°

The observed hardening at yield and the small 1° difference between the measured and calculated rotation axes do not seem consistent with each other for side C of sample FC, side C of sample CA, and sample T3. Examining the rotation of the tensile axes is helpful. Figure V-4 is a section of the stereographic projection, and shows the initial tensile axis before deformation (black symbols) and the final tensile axis after deformation (white symbols) of each of the Tokyo-Denkai (circles) and Ningxia samples (triangles). The initial and final tensile axis positions of each sample are connected by an arrow; however, the arrow does not mark the precise path of the rotation. The two intersecting <111> slip directions for side C of sample FC, side C of sample CA, and sample T3 are $[1\bar{1}1]$ and [111], and they must both be active at yield in order to explain the observed hardening at yield in those samples.

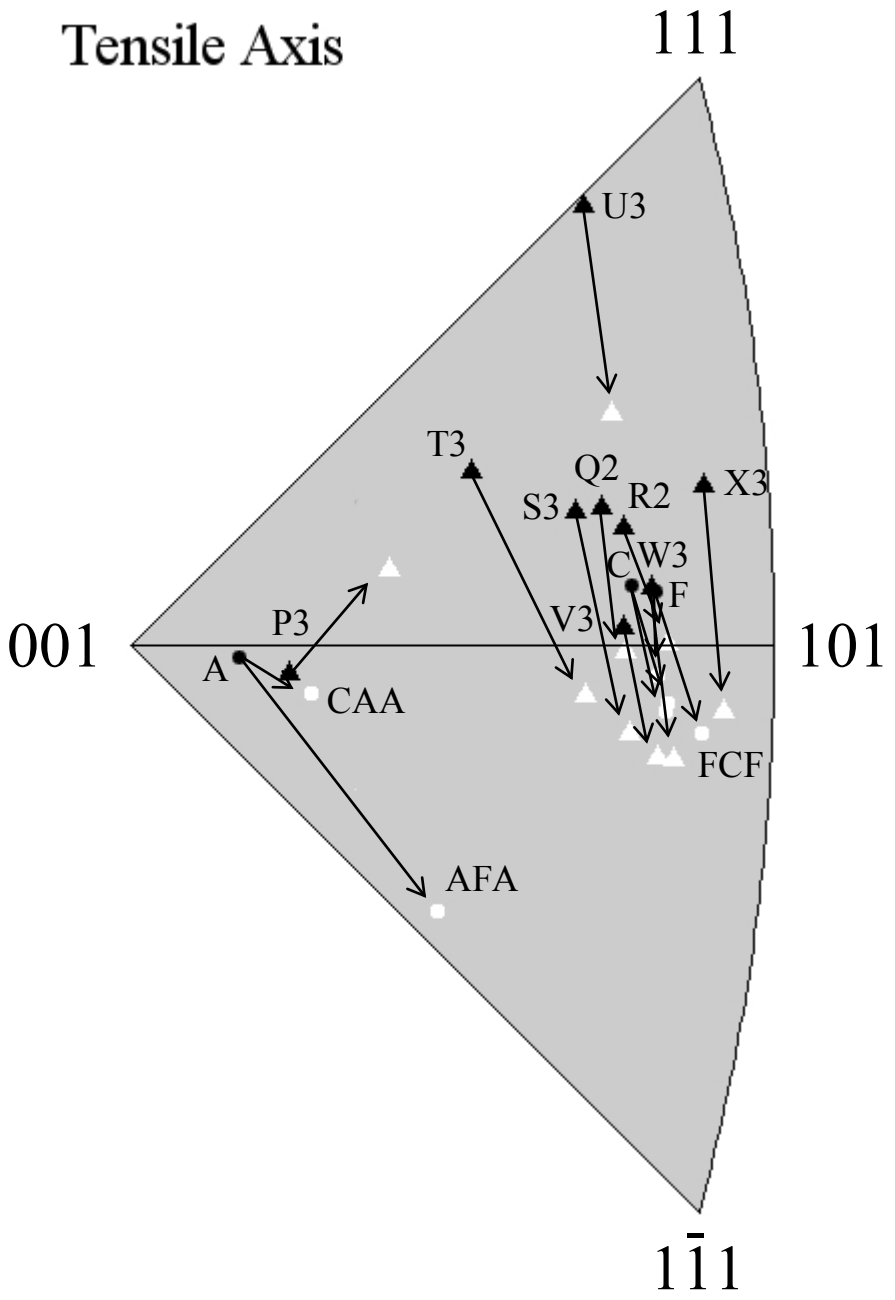

Figure V-4. A section of the stereographic projection of the initial tensile axis before deformation (black symbols) and the final tensile axis after deformation (white symbols) of each of the Tokyo-Denkai (circles) and Ningxia samples (triangles). The initial and final tensile axis positions of each sample are connected by an arrow; the arrow does not mark the precise path of the rotation.

When two or more slip systems with different slip directions are active at the same time, a resultant slip direction may be found by vector addition of each of the different active slip directions, though weighted by strain rate, so that the tensile axis rotates toward the resultant slip direction. If $[1\bar{1}1]$ and [111] were equally active, the resultant slip direction would be [101]; if $[1\bar{1}1]$ were more active than [111], then the resultant slip direction would shift away from [101] toward $[1\bar{1}1]$ accordingly. The small 1° difference between the measured and calculated rotation axes for side C of sample FC, side C of sample CA, and sample T3 indicates that $[1\bar{1}1]$ slip dominated the rotation, yet that does not exclude other rotations. The explanation of high initial hardening at yield of sample T3 by intersecting {112} slip systems with $[1\bar{1}1]$ and [111] slip directions would cause the tensile axis of T3 to rotate approximately toward [101], depending on the relative activities of those slip systems. Figure V-5 shows a section of the stereographic projection that plots the highest Schmid factors on {112} slip systems as a contour map (contours show Schmid factor x 1000) (reproduced and adapted from [72]). The red dashed lines represent boundaries between slip systems with intersecting slip directions, while the green dashed lines emphasize the lack of boundary where the slip system does not change. Note that while the Schmid factors between the adjacent slip systems are equal on the boundaries, the elliptical contours for each slip system do not actually end at a boundary as shown, rather the contours of each slip system are superimposed on each other. The combination of the twinning/anti-twinning and non-glide shear stress effects causes these boundaries to be less distinct in terms of whether a slip system is active or not, as those effects change the resolved glide stress needed to activate a {112} slip system, and may enable both systems to be active when the tensile axis is near the boundary. The initial tensile axis of sample T3 (Green triangle) results in the highest resolved glide stress on a {112} slip system on $[111](1\bar{2}1)$ (16.6 MPa),

and the highest resolved glide shear stress of an intersecting {112} slip system is actually on $[111](\bar{1}\bar{1}2)$ (15.3 MPa). While the glide shear stresses on those two intersecting systems are different, the difference is small. Figure V-3 from the previous section shows that the $[1\bar{1}1](121)$ system is anti-twinning though with a relatively large positive 1st non-glide stress (15.1 MPa), while the $[111](\bar{1}\bar{1}2)$ system is also anti-twinning though with a moderate 1st non-glide stress (11.3 MPa) that is lower than that of $[1\bar{1}1](121)$; the sum of the 2nd and 3rd non-glide stresses is nearly the same for both though is slightly higher for $[111](\bar{1}\bar{1}2)$ (1.9 MPa) than $[1\bar{1}1](121)$ (1.8 MPa). Assuming at least a small non-glide stress influence (small correction factor) for both slip systems, the two intersecting slip systems could both have been active at yield. Figure V-4 shows that the tensile axis of T3 did move to the right toward [101], consistent with simultaneous operation of $[1\bar{1}1]$ and [111] slip direction slip systems. Though the exact path of the tensile axis is unknown, the following scenario may be considered: Figure 5 shows that rotation of the tensile axis of sample T3 (green triangle) toward [101] would change the distribution of resolved shear stresses on all the slip systems of T3 until the activity of the $[1\bar{1}1](121)$ slip system was dominant. The tensile axis of T3 would then rotate down toward the $[1\bar{1}1]$ slip direction, and because so much more of the rotation occurs in that state, results in the small 1° difference between the measured and calculated rotation axes that indicate a $[1\bar{1}1]$ slip direction did indeed dominate the rotation of sample T3. The stress-strain curve of T3 in Figure IV-1 also supports that scenario, as the high initial hardening due to intersecting slip directions gives way to softening due to the change to single slip.

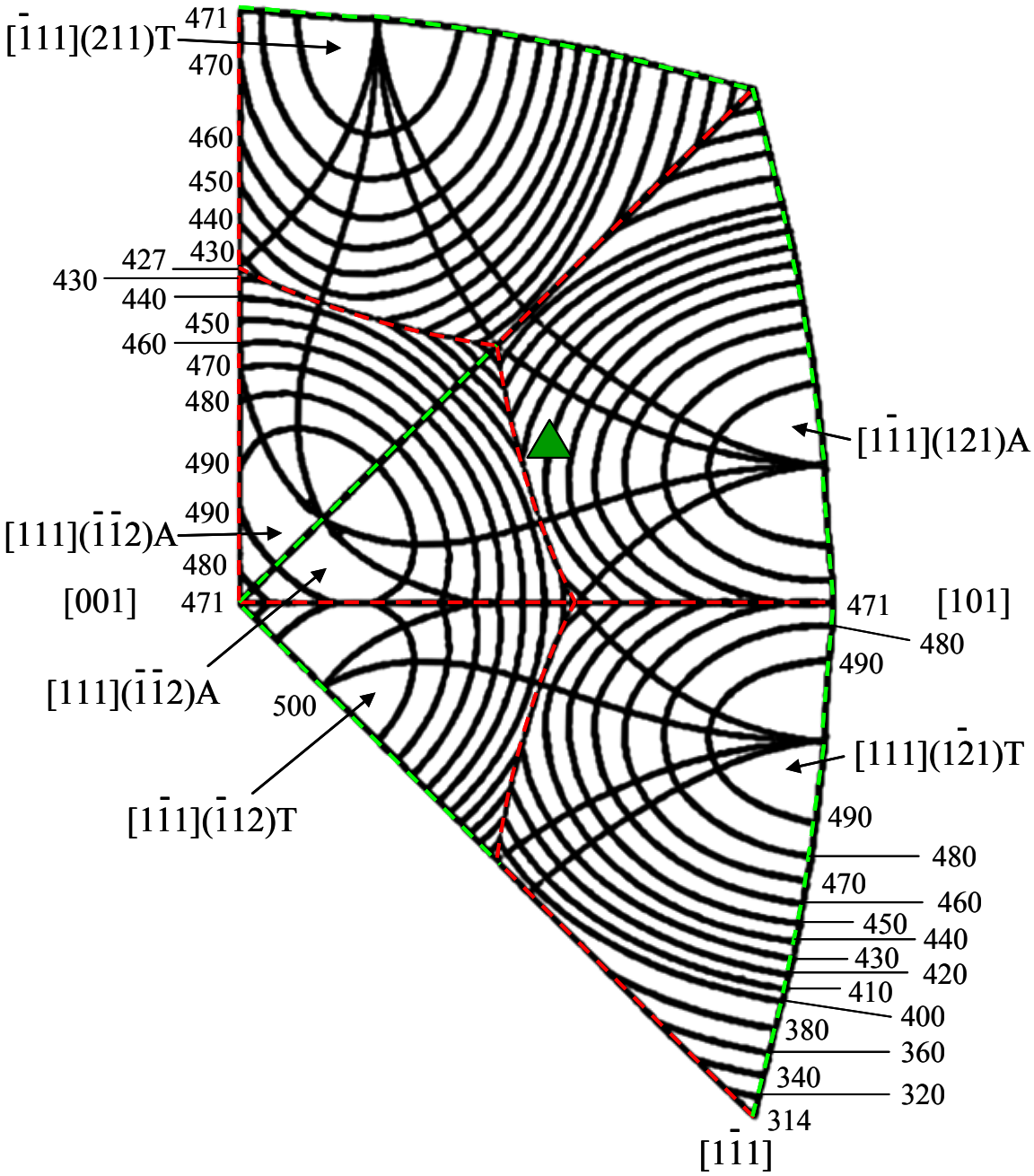

Figure V-5. A section of the stereographic projection plots the highest Schmid factors on {112} slip systems as a contour map. Schmid factors are given x1000, twinning (T), and anti-twinning (A). The red dashed lines represent boundaries between slip systems with intersecting slip directions, while the green dashed lines emphasize the lack of boundary where the slip system does not change. While the Schmid factors are equal on the boundaries, the twinning/anti-twinning and non-glide stress effects may enable both systems to be active near the boundary. The initial tensile axis of sample T3 (Green triangle) results in the highest resolved glide stress on a {112} slip system on$[1\bar{1}1](121)$, and the highest resolved glide shear stress of an intersecting {112} slip system is on the nearby$[111](\bar{1}\bar{1}2)$. Adapted from [72].

Sample C may be explained similarly to sample T3, except that the observed moderate-low initial hardening at yield never gives way to softening, suggesting that the intersecting slip directions might have been less equal in their activity and so less initial hardening at yield is observed; almost easy glide though not quite, though enough for $[1\bar{1}1]$ slip direction to dominate the rotation of the sample. That state may have persisted without transitioning to single slip, and as the tensile axis rotated, it gradually increased the resolved shear stresses and so increased the activity on the previously less active system and gradually increased the flow stress, which is consistent with the stress-strain curve of sample C seen in Figure IV-1.

Figure V-4 shows that, except sample P3, all of the tensile axes of the Tokyo-Denkai and Ningxia samples rotated toward $[1\bar{1}1]$, and while that slip direction did not necessarily dominate the rotation, that rotation does mean that a slip system with $[1\bar{1}1]$ slip direction was active in all those samples. The tensile axis of sample P3 rotates toward the [111] slip direction, and though Table V-5 indicates the [111] slip direction did not dominate the rotation, that rotation does mean a slip system with a [111] slip direction must have been active.

F. Complications to the slip trace analysis

The slip trace analysis is complicated due to the difficulties in matching visible traces to the calculated slip plane traces described in section III-L of Materials and Methods. The interstitial impurities initially present in both the Tokyo-Denkai and Ningxia sets of samples, and the possible absorption of additional hydrogen by the samples during preparation, further complicate identification of a visible trace because they may enable {110} slip and thus increase the number of calculated slip plane traces a visible slip trace matches. The theory explained in section II-F of the Literature Review asserts that in niobium of very high purity, the screw dislocations may cross slip easily and often among a set of 3 {112} planes having the same <111> slip direction,

according to the local stress state at any given time during deformation [11]. The maximum resolved shear stress (MRSS) plane is whichever crystal plane happens to be the most highly stressed crystal plane that is 90° to the most highly stressed slip direction at any given time; thus the MRSS will change as deformation rotates the crystal planes of crystal lattice of the sample and need not correspond to a crystallographic slip plane. A crystallographic slip plane is the MRSS plane if it fulfills the conditions to be the MRSS plane. The screw dislocations appear to move along the maximum resolved shear stress (MRSS) plane by alternately slipping on the crystallographic {112} slip planes via cross-slip, though over an unknown length scale between cross-slip events [11].

The consequence of frequent cross-slip is that a slip trace might be *imitated* by the slip traces of another pair of active slip systems. The possibility that a slip trace is actually being imitated by frequent cross-slip is unavoidable, as the screw dislocation could potentially cross slip with nm scale frequency in niobium [11]. For example, Figure V-6 shows how the slip trace may only *appear* to be along the MRSS plane (011) plane trace (solid line) when seen in an image of the sample surface, while actually consisting of many short slip traces of $(\bar{1}12)$ and (121) planes (dashed lines), alternating between the two planes via frequent cross-slip (at the open circles). The argument that elementary slip only took place on {112} slip planes could be made on the basis of prior experiments finding that elementary slip was on {112} planes for niobium at room temperature (though in a vacuum) [11]. This would require a sufficiently high resolved shear stresses on the slip systems containing the two {112} planes needed to imitate any observed {110} slip trace, and it assumes that slip on those two planes occurs in a homogeneous manner. On the other hand, if slip occurs on particular slip planes for a particular period of time, then the slip steps on the polished surface would reveal multiple slip plane traces if slip on multiple

planes occurred. Furthermore a burst of dislocations on a particular plane might exit the crystal surface over a finite distance related to the size of the burst (Bursts of dislocations rather than a smooth continuous movement are most commonly observed in in-situ movies of dislocation motion that is not controlled by dragging impurity atoms [73-76]). The heterogeneous dislocation entanglements observed in electron channeling contrast imaging (ECCI) images of as-received samples support the plausibility of bursts of dislocation activity at the micron scale [63, 77]. If imitation of an observed {110} slip trace were shown to not be plausible due to low resolved glide and/or non-glide stresses, this argument would be refuted.

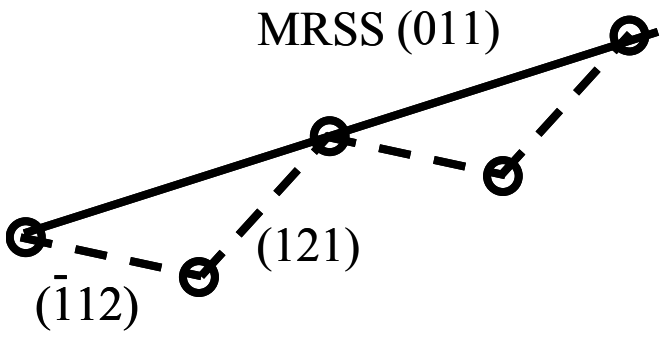

Figure V-6. Schematic of a slip trace along the MRSS plane, which appears to be a (011) slip trace (solid line), though is actually being imitated by the slip traces of a {112} slip relaxation screw dislocation (dashed lines) due to frequent cross slip (at the open circles). Imitation seems most plausible if the (121) and $(\bar{1}12)$ planes both possess reasonably high resolved shear stresses. If $(\bar{1}12)$ had a very low resolved glide shear stress or negative non-glide shear stresses, activity on $(\bar{1}12)$ would be less likely, and thus imitation less likely.

Based on the interstitial impurities already present and/or absorbed later during sample preparation, the assumption may be made that the Tokyo-Denkai and Ningxia samples were sufficiently contaminated with interstitial impurities before deformation to cause *all* elementary slip to be on {110} planes. The screw dislocations are still free to cross-slip among the {110} planes that share the same <111> slip direction, and may imitate {112} slip traces in a similar manner as described for {112} cross-slip that allowed imitation of {110} slip traces. Similarly, if imitation of an observed {112} slip trace were shown to not be plausible due to low resolved glide and/or non-glide stresses for the {110} slip systems required for the imitation, this argument would be refuted.

Finally, a mixed case argument assumes that the interstitial impurity content present in the samples was sufficient to interact with and change some screw dislocations to the {110} slip relaxation, while other screw dislocations retained {112} slip relaxations, which all together resulted in slip on both families of elementary slip planes. This explanation accommodates the interstitial impurities initially present and the possibility of further hydrogen contamination that would each cause {110} slip, and the practical consideration that real cavity forming operations do not and will not take place under high vacuum. With these three arguments in mind, {112} slip only, {110} slip only, or mixed {112} and {110} slip, the visible slip trace physical data are examined.

The results listed all the slip systems that could correspond to the observed visible traces for the Tokyo-Denkai samples (i.e. Table IV-2) and the Ningxia samples (i.e. Table IV-5), regardless of the final resolved glide shear stress on those slip systems. Tables V-6 and V-7 examine the Tokyo-Denkai and the Ningxia set more closely, to help determine which slip system(s) a visible trace may actually represent. The slip systems corresponding to a visible

trace are listed, then any other slip systems that corresponded to the same visible trace ('shared slip traces'), and finally the slip systems that could have imitated that visible trace. The slip systems given as 'shared slip traces' and those given as able to imitate the visible trace are limited to those slip systems meeting the minimum final resolved glide shear stress criteria that was used to assemble Table IV-2 and other similar tables for the Tokyo-Denkai and Ningxia samples; slip systems were omitted that did not meet the final resolved glide shear stress criteria. These limitations narrow the focus to slip systems that may have been significantly active. The Ningxia samples were examined for slip traces on both the normal and transverse surfaces, so in Table V-7, slip systems corresponding to visible traces observed on both the normal and transverse surface are marked by an asterisk, and those observed only on the Transverse surface are marked by a double asterisk. The slip systems for each sample are listed in descending order of initial resolved glide shear stress, though the value is not given here (see Tables IV-2 and IV-3 for values of the glide and non-glide stresses).

Table V-6. The slip systems with matching visible traces are listed for the Tokyo-Denkai sample set, with slip systems that correspond to the same visible trace, and slip systems that could imitate the visible trace and corresponding slip system.

Sample	Slip systems with matching slip trace	Shared slip traces on normal face	Imitation possible by combination of:
FC side C	$[1\bar{1}1](121)$	$[1\bar{1}1](110)$	$[1\bar{1}1](110)$, $[1\bar{1}1](011)$
	$[1\bar{1}1](110)$	$[1\bar{1}1](121)$	Unlikely
CA side C	$[1\bar{1}1](121)$	$[1\bar{1}1](110)$	$[1\bar{1}1](110)$, $[1\bar{1}1](011)$
	$[1\bar{1}1](110)$	$[1\bar{1}1](121)$	Unlikely
FC side F	$[1\bar{1}1](121)$	$[111](2\bar{1}\bar{1})$	$[1\bar{1}1](110)$, $[1\bar{1}1](011)$
	$[111](1\bar{2}1)$	$[1\bar{1}1](\bar{1}12)$	$[111](1\bar{1}0)$, $[111](0\bar{1}1)$
	$[1\bar{1}1](\bar{1}12)$	$[111](1\bar{2}1)$	Unlikely
	$[111](2\bar{1}\bar{1})$	$[1\bar{1}1](121)$	Unlikely
AF side F	$[1\bar{1}1](121)$	$[111](2\bar{1}\bar{1})$	$[1\bar{1}1](110)$, $[1\bar{1}1](011)$
AF side A	$[111](\bar{1}\bar{1}2)$		$[111](\bar{1}01)$, $[111](0\bar{1}1)$
	$[\bar{1}\bar{1}1](2\bar{1}1)$		$[\bar{1}\bar{1}1](1\bar{1}0)$, $[\bar{1}\bar{1}1](101)$
	$[111](1\bar{1}0)$	$[\bar{1}\bar{1}1](1\bar{1}0)$	Unlikely
	$[\bar{1}\bar{1}1](1\bar{1}0)$	$[111](1\bar{1}0)$	Unlikely
CA side A	$[1\bar{1}1](\bar{1}12)$		$[1\bar{1}1](\bar{1}01)$, $[1\bar{1}1](011)$
	$[\bar{1}\bar{1}1](101)$		$[\bar{1}\bar{1}1](2\bar{1}1)$, $[\bar{1}\bar{1}1](112)$
	$[\bar{1}11](101)$		$[\bar{1}11](1\bar{1}2)$, $[\bar{1}11](211)$
	$[\mathbf{\bar{1}\bar{1}1}](\mathbf{2\bar{1}1})$		Unlikely

Table V-7. The slip systems with matching visible traces are listed for the Ningxia sample set, with slip systems that correspond to the same visible trace, and slip systems that could imitate the visible trace and corresponding slip system. Slip systems corresponding to visible traces observed on both the normal and transverse surface are marked by an asterisk, and those observed only on the transverse surface are marked by a double asterisk.

Sample	Slip systems with matching slip trace	Shared slip traces on normal face	Shared slip traces on transverse face	Imitation possible by combination of:
P3	$[111](\bar{1}\bar{1}2)$	$[\bar{1}11](1\bar{1}2)$		$[111](\bar{1}01)$, $[111](0\bar{1}1)$
	$[111](0\bar{1}1)$**		$[\bar{1}11](0\bar{1}1)$	$[111](\bar{1}\bar{1}2)$, $[111](1\bar{2}1)$
	$[\bar{1}\bar{1}1](112)$	N/A		$[\bar{1}\bar{1}1](101)$, $[\bar{1}\bar{1}1](011)$
	$[\bar{1}11](1\bar{1}2)$	$[111](\bar{1}\bar{1}2)$		$[\bar{1}11](101)$, $[\bar{1}11](0\bar{1}1)$
	$[1\bar{1}1](\bar{1}01)$*	$[111](\bar{1}01)$	$[111](\bar{1}01)$	Unlikely
	$[111](\bar{1}01)$*	$[1\bar{1}1](\bar{1}01)$	$[1\bar{1}1](\bar{1}01)$	$[111](\bar{1}\bar{1}2)$, $[111](\bar{2}11)$
	$[\bar{1}11](0\bar{1}1)$**		$[111](0\bar{1}1)$	Unlikely
	$[\bar{1}\bar{1}1](2\bar{1}1)$*	N/A	$[\bar{1}11](211)$	Unlikely
	$[\bar{1}11](211)$**		$[\bar{1}\bar{1}1](2\bar{1}1)$	$[\bar{1}11](110)$, $[\bar{1}11](101)$
	$[111](1\bar{1}0)$**			$[111](1\bar{2}1)$, $[111](\bar{2}11)$
	$[1\bar{1}1](110)$**		$[\bar{1}11](110)$	Unlikely
	$[\bar{1}11](110)$**		$[1\bar{1}1](110)$	Unlikely
Q2	$[1\bar{1}1](011)$**		All on transverse	$[1\bar{1}1](\bar{1}12)$, $[1\bar{1}1](121)$
	$[1\bar{1}1](121)$**		All on transverse	$[1\bar{1}1](110)$, $[1\bar{1}1](011)$
	$[111](0\bar{1}1)$	$[\bar{1}11](0\bar{1}1)$		$[111](\bar{1}\bar{1}2)$, $[111](1\bar{2}1)$
	$[1\bar{1}1](\bar{1}12)$**		All on transverse	Unlikely
	$[1\bar{1}1](110)$*	$[\bar{1}11](110)$	All on transverse	Unlikely
	$[111](1\bar{1}0)$	$[\bar{1}\bar{1}1](1\bar{1}0)$		Unlikely

Table V-7 (cont'd)

R2	$[1\bar{1}1](121)$**		$[1\bar{1}1](011)$ $[1\bar{1}1](\bar{1}12)$	$[1\bar{1}1](110)$, $[1\bar{1}1](011)$
	$[1\bar{1}1](011)$*	$[111](1\bar{2}1)$	$[1\bar{1}1](121)$ $[1\bar{1}1](\bar{1}12)$	$[1\bar{1}1](\bar{1}12)$, $[1\bar{1}1](121)$
	$[111](1\bar{2}1)$	N/A		$[111](1\bar{1}0)$, $[111](0\bar{1}1)$
	$[\mathbf{1\bar{1}1}](\mathbf{110})$**		N/A	Unlikely
	$[1\bar{1}1](\bar{1}12)$*	N/A	$[1\bar{1}1](121)$ $[1\bar{1}1](011)$	Unlikely
	$[\mathbf{111}](\mathbf{\bar{1}\bar{1}2})$**		N/A	Unlikely
	$[\mathbf{111}](\mathbf{1\bar{1}0})$**		N/A	Unlikely
S3	$[1\bar{1}1](011)$**		$[1\bar{1}1](121)$ $[1\bar{1}1](\bar{1}12)$	$[1\bar{1}1](\bar{1}12)$, $[1\bar{1}1](121)$
	$[1\bar{1}1](121)$*	$[111](1\bar{1}0)$	N/A	$[1\bar{1}1](110)$, $[1\bar{1}1](011)$
	$[111](1\bar{2}1)$*	N/A	N/A	$[111](1\bar{1}0)$, $[111](0\bar{1}1)$
	$[\mathbf{1\bar{1}1}](\mathbf{\bar{1}12})$**		N/A	Unlikely
	$[111](1\bar{1}0)$	$[1\bar{1}1](121)$		Unlikely
T3	$[1\bar{1}1](011)$*	$[\bar{1}11](211)$	N/A	$[1\bar{1}1](\bar{1}12)$, $[1\bar{1}1](121)$
	$[1\bar{1}1](121)$**		$[\bar{1}\bar{1}1](112)$	$[1\bar{1}1](110)$, $[1\bar{1}1](011)$
	$[\bar{1}11](101)$**		N/A	$[\bar{1}11](1\bar{1}2)$, $[\bar{1}11](211)$
	$[111](1\bar{2}1)$**		$[\bar{1}\bar{1}1](2\bar{1}1)$	$[111](1\bar{1}0)$, $[111](0\bar{1}1)$
	$[\mathbf{\bar{1}11}](\mathbf{211})$*	$[1\bar{1}1](011)$	N/A	Unlikely
	$[\mathbf{1\bar{1}1}](\mathbf{110})$**		N/A	Unlikely
	$[\mathbf{\bar{1}\bar{1}1}](\mathbf{112})$*	N/A	$[1\bar{1}1](121)$	Unlikely
	$[\bar{1}\bar{1}1](101)$**		N/A	$[\bar{1}\bar{1}1](112)$, $[\bar{1}\bar{1}1](2\bar{1}1)$
	$[\mathbf{111}](\mathbf{1\bar{1}0})$**		N/A	Unlikely
	$[\bar{1}\bar{1}1](2\bar{1}1)$**		$[111](1\bar{2}1)$	Unlikely
U3	$[1\bar{1}1](121)$*	N/A	$[\bar{1}11](211)$	$[1\bar{1}1](110)$, $[1\bar{1}1](011)$
	$[\bar{1}11](211)$**		$[1\bar{1}1](121)$	$[\bar{1}11](110)$, $[\bar{1}11](101)$
	$[1\bar{1}1](011)$*	N/A	$[\bar{1}11](101)$	$[1\bar{1}1](\bar{1}12)$, $[1\bar{1}1](121)$
	$[\bar{1}11](101)$*	N/A	$[1\bar{1}1](011)$	$[\bar{1}11](1\bar{1}2)$, $[\bar{1}11](211)$
	$[1\bar{1}1](\bar{1}12)$	N/A		$[1\bar{1}1](\bar{1}01)$, $[1\bar{1}1](011)$

Table V-7 (cont'd)

V3	$[1\bar{1}1](121)$*	$[111](2\bar{1}\bar{1})$	N/A	$[1\bar{1}1](110)$, $[1\bar{1}1](011)$
	$[111](0\bar{1}1)$	N/A		$[111](\bar{1}\bar{1}2)$, $[111](1\bar{2}1)$
	$[111](1\bar{2}1)$**		N/A	$[111](1\bar{1}0)$, $[111](0\bar{1}1)$
	$[\mathbf{111}](\mathbf{\bar{1}\bar{1}2})$**		N/A	Unlikely
	$[111](2\bar{1}\bar{1})$	$[1\bar{1}1](121)$		Unlikely
	$[\mathbf{\bar{1}\bar{1}1}](\mathbf{2\bar{1}1})$**		N/A	Unlikely
W3	$[1\bar{1}1](121)$*	N/A	N/A	$[1\bar{1}1](110)$, $[1\bar{1}1](011)$
	$[111](0\bar{1}1)$**		N/A	$[111](\bar{1}\bar{1}2)$, $[111](1\bar{2}1)$
	$[111](\bar{1}\bar{1}2)$**		N/A	Unlikely
	$[\mathbf{\bar{1}11}](\mathbf{211})$	N/A		Unlikely
	$[111](2\bar{1}\bar{1})$	N/A		Unlikely
	$[\mathbf{\bar{1}\bar{1}1}](\mathbf{2\bar{1}1})$**		N/A	Unlikely
X3	$[1\bar{1}1](121)$*	N/A	N/A	$[1\bar{1}1](110)$, $[1\bar{1}1](011)$
	$[\mathbf{1\bar{1}1}](\mathbf{21\bar{1}})$*	N/A	N/A	Unlikely
	$[\mathbf{111}](\mathbf{2\bar{1}\bar{1}})$	N/A		Unlikely

For the Tokyo-Denkai sample set, Tables IV-2, 3, 4 show that except for side A of sample AF, a visible slip trace matched the {112} slip system with the highest initial resolved glide shear stress on all samples; even in the case of side A of sample AF a visible trace matched the second highest initial resolved glide shear stress on a {112} slip system, which was only 0.2 MPa less. Table V-6 indicates that in all cases those {112} slip systems may be imitated by {110} slip systems. This raises an important issue. The interplaner angle between the adjacent {110} and {112} planes that share a particular <111> slip direction are only 30° apart; this means that when a {112} slip system has the highest resolved glide shear stress, the resolved glide stresses on the adjacent {110} slip systems will also be high. Those adjacent {110} slip systems are the ones capable of imitating the {112} slip system between them, and so the highest stressed {112} slip system will always be at risk of imitation, presuming that the conditions allow/require {110} screw dislocation slip. The same is true if a {110} slip system has the highest resolved glide shear stress for the same reasons as the {112} slip system, except the {112} systems may imitate {110} systems.

It is interesting that the {110} slip system with the highest initial resolved glide shear stress is *not* directly observed as matching a visible slip trace in any of the Tokyo-Denkai samples, even though the slip trace images were taken after being deformed in air to 40% strain and that the final flow stress was much larger than the 0.2% offset yield stress. However, the {110} slip system with the highest initial resolved glide shear stress is listed as a possible imitator of the {112} slip system with the highest initial resolved glide shear stress, so it is possible that the magnification of the SEM images was still not great enough to reveal the frequent cross-slip on the {110} slip planes that could imitate the {112} slip traces. However, if dislocation slip was occurring as bursts [63, 73-77] , as suggested earlier, then the frequency of the cross-slip may

have been on the micrometer scale that the SEM images were taken at, rather than the nanometer scale that the SEM images could not resolve.

Table V-6 indicates that on side A of sample CA, a visible slip trace matched only the $[\bar{1}\bar{1}1](2\bar{1}1)$ slip system (highlighted in bold type); it was not shared and unlikely to be imitated. If genuine, this observation would confirm that {112} slip was occurring despite the initial impurities and deformation in air. The main difficulty with accepting this as a genuine slip trace is that Table IV-4 indicates that there are several other {112} slip systems that posses higher final resolved glide and non-glide stresses than $[\bar{1}\bar{1}1](2\bar{1}1)$ that were not observed.

For the Ningxia sample set in general, Tables IV-5, 7, 8 (and the table for the remaining Ningxia samples in the Appendix) show that a visible slip trace matched the slip system with the highest initial resolved glide shear stress whether the slip plane was {112} or {110}, and Table V-7 indicates that in all cases those slip systems may be imitated by slip systems of the other slip plane family (e.g. {112} could be imitated by {110} and vice versa). Table V-7 shows that samples R2, S3, T3, V3, W3, and X3 have visible slip traces that matched only a {112} or {110} slip system that was not shared and unlikely to be imitated (highlighted in bold type).

The Tokyo-Denkai and Ningxia sample sets contain visible traces matching only a {112} or {110} calculated slip trace that were observed for which imitation did not seem plausible on the basis of insufficient final resolved glide shear stress. This outcome can be supported even with the very inclusive final resolved shear stress criterion that assumed the twinning nature of a slip plane and/or positive non-glide stresses were capable of causing the resolved glide shear stress to be only half that of the highest initial resolved glide stresses at yield. Tables V-6 and V-7 suggest that both genuine {112} slip and genuine {110} slip (highlighted in bold type) occurred

at least sometime during deformation, though one cannot distinguish when, and that the mixed case argument best explains the results. The possible inclusion of relevant slip systems may be too broad, because many of the observed genuine {110} or {112} slip systems are shown to have lower resolved glide and non-glide stresses than other slip systems in Tables IV-2 and IV-3 for which there was no evidence of their operation. Considering all the physical evidence at once is needed to assess the appropriateness of the interpretation of the experimental data.

G. Slip systems that must be active in the Ningxia and Tokyo-Denkai sets

All of the physical evidence is considered at once to determine which slip systems would need to be active to account for the observations. Table V-8 summarizes the physical evidence for each of the Tokyo-Denkai and Ningxia samples by listing the slip systems that are consistent with the explanations based on the physical observations and inferred from the resolved shear stresses. All listed slip systems meet the minimum final resolved shear stress criteria (explained in section IV-C-1). Table V-8 lists the answers to a series of questions, whose answers indicate if activity of that slip system would be consistent with the observed physical evidence. Only slip systems with an answer of 'yes' in two of the first three columns are listed (i.e. slip systems with at least two pieces of physical evidence). In the first column: Does the slip system corresponded to a visible slip trace? In the second column: Is the slip direction of the slip system consistent with the observed overall rotation of the tensile axis seen in the <111> pole figure of the sample? Furthermore, does the slip direction of the slip system dominate the rotation? If the slip direction did dominate the rotation, activity of slip system(s) with a different slip direction is not excluded though must have been much less active compared to the dominant slip system(s). If the slip direction did not dominate the rotation, then activity of a slip system(s) with a different slip direction is probable. In the third column: Is the slip system required to be active in order to be

consistent with the initial hardening behavior immediately following yield, (suggesting that {112} slip systems were dominant at yield and {110} slip systems were not)? In the fourth column: Does the slip system correspond to a slip trace that is shared by or could be imitated by frequent cross-slip of the other slip plane family (ie. A slip system with a {112} slip plane shares the visible slip trace with a {110} slip system, and/or could be imitated by {110} slip systems). An answer of 'no' is very useful and confirms slip on that slip system and on that slip plane family[4]. More slip systems than those listed might have been active, though not active enough to noticeably affect the physical evidence. Also, the area examined for each sample is only representative, not exhaustive; the slip system may simply not have been active in the area examined.

[4] While an answer of 'yes' does admit that a slip trace cannot be attributed only to that slip system, it does not eliminate that slip system as a possible explanation because formation of a similar slip trace is not mutually exclusive. That is, the same visible slip trace could be formed by any of the slip systems that shared or could imitate the visible slip trace if they were each active at some time during deformation; this is an inherent problem due to only imaging the slip traces after deformation into Stage II.

Table V-8. The list of slip systems whose activity is consistent with the physical evidence.

Sample	Slip systems	Visible slip trace?	Slip direction consistent with overall rotation of tensile axis? / Slip direction dominates rotation?	Required if {112} slip systems dominate initial hardening?	Shared or imitated by other slip plane family?
Ningxia					
P3	$[1\bar{1}1](\bar{1}12)$	No	Yes/No	Yes	Yes
	$[111](\bar{1}\bar{1}2)$	Yes	Yes/No	Yes	Yes
	$[111](0\bar{1}1)$	Yes	Yes/No	No	Yes
	$[111](\bar{1}01)$	Yes	Yes/No	No	Yes
	$[111](1\bar{1}0)$	Yes	Yes/No	No	Yes
Q2	$[1\bar{1}1](011)$	Yes	Yes/Yes	No	Yes
	$[1\bar{1}1](121)$	Yes	Yes/Yes	Yes	Yes
	$[1\bar{1}1](\bar{1}12)$	Yes	Yes/Yes	No	Yes
	$[1\bar{1}1](110)$	Yes	Yes/Yes	No	No
R2	$[1\bar{1}1](121)$	Yes	Yes/Yes	Yes	Yes
	$[1\bar{1}1](011)$	Yes	Yes/Yes	No	Yes
	$[1\bar{1}1](110)$	Yes	Yes/Yes	No	No
	$[1\bar{1}1](\bar{1}12)$	Yes	Yes/Yes	No	No
S3	$[1\bar{1}1](011)$	Yes	Yes/Yes	No	Yes
	$[1\bar{1}1](121)$	Yes	Yes/Yes	Yes	Yes
	$[1\bar{1}1](\bar{1}12)$	Yes	Yes/Yes	No	No
T3	$[1\bar{1}1](011)$	Yes	Yes/Yes	No	Yes
	$[1\bar{1}1](121)$	Yes	Yes/Yes	Yes	Yes
	$[111](\bar{1}\bar{1}2)$	No	Yes/No	Yes	Yes
	$[1\bar{1}1](110)$	Yes	Yes/Yes	No	No

Table V-8 (cont'd)

U3	$[1\bar{1}1](121)$	Yes	Yes/No	Yes	Yes
	$[\bar{1}11](211)$	Yes	No/No	Yes	Yes
	$[1\bar{1}1](011)$	Yes	Yes/No	No	Yes
	$[1\bar{1}1](\bar{1}12)$	Yes	Yes/No	No	Yes
V3	$[1\bar{1}1](121)$	Yes	Yes/No	Yes	Yes
	$[111](1\bar{2}1)$	Yes	Yes/No	Yes	Yes
W3	$[1\bar{1}1](121)$	Yes	Yes/Yes	Yes	Yes
	$[111](1\bar{2}1)$	No	Yes/No	Yes	Yes
X3	$[1\bar{1}1](121)$	Yes	Yes/Yes	Yes	Yes
	$[1\bar{1}1](21\bar{1})$	Yes	Yes/Yes	No	No
Tokyo-Denkai					
AF side A	$[1\bar{1}1](\bar{1}12)$	No	Yes/Yes	Yes	Yes
	$[111](\bar{1}\bar{1}2)$	Yes	No/No	Yes	Yes
CA side A	$[1\bar{1}1](\bar{1}12)$	Yes	Yes/No	Yes	Yes
	$[111](\bar{1}\bar{1}2)$	No	Yes/No	Yes	Yes
CA side C	$[1\bar{1}1](121)$	Yes	Yes/Yes	Yes	Yes
	$[111](1\bar{2}1)$	No	Yes/No	Yes	Yes
	$[1\bar{1}1](110)$	Yes	Yes/Yes	No	Yes
FC side C	$[1\bar{1}1](121)$	Yes	Yes/Yes	Yes	Yes
	$[111](1\bar{2}1)$	No	Yes/No	Yes	Yes
	$[1\bar{1}1](110)$	Yes	Yes/Yes	No	Yes
FC side F	$[1\bar{1}1](121)$	Yes	Yes/Yes	Yes	Yes
	$[111](1\bar{2}1)$	Yes	Yes/No	Yes	Yes
	$[1\bar{1}1](\bar{1}12)$	Yes	Yes/Yes	No	No
AF side F	$[1\bar{1}1](121)$	Yes	Yes/Yes	Yes	Yes
	$[111](1\bar{2}1)$	No	Yes/No	Yes	Yes

Table V-8 shows that samples Q2, R2, S3, T3, and X3 have individual slip systems that match visible traces and are consistent with the physical evidence, confirming slip on both {112} and {110} slip planes to the best that these experiments are able to properly interpret the data. Slip systems that did not provide enough physical evidence to be confirmed as active may still be active, if their final resolved glide and non-glide stresses are similar or greater than those systems confirmed to be active.

H. The dislocation substructure of the Ningxia sample set

The dislocation substructure of the Ningxia sample set was investigated using EBSD to collect orientation data of the deformed samples. For each Ningxia sample, both a smaller 22 x 65 μm area with step size of 0.2 μm and a larger 112 x 327 μm area with a step size of 1 μm containing the smaller area were scanned. The smallest 0.2 μm step size was chosen based on the limit of EBSD spatial resolution in iron of 90 nm (under ideal conditions); while niobium is higher atomic weight than iron and the limit should be lower, 0.2 μm (200 nm) was chosen to be conservative (see section II-H). The Ningxia samples were not examined over larger length scales because cross-slip occurring on the nanometer scale results in the problem of slip trace imitation, though strain bursts may lead to micrometer scale cross-slip as discussed earlier; thus small areas were examined in the hopes of observing the slip traces of both the cross-slip planes rather than observing larger areas and causing a wavy trace to appear straight. The restriction to examining small areas does mean that deformation bands occurring at larger (hundreds of microns) scale would not have been observed in the Ningxia samples.

The EBSD data of each deformed Ningxia sample was used to examine the change in local crystal lattice rotation two different ways: first, the misorientation between the deformed orientation of each pixel and the initial undeformed orientation of the sample (a single average

orientation obtained from the sample before deformation) was found. This relative difference of deformed vs. undeformed orientation revealed the rotated lattice of deformation bands so that their size, spacing, and amount of rotation could be measured.

Second, the local average misorientation gives the average difference in orientation of each pixel with respect to its immediate neighbors (the local relative rotation of the lattice), which implies the presence of geometrically necessary dislocations. The geometrically necessary dislocations accommodate the crystal lattice rotations that have been imposed by the applied tensile strain. While the EBSD data is only of the sample surface, the implied geometrically necessary dislocations are assumed to extend as a sheet into the sample; this is reasonable because the dislocations have been emitted as loops from sources on slip planes, so that the concentric loops of dislocations form sheets. Also, these are referred to as geometrically necessary dislocation *boundaries*, because of the sheet-like arrangement and being forest dislocations (obstacles) to dislocations on intersecting slip systems.

These two representations of the EBSD data complement each other by showing the size and location of deformation bands (if present) in the deformed vs. undeformed orientation map, while the local average misorientation map shows the geometrically necessary dislocations that accommodate different rates of lattice rotation, including those found at the edges of deformation bands. In the case of heterogeneous slip via deformation bands, the edges of the band may be distinct and appear as a trace in the local average misorientation map because the change in orientation and rotation takes place over a short distance (large orientation gradient), or the edges of the band may be diffuse and not visible as a trace because the change in orientation and rotation takes place over a relatively large distance (small orientation gradient); in either case the

geometrically necessary dislocations accommodate the rotated lattice within a deformation band to the surrounding lattice.

Table IV-4 indicates that for Ningxia samples oriented for single slip no obvious deformation bands were observed using the relative difference in deformed to undeformed orientation (Q2, R2, S3, T3, W3, X3). The local average misorientation did reveal intersecting traces of ~1-3° rotated lattice that were typically spaced ~1-5 μm apart, with some up to ~22 μm apart. In some of the Ningxia samples oriented for single slip, these implied geometrically necessary dislocation boundaries tended to be aligned with plane traces belonging to slip systems that were the most-stressed initially or at the end of deformation, especially the $[1\bar{1}1](121)$ primary slip system (S3, W3, X3). This is consistent with the literature indicating that in the case of only one or two active slip systems, the geometrically necessary dislocation boundaries tend to be aligned with those active systems. The other single-slip oriented samples whose implied geometrically necessary dislocation boundaries were not aligned with particular slip plane traces, which suggests that no one slip system was dominant during deformation, tended to be those samples oriented so that the most-glide-stressed slip system was $[1\bar{1}1](011)$ (sample T3) or both $[1\bar{1}1](011)$ and $[1\bar{1}1](121)$ were equally most-glide-stressed (samples Q2, R2). That does not conflict with the observation that $[1\bar{1}1]$ was the dominant slip direction in those samples, since the various active systems could all have the $[1\bar{1}1]$ slip direction but different slip planes, such as (121), $(\bar{1}12)$, or (011).

Table IV-4 indicates that for Ningxia samples oriented near the [001]-[101] boundary, P3 has intersecting deformation bands ~8-54 μm wide, and sample V3 has intersecting deformation bands ~1-12 μm wide, when comparing deformed vs. undeformed orientation. The local average misorientation shows intersecting traces of ~1-3° rotated lattice that were spaced ~1-19 μm apart

in sample P3 and only spaced ~1-2 μm apart in sample V3. Ningxia sample U3, oriented near the [001]-[111] boundary, has intersecting deformation bands ~6-124 μm wide when comparing the deformed to undeformed orientation, and the local average misorientation shows intersecting traces of ~1-3° rotated lattice that were spaced ~1-124 μm apart.

The lack of deformation bands in most of the Ningxia samples may be due to the fact that 0.4 strain only deformed those samples to early Stage II. While the secondary slip system(s) have been activated, the amount of strain on the secondary systems may not yet be large enough to noticeably rotate regions of lattice and form deformation bands. The local average misorientation data is consistent with that explanation, since intersecting traces of rotated lattice due to geometrically necessary dislocations are observed; the primary and secondary dislocations are present, though had not interacted to the point that deformation bands formed. When deformation bands were observed for the Ningxia samples, the bands were ~10-124 μm wide, similar to the ~10-150 μm wide bands reported for the D&F sample set; the amount of lattice rotation of the band relative to the lattice surrounding the band for the D&F sample set was not measured. Perhaps the small representative area observed for each Ningxia sample simply missed the deformation bands that were present; however, the other 3 areas examined for each sample were taken 2-3 mm apart from each other across the center of the gage length do not contain deformation bands either (data not shown).

The relative change in local average misorientation in the Ningxia samples from before to after deformation implies a change in geometrically necessary dislocation content. Figure V-7 compares the number average local average misorientation obtained via an EBSD scan in the center of the gage length of each Ningxia sample before deformation, and the combined number average local average misorientation obtained via EBSD of at least five areas within 3mm of the

center of the gage length after deformation; all EBSD scans were of 112x327 μm areas using 1 μm step size on the normal surface. Averaging all five of the deformed scans makes the comparison less dependent on local details of dislocation substructure, and more like the aggregate behavior of dislocation substructure through the whole gage length that the stress-strain curve represents. The local average misorientation only implies the geometrically necessary dislocation population, though there will be many more statistically stored dislocations present, so that the averaged local average misorientation represents a low estimate of the total dislocation population of the areas observed. A low implied geometrically necessary dislocation population does not necessary correlate with low hardening or lower flow stress in the stress-strain curve, since the statistically stored dislocations also affect those behaviors.

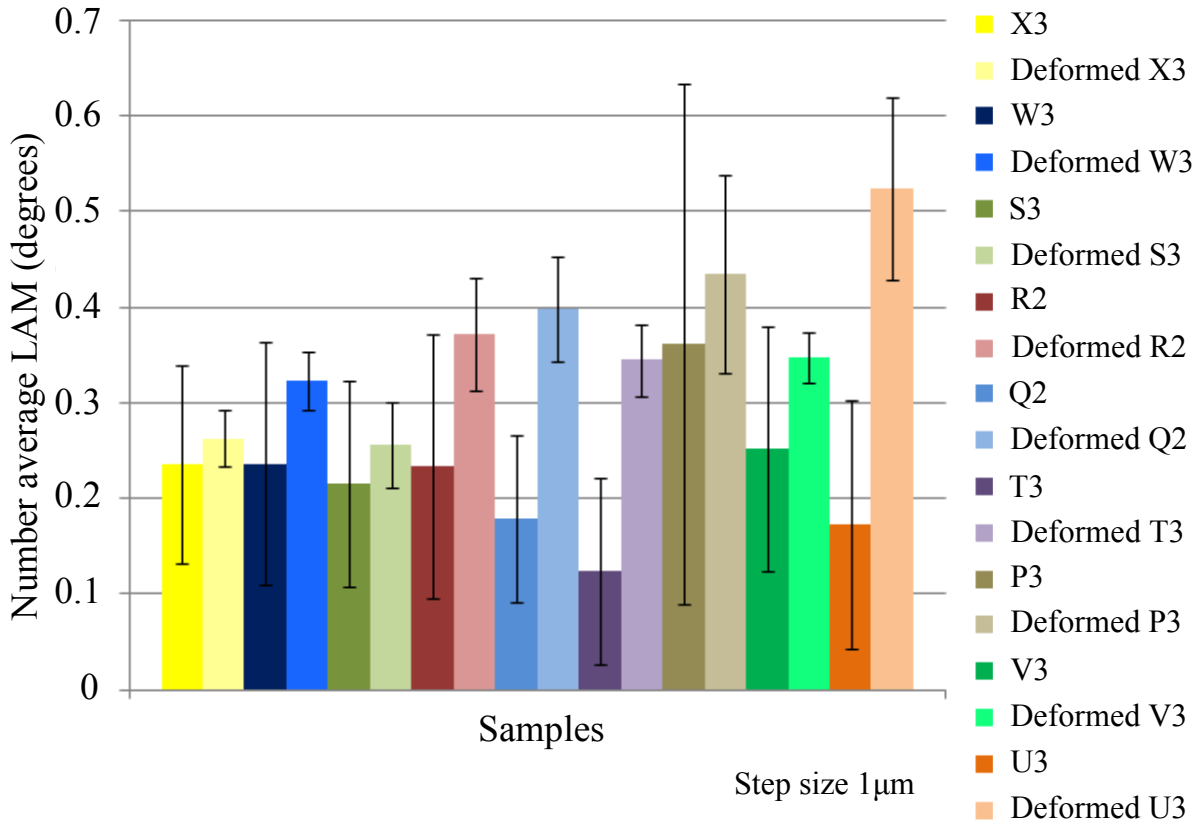

Figure V-7. The number average local average misorientation of each Ningxia sample is compared between the undeformed and deformed state. The undeformed value was obtained from a single EBSD scan in the center of the gage length, while the deformed value is the average of five separate EBSD scans within 3mm of the center of the deformed gage length. Local average misorientations were determined using 1st nearest neighbors.

The number average local average misorientation is thus an estimate of the amount of dislocations that would not be removed except by recrystallization. Dislocations may be detrimental to SRF cavity performance, and while the orientation of the dislocation line may determine if the performance is degraded, it is useful to know that not all crystal orientations beneficial for forming will retain the same number (or line directions) of dislocations that cannot be removed except by recrystallization. A larger population of geometrically necessary dislocations also represents greater defect energy, and therefore a greater tendency to recrystallize, since the reduction of defect energy is a driving force for recrystallization.

Figure V-7 shows that the implied amount of geometrically necessary dislocations for most of the samples initially oriented for easy glide (X3, W3, S3, R2) are essentially the same, because the variation in local average misorientation is not greater than the standard deviation between the undeformed and deformed state (not statistically significant). The other samples initially oriented for easy glide (Q2, T3) do have a statistically significant greater implied amount of geometrically necessary dislocations after deformation. Two of the samples initially oriented with two highly-stressed intersecting slip systems (P3, V3) do not show a statistically significant increase in implied amount of geometrically necessary dislocations after deformation, though the average does become higher. Given that the pre-existing dislocations have been argued to not significantly affect the deformation, a possible explanation is that the pre-existing dislocation population has been broken down and replaced by the dislocations activated by the uniaxial tension test. Sample U3 was initially oriented with two most-stressed intersecting slip systems and does show a statistically significant increase in implied amount of geometrically necessary dislocations after deformation, with the average becoming much higher. The intersecting slip systems in sample U3 were of the $[\bar{1}11]$ and $[1\bar{1}1]$ slip direction, whose

interaction can form immobile [001](001) dislocations, which may account for the particularly high amount of implied geometrically necessary dislocations after deformation.

While the uniaxial tension test is not the stress state for SRF cavity forming operations, it does highlight that some crystal orientations may develop fewer possibly detrimental dislocations while still being conducive to a particular forming process. For more information on strategic choice of crystal orientations and SRF cavity forming, the reader is referred to [78]. Less geometrically necessary dislocations after forming may also prevent recrystallization along welds, if the population is low enough and statistically stored dislocations have been eliminated using heat treatments.

I. Comparison of the Ningxia set with earlier high purity niobium tensile tests (Duesbery and Foxall's set)

The Ningxia sample sets and earlier high purity niobium tensile tests may be compared as the experiments were fairly similar to each other (the subset of samples from the earlier tests is referred to as the D&F sample set, named for the authors) [10, 24]. The Ningxia and D&F sample sets were deformed in tension at room temperature (295 K) in air, and at a quasi-static strain rates of $\sim 10^{-3}\ s^{-1}$ (Ningxia set) and $\sim 10^{-4}\ s^{-1}$ (D&F set). An important difference was already shown in Table V-1, which indicated that the niobium used in the D&F set had less interstitial hydrogen than the Ningxia sample set. However, Table V-1 also indicates that the D&F sample set contained at least three times the total interstitial impurities than the set [11] used to assert elementary {112} slip; given that the amount of interstitial impurities needed to cause significant amounts of {110} slip relaxation in niobium is unclear, the possibility of {110} slip must be considered in the D&F sample set and Ningxia sample set. Pre-existing dislocations

should be minimal and not significantly affect deformation in the D&F sample set because all the samples were annealed for 12 hours at >95% the melting temperature in vacuum for purification.

The D&F data provided the tensile axis of each sample in a standard triangle, from which the angles needed to rotate the tensile axis to that position were extracted using a Wulff net. The rotations correspond to the Euler angle representation of the sample's crystal orientation; the Euler angles were then used to calculate the Schmid factors and non-glide factors in the same way as for the Tokyo-Denkai and Ningxia sample sets (see section III-M). The D&F data also provided the resolved glide shear stress of the apparent primary slip system. Since the Schmid factor for the apparent primary slip system had been calculated using the Euler angles, the yield stress was found; the yield stress was then used to calculate the resolved glide and non-glide stresses of the D&F sample set so that they could be compared to the current data.

All of the D&F samples were oriented such that the highest resolved glide shear stress was resolved onto a slip system with a $[1\bar{1}1]$ slip direction; all of the tensile axes of the D&F samples rotated toward the $[1\bar{1}1]$ crystal direction, confirming activity of slip systems with $[1\bar{1}1]$ slip directions (data not shown, see [24]). Figure V-8 presents the initial tensile axis orientations at yield along with the initial resolved glide and non-glide stresses for the D&F set in the same way that Figure V-3 does for the Ningxia set. Figure V-8 shows that the highest resolved glide shear stress was resolved on the following slip systems according to the crystal direction of the tensile axis (first line listed for each sample): $[1\bar{1}1](\bar{1}12)$ for samples near [001], $[1\bar{1}1](011)$ near the center, and $[1\bar{1}1](121)$ near the [101]-[111] boundary. D&F observed that the initial resolved glide shear stresses at yield on those highest stressed slip systems tend to be larger toward the boundaries of the standard triangle. The lower initial resolved glide shear stresses at yield shown

in Figure V-8 for the D&F set as compared to those shown in Figure V-3 for the Ningxia set are consistent with the higher overall purity of the D&F set.

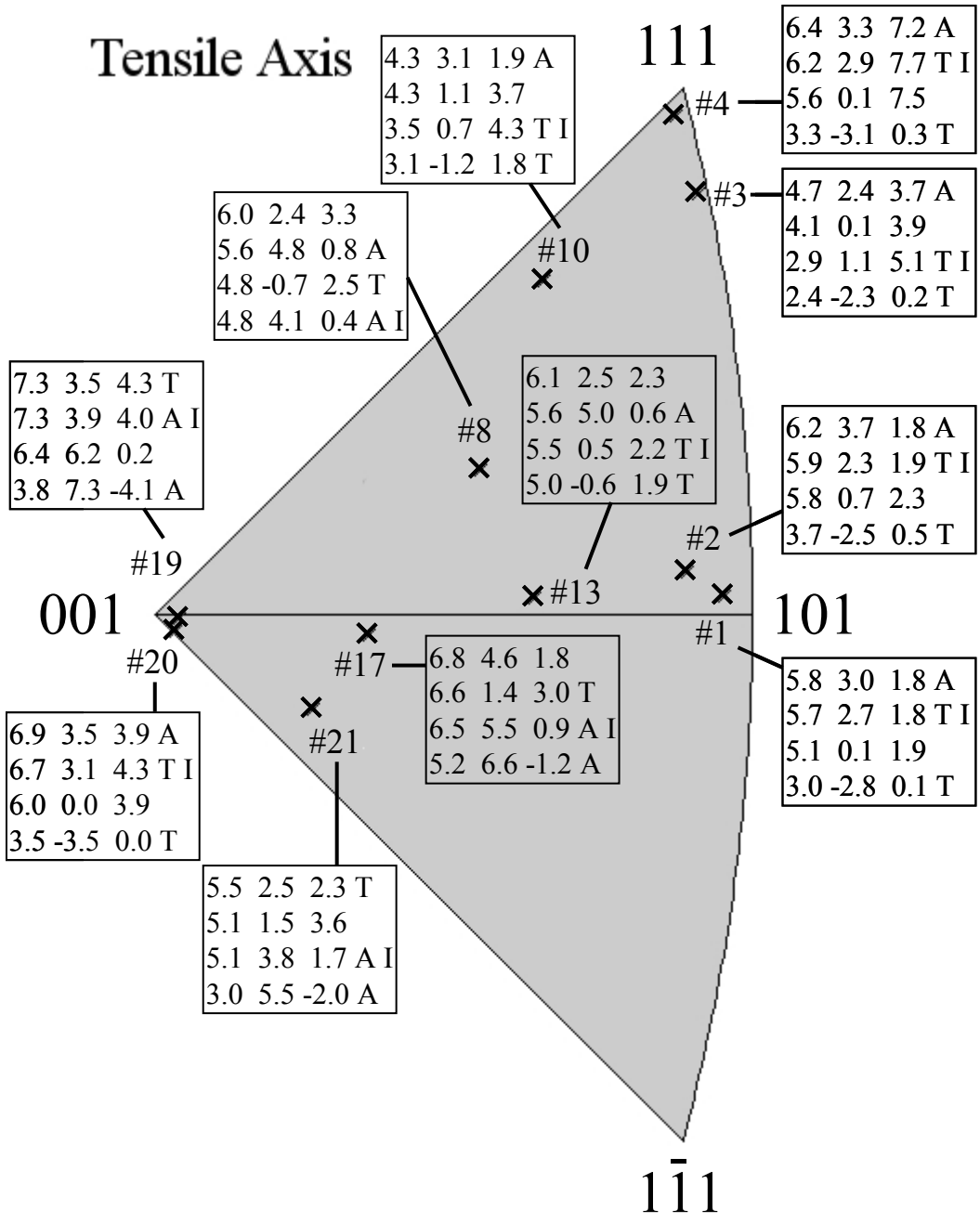

Figure V-8. This stereographic projection section shows the initial tensile direction of each D&F sample. Each sample lists the following slip planes that share the $[1\bar{1}1]$ slip direction: the twinning {112} slip plane 'T', the anti-twinning {112} slip plane 'A', and the {110} slip plane with highest resolved glide shear stress. The slip system with a slip direction that intersects $[1\bar{1}1]$, a {112} slip plane, and the next highest resolved glide shear stress is also listed (noted with an 'I', and whether the system is twinning 'T' or anti-twinning 'A'). The initial values at yield from left to right are: the resolved glide shear stress, 1st non-glide stress, and the sum of the 2nd and 3rd non-glide stresses.

Interpreting the D&F sample set shear strain curves, reported slip traces, and comparing the behavior to the Ningxia sample set is aided by another figure. Figure V-9 is a stereographic projection that shows the initial tensile axes for both the D&F and Ningxia sample sets, with colored boundaries overlaid. The slip system whose Schmid factors are greatest in the area between boundaries are labeled. The boundaries mark where the Schmid factors of all the different <111>{110} and <111>{112} slip systems are equal in this section of the stereographic projection. Those boundaries were found by overlaying the <111>{112} slip system Schmid factor contour map from Figure V-5 and a similar contour map for the <111>{110} slip system Schmid factor contour map; all contour maps originally from [72]. The line style denotes equal Schmid factor: between two different {110} slip systems with solid lines, between two different {112} slip systems with dashed lines, and between {110} and {112} slip systems with dotted lines. The boundary is green if the slip direction is the same for the two slip systems being compared, and red if the slip directions intersect.

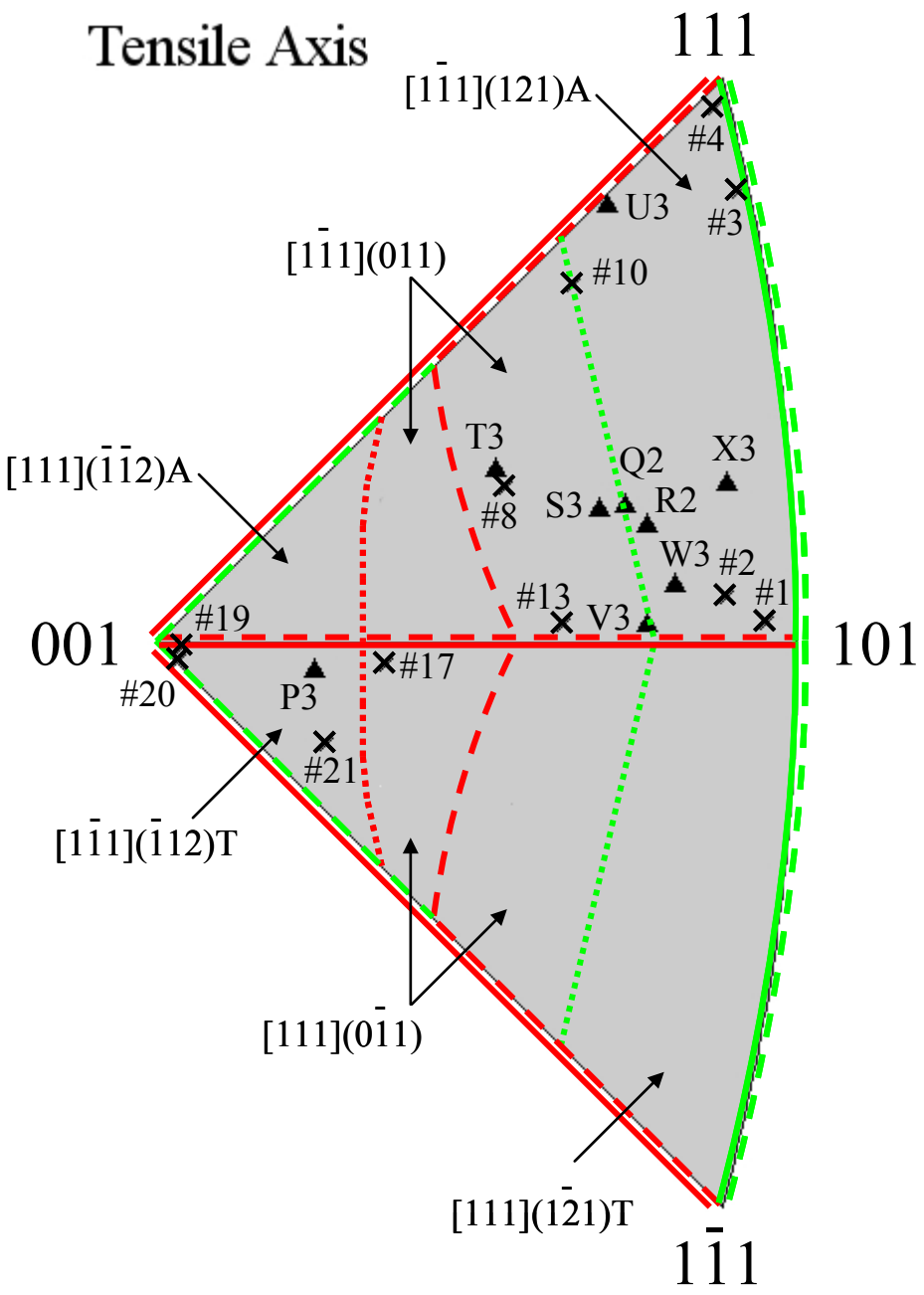

Figure V-9. This stereographic projection section shows the initial tensile axes for the D&F and Ningxia sample sets. The slip system whose Schmid factors are greatest in the area between boundaries are labeled. The boundaries mark where the Schmid factors of all the different slip systems are equal between two different: {110} slip systems (solid lines), {112} slip systems (dashed lines), {110} and {112} slip systems (dotted lines). The boundary between the slip systems is colored: same slip directions (green), intersecting slip directions (red).

In the interest of providing simple examples of how Figure V-9 is helpful in predicting initial sample behavior based on the orientation of the initial tensile axis, consider an unrealistic scenario. Supposing that the twinning/anti-twinning and non-glide shear stress effects may be ignored, then slip on both {110} and {112} planes is possible and requires the same amount of resolved shear stress, so that only the highest Schmid factor determines if the slip system is active or not. In that entirely unrealistic case, the boundaries are not only where Schmid factors between different slip systems are equal, the boundaries also sharply define the regions in which slip systems are active. Hardening at yield would be expected if a sample had an initial tensile axis directly on a red boundary, since the Schmid factor and therefore the resolved glide shear stress for intersecting <111> slip vectors would be equal. Alternatively, easy glide would be expected at yield if a sample had an initial tensile axis directly on a green boundary, since even with both slip system active at the same time, they do not significantly interfere with each other since the slip direction is the same.

Next, consider Figure V-9 more realistically: the twinning/anti-twinning and non-glide shear stress effects will cause variations in the resolved glide shear stress needed to activate slip on a slip system, whether slip on {110} and/or {112} planes occurs is thought to be dependent on temperature and purity, so that having the highest Schmid factor (and thus highest resolved glide shear stress) is only one variable that determines if the slip system will be active or not. Because the resolved glide shear stress needed to activate slip on a slip system varies to some extent, the boundaries do not sharply define which slip systems may be active. The location of the tensile axis where the activation threshold for two slip systems are 'balanced' is shifted to somewhere 'near' the boundary; the less influential the twinning/anti-twinning and/or non-glide shear stress effects are, the nearer the 'balanced' location would be to the boundary and vice versa (some of

the boundaries may not exist if slip on that family of slip planes is not possible for the experimental conditions being evaluated, e.g. purity, temperature).

According to Figure V-9, the Ningxia and D&F samples that have similar tensile axes should deform via similar slip systems. Table V-9 summarizes the behavior of the D&F samples to compare the reported primary slip plane traces observed at yield and secondary slip plane traces observed at the start of stage II from Figure II-4 and Figure II-5, and the observed easy glide or hardening at yield from Figure II-6 and Figure II-7. The visible slip traces are described as inhomogeneous by D&F whenever the visible slip traces belong to different slip systems operating in different regions, for samples oriented such that more than two intersecting slip direction slip systems are most-stressed; that condition occurs for samples near the corners of the reference triangle, near [001] for samples #19 and #20, and near [111] for sample #4. Table V-9 indicates that the D&F set shows the same trend as the Ningxia set, where decreasing difference (and ratio tending toward 1) in the resolved glide shear stresses (RGSS) of the intersecting most-stressed {112} slip systems at yield drops below a threshold that correlates with increased hardening at yield (the same trend is present in the D&F set if either the intersecting most-stressed {110} slip systems or the two most glide stressed systems are compared, though not shown in the table).

Table V-9. Summary of observed behavior in the D&F sample set.

Sample	Hardening slope at yield	Difference and ratio of RGSS between two highest {112} with intersecting slip directions	Visible slip trace at yield and as Stage I proceeds	Visible slip traces if Stage I absent	Visible slip traces at start of Stage II
#3	Slight	1.7 1.621	$[1\bar{1}1](121)$ Long, straight, diffuse to tight, wavy mesh	N/A	$[1\bar{1}1](121)$ $[111](1\bar{2}1)$ Bands
#8	Slight	0.8 1.229	$[1\bar{1}1](011)$ Long, straight, diffuse to tight, wavy mesh	N/A	$[1\bar{1}1](011)$ $[111](1\bar{2}1)$ Bands
#10	Slight	0.8 1.167	$[1\bar{1}1](011)$ Long, straight, diffuse to tight, wavy mesh	N/A	$[1\bar{1}1](011)$ $[111](1\bar{2}1)$ Bands
#21	Slight	0.4 1.078	$[1\bar{1}1](\bar{1}12)$ Long, straight, diffuse to tight, wavy mesh	N/A	$[1\bar{1}1](\bar{1}12)$ $[111](\bar{1}01)$ Bands
#2	Moderate	0.3 1.051	N/A	$[1\bar{1}1](121)$ $[111](1\bar{2}1)$ Interpenetrant	$[1\bar{1}1](121)$ $[111](1\bar{2}1)$ Interpenetrant
#4	High	0.2 1.032	N/A	Inhomogeneous	Inhomogeneous
#20	Moderate	0.2 1.030	N/A	Inhomogeneous	Inhomogeneous
#1	High	0.1 1.018	N/A	$[1\bar{1}1](121)$ $[111](1\bar{2}1)$ Interpenetrant	$[1\bar{1}1](121)$ $[111](1\bar{2}1)$ Interpenetrant
#13	Moderate	0.1 1.018	N/A	$[1\bar{1}1](011)$ $[111](0\bar{1}1)$ Interpenetrant	$[1\bar{1}1](011)$ $[111](0\bar{1}1)$ Interpenetrant
#19	Very high	0.1 1.015	N/A	Inhomogeneous	Inhomogeneous
#17	Moderate	0.1 1.000	N/A	$[1\bar{1}1](\bar{1}12)$ $[111](\bar{1}01)$ Interpenetrant	$[1\bar{1}1](\bar{1}12)$ $[111](\bar{1}01)$ Interpenetrant

Tables comparing the details of samples near the intersecting slip system boundaries are used to explain their behavior, compiling the data from the following tables: resolved stresses are excerpted for the Ningxia samples from Tables IV-5, 7, 8 (and from a table in the Appendix for the remaining Ningxia samples), and for the D&F samples from a table in the Appendix. Hardening at yield between the two sample sets come from Table V-9 for the D&F samples, and Table V-3 for the Ningxia samples; comparison of the hardening is qualitative, since the D&F set uses shear stress-shear strain curves and the Ningxia set refers to engineering stress-strain curves. Visible slip traces between the two sample sets come from Table V-9 for the D&F samples, and the visible slip traces with the most supporting physical evidence from Table V-8 for the Ningxia samples.

The following is a critical comparison between two similar samples in different data sets. Figure V-9 shows that sample T3 (Ningxia) and sample #8 (D&F) have tensile axes near each other (~2° different from each other), and so would be expected to behave similarly. The only boundary near either sample is the $[1\bar{1}1](121)/[111](\bar{1}\bar{1}2)$ boundary (the red dashed line nearest to T3 and #8): ~3° for sample T3 and ~3° for sample #8. If {112} planes are active at yield, hardening is expected to be observed due to the intersecting slip directions of the two similarly stressed slip systems at the boundary. However, the samples do not behave similarly. Table V-10 compares the stresses of the {112} boundary slip systems of samples #8 and T3. Sample T3 had high hardening at yield, while sample #8 had only slight hardening at yield. The non-glide stresses between the boundary slip systems in sample #8 are similar to each other, while less similar in sample T3; considering that the {112} non-glide stresses were calculated based on the assumption that identifying the {112} non-glide planes would follow the same pattern as the {110} planes (see section III-M), and that the details of the inferred {112} slip

relaxation are unknown, so interpreting them in detail is difficult. Given the twinning/anti-twinning effect on the {112} planes, the similarity of the non-glide stresses of the boundary systems in sample #8 would probably cause the distortion of the screw cores of both systems to be different, which implies the requirements for their activation would be different. That is, even though the values of the non-glide shear stresses of the {112} boundary systems in sample #8 are similar to each other, the requirements to activate each system may be expected to be different, not similar. Thus it may well be that the difference in the values of the non-glide stresses of the {112} boundary systems in sample T3 causes both to be active at yield and cause the observed hardening at yield. Both of the boundary slip systems are anti-twinning in sample #8 and sample T3, probably cause similar effects in each sample, and so do not explain the difference in behavior of samples #8 and T3. While the difference between the initial resolved glide shear stresses is actually smaller in sample #8 than sample T3, the ratio is smaller in sample T3 than in sample #8. That the trend of decreasing difference and ratio of the resolved glide shear stresses of the most stressed intersecting {112} slip systems correlating to increased hardening at yield is present in both the Ningxia and D&F sample sets suggests that the resolved glide shear stress is the most influential of the resolved stresses on a slip system, though the non-glide stresses cause small variations in the resolved glide stress needed to slip.

Table V-10. Comparison of the behavior and details of the boundary slip systems for samples #8 and T3.

Sample	~Degrees from boundary	Slip system boundary	Initial resolved shear stress at yield of boundary slip systems (MPa): glide, non-glide 1, 2, 3	Difference and ratio of RGSS between boundary slip systems with intersecting slip directions	Hardening slope at yield	Visible slip traces by end of test
#8	3°	$[1\bar{1}1](121)$ $[111](\bar{1}\bar{1}2)$	5.6 4.8 -2.5 3.3 A 4.8 4.1 -1.0 1.4 A	0.8 1.167	Slight	$[1\bar{1}1](011)$ $[111](1\bar{2}1)$
T3	3°	$[1\bar{1}1](121)$ $[111](\bar{1}\bar{1}2)$	16.6 15.1 -8.8 10.6 A 15.3 11.8 -2.6 4.5 A	1.3 1.085	High	$[1\bar{1}1](011)$ $[1\bar{1}1](121)$ $[1\bar{1}1](110)$

The $[1\bar{1}1](011)$ slip trace was visible on sample #8 at yield, and was visible by the end of deformation on sample T3. This observation does not necessarily contradict the argument for dominant {112} at yield. The trace of $[1\bar{1}1](011)$ could be imitated by the frequent cross-slip of screw dislocations between the $[1\bar{1}1](121)$ and $[1\bar{1}1](\bar{1}12)$ slip systems. Table V-11 shows the resolved shear stresses at yield on the imitating {112} slip systems for sample #8 and T3. The resolved glide shear stress of both imitating systems is similar while the non-glide stresses are quite different within each sample; it is unclear if the non-glide stresses alone would cause both systems to operate at the same time. In both samples, the system with the slightly lower resolved glide shear stress is a twinning system, and this may compensate for the lower resolved glide shear stress and enable both systems to be active at the same time, and thus imitate the slip trace of the $[1\bar{1}1](011)$ slip system. The imitating {112} slip systems have the same $[1\bar{1}1]$ slip direction and interfere little with each other, consistent with the observed easy glide in sample #8, while the imitating systems would still interfere with the $[111](\bar{1}\bar{1}2)$ slip system, consistent with the observed hardening at yield of sample T3.

Table V-11. Examination of the stresses of the slip systems that may imitate the visible slip traces of the most-stressed {110} slip systems for samples #8 and T3.

Sample	Visible slip traces by end of test	Imitating slip systems	Initial resolved shear stress at yield of imitating slip systems (MPa): glide, non-glide 1, 2, 3	Difference and ratio of rgss between imitating slip systems with same slip direction	Hardening slope at yield
#8	$[1\bar{1}1](011)$	$[1\bar{1}1](121)$ $[1\bar{1}1](\bar{1}12)$	5.6 4.8 -2.5 3.3 A 4.8 -0.7 3.3 -0.8 T	0.8 1.167	Slight
T3	$[1\bar{1}1](011)$	$[1\bar{1}1](121)$ $[1\bar{1}1](\bar{1}12)$	16.6 15.1 -8.8 10.6 A 15.1 -1.5 10.6 -1.8 T	1.5 1.099	High
	$[1\bar{1}1](121)$	$[1\bar{1}1](011)$ $[1\bar{1}1](110)$	18.3 7.9 1.8 8.8 10.5 18.3 -10.6 1.8	7.8 1.743	

Table V-10 also indicates a visible slip trace corresponding to one of the imitating slip systems, $[1\bar{1}1](121)$, was observed on sample T3. The observation of one of the imitating slip systems is consistent with the advantage of SEM images examining slip traces at the micrometer scale, while D&F's observations with a visible light microscope and Nomarski interference were limited to a scale of tens of micrometers. Having earlier ruled out pre-existing dislocations as a possible source of the hardening at yield in the Ningxia set, and based on the above explanations for the difference in behavior of samples #8 and T3, the argument that {112} slip dominates at yield remains the most plausible explanation for the behavior of sample T3.

Figure V-9 shows that both sample #21 and sample #17 are near the $[1\bar{1}1](\bar{1}12)/[111](0\bar{1}1)$ boundary. If hardening at yield were observed in those samples, then that would suggest that both {112} and {110} slip systems were active at yield. Table V-12 indicates that no hardening was observed in sample #21. This is not surprising, since even if slip on both {112} and {110} were possible at yield, the stresses needed to activate them are probably sufficiently different, or the relationship between the two slip systems pushes the red boundary to the right. Pushing the boundary to the right implies that {112} slip is more easily activated than {110} slip. Sample #17 is to the right and closer to this boundary compared to sample #21, and moderate hardening at yield was observed. However, sample #17 is also close to the [001]-[101] boundary, and fits the trend of the other samples close to the [001]-[101] boundary, which is discussed next.

Table V-12. The behavior and details of the boundary slip systems for samples #21 and #17.

Sample	~Degrees from boundary	Slip system boundary	Initial resolved shear stress at yield of boundary slip systems (MPa): glide, non-glide 1, 2, 3	Difference and ratio of RGSS between boundary slip systems with intersecting slip directions	Hardening slope at yield	Visible slip traces
#21	3°	$[1\bar{1}1](\bar{1}12)$ $[111](0\bar{1}1)$	5.5 2.5 0.3 2.0 T 5.1 1.5 1.7 1.9	0.4 1.078	Slight	$[1\bar{1}1](\bar{1}12)$ $[111](\bar{1}01)$
#17	1.5°	$[1\bar{1}1](\bar{1}12)$ $[111](0\bar{1}1)$	6.6 1.4 1.8 1.2 T 7.0 2.6 1.0 2.4	0.4 1.061	Moderate	$[1\bar{1}1](\bar{1}12)$ $[111](\bar{1}01)$

Figure V-9 shows the samples from both sets that have tensile axes near the [001]-[101] boundary: P3, #17, #13, V3, W3, #2, and #1. Table V-13 gives the details for the $[1\bar{1}1](\bar{1}12)/[111](\bar{1}\bar{1}2)$ (closer to the [001]corner of the triangle) and the $[1\bar{1}1](121)/[111](1\bar{2}1)$ (closer to the [101] corner of the triangle) boundaries, and Table V-9 gives the details for $[1\bar{1}1](011)/[111](0\bar{1}1)$ boundary. All those samples have hardening at yield, as expected due to the intersecting slip directions of the {110} and {112} boundary slip systems. Sample W3 was about 4° from the [001]-[101] boundary and had the least hardening relative to the rest of the samples that were near the [001]-[101] boundary, suggesting sample W3 is almost 'out-of-range' of the hardening caused by the intersecting slip directions of the boundary slip systems. The hardening at yield of the samples near the [001]-[101] boundary (P3, #17, #13, V3, W3, #2, #1) tends to increase the closer the tensile axis is to the boundary though not perfectly so. Table V-13 shows the trend that the closer the ratio between the glide shear stresses of the intersecting {112} slip systems is to 1.000 tends to correlate with a higher initial hardening slope, though not perfectly either, probably due to twinning/anti-twinning and non-glide stress effects. Table V-14 shows the same imperfect trend for the intersecting {110} slip systems as that of the {112} slip systems for this group of samples. Samples W3, P3, and #17 all had a visible slip trace that belonged to one of the {112} boundary slip systems. Samples #2, V3, and #1 had visible slip traces of both the {112} boundary slip systems. Only sample #13 had visible slip traces of the {110} boundary systems, with the $[1\bar{1}1](011)$ observed at yield. Table V-15 shows the resolved stresses of the {112} slip systems that may imitate the $[1\bar{1}1](011)$ slip trace. The {112} system with the lower resolved glide shear stress is in the twinning direction, which may compensate and allow both the {112} slip systems to be active at the same time and imitate the $[1\bar{1}1](011)$ slip trace. While the imperfect trends in the resolved

glide shear stresses at yield for both the {112} and {110} slip systems in this group of samples near the [001]-[101] boundary are ambiguous as to whether {112} or {110} slip was dominant at yield, the observed slip traces tend to be those corresponding to the {112} boundary slip systems, and the observed {110} slip trace at yield could be attributed to imitation by {112} slip. The evidence in the group of samples near the [001]-[101] boundary is consistent with dominant {112} slip at yield.

Table V-13. The details of the intersecting {112} slip systems for samples near the [001]-[101] boundary.

Sample	~Degrees from boundary	Intersecting slip system boundary	Initial resolved shear stress at yield of boundary slip systems (MPa): glide, non-glide 1, 2, 3	Difference and ratio of RGSS between boundary slip systems	Hardening slope at yield	Visible slip traces
W3	4°	$[1\bar{1}1](121)$ $[111](1\bar{2}1)$	16.6 11.5 -3.0 7.0 A 15.2 4.1 2.5 2.5 T	1.5 1.092	Moderate-low	$[1\bar{1}1](121)$
P3	2°	$[1\bar{1}1](\bar{1}12)$ $[111](\bar{1}\bar{1}2)$	17.1 5.9 3.2 5.8 T 17.0 11.5 -3.8 9.5 A	0.1 1.006	High	$[111](\bar{1}\bar{1}2)$ $[111](0\bar{1}1)$ $[111](\bar{1}01)$ $[111](1\bar{1}0)$
#2	2°	$[1\bar{1}1](121)$ $[111](1\bar{2}1)$	6.2 3.7 -0.5 2.3 A 5.9 2.3 0.5 1.4 T	0.3 1.051	Moderate	$[1\bar{1}1](121)$ $[111](1\bar{2}1)$
#17	1.5°	$[1\bar{1}1](\bar{1}12)$ $[111](\bar{1}\bar{1}2)$	6.6 1.4 1.8 1.2 T 6.5 5.5 -2.4 3.3 A	0.1 1.015	Moderate	$[1\bar{1}1](\bar{1}12)$ $[111](\bar{1}01)$
#13	1.5°	$[1\bar{1}1](121)$ $[111](1\bar{2}1)$	5.6 5.0 -1.8 2.4 A 5.5 0.5 1.8 0.4 T	0.1 1.018	Moderate	$[1\bar{1}1](011)$ $[111](0\bar{1}1)$
V3	1.5°	$[1\bar{1}1](121)$ $[111](1\bar{2}1)$	17.2 12.9 -3.7 6.8 A 16.8 3.9 3.5 2.7 T	0.4 1.024	Moderate	$[1\bar{1}1](121)$ $[111](1\bar{2}1)$
#1	1.5°	$[1\bar{1}1](121)$ $[111](1\bar{2}1)$	5.8 3.0 -0.1 1.9 A 5.7 2.7 0.1 1.7 T	0.1 1.018	High	$[1\bar{1}1](121)$ $[111](1\bar{2}1)$

Table V-14. The details of the intersecting {110} slip systems for samples near the [001]-[101] boundary.

Sample	~Degrees from boundary	Intersecting slip system boundary	Initial resolved shear stress at yield of boundary slip systems (MPa): glide, non-glide 1, 2, 3	Difference and ratio of RGSS between boundary slip systems	Hardening slope at yield	Visible slip traces
W3	4°	$[1\bar{1}1](011)$ $[111](0\bar{1}1)$	16.3 3.7 4.1 3.0 15.2 11.1 -2.5 5.0	1.1 1.072	Moderate-low	$[1\bar{1}1](121)$
P3	2°	$[1\bar{1}1](011)$ $[111](0\bar{1}1)$	16.4 13.3 -5.8 9.0 16.4 3.5 5.7 3.8	0.0 1.000	High	$[111](\bar{1}\bar{1}2)$ $[111](0\bar{1}1)$ $[111](\bar{1}01)$ $[111](1\bar{1}0)$
#2	2°	$[1\bar{1}1](011)$ $[111](0\bar{1}1)$	5.8 0.7 1.8 0.5 5.5 4.8 -1.4 1.9	0.3 1.055	Moderate	$[1\bar{1}1](121)$ $[111](1\bar{2}1)$
#17	1.5°	$[1\bar{1}1](011)$ $[111](0\bar{1}1)$	6.8 4.6 -1.2 3.0 7.0 2.6 1.0 2.4	0.2 1.029	Moderate	$[1\bar{1}1](\bar{1}12)$ $[111](\bar{1}01)$
#13	1.5°	$[1\bar{1}1](011)$ $[111](0\bar{1}1)$	6.1 2.5 0.5 1.8 6.0 3.5 -0.4 2.1	0.1 1.017	Moderate	$[1\bar{1}1](011)$ $[111](0\bar{1}1)$
V3	1.5°	$[1\bar{1}1](011)$ $[111](0\bar{1}1)$	17.4 5.0 3.2 3.7 17.1 11.9 -2.7 6.2	0.3 1.018	Moderate	$[1\bar{1}1](121)$ $[111](1\bar{2}1)$
#1	1.5°	$[1\bar{1}1](011)$ $[111](0\bar{1}1)$	5.1 0.1 1.8 0.1 5.0 4.9 -1.7 1.8	0.1 1.020	High	$[1\bar{1}1](121)$ $[111](1\bar{2}1)$

Table V-15. Examination of the stresses of the slip systems that may imitate the visible slip traces of the most-stressed {110} slip systems for sample #13.

Sample	Visible slip traces by end of test	Imitating slip systems	Initial resolved shear stress at yield of imitating slip systems (MPa): glide, non-glide 1, 2, 3	Difference and ratio of RGSS between imitating slip systems with same slip direction	Hardening slope at yield
#13	$[1\bar{1}1](011)$	$[1\bar{1}1](121)$ $[1\bar{1}1](\bar{1}12)$	5.6 4.8 -2.5 3.3 A 5.0 -0.6 2.4 -0.5 T	0.6 1.120	Moderate

Samples #20 and #19 are consistent with the hardening trend of the other samples near the [001]-[101] boundary, however those samples are also close to the $[001] - [1\bar{1}1]$ boundary, and may be subject to effects from both boundaries. Table V-16 shows the details for samples #20 and #19 for each of the intersecting slip direction slip system boundaries. The slip traces on samples #20 and #19 were reported as inhomogeneous, and specifically which traces were observed is unclear. The samples are close to the [001] corner (<3°), where four intersecting <111>{112} slip systems have similar resolved glide shear stresses, and eight intersecting <111>{110} slip systems have similar resolved glide shear stresses, with the {112} systems having higher resolved glide shear stresses than the {110} systems. The additional combination of the twinning/anti-twinning and non-glide stress effects on those slip systems means that slip is expected to be complicated near the [001] corner, which is consistent with the reported inhomogeneous slip traces. Given those complexities, and that the trend of ratio between the intersecting boundary systems tending to 1.000 only imperfectly correlates to increased hardening at yield, the following is a tentative explanation that only considers the boundaries the samples are nearest to: If {110} slip were dominant at yield, both sample #20 and #19 should have high hardening at yield since both samples have ratios for the {110} boundary systems near 1.000; however, sample #19 has high hardening and sample #19 has only moderate hardening. The ratios between the intersecting {112} boundary slip systems are more consistent with the observed hardening at yield, since the ratio for sample #20 is about 1.030 with moderate hardening, while the ratio for sample #19 is about 1.000 with high hardening. Those observations are more consistent with dominant {112} slip at yield.

Table V-16. The details of the intersecting slip systems for samples near the [001]-[101] and $[001] - [1\bar{1}1]$ boundaries.

Sample	~Degrees from boundary	Slip system boundary	Initial resolved shear stress at yield of boundary slip systems (MPa): glide, non-glide 1, 2, 3	Difference and ratio of RGSS between boundary slip systems with intersecting slip directions	Hardening slope at yield	Visible slip traces
#20	1.5°	$[1\bar{1}1](\bar{1}12)$ $[111](\bar{1}\bar{1}2)$	6.9 3.5 0.0 3.9 A 6.7 3.6 -0.4 4.3 A	0.2 1.030	Moderate	Unclear
	1.5°	$[1\bar{1}1](011)$ $[111](0\bar{1}1)$	6.0 6.0 -3.9 3.9 6.0 0.3 3.9 0.4	0.0 1.000		
	0.5°	$[111](0\bar{1}1)$ $[\bar{1}\bar{1}1](101)$	6.0 6.0 -3.9 3.9 6.0 5.7 -3.9 4.3	0.0 1.000		
#19	0.5°	$[1\bar{1}1](\bar{1}12)$ $[111](\bar{1}\bar{1}2)$	7.3 3.5 0.2 4.1 T 7.3 3.9 -0.4 4.4 A	0.0 1.000	Very high	Unclear
	0.5°	$[1\bar{1}1](011)$ $[111](0\bar{1}1)$	6.4 6.2 -4.1 4.3 6.4 0.3 4.0 0.4	0.0 1.000		
	3.0°	$[111](0\bar{1}1)$ $[\bar{1}\bar{1}1](101)$	6.4 0.3 4.0 0.4 6.2 6.0 -4.3 4.7	0.2 1.032		

Samples U3 and #4 are both near the [001]-[111] boundary. Table V-17 shows the details for samples U3 and #4 for each of the intersecting slip direction slip system boundaries. The resolved stresses for both samples do indicate that the {112} slip system with the lower resolved glide shear stress is in the twinning direction, which may compensate and allow both {112} systems to be active at yield. The high/very high hardening observed in samples #4 and U3 is due to the intersecting $[1\bar{1}1]$ and $[\bar{1}11]$ slip directions of the boundary slip systems; when equally active those directions cause the tensile axis to rotate toward [001] and continuously maintains high stresses on those slip directions, so that high hardening at yield is expected. Figure V-4 only shows the initial and final orientation of the tensile axis of sample U3, not the actual path of the tensile axis during deformation. However, the raw orientation data for sample U3 (not shown) used to prepare Figure V-4 clearly showed that the tensile axis must have rotated toward [001] before rotating toward $[1\bar{1}1]$ and reaching the final position shown in Figure V-4, which is consistent with roughly equal activation of slip systems with $[1\bar{1}1]$ and $[\bar{1}11]$ slip directions at yield. The intersecting $[1\bar{1}1]$ and $[\bar{1}11]$ slip directions may also result in the dislocation reaction that forms immobile [001](001) forest dislocations that also contribute to hardening. Finally, two of the visible slip traces in sample U3 correspond to the intersecting {112} boundary slip systems. Those observations are consistent with dominant {112} slip at yield.

Table V-17. The details of the intersecting slip systems for samples near the [001]-[111] boundary.

Sample	~Degrees from boundary	Slip system boundary	Initial resolved shear stress at yield of boundary slip systems (MPa): glide, non-glide 1, 2, 3	Difference and ratio of RGSS between boundary slip systems with intersecting slip directions	Hardening slope at yield	Visible slip traces
#4	1.5°	$[1\bar{1}1](121)$ $[\bar{1}11](211)$	6.4 3.3 -0.3 7.5 A 6.2 2.9 0.5 7.2 T	0.2 1.032	High	Unclear
	1.5°	$[1\bar{1}1](011)$ $[\bar{1}11](101)$	5.6 0.1 7.2 0.3 5.4 5.2 -7.2 7.7	0.2 1.037		
U3	1.0°	$[1\bar{1}1](121)$ $[\bar{1}11](211)$	17.5 11.4 -6.4 18.7 A 16.9 5.8 6.9 12.2 T	0.6 1.036	Very high	$[1\bar{1}1](121)$ $[\bar{1}11](211)$ $[111](\bar{1}\bar{1}2)$ $[1\bar{1}1](\bar{1}12)$
	1.0°	$[1\bar{1}1](011)$ $[1\bar{1}1](\bar{1}01)$	16.7 3.0 12.3 6.4 16.2 13.1 -12.2 19.1	0.5 1.031		

The D&F and Ningxia samples that showed easy glide in the stress-strain curves are also grouped and compared (#21, #8, #10, S3, Q2, R2, X3, #3). That grouping is useful in determining whether {110} or {112} slip was dominant at yield because the visible slip trace of the most-stressed {110} and {112} slip systems must either be genuine, or imitated by frequent cross-slip between two slip systems of the other slip plane family that have the same slip direction; imitation still results in easy glide because the two active systems have the same slip direction and interfere little with each other. Both {110} and {112} slip could occur at yield and still result in observed easy glide if the active slip systems have the same slip direction. Table V-18 shows the details for each sample of the easy glide group, giving the resolved stresses for the most-stressed {110} and {112} slip systems at yield and the slip systems that may imitate them. For most of the samples in this group the slip traces of the most-stressed {110} and {112} slip systems are distinct from each other; that is, sufficiently non-parallel to each other that they do not share the same visible slip trace and mislabeling them is unlikely (#21, #8, #10, X3, #3). The most-stressed {110} and {112} slip systems share the same visible trace and so are *not* distinct from each other for samples S3, Q2, R2, and so for these samples the question of imitation is moot since a genuine {112} and/or {110} most-stressed slip trace may already be visible. The imitating slip systems must possess resolved stresses (glide and non-glide) at yield that are sufficient to cause slip for imitation to be a plausible explanation of the visible primary slip trace. Unfortunately, the difference in resolved glide shear stresses between either the {112} pair imitating the {110} slip system (samples #8, #10) or the {110} pair imitating the {112} slip system (samples #21, X3, #3) are small, so that there is no obvious case of imitation being implausible.

Table V-18. The details of the visible primary slip systems and the slip systems that might imitate them for the samples that were oriented for easy glide.

Sample	Visible primary slip trace	Initial resolved shear stress at yield of visible slip system (MPa): glide, non-glide 1, 2, 3	Imitating slip systems	Initial resolved shear stress at yield of imitating slip systems (MPa): glide, non-glide 1, 2, 3	Difference and ratio of RGSS between imitating slip systems with same slip direction
#21	$[1\bar{1}1](\bar{1}12)$	5.5 2.5 0.3 2.0 T	$[1\bar{1}1](011)$ $[1\bar{1}1](\bar{1}01)$	5.1 1.5 1.7 1.9 4.6 -0.3 2.3 -0.3	0.5 1.109
#8	$[1\bar{1}1](011)$	6.0 2.4 0.8 2.5	$[1\bar{1}1](121)$ $[1\bar{1}1](\bar{1}12)$	5.6 4.8 -2.5 3.3 A 4.8 -0.7 3.3 -0.8 T	0.8 1.167
#10	$[1\bar{1}1](011)$	4.3 1.1 1.9 1.8	$[1\bar{1}1](121)$ $[1\bar{1}1](\bar{1}12)$	4.3 3.1 -1.8 3.7 A 3.1 -1.2 3.7 -1.9 T	1.2 1.387
S3	$[1\bar{1}1](011)$	17.8 5.7 3.7 5.5	$[1\bar{1}1](121)$ $[1\bar{1}1](\bar{1}12)$	17.3 13.6 -5.5 9.2 A 13.6 -3.7 9.2 -3.7 T	3.7 1.272
	$[1\bar{1}1](121)$	17.3 13.6 -5.5 9.2 A	$[1\bar{1}1](011)$ $[1\bar{1}1](110)$	17.8 5.7 3.7 5.5 12.1 17.8 -9.2 3.7	5.7 1.471
Q2	$[1\bar{1}1](011)$	18.9 5.2 4.9 5.1	$[1\bar{1}1](121)$ $[1\bar{1}1](\bar{1}12)$	18.8 13.9 -5.1 10.0 A 13.9 -4.9 10.0 -4.9 T	4.9 1.353
	$[1\bar{1}1](121)$	18.8 13.9 -5.1 10.0 A	$[1\bar{1}1](011)$ $[1\bar{1}1](110)$	18.9 5.2 4.9 5.1 13.7 18.9 -10.0 4.9	5.2 1.380
R2	$[1\bar{1}1](011)$	19.6 5.0 5.2 4.7	$[1\bar{1}1](121)$ $[1\bar{1}1](\bar{1}12)$	19.7 14.2 -4.7 9.8 A 14.2 -5.6 9.8 -5.2 T	5.5 1.387
	$[1\bar{1}1](121)$	19.7 14.2 -4.7 9.8 A	$[1\bar{1}1](011)$ $[1\bar{1}1](110)$	19.6 5.0 5.2 4.7 14.6 19.6 -9.8 5.2	5.0 1.343
X3	$[1\bar{1}1](121)$	17.0 9.9 -1.7 8.3 A	$[1\bar{1}1](011)$ $[1\bar{1}1](110)$	15.5 1.6 6.6 1.7 13.9 15.5 -8.3 6.6	1.6 1.115
#3	$[1\bar{1}1](121)$	4.7 2.4 -0.2 3.9 A	$[1\bar{1}1](011)$ $[1\bar{1}1](110)$	4.1 0.1 3.7 0.2 4.0 4.1 -3.9 3.7	0.1 1.025

However, for sample #10, the ratio of resolved glide shear stress between the {112} slip systems needed to imitate the {110} primary slip system is 1.387, and in Table V-3 there are other D&F samples with smaller ratios between the two most-stressed intersecting {112} slip systems that did *not* show significant hardening at yield. That suggests that the intersecting {112} slip systems were not both active at the same time, otherwise hardening would have been observed. So the even larger ratio between the two {112} slip systems needed for imitation may also suggest the two were not active at the same time and were unable to imitate the (genuine) visible {110} primary slip trace at yield. On the other hand, the details of the implied {112} core relaxation and interaction of the twinning/anti-twinning and non-glide stress effects are unclear, and the ratio merely an observed correlation and not a definitive understanding.

VI. Conclusions

The active slip systems of high purity niobium needed to be investigated, in part because of being the primary material used for superconducting radio-frequency cavities, and to further evaluate the assertion that the elementary slip plane family depends on purity. Also, dislocations are increasingly suspected to enable magnetic flux trapping, which leads to undesirable heat generation conditions. Knowing which slip systems are active in high purity niobium will allow for proper crystal plasticity finite element models to be constructed to predict deformation and therefore improve cavity forming processes, and to understand how dislocation substructures form from the interactions of those active slip systems, which in turn affect recrystallization processes. In order to better understand the relationships between active slip systems, and deformation substructure formed during processing, this thesis examined differently oriented high purity niobium single crystals, deformed in the simpler case of uniaxial tension. The primary focus was to determine the active slip systems and compare results with prior studies of similar tests that used higher purity niobium [10, 11, 24]. Knowing the active slip systems and characterizing the dislocation substructure formed by them will be useful to future studies that investigate the relationship between the dislocation substructure as a result of deformation, the recovered dislocation substructure after heat treatments, and the origin of recrystallized grains.

The dominant active slip systems at yield in high purity single crystal niobium used for manufacturing SRF cavities are <111>{112} slip systems. That conclusion is based in part on the interpretation of the stress-strain behavior of Ningxia sample T3. Sample T3 had been oriented so that the $[1\bar{1}1](011)$ slip system possessed the highest glide shear stress, and so was expected to deform by easy glide on that system at yield if elementary slip on {110} slip planes were the preferred slip planes due to the details of the screw core relaxation. Instead, sample T3

showed hardening immediately at yield. Dislocation interactions from two active slip systems with intersecting slip directions were determined to be the most likely explanation by showing that other possible contributions to the hardening were not significant: impurity effects and pre-existing forest dislocations that would have been present due to thermal stresses during ingot cooling.

The slope of the hardening at yield in sample T3 was also similar to the slope of hardening at yield in sample P3. Sample P3 was oriented so that two <111>{112} slip systems with intersecting slip directions both had the highest glide stress and hardening at yield was observed. Similar slopes imply similar mechanism, and the two <111>{112} slip systems in sample T3 with the highest glide stresses had intersecting slip directions. The stereographic projection section in Figure V-9 shows the line of tensile axes for which the two highest stressed <111>{112} slip systems have intersecting slip directions, including sample T3; additional orientations with a tensile axis near the line should be tested to confirm the behavior. This interpretation does require that the twinning/anti-twinning effect and the non-glide shear stress effect both affect the screw dislocation core relaxation and change the glide shear stress needed to enable slip on those slip systems. Unfortunately the details of the inferred {112} slip relaxation at room temperature are not known, and the values for the {112} non-glide shear stresses of each {112} slip systems are only based on the assumption that they follow the same pattern as the {110} non-glide shear stresses. However, a ratio below a threshold of ~1.1 between the glide stresses of the most-stressed intersecting <111>{112} slip systems in the Ningxia sample set does correlate with hardening at yield, suggesting that the combined twinning/anti-twinning and non-glide shear stress effects may only change the glide shear stress needed for slip by a relatively small amount. This suggests that many of these details may not be

necessary for inclusion into practical models for simulation of plastic deformation of large grain Nb, but without this level of study, it is not possible to know the extent to which simplifying modeling approaches are viable. The specific new understanding arising from this work is summarized in the following list:

- The interstitial impurity content of the Tokyo-Denkai and Ningxia sample sets is high enough that elementary slip on not only {112} but {110} slip planes must also be considered possible.

- The Tokyo-Denkai samples were cut from the edge of the ingot, where rapid cooling during ingot production might have generated a sufficiently large radial thermal stress to form dislocations. The slip systems with highest Schimd factors due to the thermal stress would indeed be forest relative to the slip systems with the highest Schmid factors (and resolved shear stresses) due to the subsequent uniaxial tensile test. Thus the work hardening immediately following yield in the Tokyo-Denkai samples C and F may have been caused, at least in part, by forest dislocation interactions between dislocations formed by the radial thermal stress and the slip systems activated by the uniaxial tensile test at yield.

- The hardening behavior immediately following yield for the Ningxia samples *cannot* be attributed to forest dislocations formed by radial thermal stress prior to the uniaxial tensile test.

- While a single {110} slip system was most favored in sample T3, the initial orientation of the tensile direction also favored two {112} slip systems having different slip directions that intersect, and therefore interfere with each other, to also

have similar high initial resolved shear stresses. The similarity between samples P3 and T3, both in initial hardening slope and presence of high shear stresses on a pair of {112} slip systems with intersecting slip directions, suggests that the initial hardening of sample T3 was predominantly caused by the two intersecting {112} slip systems interfering with each other.

- Table V-3 shows that Ningxia samples with larger differences between the initial resolved glide shear stresses acting on intersecting {112} slip systems have a lower initial hardening slope, while those samples with a small difference tend to have a high initial hardening slope. If the ratio of the two highest intersecting {112} slip systems is taken, for samples with a ratio below a threshold of 1.1 the initial hardening becomes at least moderately low in both the Ningxia and Tokyo-Denkai sample sets. A similar comparison using the {110} slip systems instead does *not* give the same correlation.

- The details of the inferred {112} slip relaxation of the screw dislocation core are not known, though some characteristics provide a basis for plausible speculation. If the core spread onto the three symmetric {112} planes, the relaxation would not be symmetric due to the twinning/anti-twinning effect even without an external stress. The non-glide shear stress planes would also be {112} planes, and also be influenced by the twinning/anti-twinning effect. Given these complications, the critical resolved shear stress required to activate a {112} slip system may vary in non-trivial ways with the crystal orientation of the sample.

- Plausible explanations for the rotation of the tensile axis can be made in the context of dominant <111>{112} slip systems at yield for the Tokyo-Denkai and Ningxia samples.

- The slip trace analysis is complicated by the ability of the screw dislocations, whether slipping on {110} or {112} slip planes, to frequently cross-slip. This leads to the problem of imitation, where frequent cross-slip between two slip planes occurs over a smaller length scale than imaged, so that the slip trace appears straight rather than serrated, and is mistaken for a slip trace of the other slip plane family. While dislocation motion unhindered by impurity drag tends to occur in bursts that should be visible at the micron scale at which the Tokyo-Denkai and Ningxia samples were imaged, it remains unclear if this was sufficient to avoid imitation.

- While {112} slip may have dominated behavior at yield, Table V-8 considers all the physical evidence for the Ningxia samples and confirms slip on both {112} and {110} slip planes by the end of deformation to the best that these experiments are able to properly interpret the data.

- The dominance of {112} slip at yield with the eventual confirmation of {110} slip by the end of deformation may be explained by the theory of Seeger et al. [11], which suggests that the high purity screw dislocation core relaxation results in slip on {112} planes while impurities change the relaxation so that slip occurs on {110} planes. That would mean that the total interstitial impurity of ~400 at. ppm in the Ningxia set (plus additional hydrogen absorbed during sample preparation) was not yet sufficient to retain significant amounts of the {110} slip relaxation at yield, and that additional

hydrogen absorbed during deformation in air increased the impurity amount enough to cause significant change to the {110} slip relaxation so that {110} slip traces were visible by the end of deformation.

- The possibility that the favored slip plane may change during deformation due to a concurrent increase in impurities presents a challenge to computational modeling of slip in niobium.

- The Ningxia samples oriented for easy glide did not develop obvious deformation bands. In some of the Ningxia samples oriented for single slip, these implied geometrically necessary dislocation boundaries tended to be aligned with plane traces belonging to slip systems that were the most-stressed initially or at the end of deformation, especially the $[1\bar{1}1](121)$ primary slip system (S3, W3, X3), consistent with the literature [18]. The other single-slip oriented samples whose implied geometrically necessary dislocation boundaries were not aligned with particular slip plane traces, which suggests that no one slip system was dominant during deformation, tended to be those samples oriented so that the most-glide-stressed slip system was $[1\bar{1}1](011)$ (sample T3) or both $[1\bar{1}1](011)$ and $[1\bar{1}1](121)$ were equally most-glide-stressed (samples Q2, R2). That does not conflict with the observation that $[1\bar{1}1]$ was the dominant slip direction in those samples, since the various active systems could all have the $[1\bar{1}1]$ slip direction but different slip planes, such as (121), $(\bar{1}12)$, or (011).

- The Ningxia samples oriented so that intersecting slip systems were both the highest stressed developed deformation bands. Geometrically necessary dislocation boundaries tended to be aligned between slip plane traces.

- The Ningxia samples X3 and Q2 both deformed by easy glide, though they possessed very different implied amounts of geometrically necessary dislocations after the same amount of strain. While the uniaxial tension test is not the stress state for SRF cavity forming operations, this highlights that strategic choices in crystal orientation may be possible to benefit a particular forming operation while minimizing possibly detrimental dislocations, and/or so that the line direction of the dislocations are not detrimental to cavity performance.

- Samples such as U3 may be more prone to recrystallization due to greater geometrically necessary dislocation content, as implied by greater local average misorientation after deformation.

- The interstitial impurity content and the experimental conditions of the tensile tests enable the behavior of D&F set and the Ningxia set to be compared, though the complication of pre-existing dislocations should be minimal in the D&F set due to annealing before deformation. The lower yield stresses in the D&F set are consistent with their higher overall purity, though the interstitial impurity content is still high enough that {110} slip must be considered.

- The D&F set shows the same trend as the Ningxia set, where a decreasing difference (and ratio tending toward 1) in the resolved glide shear stresses of the intersecting most-stressed {112} slip systems at yield drops below a threshold that correlates with

increased hardening at yield. The same trend is present in the D&F set if either the intersecting most-stressed {110} slip systems or the two most glide stressed systems are compared.

- Figure V-9 shows a stereographic projection section of possible tensile axes that shows the boundaries of equal Schmid factor (and thus resolved glide shear stress) between <111>{112} and <111>{110} slip systems whose <111> slip directions are either parallel or intersecting. Parallel slip directions interfere with each other very little and so easy glide is expected, while intersecting slip directions would interfere with each other and hardening is expected to be observed in the portion of the stress-strain curve that corresponds to that tensile axis. The twinning/anti-twinning and non-glide stress effects change the amount of glide shear stress needed to activate slip, so the 'balanced' position of the tensile axis where both systems of a given boundary may be active at the same time may be shifted to one side of the boundary. Some of the boundaries may not exist depending on the experimental conditions being evaluated (i.e. purity, temperature). This figure will be helpful in selecting orientations of samples to have favored slip systems and expected behaviors in future studies that further investigate the active slip systems in high purity niobium (and other BCC metals).

- The initial tensile axis of Ningxia sample T3 and D&F sample #8 are similar, so their behavior is expected to be similar, and they are near a boundary of intersecting <111>{112} slip systems. However, sample T3 hardens at yield while sample #8 does not. A plausible explanation of the difference in behavior is consistent with dominant {112} slip at yield.

- Overall, the detailed comparison between the behavior of the Ningxia and D&F sets is consistent with dominant {112} slip at yield. {110} slip observed at yield in the D&F set may be explained by imitation by frequent cross-slip on {112} slip planes, though this requires that the twinning/anti-twinning and non-glide stress effects enable the imitating systems to be active.

Future work for better understanding of the active slip systems and resulting dislocation substructure in high purity single crystal niobium should include:

- Two additional 'copies' of each of the Ningxia samples are available and could be used to check that the behavior observed could be duplicated.

- The stereographic projection section in Figure V-9 shows the line of tensile axes for which the two highest stressed <111>{112} slip systems at yield have intersecting slip directions, including sample T3. Additional orientations with a tensile axis near the line should be tested to confirm the hardening at yield in the stress-strain curve that is an important basis for claiming that <111>{112} slip is dominant at yield.

- Electron channeling contrast imaging and transmission electron microscopy on strategically orientated samples deformed to only a few % strain, to directly investigate and clarify active slip systems at yield. (ECCI was not possible on the Tokyo-Denkai and Ningxia samples that were already deformed to ~40% strain).

- Having established active dominant slip systems, a focus on the corresponding deformation bands as sources of rotated recrystallization nuclei is desirable.

- In situ tensile tests during which EBSD is used to monitor the changing orientation of the single crystal would reveal how the geometrically necessary dislocation substructure develops as the crystal deforms.

- Analysis of dislocation substructure from existing 3D X-ray data collected on the Ningxia sample set has not yet been analyzed, and may provide insights about the initial dislocation content.

APPENDIX

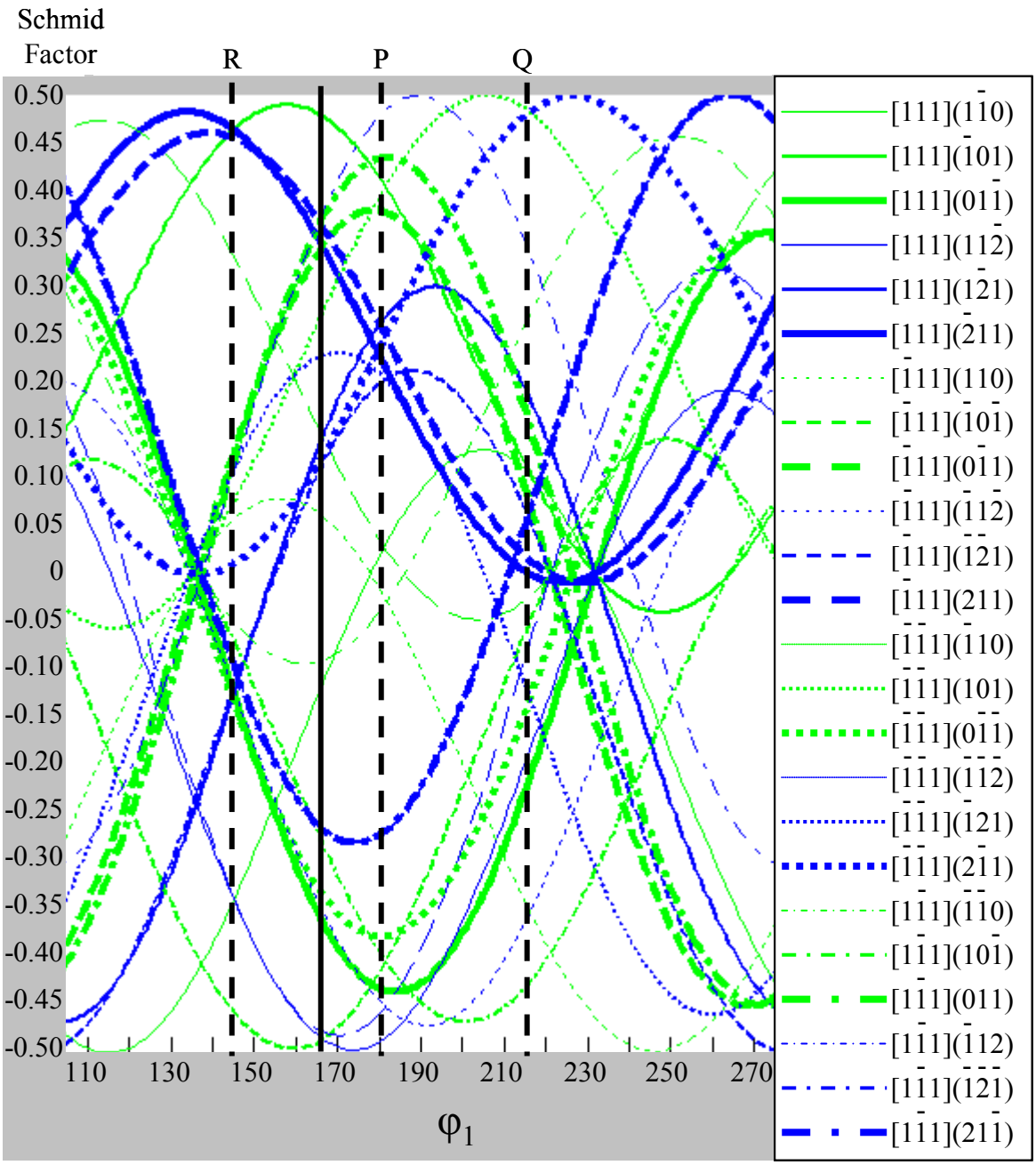

Figure A-1. Computation of Schmid factors on slip systems for the parent grain 2 orientation (166 86 263, solid black line) in the plane of a sliced ingot as a function of in-plane tensile stress orientation. The intended orientations of samples P (182 86 263), Q (216 86 263), and R (237 86 263) are shown (dashed black lines). The actual orientations of the samples are slightly different after being cut out, and a different symmetric variant of the Euler angles chosen to obtain mostly positive Schmid factors for the slip systems.

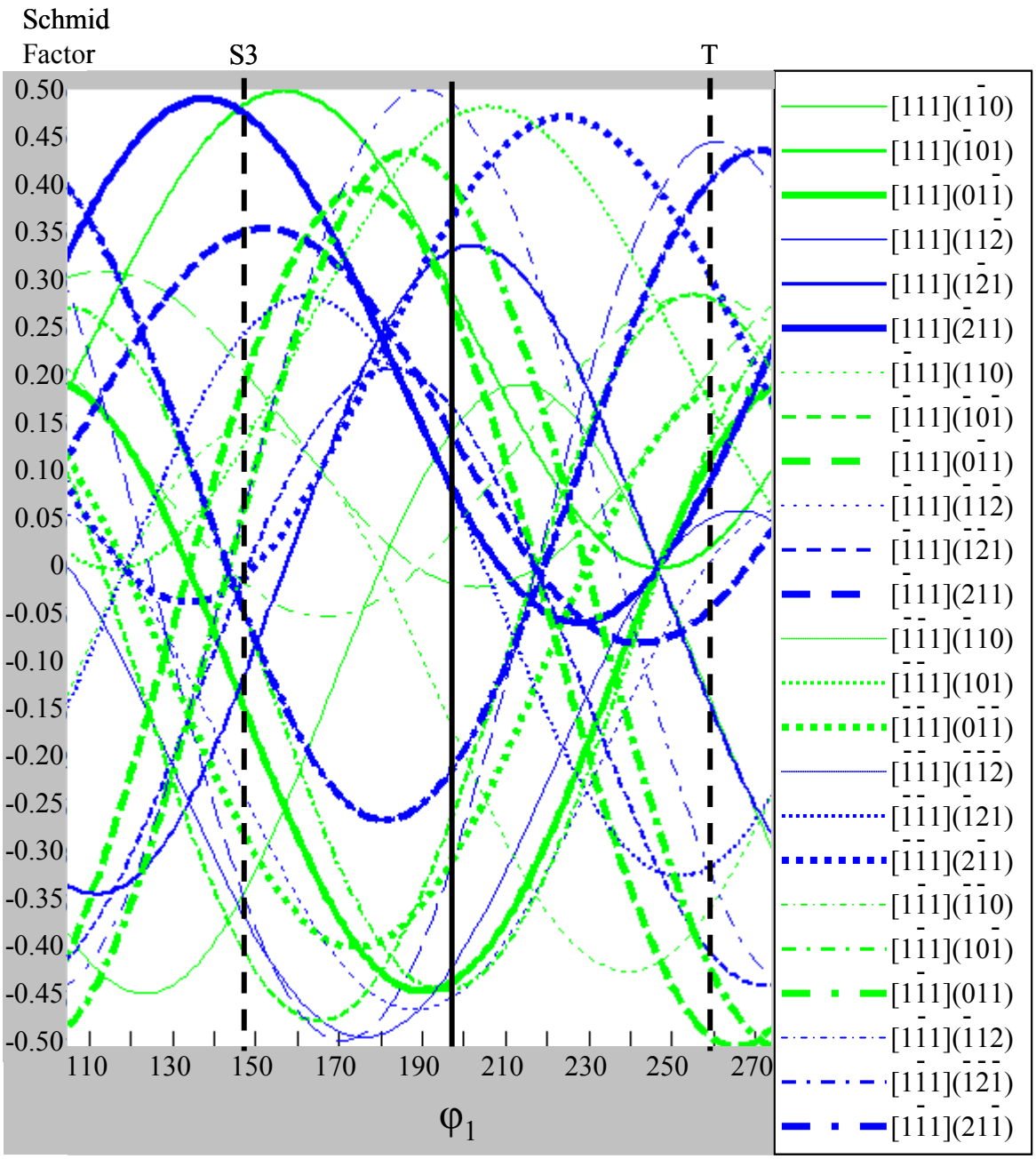

Figure A-2. Computation of Schmid factors on slip systems for the parent grain 4 orientation (198 87 245, solid black line) in the plane of a sliced ingot as a function of in-plane tensile stress orientation. The intended orientations of samples S (148 87 245) and T (260 87 245) are shown (dashed black lines). The actual orientations of the samples are slightly different after being cut out, and a different symmetric variant of the Euler angles was chosen to obtain [1-11] as the primary slip direction.

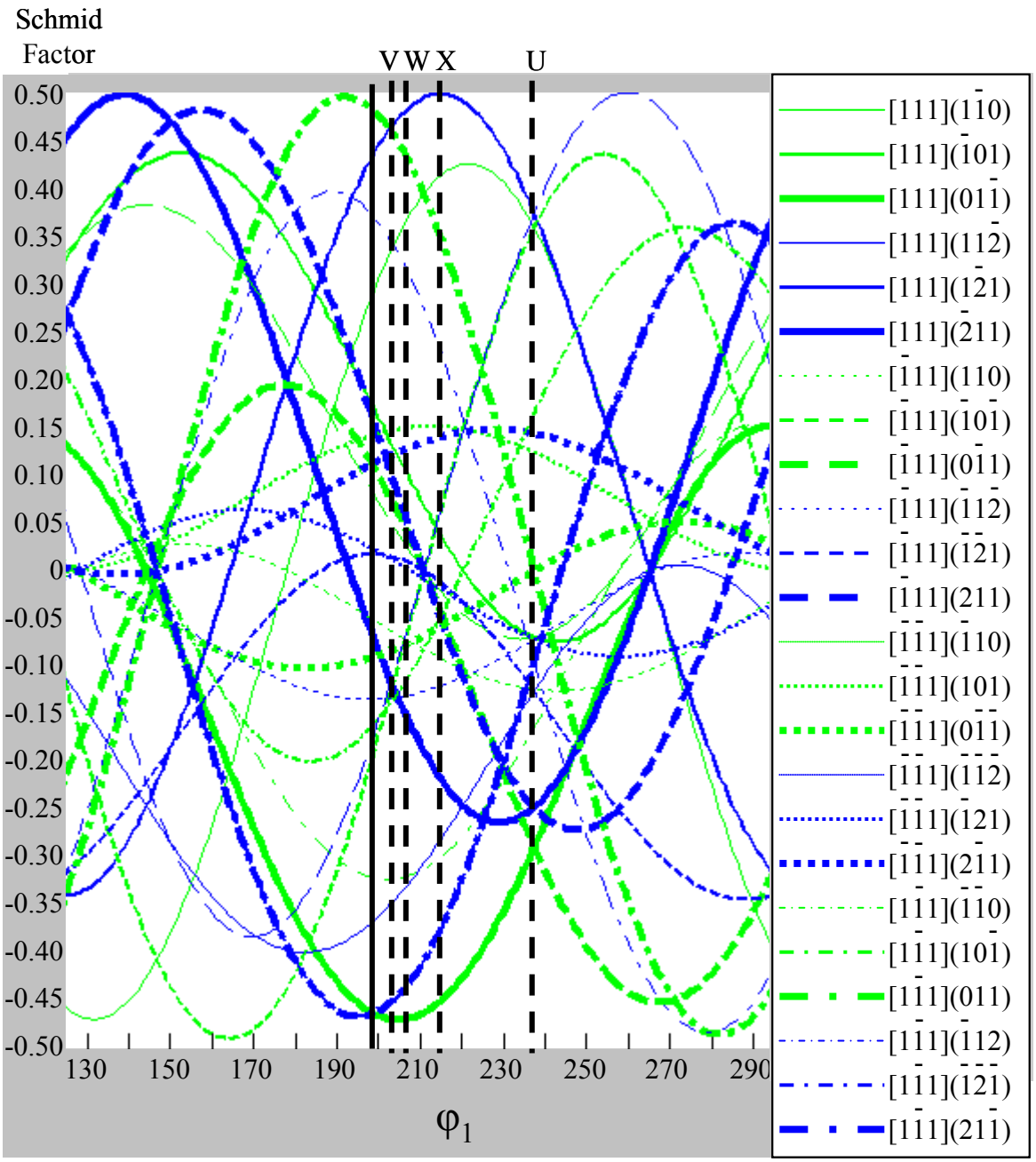

Figure A-3. Computation of Schmid factors on slip systems for the parent grain 5 orientation (199 62 231, solid black line) in the plane of a sliced ingot as a function of in-plane tensile stress orientation. The intended orientations of samples U (238 62 231), V (203 62 231), W (207 62 231),and X (215 62 231) are shown (dashed black lines). The actual orientations of the samples are slightly different after being cut out, and a different symmetric variant of the Euler angles chosen to obtain mostly positive Schmid factors for the slip systems.

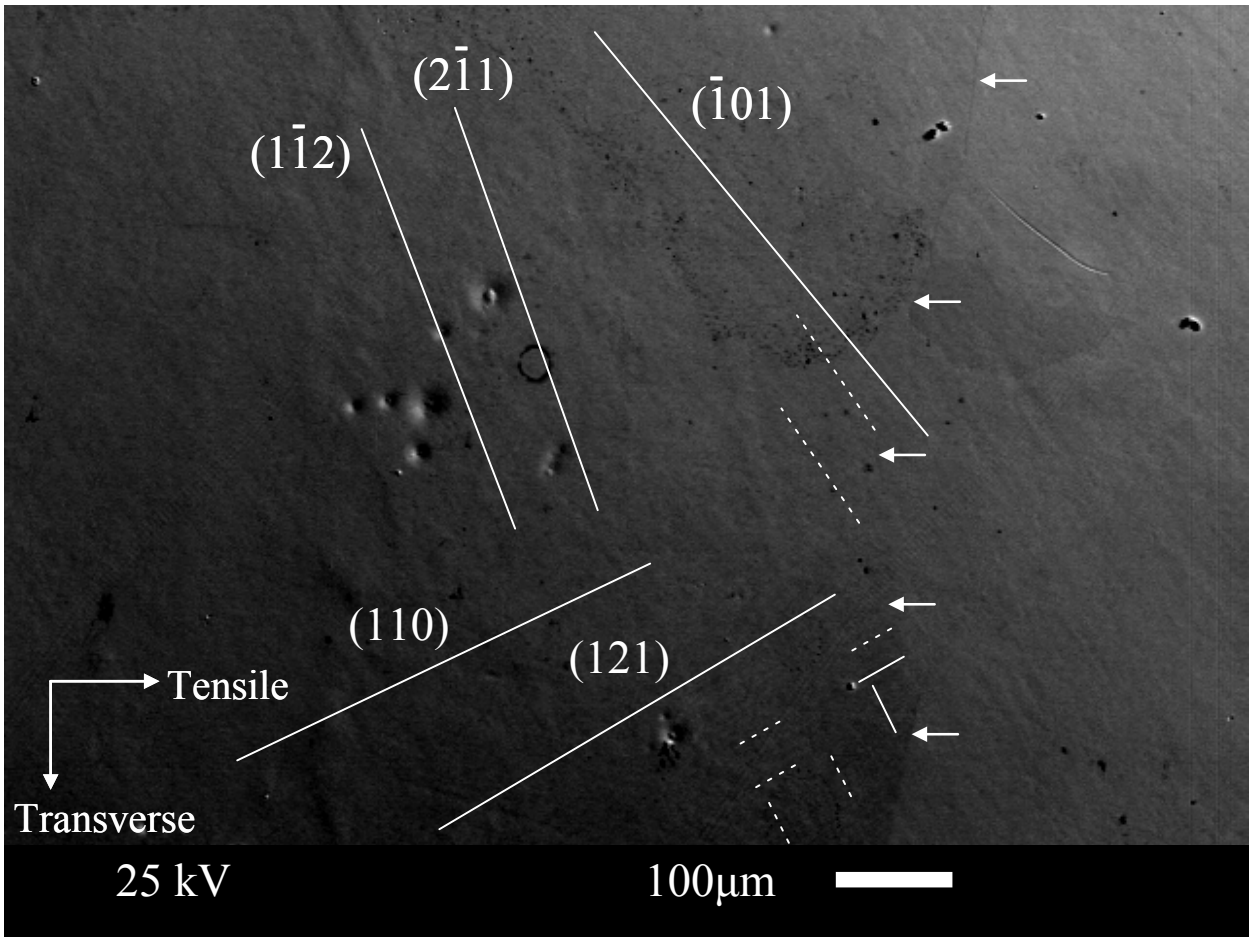

Figure A-4. Slip traces on side C of welded sample CA (SEI). The grain boundaries of the recrystallization front (white arrows) divided the recrystallized grains to the right from the recovered region on the left, where the slip traces are drawn. The estimated local tensile strain was 21%.

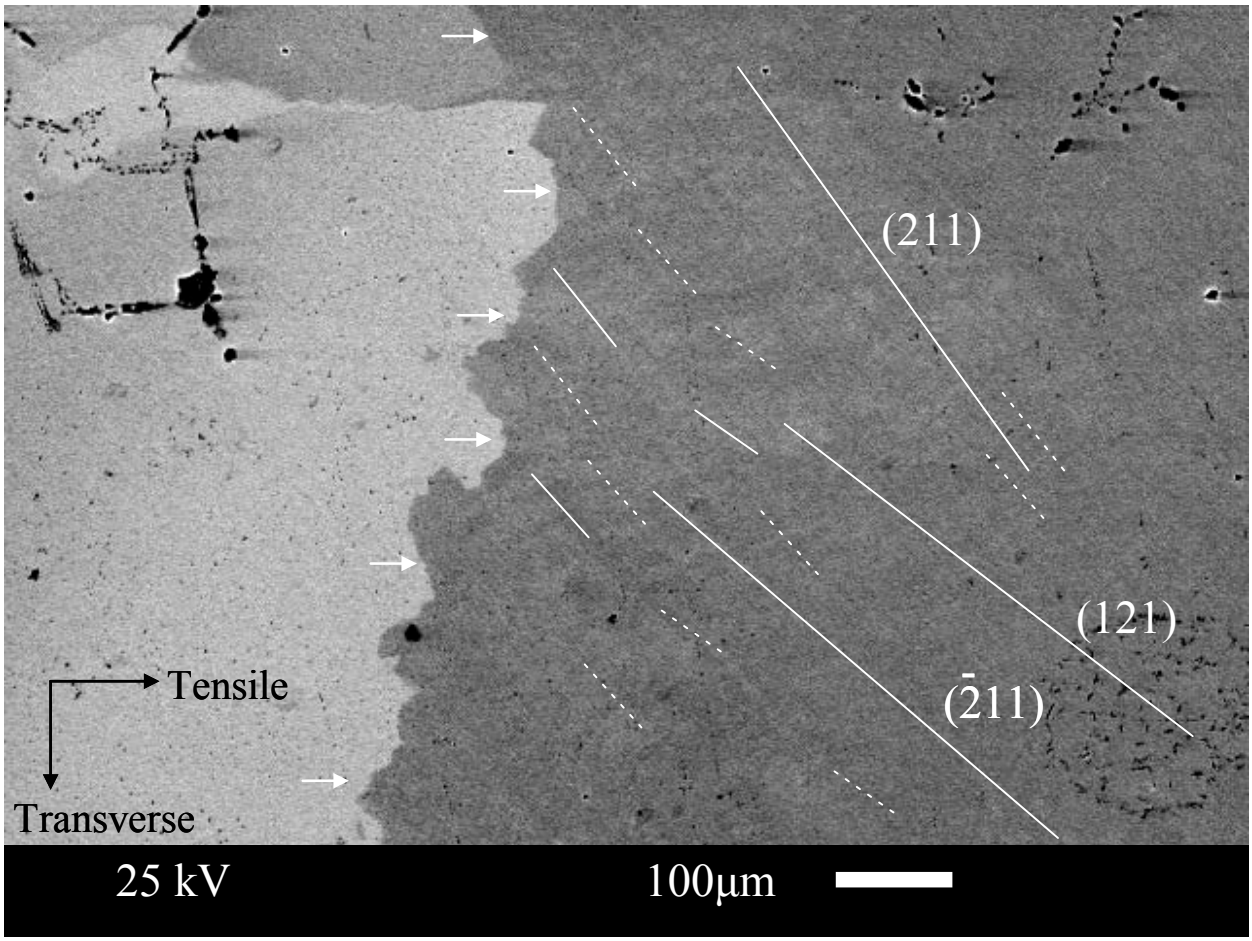

Figure A-5. Slip traces on side F of welded sample AF (BEI). The grain boundaries of the recrystallization front (white arrows) divided the recrystallized grains on the left from the recovered region on the right where there slip traces are drawn. The estimated local tensile strain was 27%.

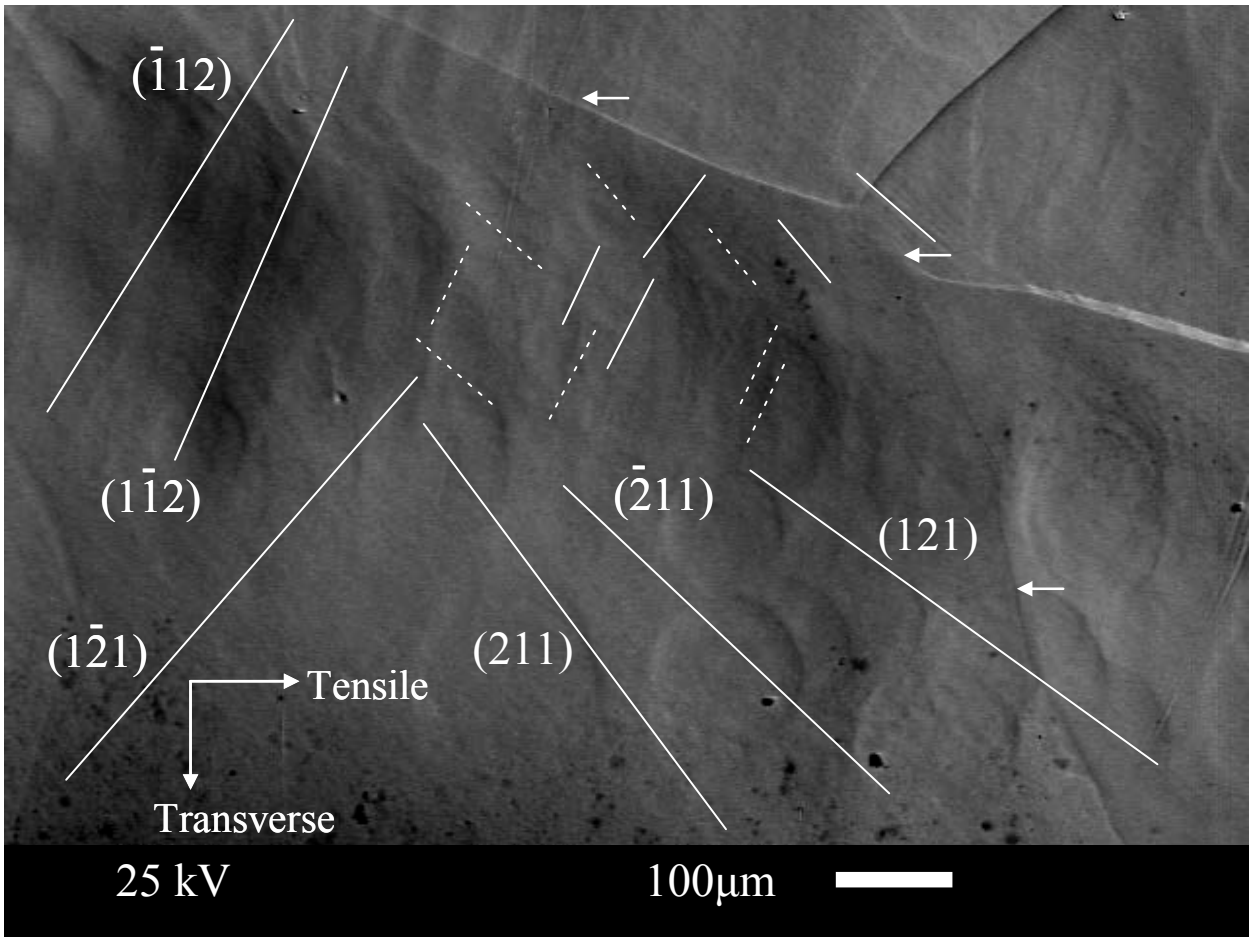

Figure A-6. Slip traces on side F of welded sample FC (SEI). The grain boundaries of the recrystallization front (white arrows) divided the recovered region on the left where the slip traces are drawn from the recrystallized grains to the right. The estimated local tensile strain was 33%.

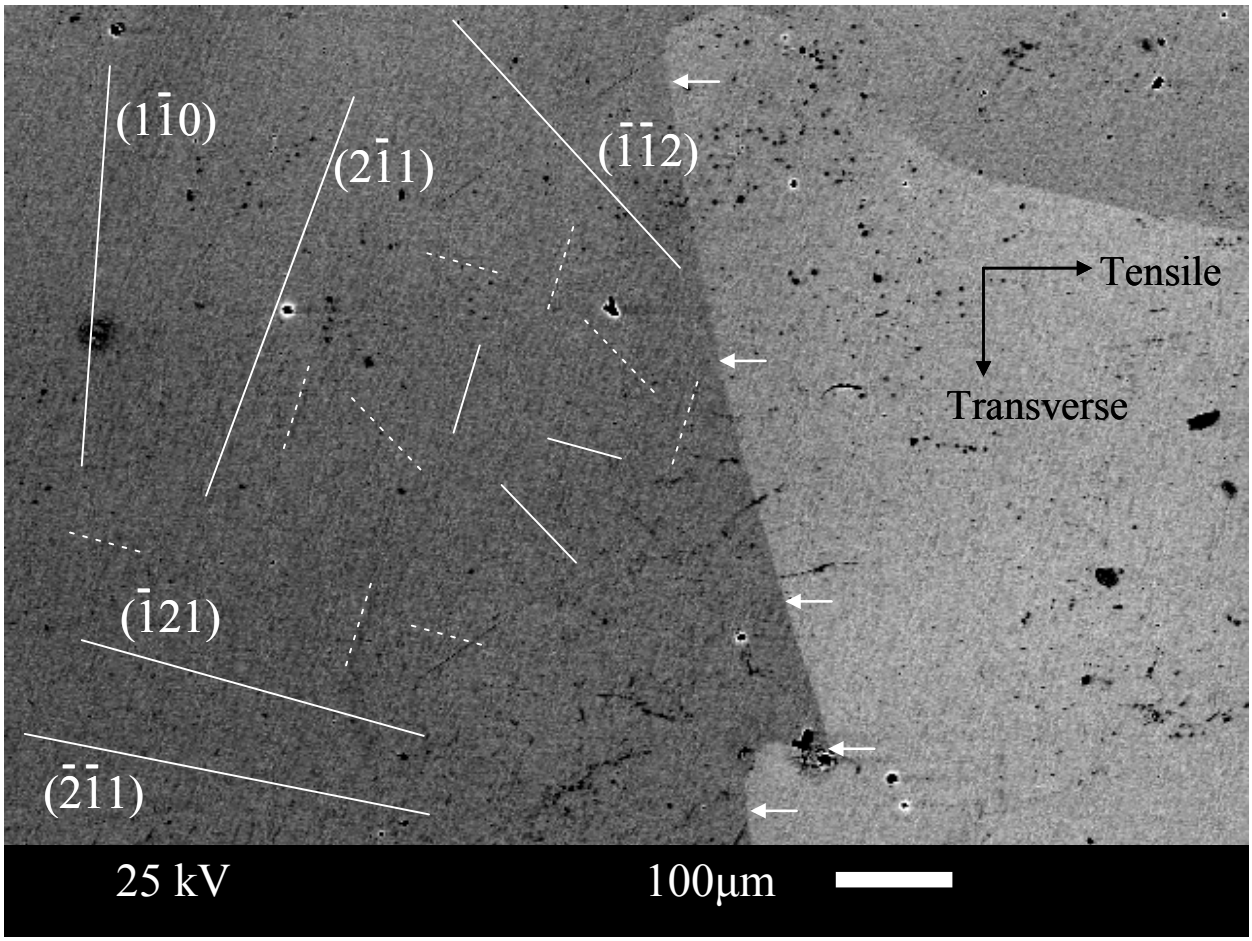

Figure A-7. Slip traces on side A of welded sample AF (BEI). The grain boundaries of the recrystallization front (white arrows) divided the recovered region on the left where the slip traces are drawn from the recrystallized grains to the right. The estimated local tensile strain was 60%.

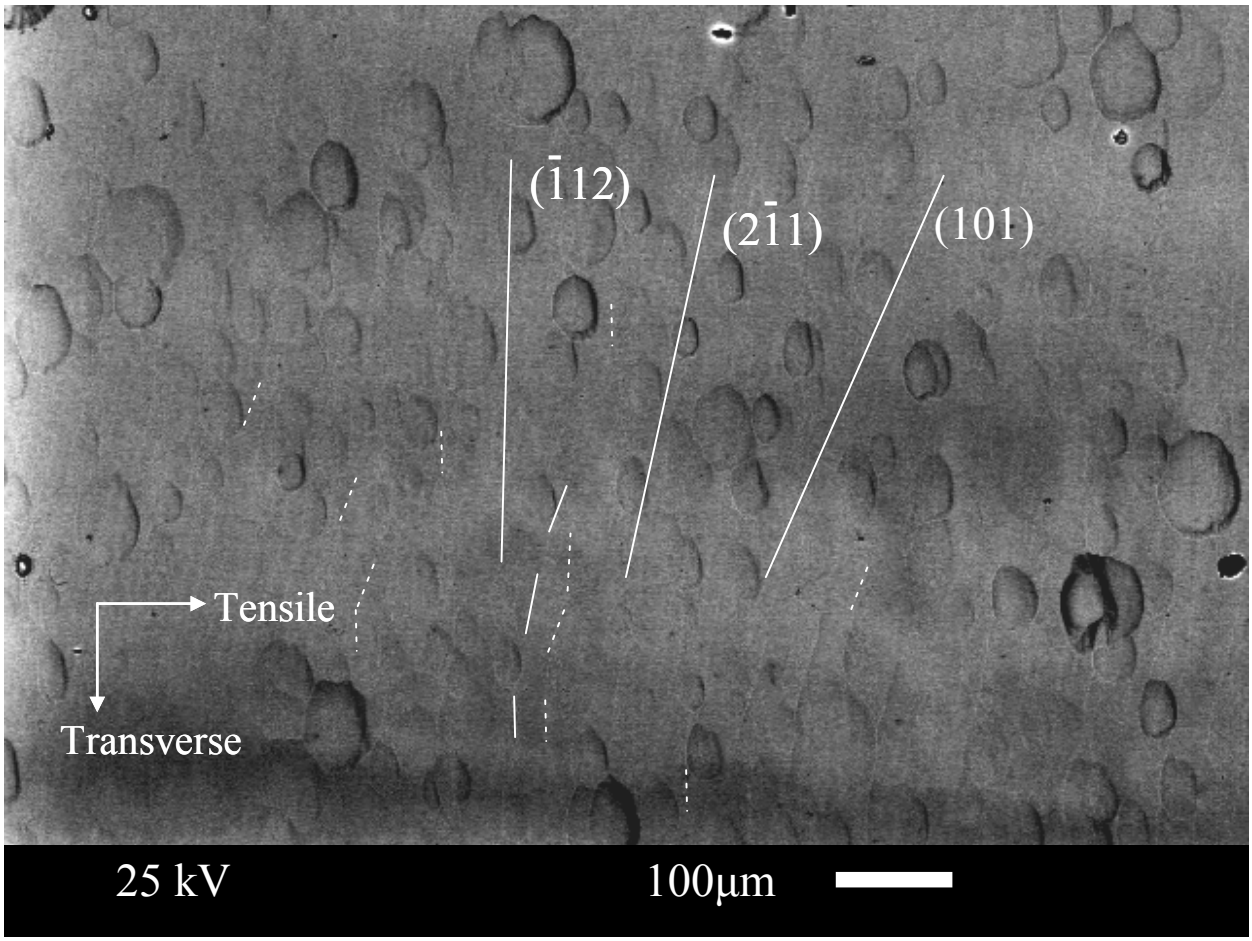

Figure A-8. Slip traces on side A of welded sample CA (BEI). Recrystallized grains are not visible and located out of frame near the upper and lower left corners. The estimated local tensile strain was 7%.

Table A-1. A list of evidence considered for potentially active slip systems for samples Q2, R2, S3, U3, V3, and W3 of the Ningxia sample set. The 0.2% strain offset yield stress and final flow stress are given under the sample name, in that order. Slip systems with matching possible and calculated slip traces are marked '*' if observed on the Normal surface, and marked '†' if observed on the Transverse surface. The greatest initial and final resolved glide shear stresses for the {110} and {112} slip system families are given in bold. Twinning (T) and anti-twinning (A) {112} planes are also indicated.

Sample, stresses (MPa), Hardening slope at yield, Slip direction that rotated toward TD, Initial Euler angles, Final Euler angles	Potentially active slip system	Initial resolved shear stress at yield (MPa): glide, non-glide 1, 2, 3	Final resolved shear stress (MPa): glide, non-glide 1, 2, 3
Q2 39.1, 56.9 Slight $[1\bar{1}1]$ 214 82 175 215 96 171	$[1\bar{1}1](011)$†	**18.9** 5.2 4.9 5.1	**26.5** 7.8 4.6 5.5
	$[1\bar{1}1](121)$†	**18.8** 13.9 -5.1 10.0 A	**26.1** 19.8 -5.5 10.1 A
	$[111](0\bar{1}1)$*	16.1 9.6 -0.9 4.1	26.4 18.6 -4.4 9.9
	$[111](1\bar{2}1)$	14.8 1.8 3.2 0.9 T	26.0 6.2 5.5 4.4 T
	$[1\bar{1}1](\bar{1}12)$†	13.9 -4.9 10.0 -4.9 T	19.8 -6.3 10.1 -4.6 T
	$[1\bar{1}1](110)$*†	13.7 18.9 -10.0 4.9	18.7 26.5 -10.1 4.6
	$[111](\bar{1}\bar{1}2)$	13.1 14.8 -4.1 3.2 A	19.8 26.0 -9.9 5.5 A
	$[111](1\bar{1}0)$*	9.6 -6.5 4.1 -3.2	18.6 -7.8 9.9 -5.5
	$[\bar{1}11](110)$*†	4.8 -4.5 16.3 -15.5	3.3 -4.6 21.0 -26.4
	$[\bar{1}11](0\bar{1}1)$*	4.5 9.3 -15.5 -0.8	4.6 7.9 -26.4 5.4
	$[\bar{1}\bar{1}1](011)$†	1.7 -0.7 19.5 -10.4	4.5 -3.2 26.5 -20.8
	$[\bar{1}\bar{1}1](1\bar{1}0)$*	0.7 2.4 -10.4 -9.1	3.2 7.7 -20.8 -5.7

Table A-1 (cont'd)

S3 36.4, 50.4 Slight [1$\bar{1}$1] 147 86 338 148 73 346	[1$\bar{1}$1](011)†	**17.8** 5.7 3.7 5.5	21.5 7.0 2.5 3.9
	[1$\bar{1}$1](121)*†	**17.3** 13.6 -5.5 9.2 A	20.8 16.5 -3.9 6.3 A
	[111](0$\bar{1}$1)	15.5 8.4 -0.4 3.9	**24.1** 18.1 -6.2 11.5
	[111](1$\bar{2}$1)*†	13.8 0.7 3.5 0.4 T	**24.4** 7.0 5.3 6.2 T
	[1$\bar{1}$1]($\bar{1}$12)†	13.6 -3.7 9.2 -3.7 T	16.5 -4.3 6.3 -2.5 T
	[111]($\bar{1}\bar{1}$2)	13.0 13.8 -3.9 3.5 A	17.4 24.4 -11.5 5.3 A
	[1$\bar{1}$1](110)	12.1 17.8 -9.2 3.7	14.5 21.5 -6.3 2.5
	[$\bar{1}$11](101)	9.4 4.7 0.2 14.5	3.4 1.1 9.0 15.8
	[111](1$\bar{1}$0)*	8.4 -7.1 3.9 -3.5	18.1 -6.0 11.5 -5.3
	[$\bar{1}$11](1$\bar{1}$2)*	8.2 8.1 -14.5 14.7 A	3.2 2.6 -15.8 24.8 A
	[$\bar{1}$11](211)*	8.1 -0.1 14.7 -0.2 T	2.6 -0.6 24.8 -9.0 T
	[111]($\bar{1}$01)†	7.1 15.5 -3.5 -0.4	6.0 24.1 -5.3 -6.2
	[1$\bar{1}$1]($\bar{1}$01)†	5.7 -12.1 5.5 -9.2	7.0 -14.5 3.9 -6.3
	[$\bar{1}\bar{1}$1](101)	3.3 2.4 -8.8 18.0	9.6 4.8 -0.2 21.1
	[$\bar{1}\bar{1}$1](112)*	3.3 0.9 9.2 8.8 T	8.4 0.0 20.9 0.2 T
	[$\bar{1}\bar{1}$1](011)†	2.4 -0.9 18.0 -9.2	4.8 -4.8 21.1 -20.9
	[$\bar{1}\bar{1}$1](1$\bar{1}$0)*	0.9 3.3 -9.2 -8.8	4.8 9.6 -20.9 -0.2
R2 40.7, 65.3 Slight [1$\bar{1}$1] 324 94 352 324 77 344	[1$\bar{1}$1](121)†	**19.7** 14.2 -4.7 9.8 A	29.9 20.8 -4.6 10.6 A
	[1$\bar{1}$1](011)*†	**19.6** 5.0 5.2 4.7	29.3 6.8 6.0 4.6
	[111](0$\bar{1}$1)	17.0 11.0 -1.6 4.7	**29.9** 23.3 -6.9 11.8
	[111](1$\bar{2}$1)*	16.2 2.8 3.1 1.6 T	**30.7** 9.6 4.9 6.9 T
	[1$\bar{1}$1](110)†	14.6 19.6 -9.8 5.2	22.5 29.3 -10.6 6.0
	[1$\bar{1}$1]($\bar{1}$12)*†	14.2 -5.6 9.8 -5.2 T	20.8 -9.0 10.6 -6.0 T
	[111]($\bar{1}\bar{1}$2)†	13.3 16.2 -4.7 3.1 A	21.1 30.7 -11.8 4.9 A
	[111](1$\bar{1}$0)†	11.0 -6.0 4.7 -3.1	23.3 -6.6 11.8 -4.9
	[$\bar{1}$11](101)†	8.6 4.4 -0.5 17.0	6.0 2.5 5.7 24.7
	[$\bar{1}$11](211)†	7.5 0.1 16.6 0.5 T	4.9 -0.5 30.5 -5.7 T
	[$\bar{1}$11](1$\bar{1}$2)*†	7.4 7.5 -17.0 16.6 A	5.5 4.9 -24.7 30.5 A
	[1$\bar{1}$1](21$\bar{1}$)†	5.6 19.7 -5.2 -4.7 N/A	9.0 29.9 -6.0 -4.6 N/A
	[$\bar{1}$11](110)†	4.4 -4.2 17.0 -16.6	2.5 -3.5 24.7 -30.5
	[$\bar{1}\bar{1}$1](101)†	2.4 1.7 -8.3 20.2	7.4 4.1 -3.7 29.6
	[$\bar{1}\bar{1}$1](112)†	2.4 0.5 11.9 8.3 T	6.6 0.4 25.8 3.7 T
	[$\bar{1}\bar{1}$1](011)*†	1.7 -0.8 20.2 -11.9	4.1 -3.3 29.6 -25.8
	[$\bar{1}\bar{1}$1](1$\bar{1}$0)†	0.8 2.4 -11.9 -8.3	3.3 7.4 -25.8 -3.7

Table A-1 (cont'd)

W3 34.7, 74.9 Moderate-low $[1\bar{1}1]$ 25 118 129 26 121 144	$[1\bar{1}1](121)$*†	**16.6** 11.5 -3.0 7.0 A	30.7 21.5 -3.8 8.6 A
	$[1\bar{1}1](011)$	**16.3** 3.7 4.1 3.0	30.1 7.1 4.8 3.8
	$[111](1\bar{2}1)$	15.2 4.1 2.5 2.5 T	**36.9** 13.3 5.5 11.5 T
	$[111](0\bar{1}1)$†	15.2 11.1 -2.5 5.0	**34.9** 29.0 -11.5 17.0
	$[1\bar{1}1](110)$	12.6 16.3 -7.0 4.1	23.0 30.1 -8.6 4.8
	$[1\bar{1}1](\bar{1}12)$	11.5 -5.1 7.0 -4.1 T	21.5 -9.2 8.6 -4.8 T
	$[111](1\bar{1}0)$	11.1 -4.0 5.0 -2.5	29.0 -6.0 17.0 -5.5
	$[111](\bar{1}\bar{1}2)$†	11.1 15.2 -5.0 2.5 A	23.6 36.9 -17.0 5.5 A
	$[\bar{1}11](211)$*	9.0 29.9 -6.0 -4.6 N/A	0.9 -0.2 36.8 -12.2 T
	$[1\bar{1}1](21\bar{1})$	5.1 16.6 -4.1 -3.0 N/A	9.2 30.7 -4.8 -3.8 N/A
	$[111](2\bar{1}\bar{1})$*	4.1 -11.1 2.5 -5.0 N/A	13.3 -23.6 11.5 -17.0 N/A
	$[\bar{1}11](0\bar{1}1)$†	2.7 5.1 -15.1 0.9	0.8 1.2 -36.8 12.2
	$[\bar{1}\bar{1}1](101)$	2.6 1.6 -4.5 16.7	11.9 5.5 3.0 30.0
	$[\bar{1}\bar{1}1](112)$	2.4 0.3 12.1 4.5 T	10.1 -0.5 33.0 -3.0 T
	$[\bar{1}\bar{1}1](2\bar{1}1)$†	2.1 2.4 -16.7 12.1 A	10.6 10.1 -30.0 33.0 A
U3 46.3, 97.6 Very high $[1\bar{1}1]$ 175 134 38 176 129 45	$[1\bar{1}1](121)$*†	**17.5** 11.4 -6.4 18.7 A	**41.2** 29.4 -16.9 36.4 A
	$[\bar{1}11](211)$†	16.9 5.8 6.9 12.2 T	34.0 7.9 23.2 17.7 T
	$[1\bar{1}1](011)$*†	**16.7** 3.0 12.3 6.4	**40.7** 10.1 19.5 16.9
	$[\bar{1}11](101)$*†	16.2 13.1 -12.2 19.1	34.7 24.1 -17.7 41.0
	$[1\bar{1}1](110)$	13.6 16.7 -18.7 12.3	30.6 40.7 -36.4 19.5
	$[\bar{1}11](110)$	13.1 -3.1 19.1 -6.9	24.1 -10.5 41.0 -23.2
	$[1\bar{1}1](\bar{1}12)$*	11.4 -6.1 18.7 -12.3 T	29.4 -11.8 36.4 -19.5 T
	$[\bar{1}11](1\bar{1}2)$	11.1 16.9 -19.1 6.9 A	26.1 34.0 -41.0 23.2 A
	$[111](\bar{1}\bar{1}2)$	8.4 4.6 -0.1 0.7 A	25.8 18.2 -1.7 3.9 A
	$[111](0\bar{1}1)$	7.5 0.5 0.6 0.1	25.4 6.1 2.2 1.7
	$[111](\bar{1}01)$	7.1 7.5 -0.7 0.6	19.3 25.4 -3.9 2.2
	$[\bar{1}\bar{1}1](\bar{1}0\bar{1})$*†	6.1 6.0 -19.3 19.8	5.2 4.8 -38.6 44.9
	$[1\bar{1}1](21\bar{1})$	6.1 17.5 -12.3 -6.4 N/A	11.8 41.2 -19.5 -16.9 N/A
	$[\bar{1}\bar{1}1](0\bar{1}\bar{1})$†	6.0 -0.1 19.8 -0.5	4.8 -0.4 44.9 -6.3
	$[111](1\bar{2}1)$	4.6 -3.8 0.7 -0.6 T	18.2 -7.7 3.9 -2.2 T
	$[\bar{1}\bar{1}1](\bar{2}1\bar{1})$†	3.6 7.0 -19.8 0.5 A	3.2 5.8 -44.9 6.3 A
	$[\bar{1}\bar{1}1](1\bar{2}\bar{1})$†	3.4 -3.6 19.3 -19.8 N/A	2.6 -3.2 38.6 -44.9 N/A
	$[\bar{1}11](0\bar{1}1)$	3.1 16.2 -6.9 -12.2	10.5 34.7 -23.2 -17.7
	$[1\bar{1}1](\bar{1}01)$	3.0 -13.6 6.4 -18.7	10.1 -30.6 16.9 -36.4
	$[111](1\bar{1}0)$†	0.5 -7.1 0.1 -0.7	6.1 -19.3 1.7 -3.9
	$[\bar{1}\bar{1}1](\bar{1}10)$†	0.1 6.1 -0.5 -19.3	0.4 5.2 -6.3 -38.6

Table A-1 (cont'd)

V3 37.1, 89.6 Moderate $[1\bar{1}1]$ 22 118 128 25 120 142	$[1\bar{1}1](011)$	**17.4** 5.0 3.2 3.7	37.5 9.5 6.0 5.4
	$[1\bar{1}1](121)$*†	**17.2** 12.9 -3.7 6.8 A	37.8 27.2 -5.4 11.3 A
	$[111](0\bar{1}1)$*	17.1 11.9 -2.7 6.2	**42.0** 33.7 -12.3 19.5
	$[111](1\bar{2}1)$†	16.8 3.9 3.5 2.7 T	**43.7** 14.7 7.2 12.3 T
	$[1\bar{1}1](\bar{1}12)$	12.9 -4.2 6.8 -3.2 T	27.2 -10.6 11.3 -6.0 T
	$[111](\bar{1}\bar{1}2)$†	12.8 16.8 -6.2 3.5 A	29.0 43.7 -19.5 7.2 A
	$[1\bar{1}1](110)$	12.4 17.4 -6.8 3.2	28.0 37.5 -11.3 6.0
	$[111](1\bar{1}0)$	11.9 -5.2 6.2 -3.5	33.7 -8.3 19.5 -7.2
	$[1\bar{1}1](\bar{1}01)$	5.0 -12.4 3.7 -6.8	9.5 -28.0 5.4 -11.3
	$[\bar{1}\bar{1}1](101)$	4.7 2.8 -4.1 17.5	14.0 6.9 0.9 37.3
	$[\bar{1}11](211)$*	4.5 -0.5 17.0 -3.1 T	3.0 -0.6 43.7 -13.5 T
	$[\bar{1}\bar{1}1](112)$	4.3 0.5 13.3 4.1 T	12.1 -0.2 38.3 -0.9 T
	$[1\bar{1}1](21\bar{1})$	4.2 17.2 -3.2 -3.7 N/A	10.6 37.8 -6.0 -5.4 N/A
	$[111](2\bar{1}\bar{1})$*	3.9 -12.8 2.7 -6.2 N/A	14.7 -29.0 12.3 -19.5 N/A
	$[\bar{1}\bar{1}1](2\bar{1}1)$†	3.8 4.3 -17.5 13.3 A	12.2 12.1 -37.3 38.3 A
	$[\bar{1}11](0\bar{1}1)$*	3.1 5.5 -17.0 3.1	2.4 3.8 -43.7 13.5

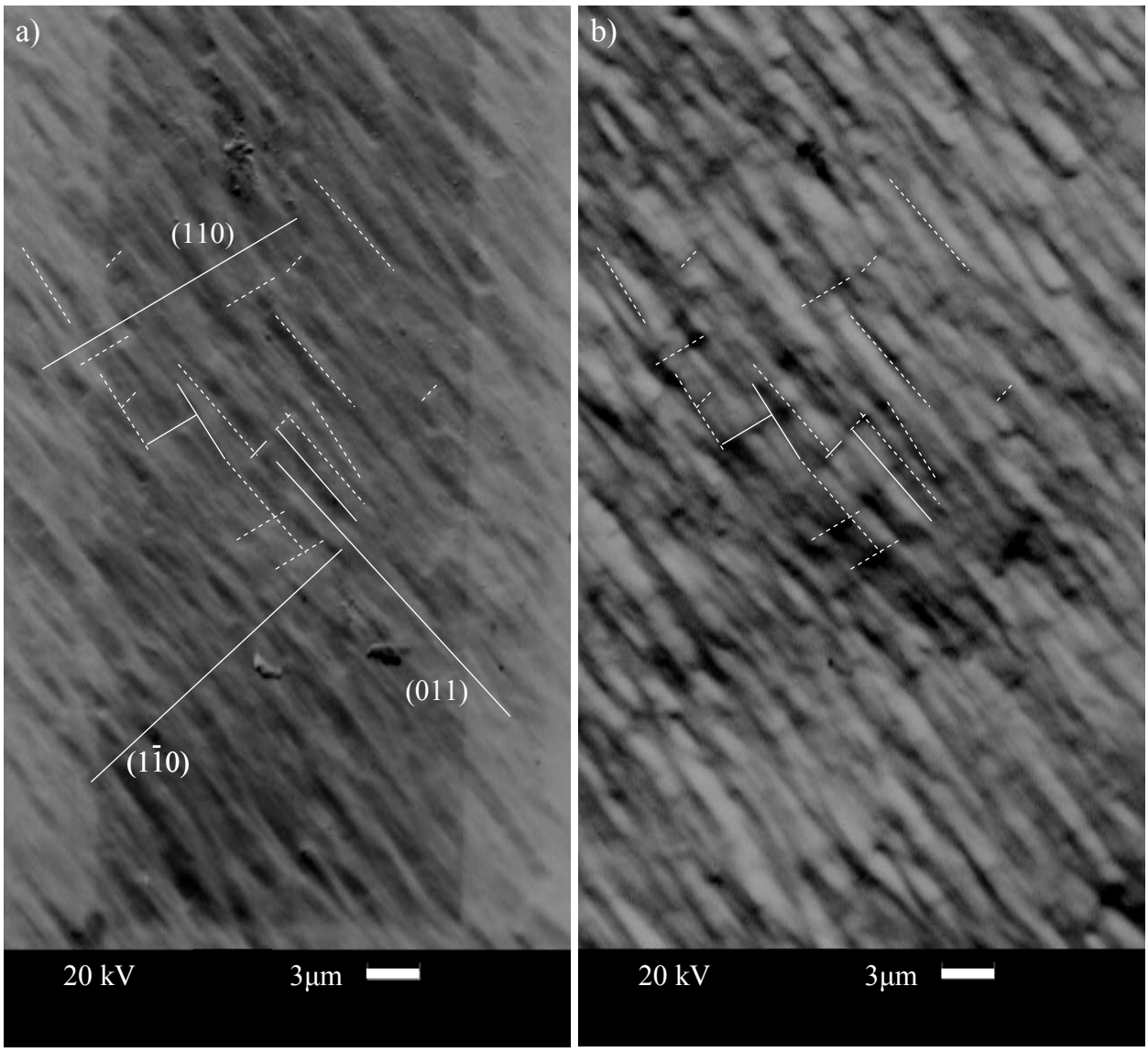

Figure A-9. Slip traces on the normal surface of sample Q2 after deformation, a) SEI and b) BEI. Calculated slip traces are the long labeled lines to which the visible traces (short white solid and short white dashed lines) were matched.

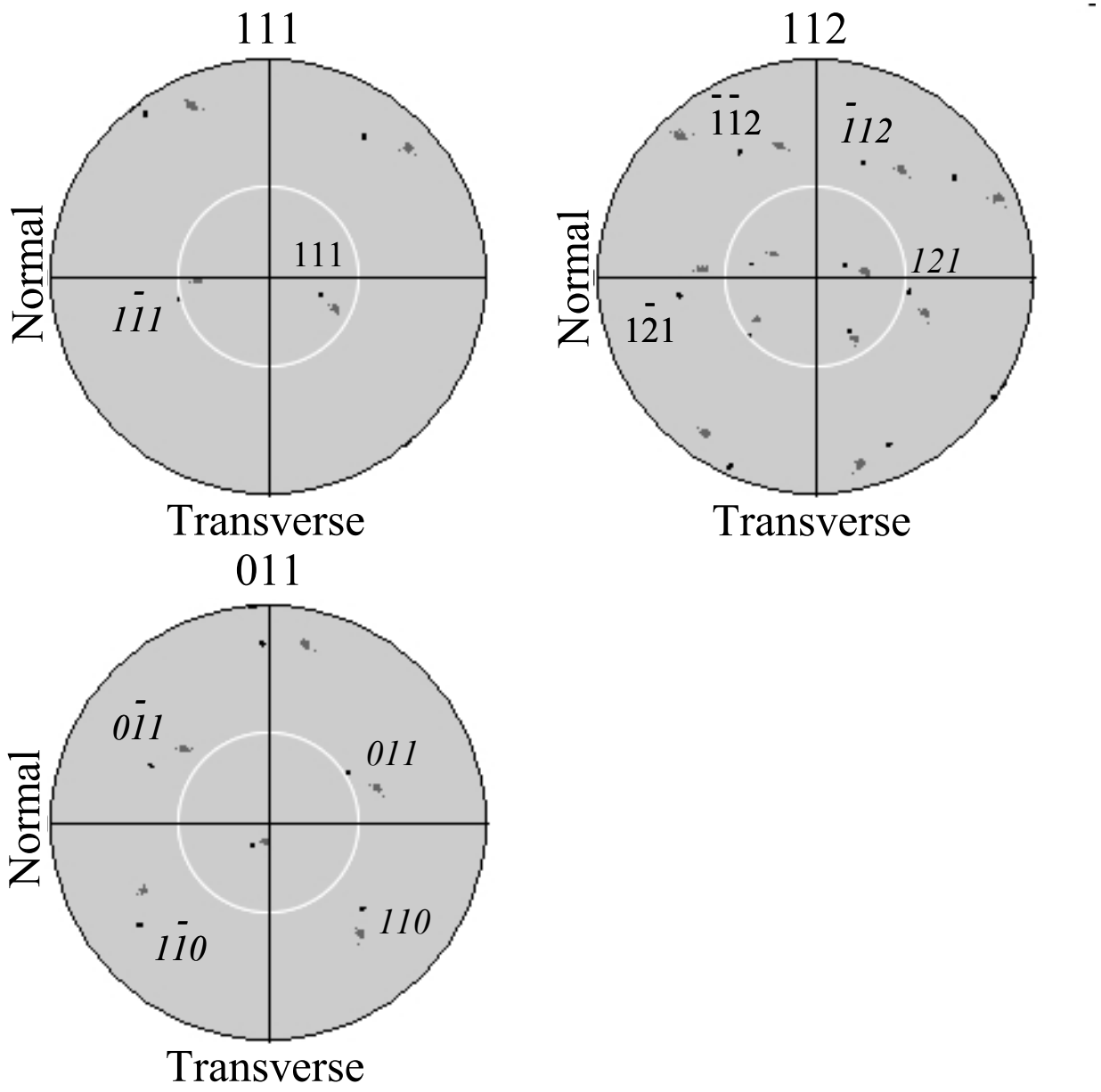

Figure A-10. Pole figures collected from sample Q2, with the tensile axis in the center of each pole figure. Initial orientation (black) and deformed orientation (grey) are overlaid. The primary (Italic text) and secondary (plain text) slip directions are labeled in the <111> pole figure. The slip plane normals of observed plane traces (italic text), and slip plane normals with no observed plane traces for slip systems that acquired enough resolved shear to possibly be active (plain text), are also labeled.

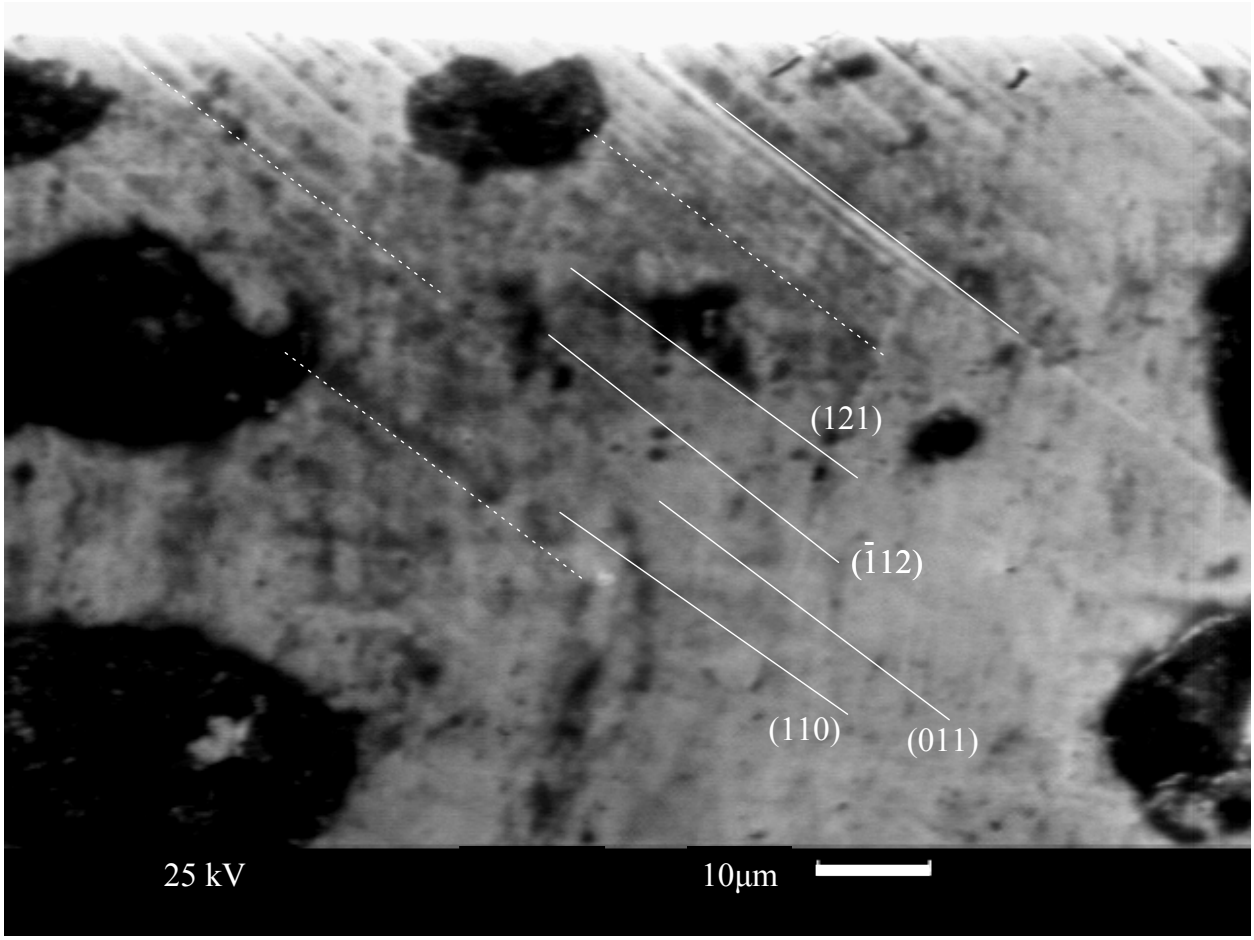

Figure A-11. Slip traces on the transverse surface of sample Q2 after deformation (SEI). Calculated slip traces are the long labeled lines to which the visible traces (short white solid and short white dashed lines) were matched.

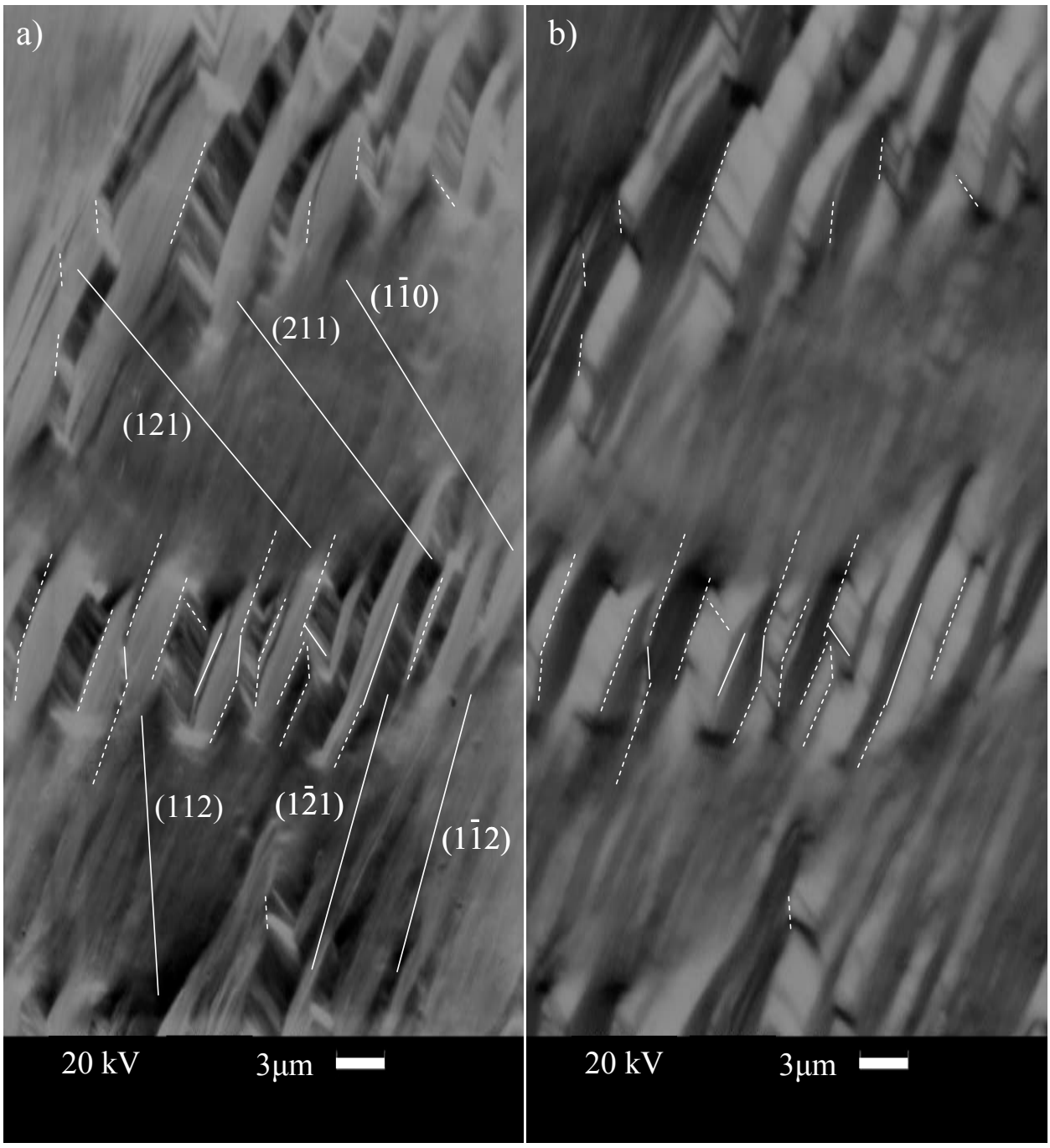

Figure A-12. Slip traces on the normal surface of sample S3 after deformation, a) SEI and b) BEI. Calculated slip traces are the long labeled lines to which the visible traces (short white solid and short white dashed lines) were matched.

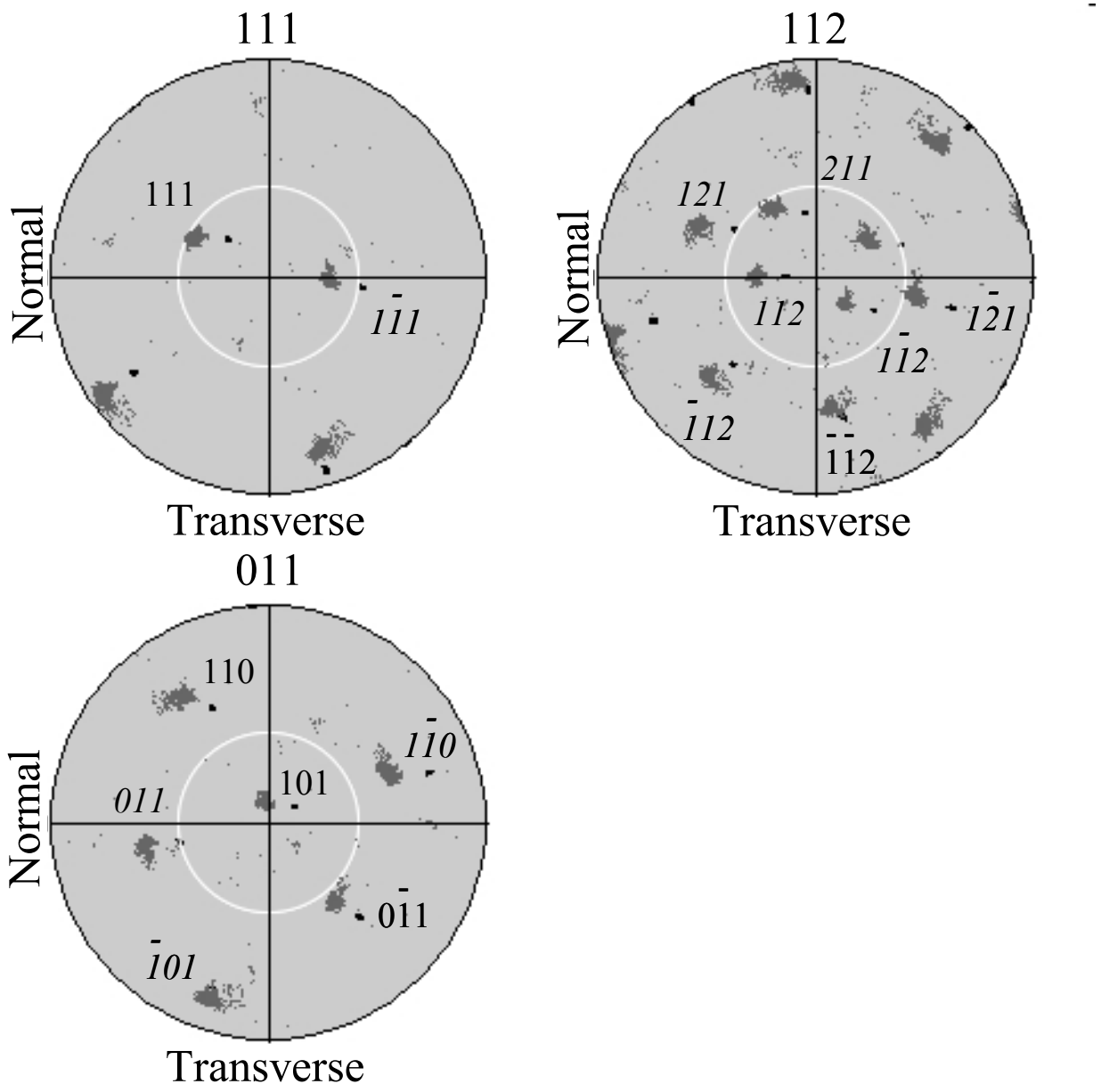

Figure A-13. Pole figures collected from sample S3, with the tensile axis in the center of each pole figure. Initial orientation (black) and deformed orientation (grey) are overlaid. The primary (Italic text) and secondary (plain text) slip directions are labeled in the <111> pole figure. The slip plane normals of observed plane traces (italic text), and slip plane normals with no observed plane traces for slip systems that acquired enough resolved shear to possibly be active (plain text), are also labeled.

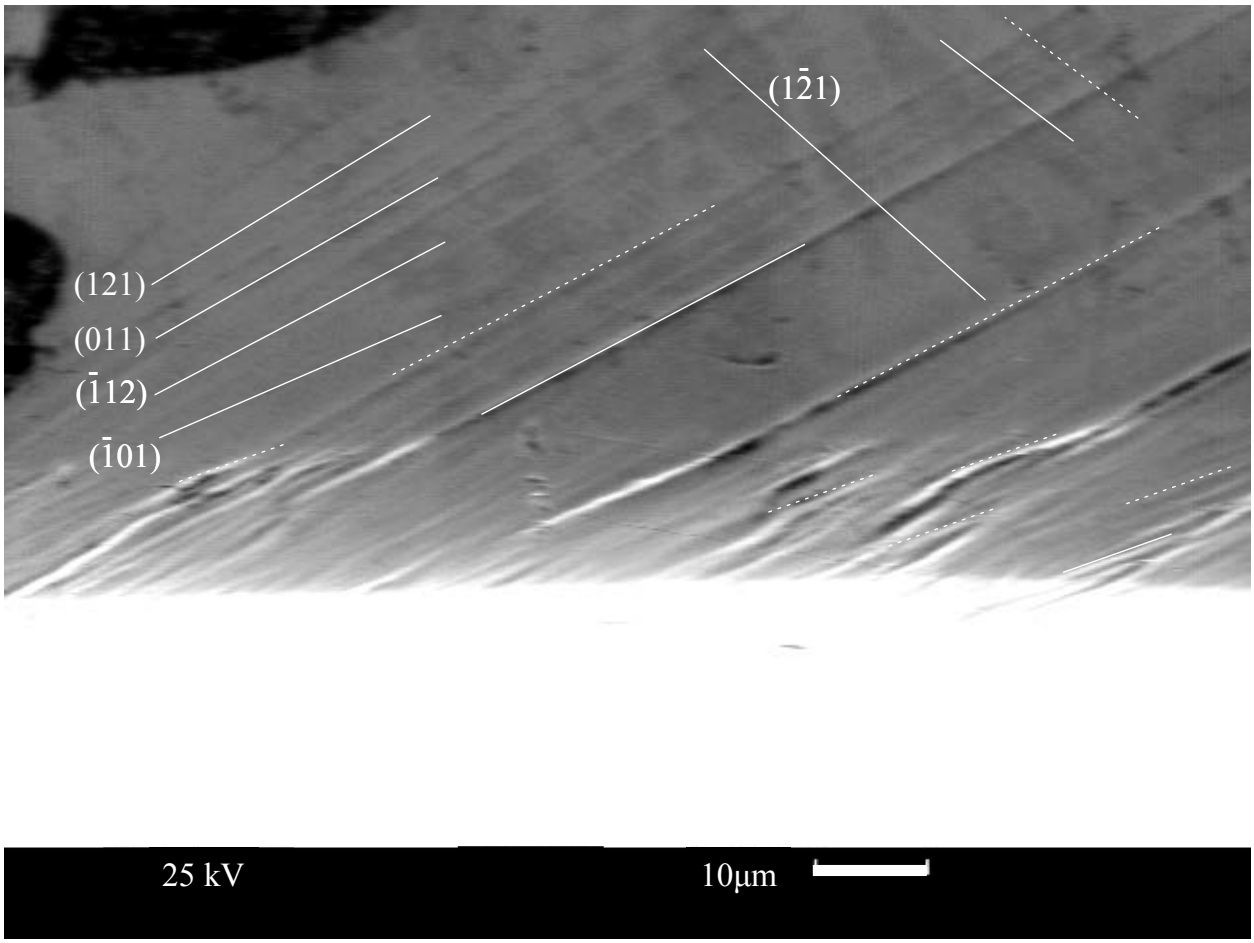

Figure A-14. Slip traces on the transverse surface of sample S3 after deformation (SEI). Calculated slip traces are the long labeled lines to which the visible traces (short white solid and short white dashed lines) were matched.

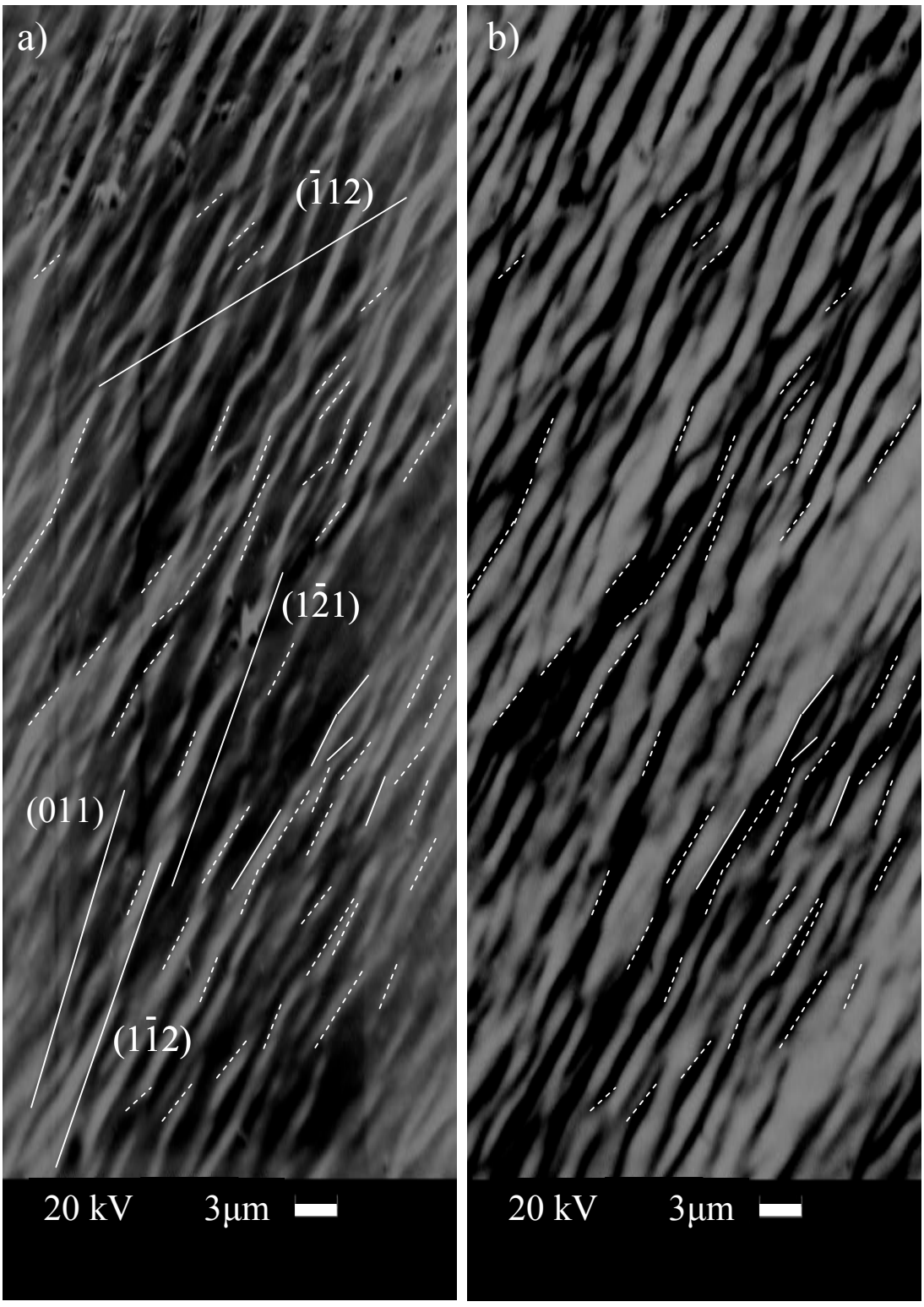

Figure A-15. Slip traces on the normal surface of sample R2 after deformation, a) SEI and b) BEI. Calculated slip traces are the long labeled lines to which the visible traces (short white solid and short white dashed lines) were matched.

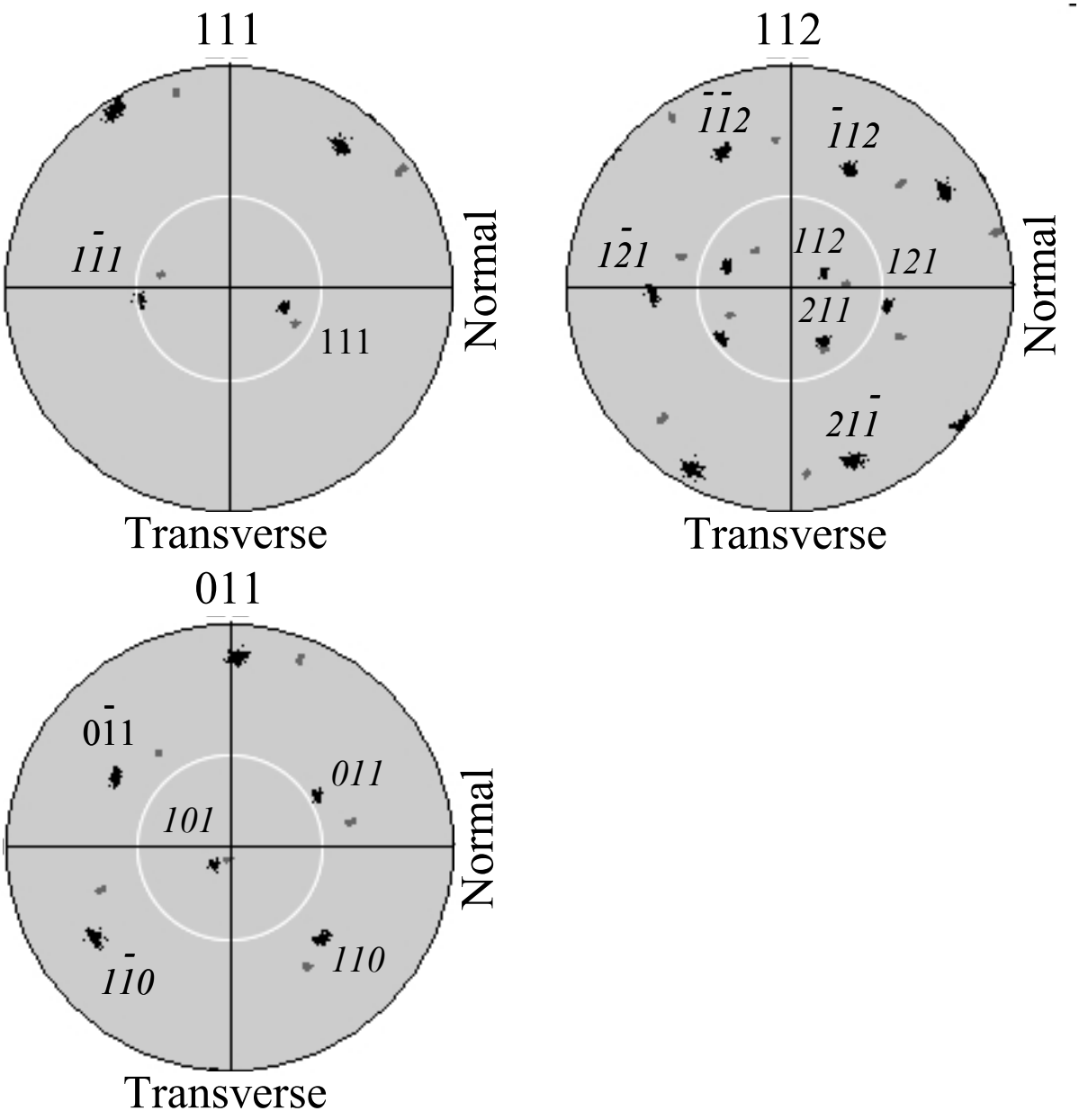

Figure A-16. Pole figures collected from sample R2, with the tensile axis in the center of each pole figure. Initial orientation (black) and deformed orientation (grey) are overlaid. The primary (Italic text) and secondary (plain text) slip directions are labeled in the <111> pole figure. The slip plane normals of observed plane traces (italic text), and slip plane normals with no observed plane traces for slip systems that acquired enough resolved shear to possibly be active (plain text), are also labeled.

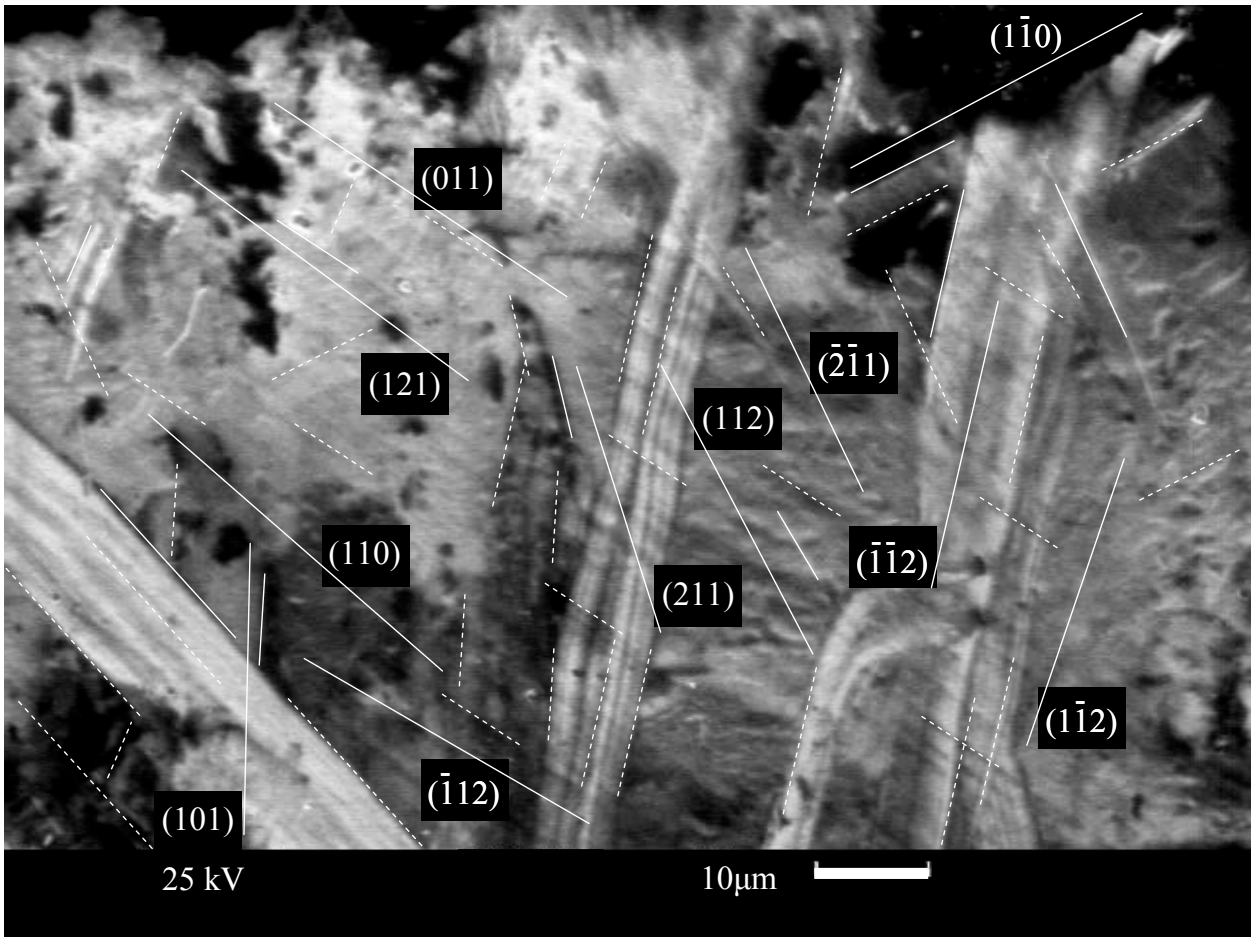

Figure A-17. Slip traces on the transverse surface of sample R2 after deformation (SEI). Calculated slip traces are the long labeled lines to which the visible traces (short white solid and short white dashed lines) were matched.

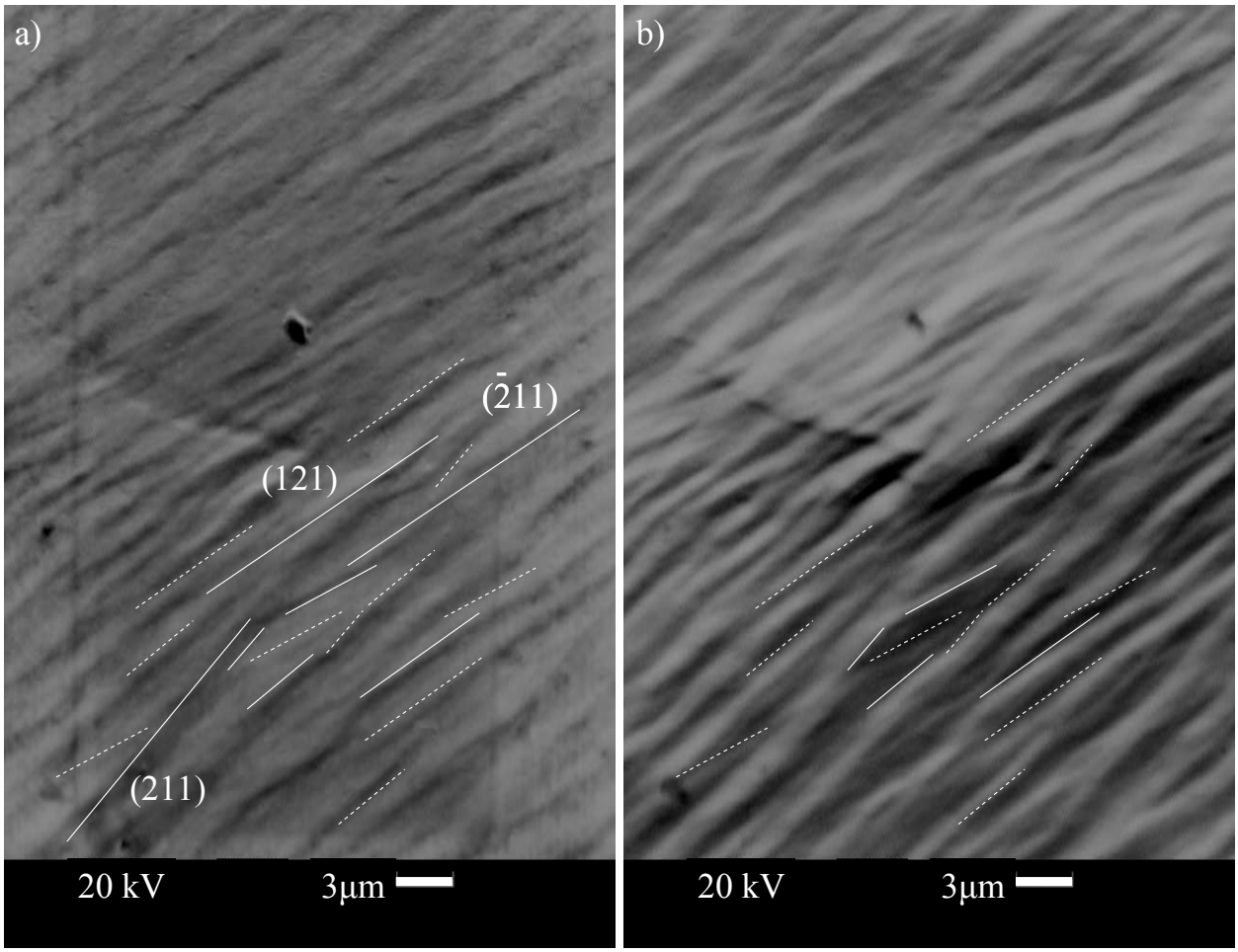

Figure A-18. Slip traces on the normal surface of sample W3 after deformation, a) SEI and b) BEI. Calculated slip traces are the long labeled lines to which the visible traces (short white solid and short white dashed lines) were matched.

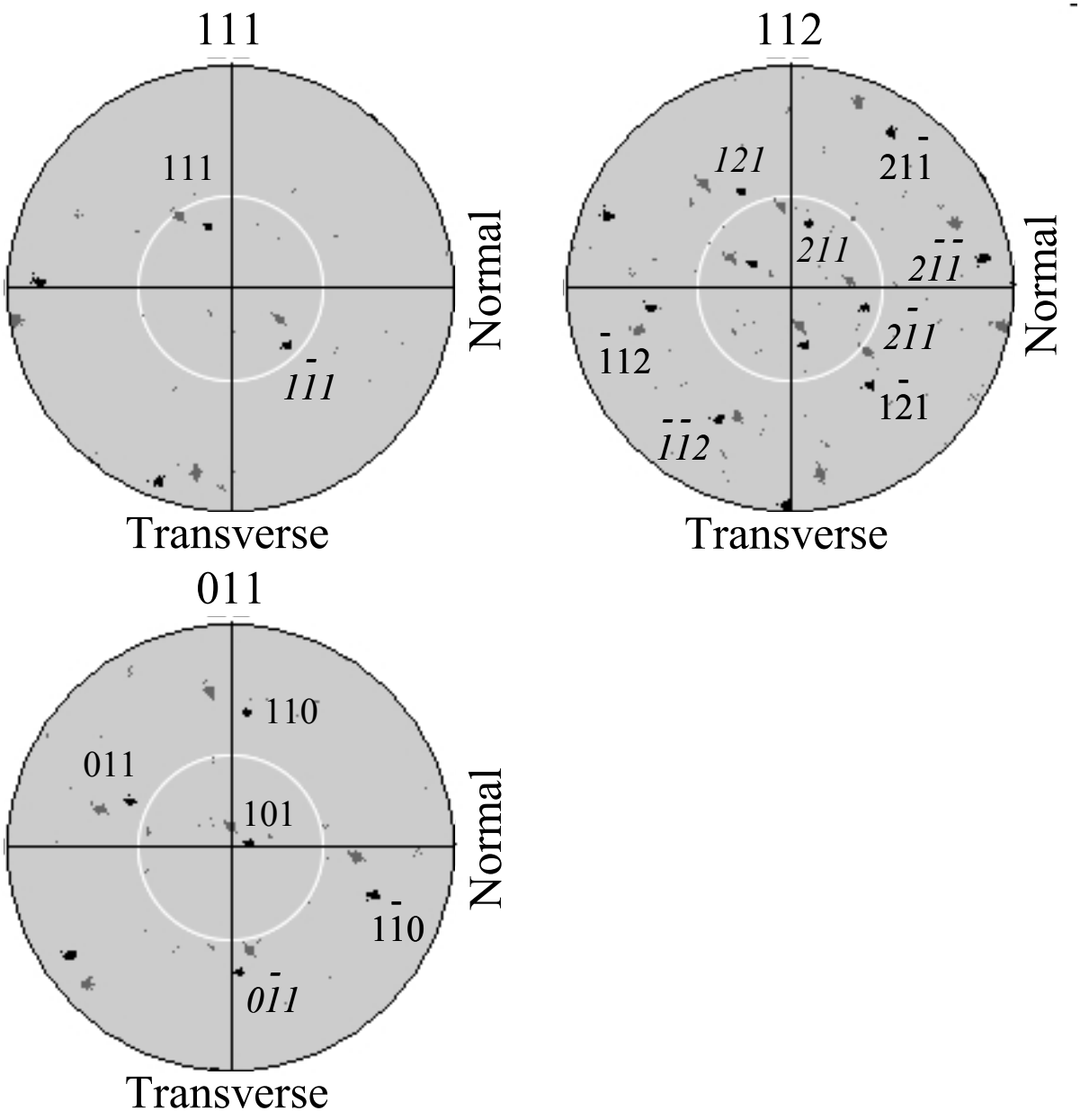

Figure A-19. Pole figures collected from sample W3, with the tensile axis in the center of each pole figure. Initial orientation (black) and deformed orientation (grey) are overlaid. The primary (Italic text) and secondary (plain text) slip directions are labeled in the <111> pole figure. The slip plane normals of observed plane traces (italic text), and slip plane normals with no observed plane traces for slip systems that acquired enough resolved shear to possibly be active (plain text), are also labeled.

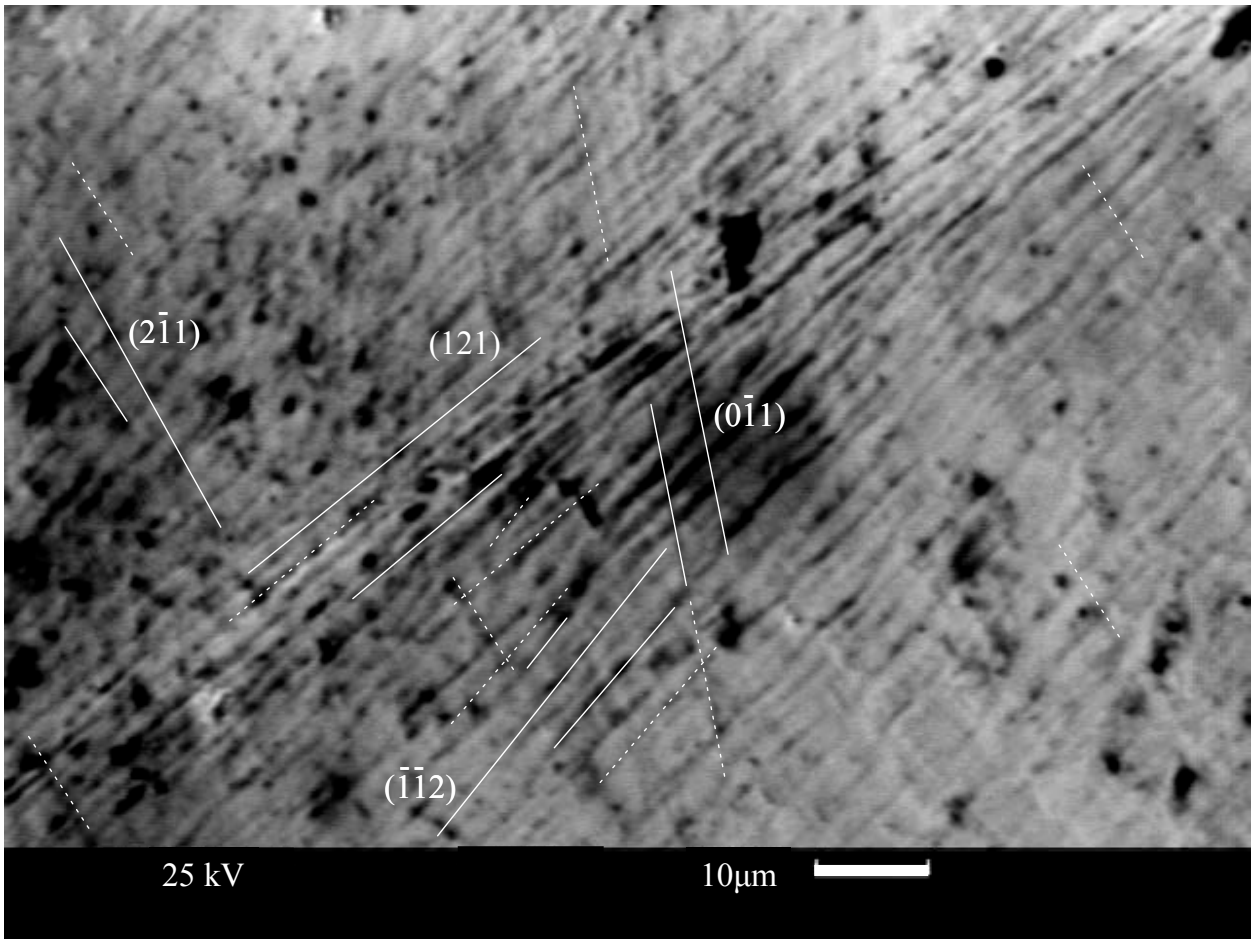

Figure A-20. Slip traces on the transverse surface of sample W3 after deformation (SEI). Calculated slip traces are the long labeled lines to which the visible traces (short white solid and short white dashed lines) were matched.

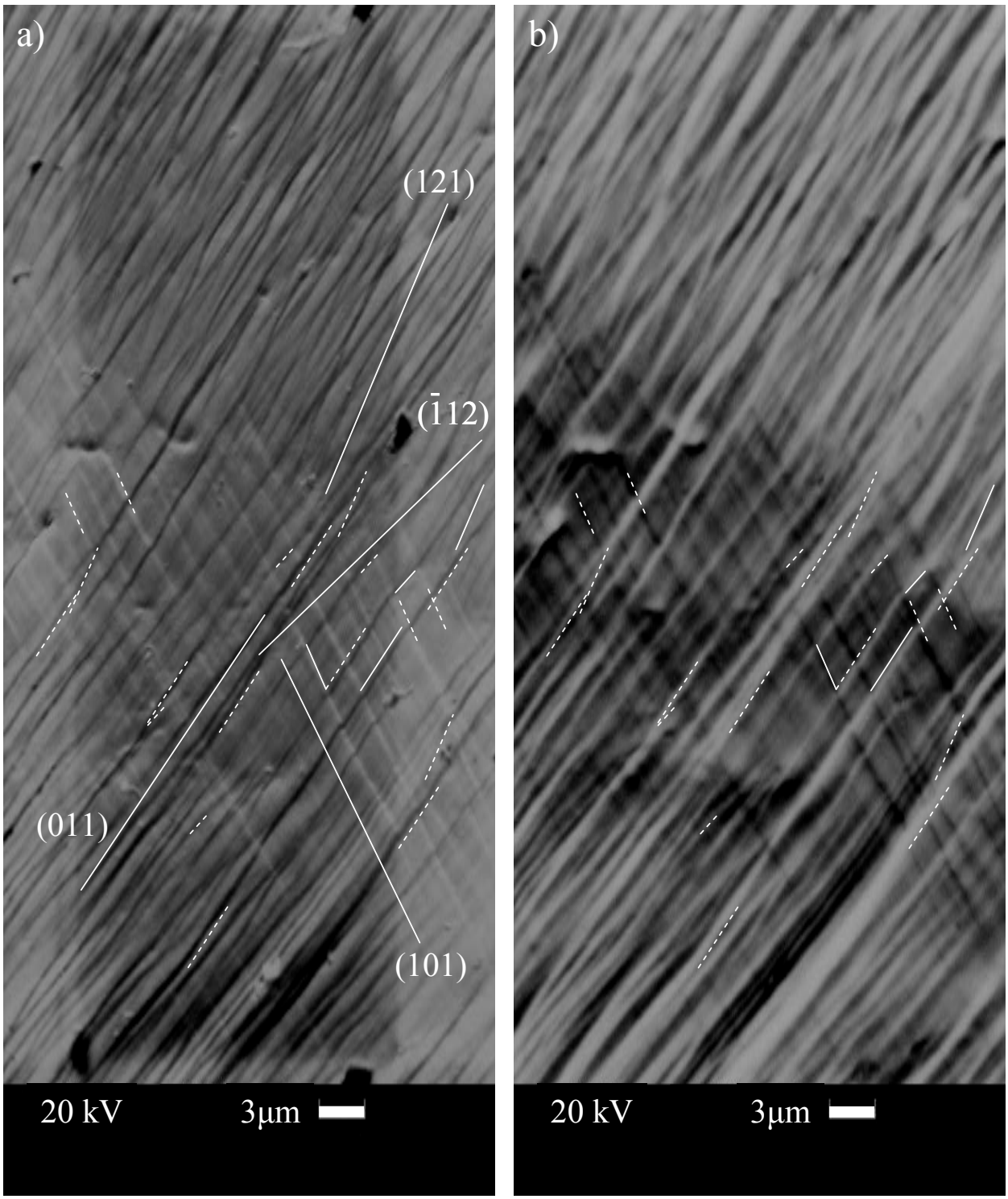

Figure A-21. Slip traces on the normal surface of sample U3 after deformation, a) SEI and b) BEI. Calculated slip traces are the long labeled lines to which the visible traces (short white solid and short white dashed lines) were matched.

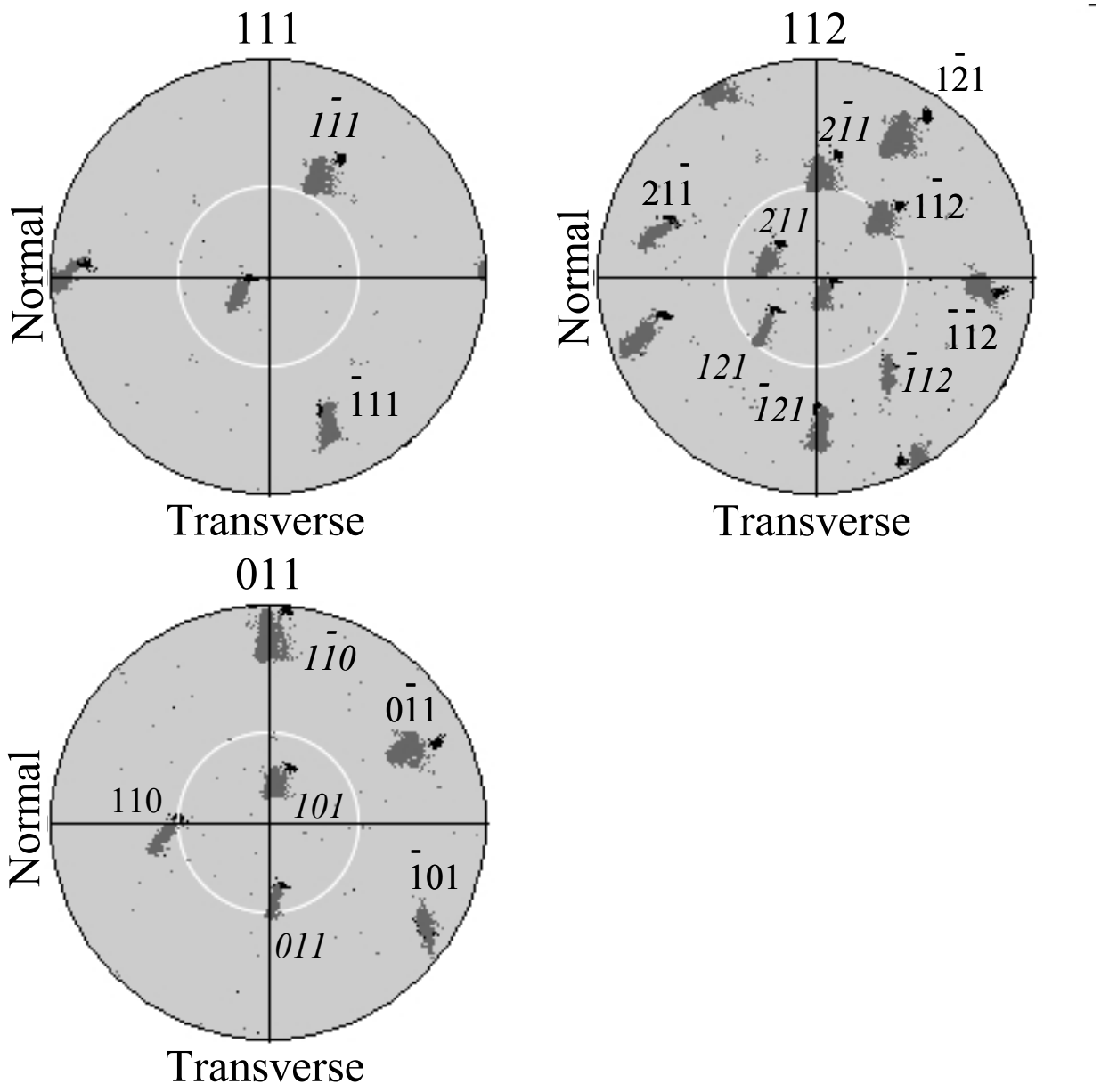

Figure A-22. Pole figures collected from sample U3, with the tensile axis in the center of each pole figure. Initial orientation (black) and deformed orientation (grey) are overlaid. The primary (Italic text) and secondary (plain text) slip directions are labeled in the <111> pole figure. The slip plane normals of observed plane traces (italic text), and slip plane normals with no observed plane traces for slip systems that acquired enough resolved shear to possibly be active (plain text), are also labeled.

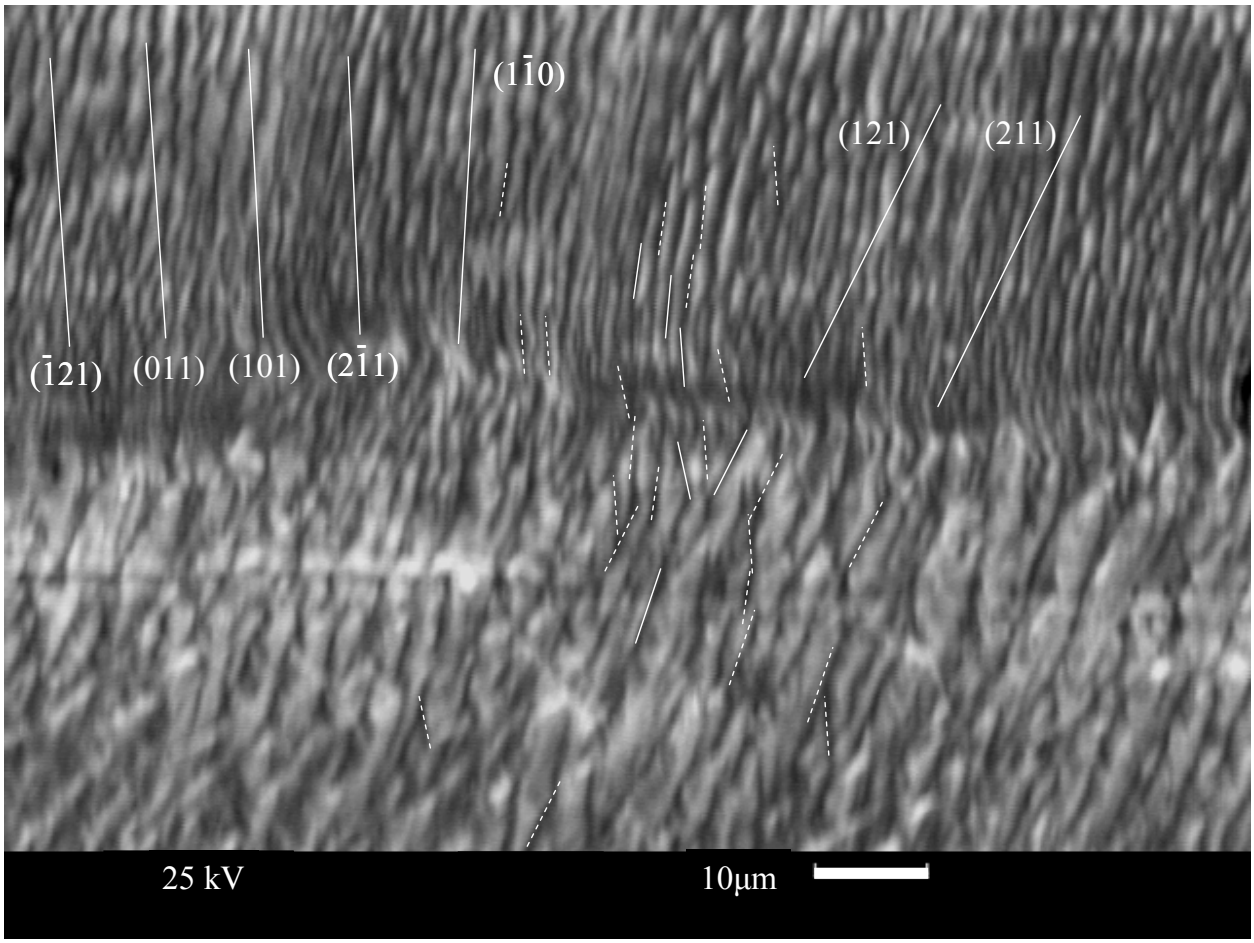

Figure A-23. Slip traces on the transverse surface of sample U3 after deformation (SEI). Calculated slip traces are the long labeled lines to which the visible traces (short white solid and short white dashed lines) were matched.

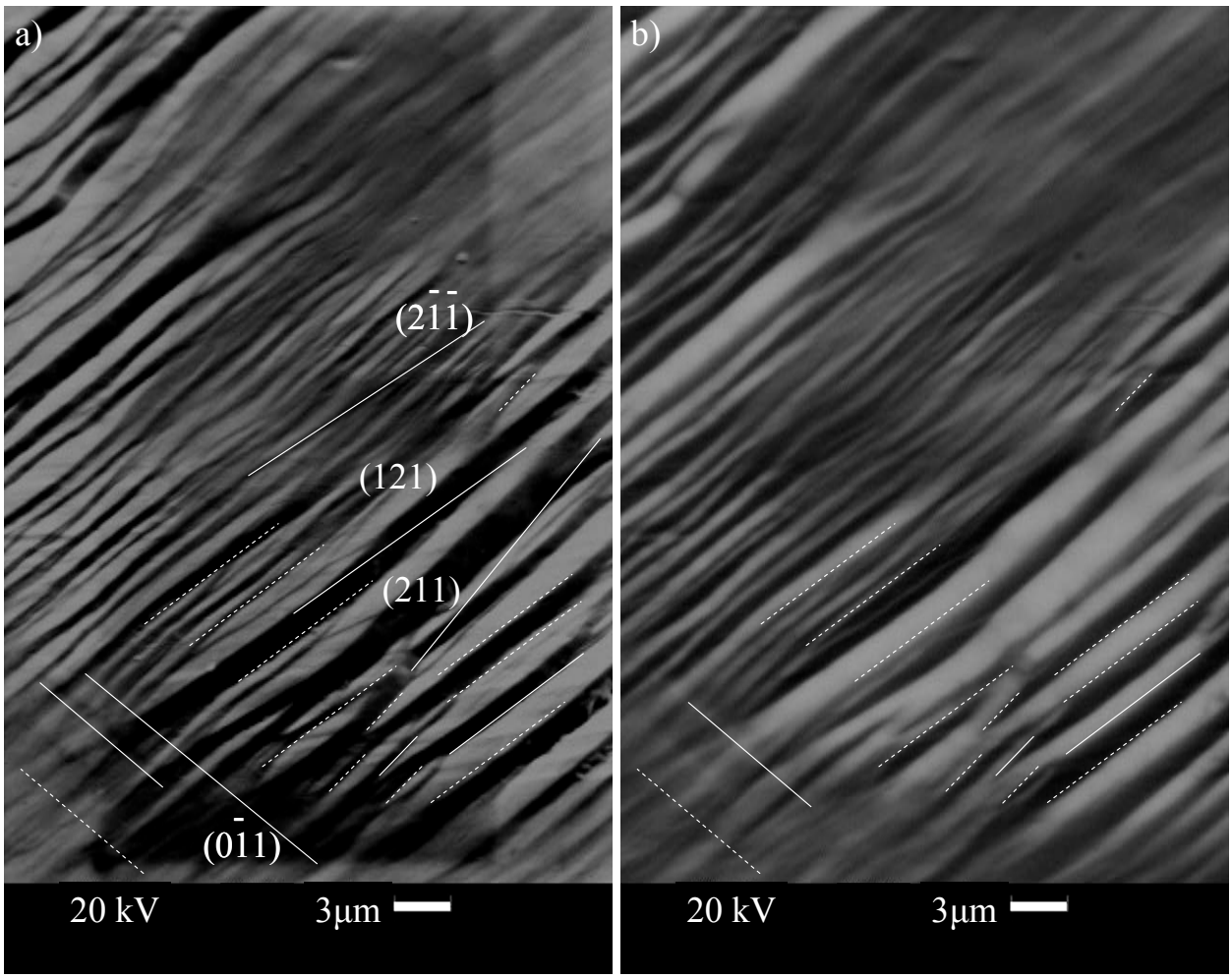

Figure A-24. Slip traces on the normal surface of sample V3 after deformation, a) SEI and b) BEI. Calculated slip traces are the long labeled lines to which the visible traces (short white solid and short white dashed lines) were matched.

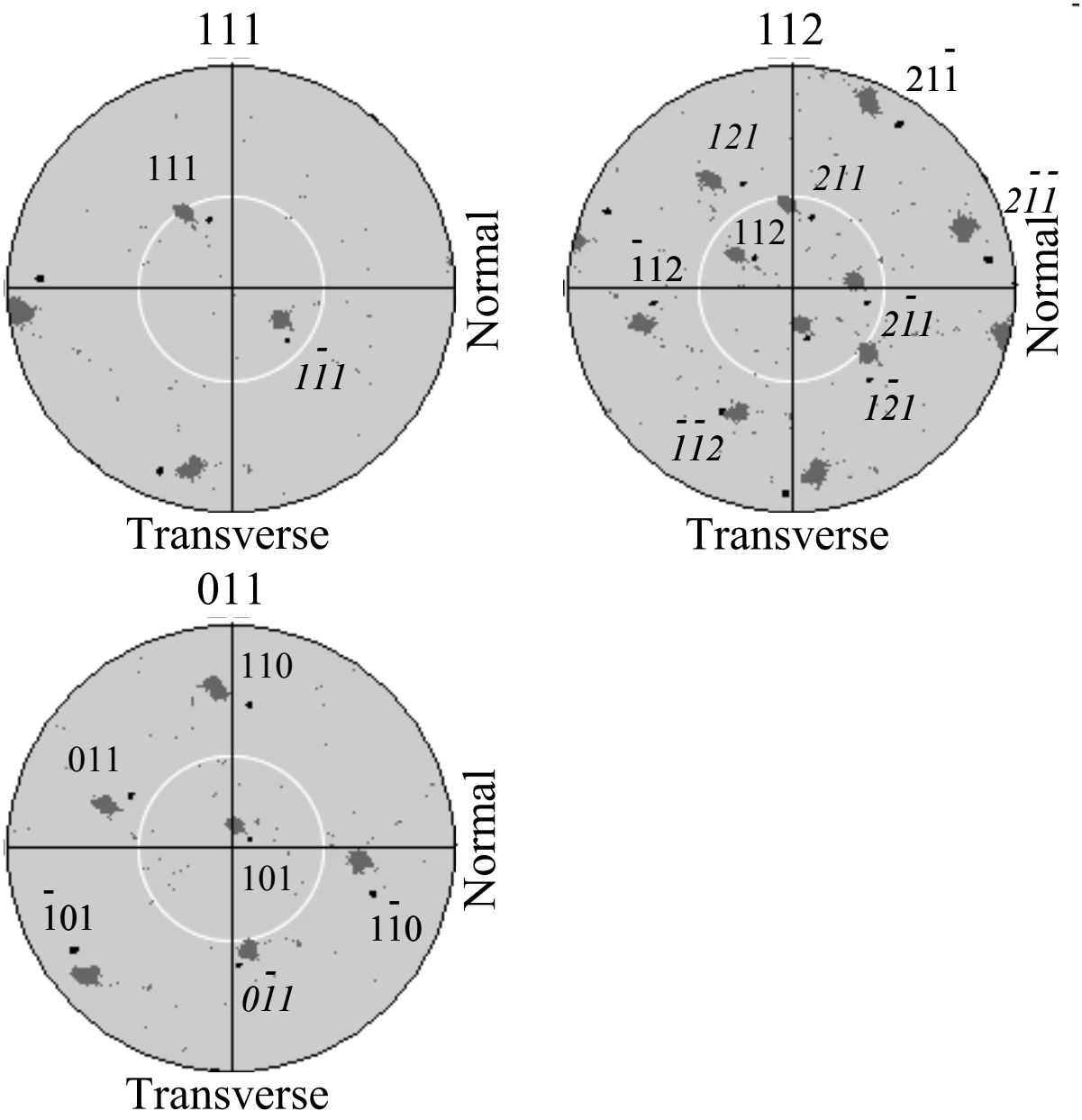

Figure A-25. Pole figures collected from sample V3, with the tensile axis in the center of each pole figure. Initial orientation (black) and deformed orientation (grey) are overlaid. The primary (Italic text) and secondary (plain text) slip directions are labeled in the <111> pole figure. The slip plane normals of observed plane traces (italic text), and slip plane normals with no observed plane traces for slip systems that acquired enough resolved shear to possibly be active (plain text), are also labeled.

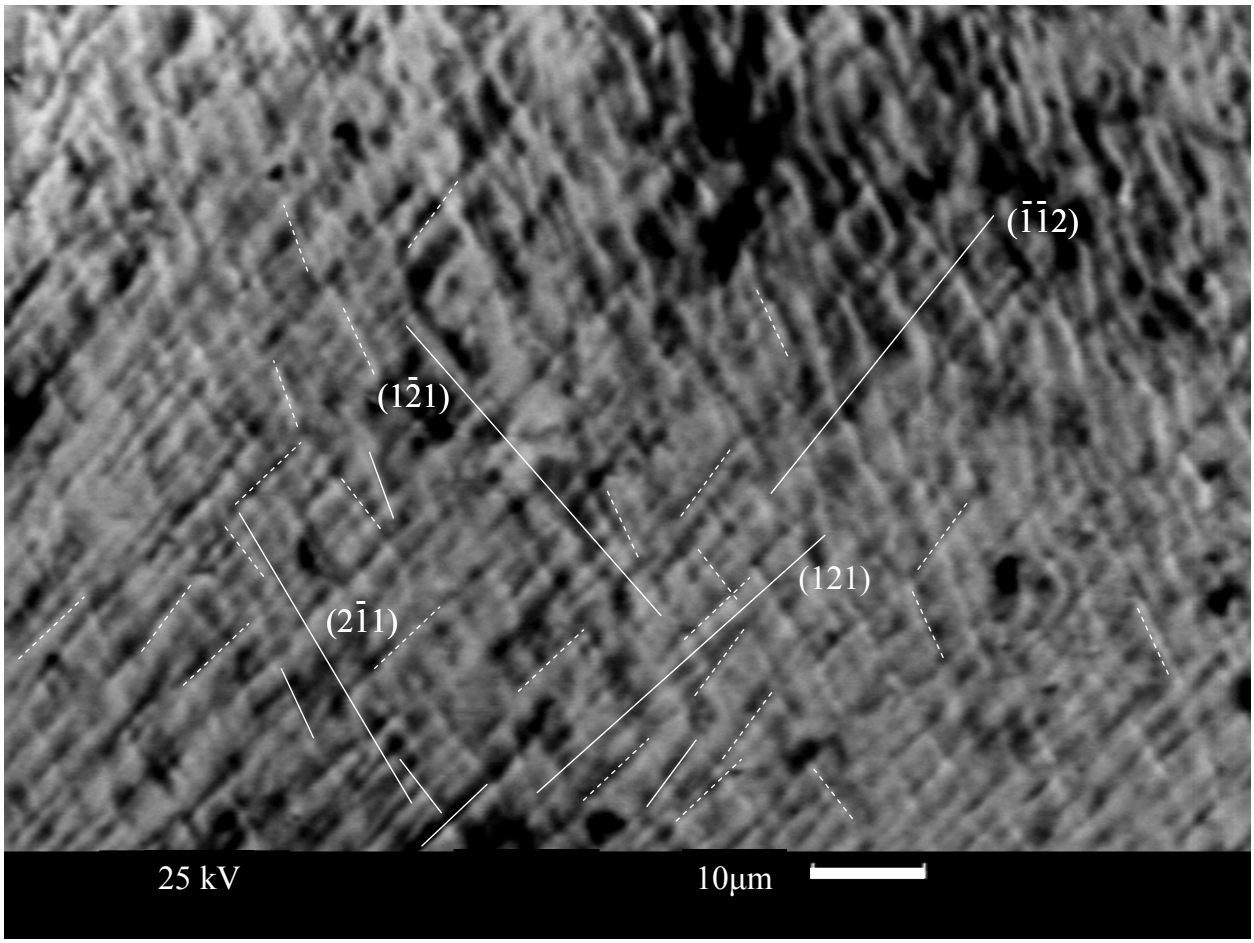

Figure A-26. Slip traces on the transverse surface of sample V3 after deformation (SEI). Calculated slip traces are the long labeled lines to which the visible traces (short white solid and short white dashed lines) were matched.

Table A-2. A list summarizing some of the initial deformation behavior and initial stresses on slip systems of the D&F sample set. The 0.2% strain offset yield stress, hardening slope at yield, and slip direction that rotated toward the tensile direction are given under the sample name in that order. Only slip systems with initial resolved glide shear stresses equal to or greater than half the highest initial resolved glide shear stress of their respective slip system family are listed. The greatest initial and final resolved glide shear stresses for the {110} and {112} slip system families are given in bold. Twinning (T) and anti-twinning (A) {112} planes are also indicated. Stresses were calculated in the same manner as the Tokyo-Denkai and Ningxia sample sets.

Sample, stresses (MPa), Hardening slope at yield, Slip direction that rotated toward TD	Potentially active slip system	Initial resolved shear stress at yield (MPa): glide, non-glide 1, 2, 3
D&F #21 11.1 barely $[1\bar{1}1]$	$[1\bar{1}1](\bar{1}12)$	**5.5** 2.5 0.3 2.0 T
	$[111](0\bar{1}1)$	**5.1** 1.5 1.7 1.9
	$[111](\bar{1}\bar{1}2)$	5.1 3.8 -1.9 3.6 A
	$[1\bar{1}1](011)$	4.9 4.6 -2.0 2.3
	$[\bar{1}\bar{1}1](101)$	4.8 3.5 -1.9 4.0
	$[\bar{1}\bar{1}1](112)$	4.8 1.3 2.0 1.9 T
	$[1\bar{1}1](\bar{1}01)$	4.6 -0.3 2.3 -0.3
	$[\bar{1}11](1\bar{1}2)$	3.9 2.1 -0.4 4.3 A
	$[111](1\bar{2}1)$	3.8 -1.3 3.6 -1.7 T
	$[111](\bar{1}01)$	3.7 5.1 -3.6 1.7
	$[\bar{1}\bar{1}1](2\bar{1}1)$	3.6 4.8 -4.0 2.0 A
	$[\bar{1}\bar{1}1](011)$	3.5 -1.3 4.0 -2.0
	$[\bar{1}11](101)$	3.4 0.2 3.9 0.4
	$[\bar{1}11](0\bar{1}1)$	3.3 3.4 -4.3 3.9
	$[1\bar{1}1](121)$	3.0 5.5 -2.3 0.3 A
D&F #8 12.2 barely $[1\bar{1}1]$	$[1\bar{1}1](011)$	**6.0** 2.4 0.8 2.5
	$[1\bar{1}1](121)$	**5.6** 4.8 -2.5 3.3 A
	$[111](0\bar{1}1)$	5.1 2.0 0.4 1.0
	$[1\bar{1}1](\bar{1}12)$	4.8 -0.7 3.3 -0.8 T
	$[111](\bar{1}\bar{1}2)$	4.8 4.1 -1.0 1.4 A
	$[111](1\bar{2}1)$	4.1 -0.7 1.4 -0.4 T
	$[\bar{1}11](101)$	4.0 1.9 0.2 4.5
	$[1\bar{1}1](110)$	3.6 6.0 -3.3 0.8
	$[\bar{1}11](1\bar{1}2)$	3.5 3.4 -4.5 4.7 A
	$[\bar{1}11](211)$	3.4 -0.1 4.7 -0.2 T
	$[111](\bar{1}01)$	3.2 5.1 -1.4 0.4

Table A-2 (cont'd)

D&F #10 10.1 slight $[1\bar{1}1]$	$[1\bar{1}1](121)$	**4.3** 3.1 -1.8 3.7 A
	$[1\bar{1}1](011)$	**4.3** 1.1 1.9 1.8
	$[\bar{1}11](101)$	3.6 2.4 -1.7 4.2
	$[\bar{1}11](211)$	3.5 0.7 2.6 1.7 T
	$[1\bar{1}1](110)$	3.2 4.3 -3.7 1.9
	$[1\bar{1}1](\bar{1}12)$	3.1 -1.2 3.7 -1.9 T
	$[111](\bar{1}\bar{1}2)$	2.8 2.0 -0.2 0.5 A
	$[111](0\bar{1}1)$	2.8 0.7 0.2 0.2
	$[\bar{1}11](1\bar{1}2)$	2.8 3.5 -4.2 2.6 A
	$[\bar{1}11](110)$	2.4 -1.2 4.2 -2.6
D&F #3 11.3 barely $[1\bar{1}1]$	$[1\bar{1}1](121)$	**4.7** 2.4 -0.2 3.9 A
	$[1\bar{1}1](011)$	**4.1** 0.1 3.7 0.2
	$[1\bar{1}1](110)$	4.0 4.1 -3.9 3.7
	$[\bar{1}11](211)$	2.9 1.1 1.5 3.6 T
	$[\bar{1}11](101)$	2.8 2.3 -3.6 5.1
	$[\bar{1}\bar{1}1](\bar{1}\bar{1}\bar{2})$	2.7 1.1 1.3 3.8 T
	$[\bar{1}\bar{1}1](\bar{1}0\bar{1})$	2.5 2.2 -3.8 5.1
	$[1\bar{1}1](\bar{1}12)$	2.4 -2.3 3.9 -3.7 T
	$[\bar{1}11](110)$	2.3 -0.4 5.1 -1.5
	$[1\bar{1}1](21\bar{1})$	2.3 4.7 -3.7 -0.2 N/A
	$[\bar{1}\bar{1}1](0\bar{1}\bar{1})$	2.2 -0.3 5.1 -1.3
D&F #19 15.2 Very high $[1\bar{1}1]$	$[1\bar{1}1](\bar{1}12)$	**7.3** 3.5 0.2 4.1 T
	$[111](\bar{1}\bar{1}2)$	**7.3** 3.9 -0.4 4.4 A
	$[\bar{1}\bar{1}1](112)$	7.0 3.3 0.4 4.3 T
	$[\bar{1}11](1\bar{1}2)$	7.0 3.6 -0.3 4.7 A
	$[111](0\bar{1}1)$	**6.4** 0.3 4.0 0.4
	$[1\bar{1}1](011)$	6.4 6.2 -4.1 4.3
	$[\bar{1}\bar{1}1](101)$	6.2 6.0 -4.3 4.7
	$[1\bar{1}1](\bar{1}01)$	6.2 -0.2 4.3 -0.2
	$[111](\bar{1}01)$	6.1 6.4 -4.4 4.0
	$[\bar{1}11](101)$	6.1 0.2 4.5 0.3
	$[\bar{1}\bar{1}1](011)$	6.0 -0.3 4.7 -0.4
	$[\bar{1}11](0\bar{1}1)$	6.0 6.1 -4.7 4.5
	$[111](1\bar{2}1)$	3.9 -3.4 4.4 -4.0 T
	$[1\bar{1}1](121)$	3.8 7.3 -4.3 0.2 A
	$[\bar{1}\bar{1}1](2\bar{1}1)$	3.8 7.0 -4.7 0.4 A

Table A-2 (cont'd)

D&F #4 19.4 high $[1\bar{1}1]$	$[1\bar{1}1](121)$	**6.4** 3.3 -0.3 7.5 A
	$[\bar{1}11](211)$	6.2 2.9 0.5 7.2 T
	$[\bar{1}\bar{1}1](\bar{1}\bar{1}\bar{2})$	5.7 2.8 0.2 7.5 T
	$[1\bar{1}1](011)$	**5.6** 0.1 7.2 0.3
	$[1\bar{1}1](110)$	5.5 5.6 -7.5 7.2
	$[\bar{1}11](101)$	5.4 5.2 -7.2 7.7
	$[\bar{1}11](110)$	5.2 -0.2 7.7 -0.5
	$[\bar{1}\bar{1}1](\bar{1}0\bar{1})$	5.0 4.9 -7.5 7.7
	$[\bar{1}\bar{1}1](0\bar{1}\bar{1})$	4.9 -0.1 7.7 -0.2
	$[1\bar{1}1](\bar{1}12)$	3.3 -3.1 7.5 -7.2 T
	$[\bar{1}11](1\bar{1}2)$	3.2 6.2 -7.7 0.5 A
D&F #1 12.2 high $[1\bar{1}1]$	$[1\bar{1}1](121)$	**5.8** 3.0 -0.1 1.9 A
	$[111](1\bar{2}1)$	5.7 2.7 0.1 1.7 T
	$[1\bar{1}1](011)$	**5.1** 0.1 1.8 0.1
	$[111](0\bar{1}1)$	5.0 4.9 -1.7 1.8
	$[1\bar{1}1](110)$	4.9 5.1 -1.9 1.8
	$[111](1\bar{1}0)$	4.9 -0.1 1.8 -0.1
	$[1\bar{1}1](\bar{1}12)$	3.0 -2.8 1.9 -1.8 T
	$[111](\bar{1}\bar{1}2)$	3.0 5.7 -1.8 0.1 A
D&F #2 13.0 moderate $[1\bar{1}1]$	$[1\bar{1}1](121)$	**6.2** 3.7 -0.5 2.3 A
	$[111](1\bar{2}1)$	5.9 2.3 0.5 1.4 T
	$[1\bar{1}1](011)$	**5.8** 0.7 1.8 0.5
	$[111](0\bar{1}1)$	5.5 4.8 -1.4 1.9
	$[1\bar{1}1](110)$	5.0 5.8 -2.3 1.8
	$[111](1\bar{1}0)$	4.8 -0.7 1.9 -0.5
	$[1\bar{1}1](\bar{1}12)$	3.7 -2.5 2.3 -1.8 T
	$[111](\bar{1}\bar{1}2)$	3.6 5.9 -1.9 0.5 A

Table A-2 (cont'd)

D&F #20 14.3 moderate $[1\bar{1}1]$	$[1\bar{1}1](\bar{1}12)$	**6.9** 3.5 0.0 3.9 A
	$[\bar{1}\bar{1}1](112)$	6.7 3.1 0.4 3.9 T
	$[111](\bar{1}\bar{1}2)$	6.7 3.6 -0.4 4.3 A
	$[\bar{1}11](1\bar{1}2)$	6.5 3.3 0.0 4.3 T
	$[\bar{1}\bar{1}1](101)$	**6.0** 5.7 -3.9 4.3
	$[111](0\bar{1}1)$	6.0 0.3 3.9 0.4
	$[1\bar{1}1](\bar{1}01)$	6.0 0.0 3.9 0.0
	$[1\bar{1}1](011)$	6.0 6.0 -3.9 3.9
	$[\bar{1}\bar{1}1](011)$	5.7 -0.3 4.3 -0.4
	$[111](\bar{1}01)$	5.7 6.0 -4.3 3.9
	$[\bar{1}11](0\bar{1}1)$	5.7 5.7 -4.3 4.3
	$[\bar{1}11](101)$	5.7 0.0 4.3 0.0
	$[\bar{1}\bar{1}1](2\bar{1}1)$	3.6 6.7 -4.3 0.4 A
	$[111](1\bar{2}1)$	3.6 -3.1 4.3 -3.9 T
	$[1\bar{1}1](\bar{2}\bar{1}1)$	3.5 -3.5 3.9 -3.9 T
	$[1\bar{1}1](121)$	3.5 6.9 -3.9 0.0 N/A
D&F #13 12.6 moderate $[1\bar{1}1]$	$[1\bar{1}1](011)$	**6.1** 2.5 0.5 1.8
	$[111](0\bar{1}1)$	6.0 3.5 -0.4 2.1
	$[1\bar{1}1](121)$	**5.6** 5.0 -1.8 2.4 A
	$[111](1\bar{2}1)$	5.5 0.5 1.8 0.4 T
	$[1\bar{1}1](\bar{1}12)$	5.0 -0.6 2.4 -0.5 T
	$[111](\bar{1}\bar{1}2)$	5.0 5.5 -2.1 1.8 A
	$[1\bar{1}1](110)$	3.6 6.1 -2.4 0.5
	$[111](1\bar{1}0)$	3.5 -2.6 2.1 -1.8
D&F #17 14.1 moderate $[1\bar{1}1]$	$[111](0\bar{1}1)$	**7.0** 2.6 1.0 2.4
	$[1\bar{1}1](011)$	6.8 4.6 -1.2 3.0
	$[1\bar{1}1](\bar{1}12)$	**6.6** 1.4 1.8 1.2 T
	$[111](\bar{1}\bar{1}2)$	6.5 5.5 -2.4 3.3 A
	$[111](1\bar{2}1)$	5.5 -1.0 3.3 -1.0 T
	$[1\bar{1}1](121)$	5.2 6.6 -3.0 1.8 A
	$[\bar{1}\bar{1}1](101)$	4.7 3.4 -2.8 6.1
	$[\bar{1}\bar{1}1](112)$	4.7 1.2 3.3 2.8 T
	$[1\bar{1}1](\bar{1}01)$	4.6 -2.2 3.0 -1.8
	$[111](\bar{1}01)$	4.4 7.0 -3.3 1.0
	$[\bar{1}11](1\bar{1}2)$	4.3 3.0 -2.7 6.3 A
	$[\bar{1}11](101)$	4.2 1.0 3.5 2.7
	$[\bar{1}\bar{1}1](2\bar{1}1)$	3.5 4.7 -6.1 3.3 A

BIBLIOGRAPHY

BIBLIOGRAPHY

1. Padamsee H, Knobloch J, Hays T. RF Superconductivity for Accelerators. Wiley, John & Sons, Incorporated, 1998.

2. Bardeen J, Cooper LN, Schriefer JR. Theory of Superconductivity. *Physics Review*, Vol. 108, pp. 1175, 1957.

3. Kneisel P, Myneni GR, Ciovati G, Sekutowicz J, Carneiro T. Preliminary Results from Single Crystal and Very Large Grain Niobium Cavities. *Proceeding of 2005 Particle Accelerator Conference*, pp. 3991, Knoxville, TN, 2005.

4. Visentin B, Charrier JP, Congretel G. Change of RF Superconductivity Parameters Induced by Heat Treatment on Niobium Cavities. *Proceedings of the 2001 Particle Accelerator Conference*, Chicago, Illinois, 2001.

5. Moura HRS. Melting and Purification of Niobium. *Proceedings of the International Symposium of Niobium*, pp. 147, Orlando, Florida, 2001.

6. Bieler TR, Baars DC, Jiang H, Compton C, Grimm TL. Mechanical Properties of Nb. *Midwestern SRF Materials Research Meeting,* NSCL, March 17th, East Lansing, 2006.

7. Kneisel P, Palmieri V. Development of seamless niobium cavities for accelerator applications. *Proceedings of the 1999 Particle Accelerator Conference*, New York, New York, 1999.

8. Jiang H, Bieler TR, Compton C, Grimm TL. Cold Rolling Evolution in High Purity Niobium Using a Tapered Wedge Specimen. *12th International workshop on RF Superconductivity (SRF 2005), Physica C*, Vol. 441, pp. 118, 2006.

9. Singer W, Kaiser H, Singer X, Weichert G, Jelezov I, Khabibuline T, Skasyrskaia A, Kneisel P, Fujino T, Saito K. Hydroforming of superconducting tesla cavities. *SRF Workshop 2001,* 2001.

10. Duesbery MS, Foxall RA, Hirsch PB. The plasticity of pure niobium single crystals. *Colloque C 3 supplement au, Journal de Physique,* Vol. 27, Nos.7-8, pp. 193, 1966.

11. Seeger A, Holzwarth U. Slip planes and kink properties of screw dislocations in high-purity niobium. *Philosophical Magazine*, Vol. 86, Nos. 25-26, pp. 3861, 1-11 September 2006.

12. Hirth JP, Lothe J. "Theory of Dislocations 2nd Edition". Wiley, 1982.

13. Hull D, Bacon DJ. "Introduction to Dislocations 4th Edition". Butterworth-Heinemann, 2001.

14. Dieter GE. "Mechanical Metallurgy, 3rd Edition". McGraw-Hill, Inc. Boston, MA, 1986.

15. Seeger A. “Dislocations and Mechanical Properties of Crystals”. John Wiley and Sons, Inc., New York, 1957.

16. Lee DN. “Texture and related phenomena”. The Korean Institute for Metals and Materials, 2006.

17. Doherty RD, Hughes DA, Humphreys FJ, Jonas JJ, Juul Jensen D, Kassner ME, King WE, McNelley TR, McQueen HJ, Rollet AD. Current issues in recrystallization: a review. *Materials Science and Engineering A,* Vol. 238, pp. 219, 1997.

18. Winther G. Slip patterns and preferred dislocation boundary planes. *Acta Materialia*, Vol. 51, pp. 417, 2003.

19. Kuhlmann-Wilsdorf D, Hansen N. Geometrically necessary, incidental, and subgrain boundaries. *Scripta Metallurgica et Materialia*, Vol. 25, pp. 1557, 1991.

20. Hansen N. Deformation microstructures. *Scripta Metallurgica et Materialia,* Vol. 27, pp. 1447, 1992.

21. Schmid E, Boas W. “Kristallplastiztät unter besonderer Berücksichtigung der Metalle”. Springer-Verlag, Berlin 1935.

22. Yalcinkaya T, Brekelmans WAM, Geers MGD. BCC single crystal plasticity modeling and its experimental identification. *Modeling and Simulation in Materials Science Engineering*, Vol. 16, pp 1, 2008.

23. Gough H. The Behaviour of a Single Crystal of α-Iron Subjected to Alternating Torsional Stresses. *Proceedings of the Royal Society of London, Series A.* Vol. 118, Iss. 780, pp. 498, 1928.

24. Duesbery MS, Foxall RA. A Detailed Study of the Deformation of High Purity Niobium Single Crystals. *Philosophical Magazine*, Vol. 20, Issue 166, pp. 719, 1969.

25. Seeger A. Progress and problems in the understanding of the dislocation relaxation process in metals. *Materials Science and Engineering*, A370, pp. 50, 2004.

26. Furubayashi E. Behavior of Dislocations in Fe-3% Si under Stress. *Journal of the Physical Society of Japan*, Vol. 27, pp. 130, 1969.

27. Louchet F, Kubin LP, Vesely D. "In situ" deformation of BCC crystals at low temperatures by HVEM. Dislocation mechanisms and rate equation. *Philosophical Magazine*, Vol. A 39, pp. 433, 1979.

28. Imura T. Mechnical properties of bcc metals. Meshii M ed., TMS-AIME, Warrendale, PA, pp. 65, 1982.

29. Foxall RA, Statham CD. Dislocation arrangements in deformed single crystals of niobium-molybdenum alloys and niobium-9 at.% rhenium. *Acta Metallurgica*, Vol. 18, pp. 1147, 1970.

30. R Peierls. The size of a dislocation. *Proc. Phys. Soc B*, Vol. 52, pp. 34, 1940.

31. Duesbery MS, Vitek V. Plastic anisotropy in B.C.C. transition metals. *Acta Materialia*, Vol. 46 No. 5, pp. 1481, 1998.

32. Ackland GJ, Thetford R, Vitek V. Validity of the second moment tight-binding model. *Journal of Physics F: Metal Physics*, Vol. 18, L153, 1988.

33. Ackland GJ, Vitek V. Many-body potentials and atomic-scale relaxations in noble-metal alloys. *Physical Review B*, Vol. 41, pp. 10324, 1990.

34. Sherwood PJ, Guiu F, Kim HC, Pratt PL. Plastic Anisotropy of Tantalum, Niobium, and Molybdenum. *Canadian Journal of Physics*, Vol. 45(2), pp. 1075, 1967.

35. Stein DF. The effect of orientation and impurities on the mechanical properties of molybdenum single crystals. *Canadian Journal of Physics*, 45(2), pp. 1063, 1967.

36. Guiu F, Pratt PL. The Effect of Orientation on the Yielding and Flow of Molybdenum Single Crystals. *Physica Status Solidi (B)*, 15(2), pp. 539, 1966.

37. Bassani JL, Ito K, Vitek V. Complex macroscopic flow arising from non-planer dislocation core structures. *Materials Science Engineering*, A319-321, pp. 97, 2001.

38. Chambers RH, Schultz J. Dislocation relaxation spectra in plastically deformed refractory b.c.c. metals. *Acta Metallurgica*, Vol. 10(4), pp. 466, 1962.

39. Chambers RH. "Physical Acoustics". Vol. III Pt. A, Chapter 4, Mason WP ed., Academic Press, New York, 1966.

40. Seeger A. Peierls barriers, kinks, and flow stress: Recent progress. *Zeitschrift für Metallkunde (now the International Journal of Materials Research)*, Vol. 93, pp. 760, 2002.

41. Eshelby JD. The Interaction of Kinks and Elastic Waves. *Proceedings of the Royal Society of London A*, Vol. 266, pp. 222, 1962.

42. Kramers HA. Brownian motion in a field of force and the diffusion model of chemical reactions. *Physica*, Vol. 7(4), pp. 284, 1940.

43. Seeger A. "Dislocations 1984". Editors Veyssiere, Kubin L, Castaing J, CNRS Paris, pp. 141, 1984.

44. Seeger A. The temperature and strain-rate dependence of the flow stress of body-centered cubic metals: A theory based on kink-kink interactions. *Zeitschrift für Metallkunde (now the International Journal of Materials Research)*, Vol. 72(6), pp. 369, 1981.

45. Shockley W. Solid state physics in electronics and in metallurgy. *American Institute of Mining and Metallurgical Engineers - Journal of Metals*, Vol. 4(8), pp 829, 1952.

46. Brunner D, Diehl J. Softening of α-iron by solute nitrogen atoms investigated between 30 and 300 K by use of stress-relaxation measurements. *Materials Science and Engineering A*, Vol. 164, pp. 350, 1993.

47. Seeger A, Wasserbach W. Anomolous Slip- A feature of high purity Body-Centered metals. *Physica Status Solidi (A)*, Vol. 189(1), pp. 27, 2002.

48. Alam MN, Blackman M, Pashley DW. High-Angle Kikuchi Patterns. *Proceedings of the Royal Society of London A*, Vol. 221, pp. 224, 1954.

49. Dingley DJ, Randle V, J. Microtexture determination by electron back-scatter diffraction. *Journal of Materials. Science*, Vol. 27(17), pp. 4545, 1992.

50. Wright SI, Adams BL. Automatic analysis of electron backscatter diffraction patterns. *Metallurgical Transactions A*, Vol. 23(3), pp. 759, 1992.

51. Krieger Lassen NC, Juul Jensen D, Conradsen K. Image processing procedures for analysis of electron back scattering patterns. *Scanning Microscopy*, Vol. 6, pp. 115, 1992.

52. Adams BL, Wright SI, Kunze K. Orientation imaging: The emergence of a new microscopy. *Metallurgical Transactions A*, Vol. 24(4), pp. 819, 24A, 1993.

53. Humphreys FJ. Review- Grain and subgrain characterization by electron backscatter diffraction. *Journal of Materials Science*, Vol. 36, pp. 3833, 2001.

54. Humphreys FJ. Quantitative metallography by electron backscattered diffraction. *Journal of Microscopy*, Vol. 195(3), pp 170, 1999.

55. Humphreys FJ, Brough I. High resolution electron backscatter diffraction with a field emission gun scanning electron microscope. *Journal of Microscopy*, Vol. 195, pp. 6, 1999.

56. Pettersen T, Heiberg G, Hjelen J. Measurements of spatial resolution of EBSD in the SEM as a function of atomic number and high voltage. *Proceedings of the 14th International Congress on Electron Microscopy*, Vol. 3, pp. 775, Calderón Benavides HA and José Yacamán M eds., Cancun, Mexico, 1998.

57. Goldstein JL, Joy DC, Romig AD, C. E. Lyman CE, C. Fiori C, Lifshin E. "Scanning Electron Microscopy and X-ray Microanalysis". Plenum, New York, 1992.

58. Schwartz AJ, Kumar M, and Adams BL, editors. "Electron Backscatter Diffraction in Materials Science". Kluwer Academic/Plenum Publishers, 2000.

59. Bunge HJ. "Texture analysis in materials science: mathematical methods". Butterworths, 1982.

60. Zamiri A, Pourboghrat F. A novel yield function for single crystals based on combined constraints optimization. *International Journal of Plasticity*, Vol. 26(5), pp. 731, 2010.

61. Zamiri AR. "Computationally efficient crystal plasticity models for polycrystalline materials". Thesis (PH. D.)--Michigan State University. Mechanical Engineering, 2008.

62. ABAQUS manual (2002). Hibbit, Karlsson & Sorensen Inc, Providence, RI, Version 6.3.

63. Baars D, Bieler TR, Zamiri A, Pourboghrat F, Compton C. Crystal Orientation Effects During Fabrication of Single or Multi-Crystal Nb SRF Cavities. *Proceedings of the 13th International Workshop on RF Superconductivity: Beijing, China, 2007*. Hao JK, Huang SL, Zhao K, Editors, Peking University, Beijing, China, pp. 111, 2009.

64. Mapar A. Unpublished research.

65. V Vitek, M Mrovec, JL Bassani. Influence of non-glide stresses on plastic flow: atomistic to continuum modeling. *Materials Science and Engineering A*, Vol. 365, pp. 31, 2004.

66. Bassani JL, Racherla V, Vitek V, Groger R. Effects of Non-Glide Stresses on Plastic Flow and Failure Mechanisms arising from Non-planer Dislocation Core Structures: Multiscale Simulations of Non-Associated Flow. Mechanics of Materials presentation, June 2004.

67. Wipf H editor. Topics in Applied Physics. Vol. 73, pp. 51, Springer-Verlag Berlin Heidelberg, 1997.

68. Kingery WD, Bowen HK, Uhlmann DR. "Introduction to Ceramics, 2nd Edition". John Wiley & Sons, New York, 1976.

69. Cottrell AH. Theory of brittle fracture in steel and similar metals. *Transactions of the Metallurgical Society AIME*, Vol. 212, pp. 192, 1958.

70. Seeger A. The Flow Stress of High-Purity Refractory Body-Centred Cubic Metals and its Modification by Atomic Defects. *Journal de Physique IV (France)*, Vol. 5, C7-45, 1995.

71. Groger R, Bailey AG, Vitek V. Multiscale modeling of plastic deformation of molybdenum and tungsten: I. Atomistic studies of the core structure and glide of 1/2[111] screw dislocations at 0 K. *Acta Materialia*, Vol 56, pp. 5401, 2008.

72. Calnan EA, Clews CJB. LXV. The development of deformation textures in metals. -Part II. Body-centred cubic metals. *Philosophical Magazine Series 7*, Vol. 42, pp. 616, 1951.

73. Xie KY, Wang Y, Ni S, Liao X, Cairneya JM, Ringera SP. Insight into the deformation mechanisms of α-Fe at the nanoscale. *Scripta Materialia*, Vol. 65, pp. 1037, 2011.

74. Xie KY, Shrestha S, Cao Y, Felfer PJ, Wang Y, Liao X, Cairney JM, Ringer SP. The effect of pre-existing defects on the strength and deformation behavior of a-Fe nanopillars. *Acta Materialia*, Vol. 61, pp. 439, 2013.

75. Friedman N, Jennings AT, Tsekenis G, Kim J, Tao M, Uhl JT, Greer JR, Dahmen KA. Statistics of Dislocation Slip Avalanches in Nanosized Single Crystals Show Tuned Critical Behavior Predicted by a Simple Mean Field Model. *Physical Review Letters*, Vol. 109, pp. 095507, 2012.

76. Papanikolaou S, Dimiduk DM, Choi W, Sethna JP, Uchic MD, Woodward CF, Zapperi S. Quasi-periodic events in crystal plasticity and the self-organized avalanche oscillator. *Nature*, Vol 490, pp. 517, 2012.

77. Bieler TR, Wright NT, Pourboghrat F, Compton C, Hartwig KT, Baars D, Zamiri A, Chandrasekaran S, Darbandi P, Jiang H, Skoug E, Balachandran S, Ice GE, Liu W. Physical and mechanical metallurgy of high purity Nb for accelerator cavities. *Physical Review Special Topics - Accelerators and Beams*, 13, pp. 031002, 2010.

78. Srinivasin R, Viswanathan GB, Levit VI, Fraser HL. Orientation effect on recovery and recrystallization of cold rolled niobium single crystals. *Materials Science and Engineering A*, Vol. 507, pp. 179, 2009.